Effective modeling of charge-transferring atom-surface collisions

Inauguraldissertation

zur

Erlangung des akademischen Grades eines

Doktors der Naturwissenschaften (Dr. rer. nat.)

der

Mathematisch-Naturwissenschaftlichen Fakultät

der

Universität Greifswald

vorgelegt von
Mathias Pamperin
geboren am 6. September 1986
in Grevesmühlen

Greifswald, 8. März 2019

Dekan:	Prof. Dr. Werner Weitschies
1. Gutachter:	PD Dr. Franz Xaver Bronold
2. Gutachter:	Prof. Dr. Frithjof Anders
Tag der Promotion:	27. September 2019

Contents

1 Summary

1.1 Introduction

This thesis deals with charge-transferring atom-surface collisions. They are of central interest in surface science [Bra89; Los90; Mod87a; New83; Win02; Yos86], a good overview can be obtained from [Mon14; Rab94; Win07]. Their importance for plasma science, for instance, arises mainly from the technical significance of secondary electron emission from surfaces, which may occur, under certain circumstances, in the course of a collision, see Fig. 1. They affect the modus operandi of low-temperature plasmas, for example, in flat-panel displays and basic properties of a gas discharge like the electric breakdown [Lie05] as well as the structure of the plasma sheath [Cam16; Lan15; Syd09; Tac04]. Another important application is neutral gas heating of plasmas in thermonuclear fusion reactors such as ITER which utilizes surface-based production of negative hydrogen ions [Kra08]. In addition to their importance for plasma science, many surface diagnostics used in other areas such as secondary ion mass spectrometry [Cza91] or metastable atom de-excitation spectroscopy [Har97] are based on charge-transferring processes as well and allows one to gain insight into the constituents and structure of a surface.

In principle, any number of charges may be involved in a particular charge-transferring process. In practice, however, it is typically dominated by resonant and Auger processes which involve one, respectively, two electrons as charges. The aforementioned secondary electron emission, for example, is a by-product of an Auger process–in case the emission is driven by the potential energy stored in the configuration of the incoming ion–and was in the focus since the early studies dating back right to the beginnings of modern condensed matter physics in the first half of the 20th century. Some most notable studies to mention are [Cob44; Mas30; Oli30] where already the combination of a resonant charge transfer followed by an Auger de-excitation is proposed. Also notable is Shekhter [She37] who first outlined the Auger character. His work in turn set the basis for Hagstrum [Hag53; Hag54] who pioneered, amongst other things, the ion neutralization spectroscopy, see [Rab03] for an overview, as well as surface physics in general, which was a mere niche topic before his contributions.

In contrast, the emission of secondary electrons from the surface may also be driven by the projectile's kinetic energy which is relevant in ion-surface scattering and sputtering [Gna99; Sig92]. The importance of potential electron emission, however, increases for lower projectile velocities and multiple charged ions which can store considerably more potential energy [Aum07]. Low temperature plasmas operate typically in the potential-driven regime due to kinetic energies of around ten electronvolts [Pie10]. Auger neutralization and de-excitation of ions/metastable species are thus the main channels of secondary electron emission at plasma boundaries [Phe99]. Being that important for surface physics, it is not surprising that they have been already reviewed several times in the last few decades [Bar94; Bra89; Los90; Mod87a; New83; Yos86]

and also more recently [Mon14; Win02; Win07] and it is by now certain that the basic mechanisms of secondary electron emission from solid surfaces have been identified.

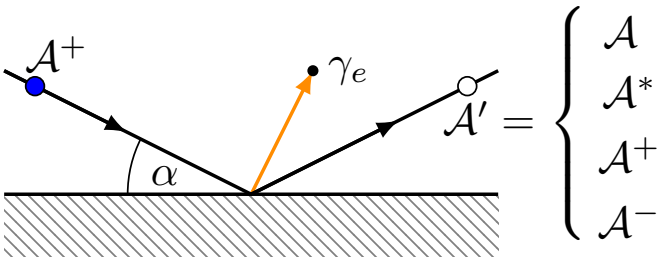

Fig. 1: Schematic representation of a positive ion $\mathcal{A}^+$ colliding with a surface with an angle of incident α. This process may induce secondary electron emission γ_e and/or change the configuration of the projectile.

Besides their great technological importance, charge-transferring atom-surface collisions are also of fundamental interest. By coupling the local quantum system of a projectile with its finite number of discrete electronic states to the large reservoir of continuous electronic states of a surface, the scattering of a single atomic or molecular projectile on a solid surface is a particular realization of a time-dependent quantum-impurity system [Mer98; Sha96]. In solid-state physics the coupling of a local moment, in the form of a local spin, in a metal to the itinerant electrons of the conduction band is the archetypal quantum impurity system with well documented properties and features [Ful91; Hew93]. One of these is the Kondo resonance, also referred to as Abrikosov-Suhl resonance. It arises at the metal's Fermi level and dissolves with increasing temperature. These physical effects appear in other quantum systems with a finite number of correlated internal states as well, if they are interacting with a reservoir of external states. One example are semiconductor quantum dots coupled to metallic leads [Agu03; Cha09; Pus04; Win94]. They allow to study local-moment physics in a well-controlled setting by fine tuning many parameters, for instance, by means of a tunable gate voltage [Cro98] or adatoms [Ter09]. A potential technological application is a single-electron transistor [Gol98a; Gol98b; Gra92]. Recent theoretical research [Coh11; Lec14; Müh11; Ngh14] aimed for a better understanding of temporal changes to the transport properties of quantum dots during the buildup and decay of local-moment type correlations.

Experimentally, charge-transferring atom-surface collisions require quite a lot of effort if one is interested in the intrinsic mechanisms of local-moment-type correlations or seeks to make quantitative statements about the secondary electron coefficient. As a result, only a handful of measured secondary electron coefficients exist. However, in the future this could change with newly introduced techniques [Dak16; Mar15].

The availability is different for measured energy distributions of emitted secondary electrons even though one has to note that the obtained spectra are in general–due to technical reasons–unweighted and allow thus no conclusion about the strength of the secondary electron coefficient. Over the years a variety of emission spectra were measured [Lan03; Lan07; Ses87] with different projectile and surface combinations such as helium ions scattering from aluminum [Hec98; Win93] or cesiated [Mül93] and potassium-covered [Bre92b] tungsten surfaces for example. Beyond the measurement

of the secondary electron coefficient and energy distribution, a recent experiment by He and Yarmoff provided strong, but indirect, evidence that the neutralization probability of a beam of strontium ions scattering on a clean gold surface is affected by local-moment-type correlations [He10; He11] by measuring an unusual temperature dependence of the neutralization probability of the strontium ions.

Theoretically, a charge-transferring atom-surface collision is quite a challenge to find an efficient way to deal with the many-body scattering problem. Thus, many approaches [Bon16; Igl13; Mas09; Mon13; Mor98; Wan01] exist. Especially when it is giving rise to a great variety of collision pathways such as during the scattering of helium ions from aluminum surfaces [Caz98; Gar03; Igl14; Lor98; Som00]. The number and type of reaction channels depends not only on the choice of the surface, but also on the projectile. For instance, alkali ions [Mar93], respectively, helium ions [Lor94] scattering on a copper surface are two very differing situations. Calculated emission spectra of secondary electrons [Mod87b; Pro63] allow then for a stepwise interpretation of the measured ones by adding channel by channel. Contrary to the low-temperature plasma environment where the ions travel perpendicular towards the surface, many atom-surface scattering experiments occur under grazing incident and occasionally with higher kinetic energies. This results in high lateral velocities compared to the perpendicular portion and has to be considered [Kim93; Sos03].

In this work, we theoretically investigate both aspects of charge-transferring atom-surface collisions: local-moment-type correlations and emission of secondary electrons from surfaces. Ideally, one chooses an approach that keeps as many electronic and lattice degrees of freedom at an ab-initio level as possible. In practice, however, this sophistication is hard to maintain. In this work, we do not aim to perform a description from first principles [Gar03; Igl13; Mon13; Mor98] which could utilize density functional theory or quantum-chemical techniques. Instead, we keep only the most important degrees of freedom of the scattering process and use effective models for them. These are basically the Anderson-impurity model [Baj07; Gol05; Kas87; Nak88; Onu96; Rom09] leading to time-dependent Anderson-Newns Hamiltonians and Gadzuk's semiempirical approach [Gad09; Gad67a; Gad67b] to describe the projectile-target interaction from classical image shifts. In direct comparison with the description from first principles, the semiempirical approach offers a flexible basis for the modeling of a great variety of projectile-target combinations. The addition of further effective models to increase the general quality of the results is possible since the approach is very modular. The clear physical interpretation of each effective model, as well as the requirement for only a few and generally available parameters are further advantages of this approach. Rewritten in terms of Coleman's pseudo-particle operators [Col84; Kot86], the model is then numerically analyzed. This is done within a non-crossing approximation for the hybridization self-energies [Lan91; Nor93; Sha94a; Sha94b] which are utilized by contour-ordered Green functions [Kad62; Kel64] for each relevant electronic state of the projectile.

In the first part of this thesis we employ our strategy of effective models and analyze the experiments of He and Yarmoff [He10; He11] from the outlined genuine many-body theoretical point of view. They found strong evidence for a local moment-type correlation that causes a non-monotonous temperature dependence of the neutralization probability of strontium ions on gold surfaces: it first increases and then decreases with

temperature. While the initial increase is most likely a combined thermal single-particle and a correlated many-body effect, the decrease, however, could be the long sought fingerprint for a transient mixed-valence resonance formed during an electron transfer taking place between a surface and an atomic projectile [Mer98; Sha96]. We employ the same strategy for magnesium where such evidence is not found.

In the second part we make extensive use of the projection technique which is an essential part of the Anderson-Newns model and modify our semiempirical theory with auxiliary bosons [Mar12] that essentially make the construction of any interaction and atomic configuration possible. We apply our model to the multi-channel problem of helium ions inducing secondary electron emission by scattering on metallic surfaces. Depending on the metal and the collision parameters, different reaction channels like Auger neutralization or resonant transfer followed by Auger de-excitation are open or closed. An unbiased description of the collision therefore requires a theoretical model that treats all channels equally and allows them to act simultaneously. This is ensured by the just mentioned projection technique and the employment of auxiliary bosons. In addition, the calculation of the secondary electron emission coefficient end energy distribution requires that we introduce surface transmission functions. They abstract the complex physical processes involved after a secondary electron is created but before it is emitted from the surface.

The third part reveals details of our numerical schemes that we used in each scenario. For strontium and magnesium we adapt the strategy of Shao and coworkers [Sha94a] for calculating the two-time Green functions numerically exact to our particular modeling of He and Yarmoff's experiment. For helium, we describe in detail how we deal with the different multidimensional integrations that arise for each transition matrix element of each involved Auger process and give a general overview of our numerical approach.

1.2 Mixed-valence correlations

In this section we comment on Article I and Article II and use the opportunity to give a general summary of our effective approach. The section is ordered as follows: First, we recall the Kondo effect from solid-state physics. Second, we present Gadzuk's semiempirical approach which we use to describe and interpret He's and Yarmoff's experiment [He10; He11] in terms of the afore recalled Kondo effect. Then, we construct a suitable Anderson-Newns Hamiltonian by using the Anderson-impurity model, summarize the quantum kinetic modus operandi and finally present some of our results of Article I, Article II and a few unpublished ones.

Kondo effect The Kondo effect, named after Jun Kondo who developed the first theoretical description [Kon64], is the unusual occurrence of a minimum in the electrical resistivity at low temperatures in metals. It arises from spin-flip scattering of itinerant conduction band electrons at local magnetic impurities. Kondo's original approach was application of third order perturbation theory to take the alignment of the scattering spin into account. This contributed an additional logarithmic term to the electrical resistivity. Although the new term explained the measured minimum [Haa34], it also diverges as the temperature approaches absolute zero. Other non-perturbative techniques, such as the Bethe ansatz, were later used in the development of new, exact

and singularity-free models [And80; Vig80]. This search for better models is known as the Kondo problem in solid-state physics and it is still an ongoing one due to the high variety and complexity of many materials, such as rare-earth or actinide-metallic compounds, generally known as heavy fermion systems [Lai18; Shi18], which commonly require tailored approaches.

The local magnetic impurities are in general unpaired valence electrons of a finite electronic system with a discrete energy distribution. Adatoms sticking on surfaces and quantum dots with metallic leads are, thus, ideal realizations [Cro98; Ter09]. Depending on the energies, three different regimes can be distinguished. In Fig. 2 they are shown for a two level system. The shaded areas are occupied, the non-shaded areas unoccupied electronic states of the metal's conduction band. Filled (empty) dots mark occupied (empty) levels of the impurity. The Fermi level is indicated by the thin horizontal line. In the non-magnetic regime, also known as filled (I) and empty orbital (V) regime, the local impurity acts like a crystallographic defect. Together with any other non-magnetic defects of the lattice it contributes to the constant residual resistivity of the metal. The magnetic case (III) is in fact the Kondo regime. The local impurity has one unpaired spin and, hence, contributes fully to the Kondo effect. Scenario (II) and (IV) show the mixed-valence regime where the electronic spin at the Fermi level is able to transfer to and fro between metal and impurity, which results in a lower than unity occurrence probability at the impurity. The total magnetic moment is, thus, lower than in the Kondo, but higher than in the non-magnetic regime.

In addition, the strength of the coupling Γ between metal and impurity plays a decisive role. For instance, if the difference between any discrete level and the Fermi level is less than the corresponding coupling strength, the system is in the mixed-valence regime. In terms of Sosolik and coworkers [Sos03], the system is then dominated by coupling. For small surface temperatures T_S a narrow resonance forms in the solid's density of states at the Fermi level. Its width is equal to the Kondo temperature T_K and, depending on the regime, it is either called Kondo (III) or mixed-valence (II and IV) resonance. These states build up to shield the spin-flipping of the magnetic impurity. This is the source of the Kondo effect [Ful91]. The mechanism breaks down for $T_\mathrm{S} \gtrsim 4T_\mathrm{K}$ as lattice vibrations interfere with the screening and effectively weaken the coupling between impurity and conduction band. This explains, however, the unusual temperature dependence of the electrical resistivity [Hew93] at low temperatures. As a final remark, strong coupling enhances Kondo-type effects [Sch66], as suitable electronic conduction band and impurity moments pair stronger together and more easily form a non-magnetic state.

Semi-empirical approach We now turn our attention to Gadzuk's semiempirical approach [Gad67a; Gad67b]. It combines the advantage of a clear physical picture [Gad09] with comparably good qualitative results for separation lengths greater than 6–7 Bohr radii between surface and projectile [Bor95b]. It is based on image shifts for the on-site variation of the projectile energy levels and on a golden rule calculation of the level width, i.e. the hybridization induced coupling Γ of the energy levels, which takes the non-orthogonality between surface states $|\vec{k}\rangle$ and projectile states $|\psi_{nlm}\rangle$ for resonant charge transfer already into account.

For later purposes, we assume an effective two level system. It can be employed for

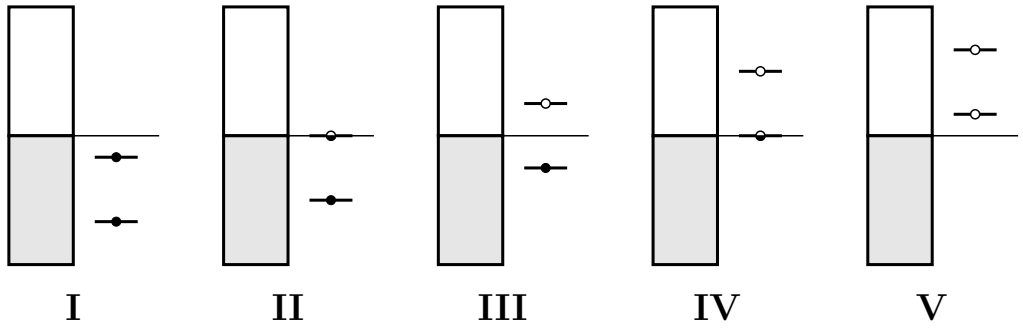

Fig. 2: Possible ground states for the Anderson model with two discrete levels. The square marks the conduction band of the metal, the thin horizontal line the Fermi level. Filled circles indicate the occupation of the corresponding level. Due to Pauli principle, two filled levels cancel the local moment. Hence, one can distinguish the non-magnetic (I and V), the mixed-valence (II and IV) and the magnetic (III) regime.

any alkali and alkaline earth metal projectile, provided the s-valence orbital plays the physically deciding role. Lower bound electrons of other shells contribute then only to the screening of the atomic core's charge. This alone allows us to model a wide range of possible target-projectile combinations as effective two-level systems. Each having two one-electron levels coupled to a continuum of states and an intra-atomic Coulomb repulsion U acting between both levels, enabling thereby correlation induced spin-flipping. Of course, if more than one shell has reactive levels this model has to adapt.

Without any interaction between projectile and surface the upper of the two levels ε_U coincides with the first ionization energy of the projectile I_1. The lower level ε_0 with the second ionization energy I_2. Polarization of the surface, however, let the ionization levels shift upward,

$$\varepsilon_U(t) = -I_1 + \frac{e^2}{4|z(t) - z_i|} \,, \tag{1}$$

$$\varepsilon_0(t) = -I_2 + \frac{3e^2}{4|z(t) - z_i|} \,, \tag{2}$$

with z_i the position of the metal's image plane measured from the crystallographic ending at $z = 0$. The collision trajectory of the projectile

$$z(t) = z_{\mathrm{TP}} + v_\perp |t| \,, \tag{3}$$

with z_{TP} the turning point and $v_\perp$ the projectile's velocity component perpendicular to the surface describes the classical center-of-mass motion of the projectile. It is the result of the trajectory approximation and is justified due to the high mass of the projectile [Mod87a]. Small turning points introduce the need for corrections from first-principles for the image shifts. However, we estimated them to not yet play a role for strontium and magnesium ions scattered by a gold surface, the experimental situation investigated by He and Yarmoff [He10; He11]. For the set of parameters used, we refer to Article I and Article II.

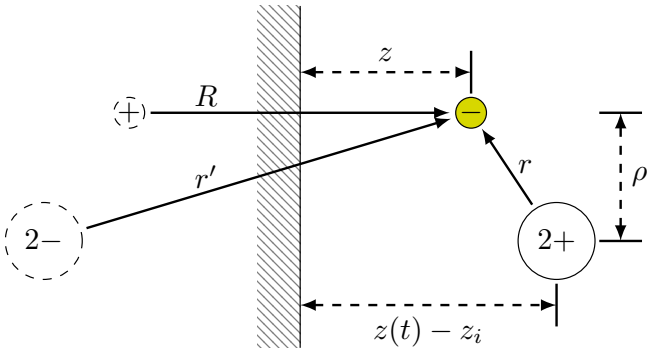

Fig. 3: Schematic representation of an ion (solid) inducing image charges (dashed) in a metal surface. The residual valence electron of the ion (colored) interacts with the projectile's screened core, the core's and its own image.

In Article II we offer an explanation of the strength and direction of the image shift by introducing virtual processes of energy gain and loss. Similarly, the shifts can be approximated by classical pictures [Gad09] as in Fig. 3 where a positive atomic core and an electron induce image charges in the metal's surface. The potential felt by the electron (colored) is

$$V(z,\rho) = -\frac{e^2}{2R} + \frac{2e^2}{r'} + V_C(r)\,, \tag{4}$$

with the effective Coulomb potential $V_C(r)$, which includes the entirety of intra-atomic exchange and interaction terms, $R = 2z$ and $r' = \sqrt{\big(z(t) - z_i + z\big)^2 + \rho^2}$, if the electron is at $\vec{r}_e = (z, \rho)$. Note that the charges are mirrored at the image plane at $z_i > 0$ before the crystallographic ending at $z = 0$. The effective Coulomb potential is in general $V_C(r) \geq 2e^2/r$ since the atomic charge is only partly screened by the $Z - 2$ closer bound electrons in lower lying orbitals [Cle63; Sla30]. Here, Z is the number of protons in the projectile's core. In addition, we can assume that the atomic radius of the projectile is with $R_\mathrm{A} \approx 3\ a_\mathrm{B}$ for magnesium and $R_\mathrm{A} \approx 4\ a_\mathrm{B}$ for strontium [Cle67; Sla64] much smaller than its distance to the surface's image plane for the longest part of the trajectory. The charge of the core's image $Z_{image} = -2$, whose absolute value is thus identical to the total screened charge of the atomic nucleus, not the effective one. In this regime $r \ll z(t) - z_i$ is then true up to and near the turning point. In this case, we can set $z \approx z(t) - z_i$ as well as $\rho \approx 0$ and approximate Eq. (4) with

$$V(r,t) = \frac{3e^2}{4|z(t) - z_i|} + V_C(r)\,. \tag{5}$$

The corresponding time-dependent on-site energy can be calculated quantum mechanically,

$$\varepsilon_0(t) = \left\langle \psi \middle| \frac{p^2}{2m_e} + V(r,t) \middle| \psi \right\rangle, \tag{6}$$

where ψ are orthonormal eigenfunctions of the Coulomb problem. We then find that the time-dependent part of Eq. (5) is identical to the image shift of Eq. (2) and that I_2 is completely determined by $V_C(r)$. As I_1 and I_2 are tabled [Cle74], we can simply ignore the effective Coulomb potential. A similar derivation with an additional electron outside the surface, thus, a total of two, leads to Eq. 1, the time-dependent on-site energy of the upper level.

In contrast to the mechanism of virtual processes we applied in our articles, this type of derivation of the image shift is substantially more involved in the mathematical description and therefore offers the possibility of qualitative improvement by omitting applied approximations. That being said, for small separation lengths, corrections resulting from first-principles are probably more necessary [Mon14].

The collision of the projectile with the target rearranges the charges between them via resonant charge transfer (RCT) and via various Auger processes which we outline in the next section. The absolute value of the matrix-elements describing the transport from the surface to the projectile $V_{\vec{k}}^{s\to p}(t)$ and vice-versa $V_{\vec{k}}^{p\to s}(t)$ must be equal. They differ only in phase so that

$$V_{\vec{k}}^{s\to p}(t) = \left[V_{\vec{k}}^{p\to s}(t)\right]^* . \tag{7}$$

The time-dependent Hamiltonian describing the interaction is $H(t) = p^2/2m + V_S(t) + V_P(t)$ where $V_S(t)$ is the surface's electronic potential including all polarization effects and $V_P(t)$ the residual Coulomb potential of the projectile. Instead of calculating the eigenfunctions for such a combined Hamiltonian, which is an extremely difficult undertaking, Gadzuk assumed [Gad67a; Gad67b] two things:

The potential $V_S(t)$ is a perturbation for any projectile electron described by $H_P(t) = p^2/2m_e + V_P(t)$ with eigenfunctions $|\psi\rangle$. Similarly, the potential $V_P(t)$ is a perturbation for any surface electron described by $H_S(t) = p^2/2m_e + V_S(t)$ with eigenfunctions $|\vec{k}\rangle$. In this semiclassical picture the electron may change its state from $|\vec{k}\rangle \to |\psi\rangle$ or from $|\psi\rangle \to |\vec{k}\rangle$ if it is perturbed by the corresponding potential thereby switching its position from the surface to the projectile or vice versa. In essence, that means that Eq. (7) becomes

$$V_{\vec{k}}(t) = \left\langle \vec{k}\middle| V_S(t)\middle|\psi\right\rangle + \gamma = \left[\left\langle \psi\middle| V_P(t)\middle|\vec{k}\right\rangle + \gamma'\right]^* , \tag{8}$$

where the functions γ and γ' arise as corrections from non-orthogonality between $|\vec{k}\rangle$ and $|\psi\rangle$. In general, the orthonormal basis of the complete Hilbert space can not be formed by combining basis states of isolated Hilbert sub-spaces, which $|\vec{k}\rangle$ and $|\psi\rangle$ essentially are. However, Gadzuk showed [Gad67b] that the correction

$$\gamma' = \sum_{\vec{k}\neq\vec{k}'} \left\langle n\middle|\vec{k}'\right\rangle \left\langle \vec{k}'\middle| V_P(t)\middle|\vec{k}\right\rangle \stackrel{!}{=} 0 , \tag{9}$$

for Wannier-like functions $|\vec{k}\rangle$ and $|\vec{k}'\rangle$ and that it is independent of the actual form of the intra-atomic Coulomb interactions encoded in $V_P(t)$.

We can thus very accurately calculate the matrix element by employing $V_P(t)$ as potential, using tabled one-electron Roothaan-Hartree-Fock atomic wavefunctions [Cle74] and choosing reasonable surface wavefunctions from an additional effective model. In

practice, we ignore any lateral variation of the surface and employ wave functions of a simple step potential $\psi_{\vec{k}}(\vec{r})$ with depth $V_0 = \phi + E_\mathrm{F}$ with ϕ the work function and E_F the Fermi energy of the metal. More details concerning the calculation of the matrix elements can be found in Article I and Article II. Qualitative improvements are possible by employing more sophisticated models such as the one from Jenning and Jones [Jon84] although Kürpick and Thumm [Kür96] came to the conclusion that the actual impact of such improvements is rather limited.

To actually interpret $V_{\vec{k}}(t)$, it is helpful to utilize Fermi's golden rule [Dir27; Fer50] to determine the strength of the coupling

$$\Gamma_{\varepsilon\sigma}(t) = 2\pi \sum_{\vec{k}} |V_{\vec{k}\sigma}(t)|^2 \delta(\varepsilon_{\vec{k}\sigma} - \varepsilon)\,. \tag{10}$$

Generally, Eq. 10 is interpreted as level width of the energy level ε, in our case $\varepsilon_0(t)$, respectively, $\varepsilon_U(t)$, or as inverse lifetime of the hybridized state.

Knowing the shifts and widths is crucial to choosing the right model. With this in mind, we can now perform a preliminary discussion of He and Yarmoff's experiment in the following paragraph.

He and Yarmoff's experiment He and Yarmoff's experiment [He10; He11] was carried out using positive gallium, magnesium and strontium ions as scattering projectiles. It was performed in vacuum where they positioned a cleaned polycrystalline gold foil as target. The purity and work function of the foil were monitored by Auger spectroscopy. The projectiles were produced and accelerated in a Colutron ion source chamber by heating a gallium, magnesium or strontium metal in argon plasma. Neutral projectiles were filtered out by electrostatically bending the beam. Time-of-flight spectroscopy and a microchannel plate detector were used to analyze the scattered projectiles. In Article I we perform a preliminary examination of the experiment for magnesium and strontium. In Article II we carry out an in depth analysis for strontium. We did only a very few preliminary investigations concerning gallium since its p-shell valence electrons introduce complicated issues compared to magnesium and strontium, which are both alkaline earth metals and have a completely filled s-valence orbital in their ground state. As a result, their ground state has no magnetic moment, that of gallium has one.

Fig. 4 shows the on-scale energetic situation for the magnesium 3s and strontium 5s valence orbital in front of a gold surface during scattering. At the end of the trajectory, the figure shows the expected final configurations of magnesium in the non-magnetic and of strontium in the mixed-valence regime. However, the gold surface is bombarded with positive ions and Mg^+ as well as Sr^+ carry a magnetic moment in a correlated two-level system from the beginning until they neutralize. Thus, the question is not whether a Kondo-type resonance manifests, as there will always temporarily occur one, but whether it significantly influences the charge transfer. This only happens if the system is in the mixed-valence regime for a while. Then, at least one electron level of the projectile overlaps with the occurring resonance at the Fermi level at $-\phi$ electronvolts. Thereby, the electron transport between surface and projectile is increased, see Fig. 5. The better the Kondo-type resonance is sampled by the widths of the few level system, the stronger the enhancement will be [Sha96]. In case of magnesium, we thus expect

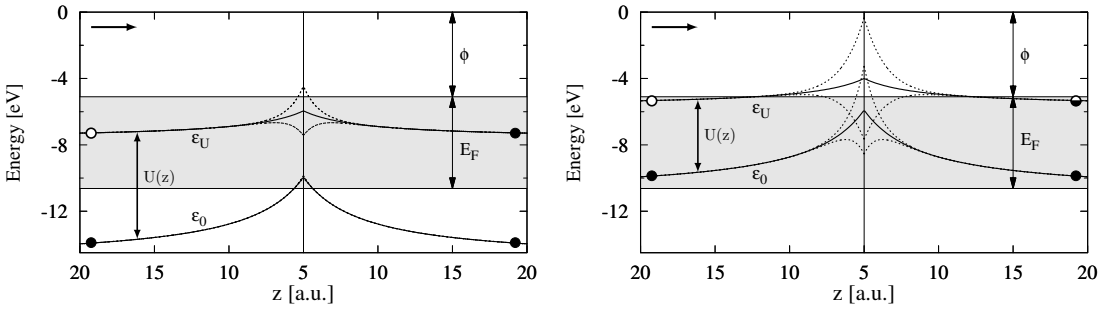

Fig. 4: Level shifts (solid) and widths (dotted) for magnesium (left) and strontium (right) during the scattering process. The projectile starts at $z = 20\ a_\mathrm{B}$ on the left, travels to the turning point at $z = 5\ a_\mathrm{B}$ and returns to its staring distance on the right side. The Fermi level $\varepsilon_\mathrm{F} = -\phi$ and $U(z)$ is the intra-atomic Coulomb interaction. The shaded area is the region of occupied electronic conduction band states at $T = 0$ K. Full circles indicate occupation of the corresponding level.

nearly no effect due to the resonance. The overlap is simply too small and occurs only directly at the turning point. When a model description is chosen, one could thus, in principle, ignore any resonance inducing on-site correlations. This is, however, not the case for strontium. The overlap with the region of the Fermi level is very extensive, as even the lower level ε_0 overlaps more with it than the upper level ε_U for magnesium did. Knowing this, we need, thus, a model capable of handling both levels simultaneously as well as the intra-atomic Coulomb interaction, which is key for any on-site spin-flipping event that causes the formation of Kondo-type resonances.

When the temperature increases, the Kondo resonance broadens and is better sampled by small widths. This increases the neutral fraction [Sha96] in addition to any thermal increase or decrease as, for example, shown by the blue curve on the right side of Fig. 5 for low temperatures. The thermal behavior is dependent on the actual position of the electron level of the projectile. If it is below the Fermi level when the transport typically occurs, it decreases with temperature and increases otherwise. In any case, when the resonance breaks down, the enhancement will end. The neutralization probability thus decreases from a certain point on with temperature until it is on the thermal level (total absence of any Kondo-type resonance). After the breakdown, the neutral fraction is solely dominated by the thermal smearing of the Fermi edge. The combined curve in a mixed-valence scenario may look like the curve in Fig. 5, which resembles the measured one of He and Yarmoff [He10], but is very dependent on the actual parameters of the system.

Likewise, the spectral density of the projectile should show a pronounced peak directly at the Fermi level caused by spin fluctuations for low temperatures, see left side of Fig. 5. If the temperature is increased, the peak broadens at first, increasing thereby transport due to better sampling of the peak [Sha96], but ultimately losing its spectral weight to the actual positions (caused by charge fluctuations) of the energy levels. This marks the transition from a coupling dominated system to an energy driven one [Sos03].

Only a system in the mixed-valence regime is able to feature the anomalous temperature dependence. In the non-magnetic and magnetic scenario the Kondo resonance at

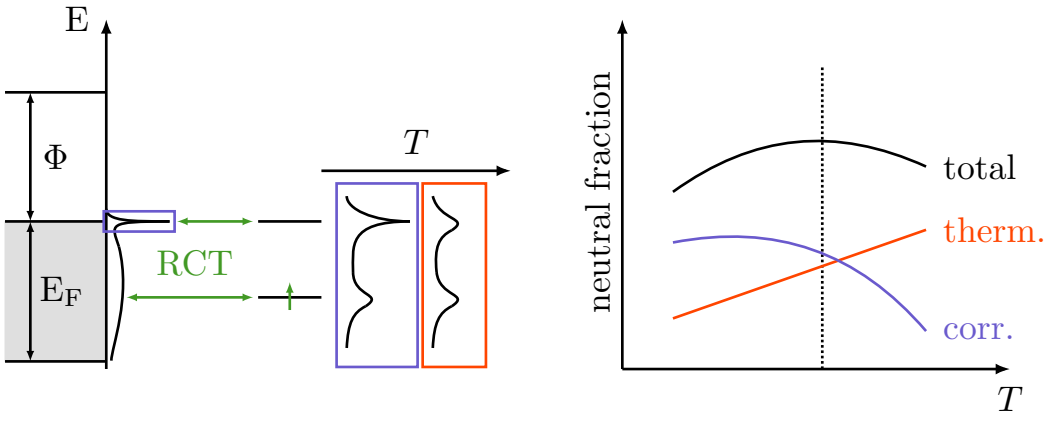

Fig. 5: Left: Schematic representation of the mixed valence scenario. At low temperatures the emergent Kondo-type resonance in the density of states enhances the transport into the projectile's levels. Right: Schematic temperature dependence of the neutral fraction.

the Fermi level does not hybridize, cf. Fig. 2, and is thus simply not sampled by any of the atomic levels of the projectile.

Anderson impurity model As a prerequisite for our quantum kinetic analysis we construct an Anderson-Newns Hamiltonian [Bra89; Los90; Mod87a; Yos86] for our two level system. Note that this Hamiltonian needs to be time-dependent due to the movement of the projectile which leads to time-dependent energy shifts and matrix elements. As a result, common known approaches to the Kondo problem from solid state physics, such as the Bethe ansatz [Hew93], can not be used. They were simply designed for scenarios in equilibrium.

With the time-dependent energy shifts and single matrix elements at hand, the Anderson-Newns Hamiltonian for a two level system interacting with a continuum of states is

$$\begin{aligned} H(t) = &\sum_{\sigma} \varepsilon_0(t)\, c_\sigma^\dagger c_\sigma + \sum_{\vec{k}\sigma} \varepsilon_{\vec{k}\sigma}\, c_{\vec{k}\sigma}^\dagger c_{\vec{k}\sigma} + \frac{1}{2} U(t) \sum_{\sigma} c_\sigma^\dagger c_\sigma c_{-\sigma}^\dagger c_{-\sigma} \\ &+ \sum_{\vec{k}\sigma} \left[V_{\vec{k}\sigma}(t)\, c_{\vec{k}\sigma}^\dagger (P_\sigma^0 + P_{-\sigma}^U) c_\sigma + \text{H.c.} \right]. \end{aligned} \tag{11}$$

The $c_\sigma^{(\dagger)}$ annihilate (create) an electron with spin polarization $\sigma = \{\uparrow, \downarrow\}$ in the valence orbital of the projectile that is the $3s$ shell for magnesium, respectively, the $5s$ shell for strontium. In an analogous manner, $c_{\vec{k}\sigma}^{(\dagger)}$ annihilates (creates) an electron with spin polarization σ and momentum $\vec{k}$ in the conduction band of the metal.

The first term in conjunction with the third controls the correct order of filling the two-level system. The first electron is always added with an energy of $\varepsilon_0(t)$. In principle, the second one adds the same energy $\varepsilon_0(t)$ to the system. However, the third term immediately adds $U(t)$, so that the second electron is at $\varepsilon_\mathrm{U}(t) = \varepsilon_0(t) + U(t)$. The intra-atomic Coulomb interaction $U(t) = \varepsilon_\mathrm{U}(t) - \varepsilon_0(t)$ and the level $\varepsilon_0(t)$ is filled before

$\varepsilon_{\mathrm{U}}(t)$. Likewise $\varepsilon_{\mathrm{U}}(t)$ donates an electron to the conduction band (second term) via charge transfer (last term) before $\varepsilon_0(t)$ does so. In addition, the spin can be arbitrarily chosen when an electron is transfered from $\varepsilon_{\mathrm{U}}(t)$ to the surface's conduction band as they are indistinguishable. This correlation introduces the spin fluctuations that are necessary for the Kondo-type resonance to occur and are only possible due to the third term. Note that H.c. stands for the Hermitian conjugated, the reversed process in the last term (in case of Eq. (11), charge transfer from the surface into one of the two atomic levels).

In physical reality the intra-atomic Coulomb interaction is generally large. As Coleman [Col84] and Langreth and Nordlander [Lan91] pointed out, one usually employs projection operators, here P^0_σ and $P^U_{-\sigma}$, which project non-fluctuating states out to effect this scenario and we make extensive use of them in Article III. The disadvantage is that the projected operators $P^0_\sigma c^{(\dagger)}_\sigma$ and $P^U_{-\sigma} c^{(\dagger)}_\sigma$ do not satisfy standard commutation relations and that, thus, the conventional quantum kinetic analysis based on diagrammatic expansion with Wick's theorem [Wic50] is complicated.

Two options are feasible. First, one could ignore the intra-atomic Coulomb interaction altogether. We henceforth call this option the $U = 0$ model. Here one does not project but rather has a set of single levels interacting with the continuum but not with each other. Within this model, the filling order of the electrons is neither controlled nor does any correlation induced effect manifest in the numerical results due to the impossibility of spin-flips. Note that to change Hamiltonian (11) to the $U = 0$ model one has to set, obviously, $U(t) = 0$ and change one of the energies $\varepsilon_0(t)$ in the sum of the first term to $\varepsilon_{\mathrm{U}}(t)$, in order to match the total ionization energy. This model may give excellent numerical results as long as certain conditions are met: Most importantly, none of the levels is allowed to significantly reach into the region of the Fermi level of the surface. Then one can be sure from the outset that no correlation-induced Kondo-type resonance plays a significant role. Magnesium scattering from a gold surface would thus be an ideal candidate, cf. Fig. 4. However, although the $U = 0$ model does allow accurate numerical statements about the neutral fraction under certain conditions, it can not predict anything depending on the actual spin alignment since those are hard coded by the model.

The second more refined option is to apply Coleman's pseudo-particle representation [Col84; Kot86]. Then, we can express the projection operators as well as $c^{(\dagger)}_\sigma$ in terms of pseudo-particle operators which obey fermion or boson commutation rules and thus can be treated using standard field theory. For the time-dependent case, this approach was first adapted by Langreth and Nordlander [Lan91] and was subsequently thoroughly investigated by Shao [Sha94a; Sha94b] together with the former two. One has, again, two ways to proceed. If one can identify one of the two levels as inactive or always projected out, e.g. the upper level in the magnetic regime (III) or the lower level in the non-magnetic regime (I) in Fig. 2, beforehand, one can apply $U \to \infty$, sending effectively the inactive level to plus or minus (by working with holes) infinity. Using this $U \to \infty$ model, one discards this way either a projectile configuration with two valence electrons (plus infinity) or an empty one (minus infinity). Unfortunately, from Fig. 4 we know that both valence levels of strontium reach with their width just to the Fermi level of the gold surface. We can thus conclude that both mentioned discardable configurations play a role and that we have to use a pseudo-particle representation

which takes a finite $U \neq 0$ into account.

In Article I and Article II, we simply applied the pseudo-particle representation for the ladder operators $c_\sigma^{(\dagger)}$ used by Shao and coworkers [Sha94b]. As we will discuss in the next section, for Article III we had to develop a pseudo-particle representation for an effective three-level system. The outlined approach in Article III is in principle the same for an effective two-level system:

Without limiting the generality, one chooses any completeness that contains each of the possible states of the two-level system. For example,

$$Q = |00\rangle\langle 00| + |10\rangle\langle 10| + |01\rangle\langle 01| + |11\rangle\langle 11| = 1 \tag{12}$$

works if we agree that the first entry of any given Fock-vector with occupancy number basis accounts henceforth for a spin-up, the second for a spin-down electron. The first term represents a double ionized projectile, i.e. Mg^{2+} or Sr^{2+}, the second and third term the positive ion Mg^+ or Sr^+ either with an unbound spin-up or spin-down electron and the last term the neutral atom Mg^0 or Sr^0. The corresponding projection operators

$$\begin{aligned} P_\uparrow^0 &= |00\rangle\langle 00| + |10\rangle\langle 10|\,, \\ P_\downarrow^0 &= |00\rangle\langle 00| + |01\rangle\langle 01|\,, \\ P_\uparrow^U &= |10\rangle\langle 10| + |11\rangle\langle 11|\,, \\ P_\downarrow^U &= |01\rangle\langle 01| + |11\rangle\langle 11| \end{aligned} \tag{13}$$

are the projection operators for RCT into the lower, respectively, the upper Ionization level. Note that $P_\sigma^0 + P_{-\sigma}^U = 1$ is a special case and does not apply in general. However, conveniently it is, therefore, often omitted in Hamiltonian (11) or similar ones by many authors (we did so in Article II) or, in case of $U \to \infty$, often $c_\sigma^{(\dagger)}$ is already the projected operator $P_\sigma^0 c_\sigma^{(\dagger)}$.

In the next step, we define that each physical configuration can be created by its corresponding pseudo-particle operator,

$$|00\rangle = e^\dagger|vac\rangle\,,\ |10\rangle = p_\uparrow^\dagger|vac\rangle\,,\ |01\rangle = p_\downarrow^\dagger|vac\rangle\,,\ |11\rangle = d^\dagger|vac\rangle \tag{14}$$

and analogously annihilated by e, p_σ and d. Operators representing configurations with an even number of electrons obey Bose statistics, that is $e^{(\dagger)}$ and $d^{(\dagger)}$, whereas $p_\sigma^{(\dagger)}$ belonging to a configuration with an uneven number of electrons should obey Fermi statistics. The pseudo-particle representation treats thus whole projectile configurations as a single particle allowing thereby to add (remove) more than one electron with a single application of an operator to (from) the projectile.

To express Hamiltonian (11) in this pseudo-particle representation, we let the original operators $c_\sigma^{(\dagger)}$ act on the completeness (12). Remember that $c_\uparrow^{(\dagger)}$ acts only on the first and $c_\downarrow^{(\dagger)}$ only on the second entry of any given vector due to our previous agreement. Then,

$$c_\uparrow^\dagger = c_\uparrow^\dagger * 1 = |10\rangle\langle 00| + |11\rangle\langle 01|\,, \tag{15}$$

$$c_\uparrow = c_\uparrow * 1 = |00\rangle\langle 10| + |01\rangle\langle 11|\,, \tag{16}$$

$$c_\downarrow^\dagger = c_\downarrow^\dagger * 1 = |01\rangle\langle 00| - |11\rangle\langle 10|\,, \tag{17}$$

$$c_\downarrow = c_\downarrow * 1 = |00\rangle\langle 01| - |10\rangle\langle 11|\,, \tag{18}$$

where the minus sign in (17) and (18) is by definition to satisfy the anti-commutation rules, in specific

$$\begin{aligned}[c_\uparrow^\dagger, c_\downarrow]_+ &= |10\rangle\langle 01| - |10\rangle\langle 01| \stackrel{!}{=} 0\,,\\ [c_\downarrow^\dagger, c_\uparrow]_+ &= |01\rangle\langle 10| - |01\rangle\langle 10| \stackrel{!}{=} 0\,.\end{aligned} \tag{19}$$

Using Eq. (15)–(18), we can easily calculate any product of $c_\sigma^{(\dagger)}$ with $c_{\sigma'}^{(\dagger)}$ or P_σ^0 and $P_{-\sigma}^U$ appearing in Hamiltonian (11) algebraically. With respect to the pseudo-particle operators (14), it becomes [Sha94b]

$$\begin{aligned}H(t) = &\sum_\sigma \varepsilon_0(t)\, p_\sigma^\dagger p_\sigma + [\varepsilon_0(t) + \varepsilon_U(t)]\, d^\dagger d \;+ \sum_{\vec{k}\sigma} \varepsilon_{\vec{k}\sigma}\, c_{\vec{k}\sigma}^\dagger c_{\vec{k}\sigma}\\ &+ \sum_{\vec{k}\sigma} \left[V_{\vec{k}\sigma}(t)\, c_{\vec{k}\sigma}^\dagger e^\dagger p_\sigma + \text{H.c.}\right] + \sum_{\vec{k}\sigma} \text{sgn}(\sigma) \left[V_{\vec{k}\sigma}(t)\, c_{\vec{k}\sigma}^\dagger d\; p_{-\sigma}^\dagger + \text{H.c.}\right].\end{aligned} \tag{20}$$

The Hamiltonian does not have an entry proportional to $e^\dagger e$ since the associated energy is equal to zero.

A constraint to the pseudo-states is obtained from the chosen completeness. In case of completeness (12), we obtain directly

$$Q = e^\dagger e \;+ \sum_\sigma p_\sigma^\dagger p_\sigma + d^\dagger d \;= 1\,, \tag{21}$$

by applying the pseudo-particle representation (14) to it. This ensures that only one of the four pseudo-particle states is ever realized. Note, if we use a completeness where only a subspace of states participates in the fluctuations, the completeness must be projected onto that subspace before the pseudo-particle representation is applied. However, the relationship between $c_\sigma^{(\dagger)}$ and the pseudo-particle states is always obtained using the total unprojected completeness as this ensures that all Hermitian conjugated processes transform correctly. Here all non-fluctuating states are intermediate and disappear after carrying out all algebraic calculations. For more informations, see Article III and the following section.

Quantum kinetics We employed the formalism developed by Langreth and Nordlander [Lan91; Sha94a; Sha94b] to calculate the occurrence probability for each projectile configuration. It is based on contour-ordered Green functions [Kad62; Kel64] and offers the possibility to derive rate equations with different degrees of approximation. However, these are not presented here, but in the above-mentioned original publications as well as in the appendix of Article II.

For the formalism to work, we need a contour-ordered Green function as propagator for each projectile configuration, one for the empty, single-, and double-occupied projectiles, and one for the conduction band electrons of the metal surface,

$$iE(t,t') = \left\langle T_\mathcal{C}\, e(t)\, e^\dagger(t')\right\rangle, \tag{22}$$

$$iP_\sigma(t,t') = \left\langle T_\mathcal{C}\, p_\sigma(t)\, p_\sigma^\dagger(t')\right\rangle, \tag{23}$$

$$iD(t,t') = \left\langle T_\mathcal{C}\, d(t)\, d^\dagger(t')\right\rangle, \tag{24}$$

$$iG_{\vec{k}\sigma}(t,t') = \left\langle T_\mathcal{C}\, c_{\vec{k}\sigma}(t)\, c_{\vec{k}\sigma}^\dagger(t')\right\rangle, \tag{25}$$

where the time variables run over the complex Keldysh contour as shown in Fig. 6. Their time arguments are thus complex. The operator $T_{\mathcal{C}}$ orders all objects on the contour. So Fig. 6 shows the case where $t' < t$ but an event occurs at t before an other occurs at t' because they happen on different branches of the contour. The operators making up the Green functions evolve in time with the full Hamiltonian (20). The statistical average with respect to the density matrix is marked by the brackets.

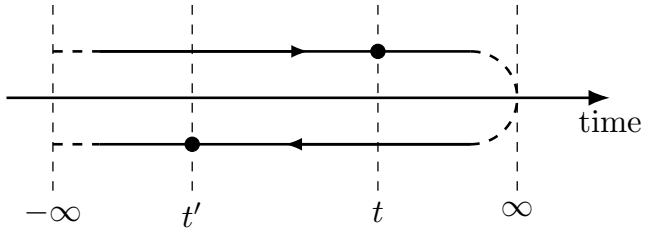

Fig. 6: Keldysh contour in the complex time domain. The Green functions (22)–(25) have time arguments t and t' slightly above or below the real time axis unlike their analytic pieces. The upper part of the contour runs from $t = -\infty$ to $t = \infty$, the lower back to $t = -\infty$.

Contrary to the Green functions (22)–(25), their analytic pieces have real time arguments, making them much more convenient to use. The less- and greater-than Green functions are given by

$$iH(t,t') = \Theta_{\mathcal{C}}(t-t')\,H^{>}(t,t') \mp \Theta_{\mathcal{C}}(t'-t)\,H^{<}(t,t')\,, \tag{26}$$

where H is a placeholder for E, P_σ, D or $G_{\vec{k}\sigma}$ and where $\Theta_{\mathcal{C}}$ is the Heaviside function defined on the complex Keldysh time contour. The upper sign is for fermionic (P_σ and $G_{\vec{k}\sigma}$) the lower sign for bosonic (E and D) Green functions. The advanced and retarded Green functions can be constructed from them,

$$iH^{R}(t,t') = \theta(t-t')\big[H^{>}(t,t') \pm H^{<}(t,t')\big]\,, \tag{27}$$

$$-iH^{A}(t,t') = \theta(t'-t)\big[H^{>}(t,t') \pm H^{<}(t,t')\big]\,, \tag{28}$$

where the upper sign is again for fermionic the lower for bosonic functions. Note that the retarded and advanced functions have to be projected onto the right subspace $Q = 1$ enforced by the constraint (21). Also, $H^{A}(t,t') = [H^{R}(t',t)]^*$ applies due to commutativity of complex numbers. Similarly, $H^{\gtrless}(t,t') = [H^{\gtrless}(t',t)]^*$ holds. The Heaviside function θ is defined on the real time axis.

All the information we are interested in can be accessed through the analytical parts of the pseudo-particle Green functions. This includes the occurrence probabilities for any projectile configuration as well as all spectral information. Explicit rules for obtaining them can be found in Article II. Note that for the latter, knowledge about the full solution of the two-time pseudo-particle Green functions is a prerequisite. For this matter, this circumstance essentially prevents the use of a rate equation.

Out of convenience, we use atomic units. Length is thus measured in Bohr radii a_{B}, energy in Hartree E_{H}, mass in electron mass m_e and $\hbar = 1$. Note that the time scale

of the scattering process is in the range of femtoseconds. Then, the Dyson equations, which determine the pseudo-particle Green functions, are

$$\left[i\frac{\partial}{\partial t} - \varepsilon_H(t)\right] H^<(t,t') = \int_{-\infty}^{\infty} d\bar{t}\, \Sigma_H^R(t,\bar{t}) H^<(\bar{t},t') + \int_{-\infty}^{\infty} d\bar{t}\, \Sigma_H^<(t,\bar{t}) H^A(\bar{t},t') \tag{29}$$

and

$$\left[i\frac{\partial}{\partial t} - \varepsilon_H(t)\right] H^R(t,t') = \delta(t-t') + \int_{-\infty}^{\infty} d\bar{t}\, \Sigma_H^R(t,\bar{t}) H^R(\bar{t},t')\,. \tag{30}$$

The analytic pieces of the self-energies $\Sigma_H^<(t,t')$ and $\Sigma_H^R(t,t')$ are obtained analogous to Eq. (26)–(28). Depending on H the self-energy Σ_H is either Σ_σ if $H = P_\sigma$, Π_e if $H = E$ or Π_D if $H = D$. Likewise, ε_H is either ε_0 for $H = P_\sigma$, or $\varepsilon_0 + \varepsilon_U$ for $H = D$. In case of $H = E$, $\varepsilon_H = 0$ applies, since none of two possible electrons is present in the valence shell.

The self-energies are the energies of the dressed pseudo-particles. They take changes to the environment into account which are caused by the interaction of the pseudo-particles with their system. For the self-energies at hand we use the so called non-crossing approximation (NCA) which is self-consistent and captures all diagrams with non-crossing propagators. It is a universally accepted approximation for heavy-Fermion systems in solid state physics and is generally applicable for systems with strong correlation compared to hybridization [Ful91; Hew93].

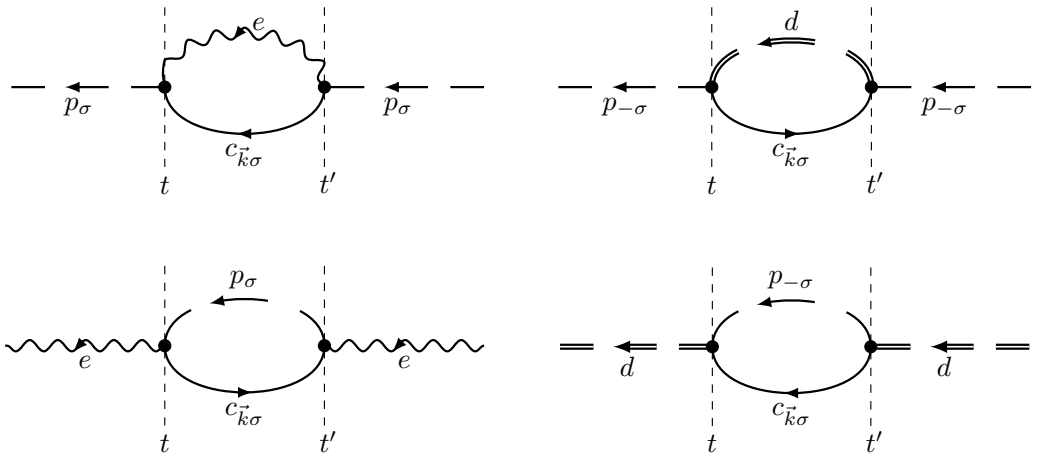

Fig. 7: Self-energies of the pseudo-particles. Only propagators between t and t' contribute, the other ones display the correct connection. The dots represent the transition matrix elements. $\Sigma_\sigma(t,t')$ is the sum of both top diagrams, $\Pi_e(t,t')$ equals the bottom left and $\Pi_D(t,t')$ the bottom right diagram.

In Fig. 7 we present all NCA self-energy diagrams which arise from the interactions encoded in Hamiltonian (20). Using standard diagrammatic rules [Lif81], any diagram can be translated into an equation. For instance,

$$-i\Pi_e(t,t') = -\,(i)^2 \sum_{\vec{k}\sigma} V_{\vec{k}\sigma}(t) V^*_{\vec{k}\sigma}(t')\, iP_\sigma(t,t')\, iG_{\vec{k}\sigma}(t',t)\,, \tag{31}$$

whose analytic pieces, using (26)–(28), are

$$\Pi_e^{\gtrless}(t,t') = \sum_{\vec{k}\sigma} V_{\vec{k}\sigma}(t) V_{\vec{k}\sigma}^*(t')\, P_\sigma^{\gtrless}(t,t')\, G_{\vec{k}\sigma}^{\lessgtr}(t',t)\,, \tag{32}$$

$$\Pi_e^{R}(t,t') = \sum_{\vec{k}\sigma} V_{\vec{k}\sigma}(t) V_{\vec{k}\sigma}^*(t')\, P_\sigma^{R}(t,t')\, G_{\vec{k}\sigma}^{<}(t',t)\,. \tag{33}$$

Normally, the NCA assumes that the surface states remain in thermal equilibrium. This is justified if the interaction $V_{\vec{k}\sigma}(t)$ is short-lived and relatively weak. This allows us to neglect any dressing for the bulk propagator and use

$$G_{\vec{k}\sigma}^{\gtrless}(t,t') = f^{\gtrless}(\varepsilon_{\vec{k}\sigma})\, e^{-i\varepsilon_{\vec{k}\sigma}(t-t')}\,, \tag{34}$$

with $f^<$ the Fermi-Dirac distribution function and $f^> = 1 - f^<$.

Earlier, we introduced the level width (10), a measure of strength of the coupling. As an approximation, the self-energies (32)–(33) can be expressed in proportion to the level width by inserting the delta function $\delta(\varepsilon_{\vec{k}\sigma} - \varepsilon)$ and adding an integration over ε. Then,

$$2\pi \sum_{\vec{k}} V_{\vec{k}\sigma}^*(t) V_{\vec{k}\sigma}(t')\, \delta(\varepsilon_{\vec{k}\sigma} - \varepsilon) \simeq \sqrt{\Gamma_{\varepsilon\sigma}(t)\Gamma_{\varepsilon\sigma}(t')}\,. \tag{35}$$

For equal times, this approximation gives the correct result. For sufficiently unequal times, large deviations can occur, which nevertheless play a minor role: $V_{\vec{k}\sigma}^*(t)V_{\vec{k}\sigma}(t')$ decreases exponentially with unequal times. In a time integration, the leading contribution comes, thus, from the argument at equal times! The utility of this approach becomes clear when we look at the second approximation we adopted. It concerns the integration over ε we just introduced and exploits the exponential behavior of $\Gamma_{\varepsilon\sigma}(t)$ even further. For example, for $H = E$, the ε-dependent part of the right hand side of (30) can be approximated as follows:

$$\begin{aligned}
&\int \frac{d\varepsilon}{2\pi}\, \sqrt{\Gamma_{\varepsilon\sigma}(t)\Gamma_{\varepsilon\sigma}(t')}\, f^<(\varepsilon)\, \exp\left[-i \int_t^{t'} d\tau(\varepsilon_0(\tau) - \varepsilon)\right] \\
&\qquad \simeq \sqrt{\Gamma_{\varepsilon_0(t)\sigma}(t)\Gamma_{\varepsilon_0(t')\sigma}(t')} \int \frac{d\varepsilon}{2\pi}\, f^<(\varepsilon)\, \exp\left[-i \int_t^{t'} d\tau(\varepsilon_0(\tau) - \varepsilon)\right],
\end{aligned} \tag{36}$$

which applies analogously to all other Dyson equations as well. We did not attempt to derive this approximation mathematically by an asymptotic stationary-phase analysis [Ble86]. Instead we adopted the qualitative, physics based reasoning of Langreth and Nordlander [Lan91]. In principle, this is a semiclassical approximation (SCA) which exploits that the action-type integral of the exponential function of Eq. (36),

$$S(t,t') = \int_t^{t'} d\tau(\varepsilon_0(\tau) - \varepsilon)\,, \tag{37}$$

becomes minimal for

$$\varepsilon_0(\tau) = \varepsilon \tag{38}$$

at any time. This corresponds to the classical resonance condition of resonant charge transfer. If (38) is met, the transfer is thus particularly efficient. Following Langreth's and Nordlander's arguments, this sets the leading order of the oscillating integrand to $\Gamma_{\varepsilon_0(t)\sigma}(t)$. Hence, $\Gamma_{\varepsilon\sigma}(t)$ can be pulled outside the integrand by setting ε to $\varepsilon_0(t)$, respectively $\varepsilon_U(t)$ for other right hand sides in (29) and (30).

In concert, both approximation are numerically quite beneficial. Without any approximations, the $\vec{k}$-sum on the left hand side of (35) has to be computed for three changing variables, namely t, t' and ε. Depending on the grid size, this may require quite a lot of memory and computation time. The level widths $\Gamma_{\varepsilon_0\sigma}(t)$ and $\Gamma_{\varepsilon_U\sigma}(t)$ on the other hand depend only on one variable and omit, in addition, any imaginary part which is presumably suppressed anyway by the strong oscillations of the residual integrand [Lan91]. Much more important, however, is that the level widths offer an intuitive physical interpretation and are easily visually comparable to each other. This makes them a central component of our effective approach.

Temperature dependence of the neutral fraction The self-energies $\Sigma_\sigma(t,t')$, $\Pi_e(t,t')$ and $\Pi_d(t,t')$ effectively couple the pseudo-particle Green functions with each other. To calculate the temperature dependence of the neutral fraction, it is thus imperative to solve the Dyson equations (29) and (30) for each pseudo-state. Numerically, this is done on a time-grid where one first calculates all retarded and afterwards all less-than Green functions simultaneously. A much more detailed description concerning the numerical scheme can be found in Article II and in the section after the next.

Knowing all pseudo-particle Green functions, the neutral fraction

$$\alpha_w = \lim_{t\to\infty} D^<(t,t)\,. \tag{39}$$

From a programming point of view, this, of course, means that the maximum time t_{max} must be selected appropriately to allow $D^<(t,t)$ to equilibrate. The Fermi-Dirac distribution function $f^<$, introduced in (34), makes all pseudo-particle Green functions dependent on the surface temperature T_S. Therefore, the Dyson equations (29) and (30) need to be redissolved for each individual temperature.

Fig. 8 shows our results from Article I and Article II. For the parameter set required for the calculation, we refer to these articles. The temperature dependence of the neutral fraction for magnesium (left) is well within the stated error of He and Yarmoff [He11]. The zoom reveals that the neutralization probability decreases very weakly but monotonically with increasing temperature. Since the upper level $\varepsilon_U(t)$ is well below the Fermi-level at all times, see Fig. 4, this is indeed the expected behavior: As the surface temperature T_S increases, more and more hole excitation occur below the Fermi-level in the conduction band of the gold surface. Statistically, less surface states can release an electron to an empty projectile level that remains below the Fermi level. For $T_\mathrm{S} = 900$ K this smearing is less than one tenth of one electronvolt. In direct comparison to the Fermi energy $E_\mathrm{F} = 5.53$ eV and the work function $\phi = 5.1$ eV this is a small effect, which therefore can only cause a slight decrease of the neutral fraction with temperature. There is no indication whatsoever that a possibly occurring Kondo-type resonance is sampled at all by the projectile levels of magnesium. Considering magnesium as a benchmark, we believe that our effective modeling provides excellent

results for the neutralization probability for other non-magnetic and magnetic scenarios as well.

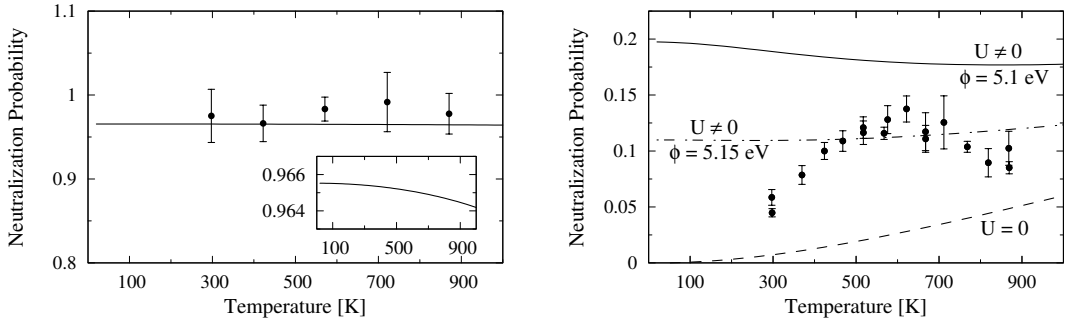

Fig. 8: Temperature dependence of the neutralization probability $\alpha = n_d(\infty)$ for magnesium (left panel) and strontium (right panel) ions after hitting a gold surface. The experimental data is from [He11] for magnesium and [He10] for strontium. For the set of parameters used, we refer to the articles.

The neutral fraction differs dramatically in a mixed-valence scenario, see the right panel of Fig. 8. It shows our numerical results for strontium. Using the usual work function of gold, $\phi = 5.1$ eV, our approach obviously overestimates the neutralization probability compared to the measured data of He and Yarmoff [He10]. However, it is still of the correct order of magnitude which is not self-evident in terms of our effective modeling. In addition, we also found a relatively strong negative temperature dependence that extends over the entire range of considered temperatures. This is a clear indication of the occurrence of a Kondo-type mixed-valence resonance at the Fermi level: Remembering from Fig. 4 that the upper level $\varepsilon_U(t)$ is already above the Fermi level when its level width is strongest, one typically expects an increase of the neutralization probability with temperature analogous to the decrease in the magnesium scenario if any kind of occurring Kondo-type resonance is not sampled at all. This is the case for the $U = 0$ model, see Fig. 8. Here, any kind of intra-atomic Coulomb correlation $U(t)$ is neglected on purpose which specifically eliminates the possibility of electronic spin fluctuations on the projectile. These are, however, elementary to the Kondo effect [Kon64]. As a consequence, no Kondo-type resonance will occur as we will see in the next paragraph. In addition, the correlated $U \neq 0$ result is greatly enhanced compared to $U = 0$ to a point where the strong increase of the neutralization probability with temperature of the experiment can no longer be represented with our model. Most certainly, either the energy shifts and, depending on them, the level widths need fine tuning or, also likely, the NCA diagrammatic expansion for the self-energies in Fig. 7 has to be supplemented with higher order diagrams (vertex corrections), essentially upgrading the expansion to the one-crossing approximation (OCA), see [Tos10] for a qualitative comparison for quantum dots.

To give an impression, Fig. 9 shows the fourth order diagram for $\Pi_e(t, t')$ utilizing the same diagrammatic rules as before. We performed, however, only preliminary calculations so far. The increased complexity compared to the NCA, see Fig. 7, should not be underestimated.

Apart from the smearing of the Fermi edge, the only reasonable interpretation of

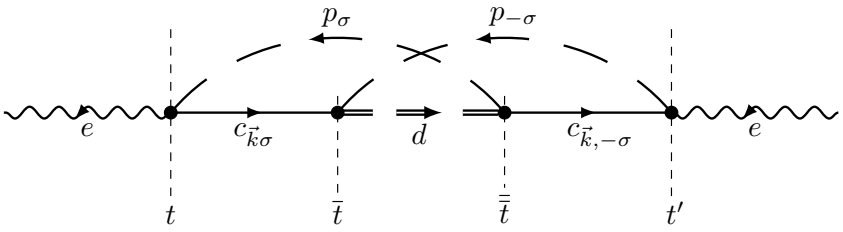

Fig. 9: One-crossing approximated self-energy $\Pi_e(t, t')$.

the decrease is that a mixed-valence resonance decays with temperature as described earlier. In the paragraph after the next, we show that this occurs indeed.

The enhancement depends strongly on the difference between the crossing upper level $\varepsilon_U(t)$ and the Fermi level. For example, when the work function is slightly changed by $\Delta\phi = 0.05$ eV to $\phi = 5.15$ eV, see Fig. 8, the enhancement is halved. In Article I we used $\phi = 5.2$ eV, with the result that the enhancement compared to the uncorrelated $U = 0$ calculation is almost gone. As the work function increases, the relative distance between the upper level $\varepsilon_U(t)$ and the Fermi level increases, too. Due to less overlap between them, this in turn leads to less sampling of the mixed-valence resonance by the broadened level. The effect is so pronounced because a lot of spectral weight is transferred to the resonance, as we will see in the following paragraph.

As a last note, at around $T_S = 800$ K the negative slope ends and a slight positive temperature dependence of the neutralization probability becomes visible. This is almost the maximum temperature used in the experiment. At this point the mixed-valence resonance does not dissolve, as our numerical results in the paragraph after the next show. The dwindling negative temperature dependence is rather superimposed by the increasing positive temperature dependence caused by thermal excitations in the conduction band of the surface. It would be very interesting to know if the experimentally obtained neutralization probability possesses such behavior as well and if so, does it agree with the results of the uncorrelated $U = 0$ model from this point on?

Projectile spectral densities The spectral densities for removing or adding a physical electron at time T with energy ω are defined by

$$\rho^{\gtrless}(\omega, T) = \frac{1}{2\pi} \sum_\sigma \int_{-\infty}^{\infty} d\tau \, G_\sigma^{\gtrless}(T + \tau/2, T - \tau/2) \, e^{i\omega\tau} \tag{40}$$

where $T = (t + t')/2$ and $\tau = t - t'$ are difference variables and $G_\sigma^{\gtrless}(t, t')$ the physical electronic Green functions of the projectile. For $U = 0$, $G_\sigma^{\gtrless}(t, t')$ can be calculated directly using the Dyson equations. For $U \neq 0$ on the other hand, the physical Green functions must be constructed from the pseudo-particle ones we introduced earlier,

$$G_\sigma^<(t, t') = P_\sigma^<(t, t') e^R(t', t) + D^<(t, t') p_{-\sigma}^R(t', t) \,, \tag{41}$$

$$G_\sigma^>(t, t') = p_\sigma^R(t, t') E^<(t', t) + d^R(t, t') P_{-\sigma}^<(t', t) \,, \tag{42}$$

where $H^R(t, t') = -i\Theta(t - t') h^R(t, t')$ has been used with $H^R(t, t')$ and $h^R(t, t')$ being placeholders, see Article II for a detailed derivation.

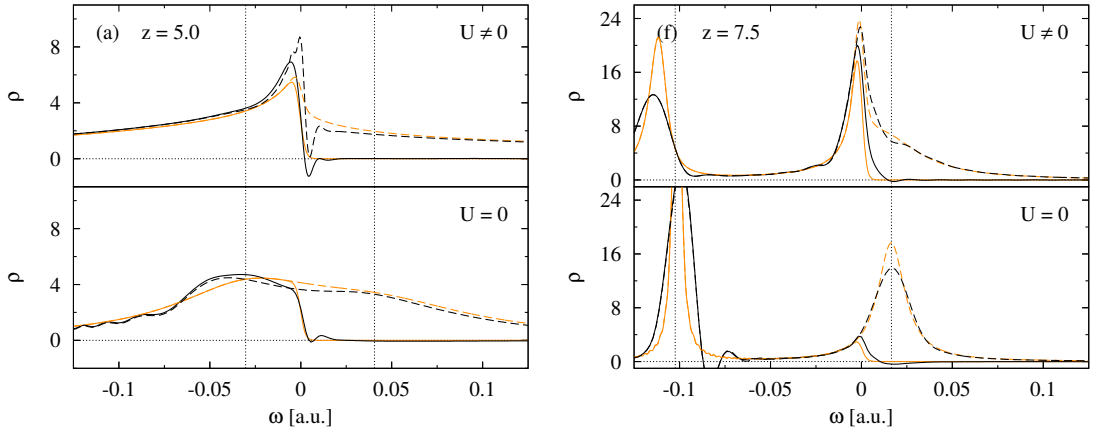

Fig. 10: Strontium projectile spectral densities summed over the two spin orientations at $z = 5$ a_B and $z = 7.5$ a_B of the outgoing branch of the trajectory. The upper panels show the correlated ($U \neq 0$), the lower panels the uncorrelated ($U = 0$) case. The surface's temperature $T_S = 400$ K. The black lines show the instantaneous, the orange ones the equilibrated spectral densities. Solid/dashed lines give the occupied/total spectral densities. The surface's Fermi level is located at $\omega = 0$ and the thin vertical lines indicate the instantaneous position of the energy levels.

In Fig. 10 we calculated the instantaneous (black curves) and equilibrated (orange curves) spectral densities on the outgoing branch of the trajectory for strontium ions scattering from a gold surface. The equilibrated ones were obtained by holding the projectile in position until the occupancies equilibrated. In addition, the instantaneous spectral densities $\rho^{\gtrless}(\omega, T)$ are Wigner distributions in energy ω and time T which can not be measured simultaneously. To deal with these quantum mechanical uncertainties, Wigner distributions become negative in some regions of its defined space. This seems to happen in Fig. 10 for both compared models. We can, however, not rule out the Gibbs phenomenon [Gib98; Gib99; Wil48] from occurring during the numerical Fourier transformation. The equilibrated results, though, speak against this possibility.

If one compares the spectral densities for strontium using both models (the $U \neq 0$ results are from Article II, the $U = 0$ ones are to date unpublished) in Fig. 10, two things become obvious: First, clearly spectral weight is transfered to form a strong mixed-valence resonance at the Fermi level at $\omega = 0$ in the $U \neq 0$ scenario. Thus, the $U \neq 0$ model works as intended and a Kondo-type resonance is indeed generated by spin fluctuations. The resonance is not only formed directly at the turning point ($z_{TP} = 5\, a_B$), but in advance, resulting in a significant contribution to the neutralization probability over a comparatively long period of time. Second, and a little more subtle, the presence of a resonance actively reduces the portion of unoccupied states. The number of total states (dashed lines) above the Fermi level ($\omega > 0$) is reduced using the $U \neq 0$ model compared to $U = 0$. These mostly unoccupied states are transferred to the resonance at the Fermi level and recombined there, resulting in an increased number of occupied states (solid lines). This can be observed for both presented separations lengths in Fig. 10. The strength of the overlap between level width $\Gamma_{\varepsilon_U(t)\sigma}(t)$ and

resonance governs the portion of occupied states of the resonance.

If, for some reason, the position of the Fermi level changes with respect to the energy levels of the projectile (thin vertical dotted lines), the number of occupied states may vary dramatically. This is due to the Lorentzian shape of the broadened level and the resonance, which leads to an exponential dependence of the overlap between the two. This is the reason why a very small increase in the work function as in Fig. 8 of just $\Delta\phi = 0.05$ eV is responsible for the loss of neutralization probability of at least 30 %.

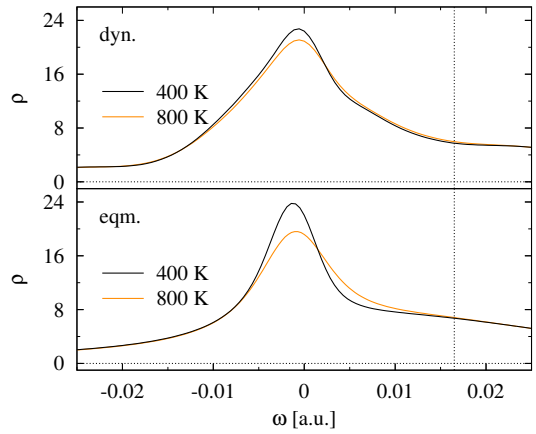

Fig. 11: Temperature dependence of the strontium projectile total spectral density summed over the two spin orientations at $z = 7.5$ a_B on the outgoing branch of the trajectory. The upper panel shows the dynamic, the lower the equilibrated scenario. The surface's Fermi level is located at $\omega = 0$ and the thin vertical line indicates the instantaneous position of $\varepsilon_U(t)$. We use the same set of parameters as in Article I and Article II.

Temperature dependence of the projectile spectral densities According to the literature on strongly correlated systems [Ful91; Hew93], the mixed-valence resonances of the spectral densities we presented in the last paragraph should decay with increasing temperature, causing thereby the negative temperature dependence of the neutralization probability shown in Fig. 8. So far, we have not addressed this in any publication. Our new results presented here, however, fit very well into the reasoning of Article I and Article II.

When the resonance decays, we expect that spectral weight from the total spectral density (dashed lines in previous paragraph) is transferred from the resonance to the position of the energy levels of the projectile. In other words, spin fluctuations become less import in favor of charge fluctuations [Ful91]. Using a strontium projectile, the upper level $\varepsilon_U(t)$ is actually above the Fermi level for the most reactive part of the flyby. Therefore, a large portion of transferred weight represents newly unoccupied states when the temperature increases which explains the negative temperature dependence of the neutralization probability.

Fig. 11 shows the shape of the resonance for strontium at two different temperatures, once for the dynamic (dyn.) and once for the equilibrated (eqm.) scenario, as described in the last paragraph. As expected, the resonance dissipates with increasing

temperature. In addition, spectral weight is transfered in the general direction of the upper level $\varepsilon_U(t)$ (vertical thin dotted line). The temperature dependence is, however, much more pronounced, and the actual shape of the resonance more thinner, in the equilibrated scenario where the projectile is held just in front of the surface. Using our effective model, a high projectile velocity seems to suppress the overall temperature dependence. It would be very interesting and also beneficial to repeat the experiments of He and Yarmoff [He10; He11] at lower projectile velocities in order to clarify the question of how the neutralization probability changes with temperature From our theoretical results we expect it to become even more pronounced.

1.3 Ion-induced secondary electron emission

In this section we comment on Article III. The main goal was to provide an effective model and a numerical scheme that allow quantitative statements about the secondary electron emission coefficient γ_e and its energy spectrum $\gamma_e(\varepsilon)$. In addition, we wanted to reuse most of the concepts we discussed in the previous section as well. For the most part, we succeeded. Nevertheless, there are some important differences and changes which we will discuss below. Before we come to this, we briefly describe the physical situation of the helium-metal system. We conclude this section with a few comments on our numerical results.

Physical situation The helium-metal system was selected by us because of the relatively high number of availably experimental data that is indispensable for comparison with our results. That being said, the absolute number of measured and theoretical secondary electron coefficients is nevertheless comparatively small, and only recently were experiments proposed to change this [Dak16; Mar15].

The ionization energy needed to extract a single electron from the ground state of a helium atom $\mathrm{He}^0(1\mathrm{s}^2, 1^1\mathrm{S}_0)$ is about $I_{1^1\mathrm{S}_0} \approx 24.6$ eV. This is more than a factor of two greater than the typical binding energy of electrons in the conduction band of a common metal [Ash76; Höl79]. Resonant charge transfer between the conduction band of the target and the ground state level of the projectile can thus be excluded. Instead, it is possible that $\mathrm{He}^+(1\mathrm{s}, 1^2\mathrm{S}_{1/2})$ recombines directly into the ground state via Auger neutralization (AN) as illustrated in Fig. 13. However, in the direct vicinity of the surface edge, it is predicted [Mon14] that the first ionization level of the projectile will hybridize with lower lying bands of the surface, thereby enabling resonant transfer of electrons into the ground state.

This scenario is especially important for high projectile velocities perpendicular to the surface, as they are usually accompanied by smaller turning points. With a perpendicular velocity of the order of $v_\perp \approx 10$ eV, the low temperature plasma-wall interface (the plasma sheath) partly falls into this category [Pie10]. As already mentioned, the experimental data collection is rather scarce. In general, experiments are performed under grazing incidence and with small projectile velocities. In this thesis we will therefore discard the resonant charge transfer into the first ionization level. On the other hand, there are excited helium states with ionization energies close to the Fermi level of a typical metal (work function and Fermi energy are approximately five electronvolts).

From these states we choose $\mathrm{He}^*(1\mathrm{s}2\mathrm{s}, 2^1\mathrm{S}_0)$ and $\mathrm{He}^*(1\mathrm{s}2\mathrm{s}, 2^3\mathrm{S}_1)$ which have one of

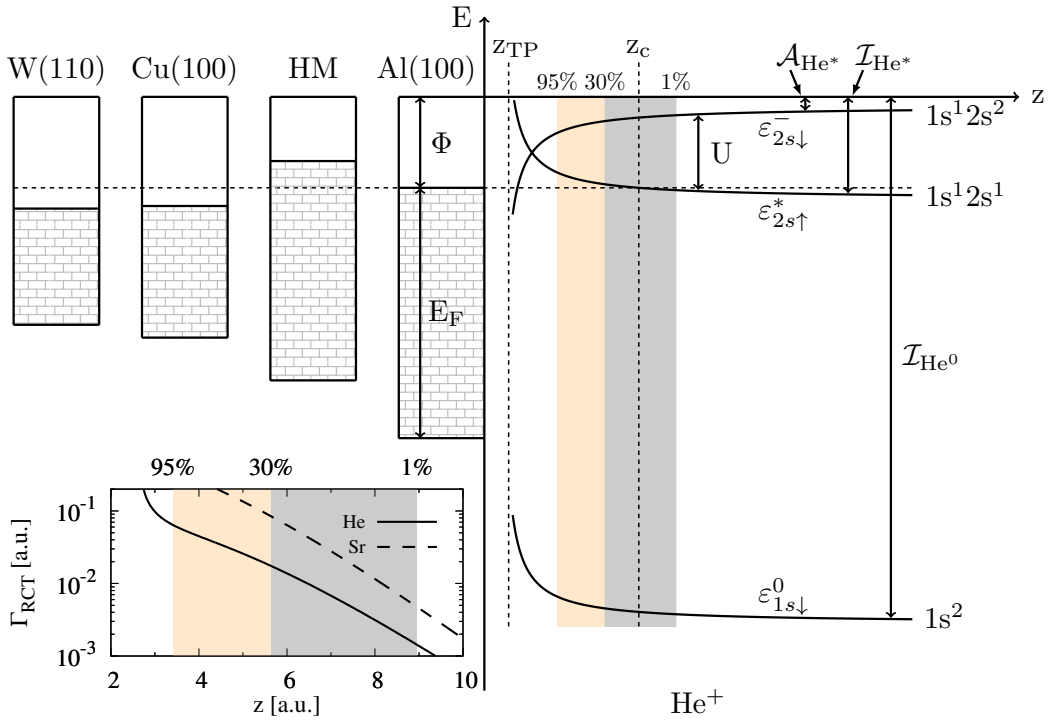

Fig. 12: On scale energetic representation of studied helium-metal systems. Note that the energy levels corresponding to the $He^*(1s2s)$ and $He^-(1s2s^2)$ configurations are actually spin dependent and thus non-degenerate. The diagram on the left compares the level widths of the level crossing the Fermi level at z_c for the helium-aluminum and strontium-gold system. For the helium-aluminum system with an angle of incidence of $\alpha = 15°$ and a kinetic energy of $E_{kin} = 60$ eV of the projectile, the shaded area shows the region where already 95 % of the reaction occurred on the incoming branch of the trajectory.

the largest ionization energies ($I_{2^1S_0} \approx 4$ eV and $I_{2^3S_1} \approx 4.8$ eV) of all possible excited states. These levels are in some situations therefore capable of resonantly exchanging charges with the target's conduction band and serve as starting points for direct and indirect Auger de-excitation (DAD and IAD) into the ground state, as shown in Fig. 13. Note that the $He^*(1s2p, x)$ configurations may be important in some scenarios [Igl13; Igl14] but rates solely based on s-orbital wave functions tend to have a greater impact on the outcome. The energy levels of these states shifts upward, as described in the last section, see Eq. (1). The resonant charge transfer from the surface to one of these metastable states may be either open or closed, i.e. the formation of excited helium species by means of RCT can be effectively prevented by large work functions. To test our model, we used a hypothetical metal (HM) that has a smaller work function than usual, see Fig. 12 for an energetic true-to-scale representation and comparison of all investigated helium-metal systems. In practice, cesiated [Des80; Mül93; Pap80] or K and Li covered metal surfaces [Bre92a; Bre92b] provide, for instance, this flexibility. However, this may also introduce new surface states which enable new reaction channels. Therefore, our hypothetical metal is used exclusively to test the interaction of all considered channels of our model.

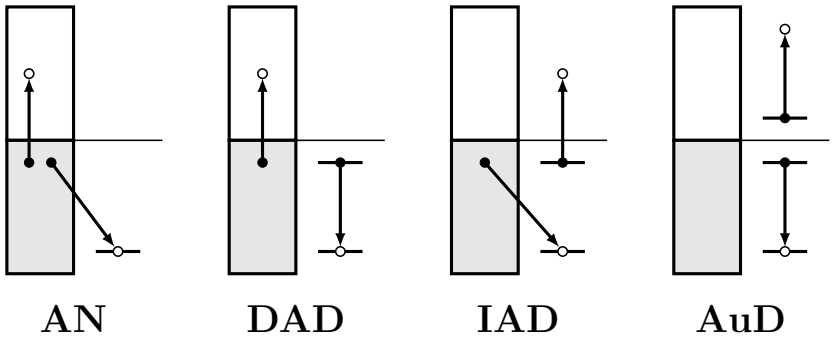

Fig. 13: Implemented Auger processes. From left to right: Auger neutralization (AN), direct and indirect Auger de-excitation (DAD and IAD) and autodetachment (AuD).

Looking at Fig. 12, excited states may become important for aluminum as well. The $He^*(1s2s, 2^3S_1)$-level starts just below the aluminum's Fermi level and crosses it at $z_c = 14.44\ a_B$ which is farer away than it was for strontium. We do not think that Kondo-type physics play a significant role for this particular helium-metal combination:

First, the level width which potentially samples the Kondo-type resonance is about a factor five smaller than its strontium counterpart, see lower left panel in Fig. 12 for comparison. This is due to the higher spatial extension of the 5s strontium wave functions compared to their 2s helium versions, resulting overall in a smaller overlap with the surface's electronic wave functions for helium. And secondly, even if a mixed-valence scenario enhances the generation of excited states, it is likely that its impact on the neutralization probability is small due to the number of simultaneously acting reaction channels. Due to its subtle role, we decided to neglect Kondo-type physics and concentrate on the interplay of the numerous reaction channels. This decision allowed us to approximate the set of pseudo-particle Dyson equations, cf. Eq. (29), with Langreth and Nordlander's approach to simple master equations [Lan91; Sha94a; Sha94b] which essentially leads to a set of coupled rate equations.

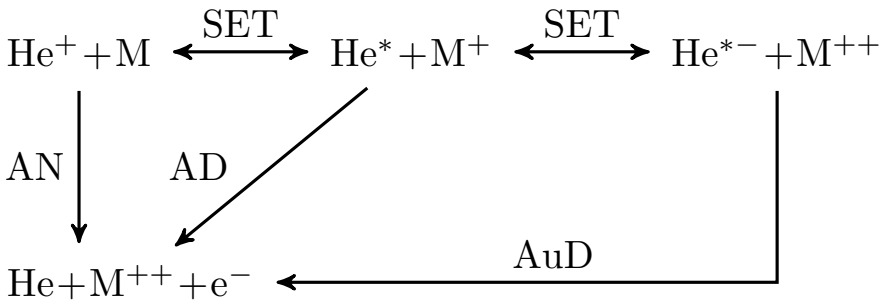

Fig. 14: Interplay of possible charge transfer processes during the collision of a He^+ ion with a metal surface. The charge of the metal M appears here just for charge conservation purposes and is not part of the actual model.

It is possible that after one of the metastable states $He^*(1s2s, 2^1S_0)$ or $He^*(1s2s, 2^3S_1)$ has been realized, yet another electron transfers resonantly into the 2s shell of the

helium projectile. The corresponding affinity levels shift downwards, see Fig. 12. In this process $He^{*-}(1s2s^2, 2^2S_{1/2})$ is generated. This state may decay independently from the surface into the ground state. This is a process called autodetachment (AuD) and is also schematically shown in Fig. 13. As we will see, this process leads to a very distinct high energy feature in the spectrum of emitted secondary electrons.

To keep track, Fig. 14 summarizes the discussed reaction scheme. Note that from now on we use single-electron transfer (SET) synonymously with resonant charge transfer (RCT) to separate it more clearly from the Auger processes, which always involve two electrons. Compared with the scenario outlined in the previous section, the added number of levels, processes and states require an adjusted approach.

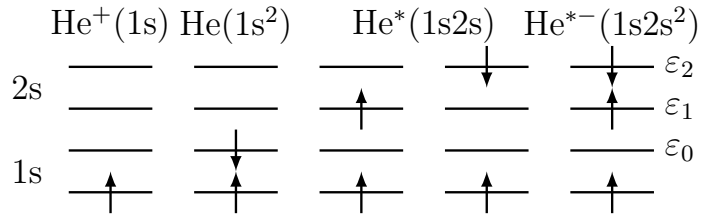

Fig. 15: Representation of the five considered helium configurations.

Adjusted model The cornerstones of our effective model, as presented in the previous section, remain unchanged. This was also one of our main premises. The projectile can be modeled by a three-level system with energies ε_0, ε_1 and ε_2 as illustrated in Fig. 15 if the 1s shell is assumed to be always at least occupied by, for instance, a spin-up electron. The exact value of these energies depends on two things: on the occupancy of the shells and on the sequence they were occupied. Another difficulty is that the completeness of a three-level system is composed of nine states, of which only the five in Fig. 15 are of interest. The representation in Fig. 14 is also exclusive. Therefore, configurations other than those associated with each reaction can not participate even if an electron in another configuration occupies an appropriate energy level. For instance, $He^{*-}(1s2s^2)$ shall not be subject to DAD or IAD even though there are suitable electrons in the 2s shell. These points are accounted for by employing projection operators

$$P_{n_0n_1n_2} = |n_0n_1n_2\rangle\langle n_0n_1n_2| \,. \tag{43}$$

They project any part of the Anderson-Newns Hamiltonian onto the desired subspace of states $|n_0n_1n_2\rangle$ of the three-level system with $n_i = 0, 1$ electrons in the energy levels ε_0, ε_1 and ε_2. The energy that results from applying the projection operators to ε_i is freely definable. Consistently applied, this technique zeros the weight of the four non-participating excess-states in the completeness

$$Q = \sum_{n_0}\sum_{n_1}\sum_{n_2} |n_0n_1n_2\rangle\langle n_0n_1n_2| = 1 \,. \tag{44}$$

This makes the construction of even the most complicated reaction schemes possible, as this can be used to describe intra-atomic Coulomb interactions, switches between

ionization and affinity levels or non-degenerate energies. In practice, each term of the Anderson-Newns-Hamiltonian must be complemented with a sum of projection operators of the participating projectile configurations which makes the Hamiltonian slightly more complicated. However, the projection operators vanish when a pseudo-particle transformation is performed.

There are other minor changes to three of the effective descriptions in our previous model. These can be found in detail in Article III. In short: i) We employed modified hydrogen wavefunctions instead of the tabulated Roothaan-Hartree-Fock wavefunctions provided by Clementi and Roetti [Cle74] due to lack of data for excited states. ii) Since Gadzuk's effective approach to the matrix elements [Gad67a; Gad67b] does not take modifications of the step potential mimicking the surface by the Coulomb potentials of the He^+ ion into account, we added–inspired by Probst [Pro63] and Penn and Apell [Pen90]–a semiclassical correction using the WKB approximation to the wavefunction of the surface electron that fills the 1s shell of the He^+ projectile during AN and IAD. This usually enhances the transfer and brings it within reasonable agreement with other methods and calculations [Lor96; Val05; Wan01]. iii) We take gracing angles of incidence into account by replacing the Fermi-Dirac distribution with the angle-averaged velocity-shifted distribution of Sosolik and coworkers [Sos03].

In addition to these three points, we neglected the issue of non-orthogonality [Val05] between target and projectile wavefunctions in the effective Auger matrix elements. In our estimation, see Article III, this should lead to deviations only in case of near perpendicular incidence of the projectile. For grazing incidence on the other hand, much of the charge transfer is completed before they come into effect, see Fig. 12.

Secondary electron emission Using the same reasoning as in the previous section, each helium configuration in Fig. 15 can be defined by a pseudo-operator:

$$\begin{aligned} &|000\rangle = e^\dagger|vac\rangle\,,\ |011\rangle = d^\dagger|vac\rangle\,,|100\rangle = s^\dagger_{1\downarrow}|vac\rangle\,,\\ &|010\rangle = s^\dagger_{2\uparrow}|vac\rangle\,,\ |001\rangle = s^\dagger_{2\downarrow}|vac\rangle\,. \end{aligned} \tag{45}$$

Again the pseudo-operators obey Fermi (Bose) statistics if the number of electrons of the configuration is odd (even). Note, however, that the selected form of Fock state omits the first 1s electron, as it is present in every configuration of the projectile. The labeling is a reminder to the type of configuration of the three level system: (e)mpty, (d)ouble and (s)-shell or (s)ingle with the index accounting the number of the shell.

If we employ the same reasoning as before, distinguish internal surface state excitations $c^{(\dagger)}_{\vec{k}\sigma}$ from external continuum ones $c^{(\dagger)}_{\vec{q}\sigma}$, carefully project all interactions as outlined above to the correct subspaces of (44) and include auxiliary Bose operators $b^{(\dagger)}_\sigma$ which conserve the total energy of the Hamiltonian during the transitions between ionization and affinity levels and is a technique that was already used in the description of charge-transferring molecule-surface collisions [Mar12], the Anderson-Newns Hamiltonian in

pseudo-particle representation becomes

$$\begin{aligned}
H(t) = {} & \varepsilon^0_{1s\downarrow}(t) s^\dagger_{1\downarrow} s_{1\downarrow} + \sum_\sigma \varepsilon^*_{2s\sigma}(t) s^\dagger_{2\sigma} s_{2\sigma} + \left[\varepsilon^-_{2s\uparrow}(t) + \varepsilon^-_{2s\downarrow}(t)\right] d^\dagger d \; + \sum_\sigma \omega_\sigma(t) b^\dagger_\sigma b_\sigma \\
& + \sum_{\vec{k}\sigma} \varepsilon_{\vec{k}\sigma} c^\dagger_{\vec{k}\sigma} c_{\vec{k}\sigma} + \sum_{\vec{q}\sigma} \varepsilon_{\vec{q}\sigma}(t) c^\dagger_{\vec{q}\sigma} c_{\vec{q}\sigma} + \sum_{\vec{k}\sigma} \left[V^{\mathrm{SET}}_{\vec{k}\sigma}(t) c^\dagger_{\vec{k}\sigma} e^\dagger s_{2\sigma} + \mathrm{H.c.}\right] \\
& - \sum_{\vec{k}\sigma} \left[\,\mathrm{sgn}(\sigma) V^{\mathrm{SET}}_{\vec{k}\sigma}(t) c^\dagger_{\vec{k}\sigma} b^\dagger_\sigma s^\dagger_{2-\sigma} d \; + \mathrm{H.c.}\right] + \sum_{\vec{q}} \left[V^{\mathrm{AuD}}_{\vec{q}}\, c^\dagger_{\vec{q}\uparrow} s^\dagger_{1\downarrow} d \; + \mathrm{H.c.}\right] \\
& + \sum_{\vec{k}\vec{k}'\sigma} \left[V^{\mathrm{DAD}}_{\vec{k}\vec{k}'\sigma}(t) c^\dagger_{\vec{k}'\sigma} s^\dagger_{1\downarrow} c_{\vec{k}\sigma} s_{2\downarrow} + \mathrm{H.c.}\right] + \sum_{\vec{k}\vec{q}\sigma} \left[V^{\mathrm{IAD}}_{\vec{k}\vec{q}\sigma}(t) c^\dagger_{\vec{q}\sigma} s^\dagger_{1\downarrow} c_{\vec{k}\downarrow} s_{2\sigma} + \mathrm{H.c.}\right] \\
& + \sum_{\vec{k}_1\vec{k}_2\vec{k}'\sigma} \left[V^{\mathrm{AN}}_{\vec{k}_1\vec{k}_2\vec{k}'\sigma}(t) c^\dagger_{\vec{k}'\sigma} s^\dagger_{1\downarrow} e \; c_{\vec{k}_1\downarrow} c_{\vec{k}_2\sigma} + \mathrm{H.c.}\right]. \qquad (46)
\end{aligned}$$

Thanks to the pseudo-particle representation, the physical meaning is particularly easy to grasp. For instance, the last term describes Auger neutralization: two internal electronic surface states as well as the empty projectile configuration, that is He^+, are annihilated altogether and at the same time, the ground state He^0 is generated by $s^\dagger_{1\downarrow}$ along with a surface state.

Knowing the Hamiltonian, we can analyze it within the same quantum-kinetic approach [Lan91; Sha94a; Sha94b] as before. This includes a set of pseudo-particle Green functions determined by Dyson equations and non-crossing approximated self-energies. This time, however, the Dyson equations can be simplified to a linear set of coupled ordinary first order differential equations due to negligible influence of the Kondo effect. In such a case the Dyson equation can be evaluated within a saddle-point approximation which utilizes that the various two-time functions are peaked around the time-diagonal. This is equivalent to Langreth and Nordlander's simple master equation (SME) [Lan91]. For the ground state, for example, one obtains the rate equation

$$\begin{aligned}
\frac{d}{dt} n_g(t) = {} & \Gamma^<_{\mathrm{AN}}(t)\, n_+(t) + \Gamma^<_{\mathrm{IAD}\uparrow}(t)\, n_\uparrow(t) \\
& + \left[\Gamma^<_{\mathrm{IAD}\downarrow}(t) + \Gamma^<_{\mathrm{DAD}\downarrow}(t)\right] n_\downarrow(t) + \Gamma^<_{\mathrm{AuD}}\, n_-(t) \qquad (47)
\end{aligned}$$

where $n_g(t)$, $n_+(\mathrm{t})$, $n_\uparrow(t)$, $n_\downarrow(t)$ and $n_-(t)$ denote, respectively, the instantaneous occurrence probability of the ground state, the positive ion, the triplet and singlet metastable state and the negative ion. The rates $\Gamma^{\gtrless}_{\ldots}(t)$ were constructed in the style of the golden rule [Fer50]. For example,

$$\Gamma^<_{\mathrm{AN}}(t) = 2\pi \sum_{\vec{k}_1\vec{k}_2\vec{k}'\sigma} |V^{\mathrm{AN}}_{\vec{k}_1\vec{k}_2\vec{k}'\sigma}(t)|^2 \rho_{\vec{k}_1\vec{k}_2\vec{k}'\sigma}(t) \qquad (48)$$

with

$$\rho_{\vec{k}_1\vec{k}_2\vec{k}'\sigma}(t) = f^<(\varepsilon_{\vec{k}_1\downarrow}) f^<(\varepsilon_{\vec{k}_2\sigma}) f^>(\varepsilon_{\vec{k}'\sigma})\, \delta(\varepsilon^0_{1s\downarrow}(t) - \varepsilon_{\vec{k}_1\downarrow} - \varepsilon_{\vec{k}_2\sigma} + \varepsilon_{\vec{k}'\sigma}) \qquad (49)$$

is a representative of Auger-type rates. Similarly, single-electron transfer rates are akin to

$$\Gamma^{\gtrless}_{\mathrm{SET},\sigma}(t) = 2\pi\, f^{\gtrless}(\varepsilon^*_{2s\sigma}(t)) \sum_{\vec{k}\sigma} |V^{\mathrm{SET}}_{\vec{k}\sigma}(t)|^2 \delta(\varepsilon^*_{2s\sigma}(t) - \varepsilon_{\vec{k}}). \qquad (50)$$

The rate equation (47) makes it particularly easy to deduce a differential equation for the probability of emitting a secondary electron with energy ε at time t since every process in Fig. 14 that ends with the occurrence of the ground state of helium also generates an excited electron. It reads

$$\begin{aligned}\frac{d}{dt}\gamma_e(\varepsilon,t) = &\bar{\Gamma}^{<}_{\mathrm{AN}}(\varepsilon,t)\, n_+(t) + \bar{\Gamma}^{<}_{\mathrm{IAD}\uparrow}(\varepsilon,t)\, n_\uparrow(t) \\ &+ \left[\bar{\Gamma}^{<}_{\mathrm{IAD}\downarrow}(\varepsilon,t) + \bar{\Gamma}^{<}_{\mathrm{DAD}\downarrow}(\varepsilon,t)\right] n_\downarrow(t) + \bar{\Gamma}^{<}_{\mathrm{AuD}}(\varepsilon)\, n_-(t)\,. \end{aligned} \tag{51}$$

Due to their relationship, rate equation (47) and (51) share the same general structure. However, the spectrally resolved rates $\bar{\Gamma}^{\gtrless}_{\dots}(\varepsilon,t)$ have been modified [Bar94; Feu76] to take transmission conditions into account since not all excited electrons can leave the surface. Otherwise they are the same as in Eq. (48), except that the $|\vec{k}|$-integration of the excited electron was not carried out. More details are given in Article III.

The emission spectrum of secondary electrons is obtained by solving Eq. (51) and

$$\gamma_e(\varepsilon) = \lim_{t\to\infty} \gamma_e(\varepsilon,t)\,. \tag{52}$$

The secondary electron emission coefficient, also known as γ-coefficient, is obtained by integrating the spectrum (52) over all energies,

$$\gamma_e = \int \gamma_e(\varepsilon)\, d\varepsilon\,. \tag{53}$$

It is thus the total probability that an electron is emitted at all from the surface.

In Fig. 16 we compare our results based on eqs. (51) and (52) with experimental data. For tungsten the data comes from Müller and coworkers [Mül93] and from Lancaster and coworkers [Lan03] for aluminum and copper. For technical reasons, measured spectra are generally not normalized to the γ-coefficient, as shown in Eq. (53). In principle, this summarizes the experimental problems: The secondary electron emission spectra have been readily accessible for decades, the γ-coefficients not. However, Müller and coworkers give an educated estimate of $\gamma_e^{exp} = 0.22$. For tungsten we could therefore compare absolute numbers, but not for aluminum and copper, since the experimentalists did not provide any coefficients and presented their spectra in arbitrary units with no way to normalize the area enclosed by the emission spectra according to Eq. 53.

As far as the high-energy side of the spectrum is of concern, the agreement between our numerical result obtained from Eq. (51) and (52) (solid line) and the experimental data turns out quite satisfactory for tungsten. The low-energy side, however, deviates drastically. The reason is this: the model lacks an effective description of relaxing surface processes for excited electrons, e.g. scattering cascades [Lan07; Pro63], and of higher order Auger processes with more than two electrons [Bre92b]. In Fig. 16 the energy distribution of the missing processes (dashed line) was guessed by us to give the best combined (dotted line) result. In our opinion, most of the low-energy secondary electrons come from cascade processes, since three-electron Auger processes should have significantly smaller amplitudes in the spectral density than an Auger process with two electrons.

For aluminum and copper, we opt for another strategy, which is only an option due to the good high-energy agreement of the theoretical and experimental data for

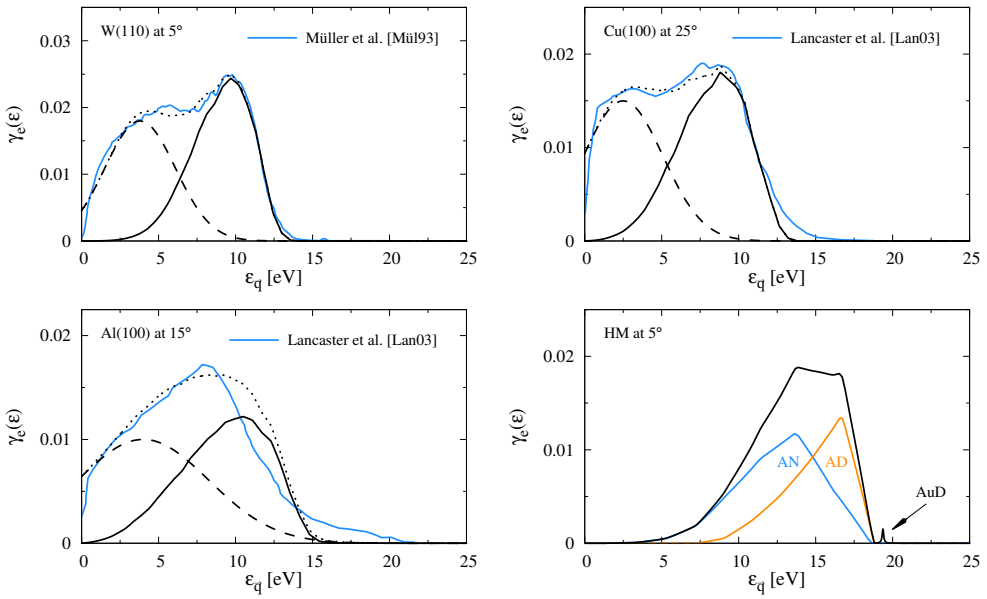

Fig. 16: Spectral density of secondary electrons emitted from various surfaces hit by a positive helium ion.

tungsten. Assuming that the ratio of experimental and theoretical γ-coefficients for each metal is nearly constant, we can predict the experimental coefficients and use them to weight the measured spectra for comparison. The reason for this is that the contribution of the unknown, missing low energy process should be nearly identical for similar metals. In case of tungsten, we calculated $\gamma_e^{theo} = 0.12$ for the parameters of the experiment. The ratio $r = \gamma_e^{theo}/\gamma_e^{exp}$ for tungsten is then roughly one-half. The aluminum and copper emission spectra of Lancaster *et al* are then scaled by setting $\int d\varepsilon \gamma_e^{theo}(\varepsilon, t \to \infty)/\int d\varepsilon \gamma_e^{exp}(\varepsilon) = r$, where r is ratio obtained from the tungsten data of Müller *et al* and from us. In principle, this trick can only be applied to tungsten-like surfaces (work function of about five electronvolts), as a more general statement still lacks experimental and theoretical data. Applied to copper in Fig. 16, however, it provides a good high-energy match between experimental and theoretical data. Using this method, we estimated $\gamma_e^{exp} = 0.19$ for copper. For aluminum the high-energy tail of the spectrum does not match as good as for the former two metals. The smaller work function in conjunction with a large Fermi energy lead to broad spectrum for the electron emitted by the Auger neutralization process. In addition, indirect Auger de-excitation is enabled by the small work function although it provides only a small number of secondary electrons between 15 and 20 eV. The estimated experimental value is $\gamma_e^{exp} = 0.18$. Using our scaling approach, the height of the emission spectra does not match nor does a flat low-energy shoulder appear in the experimental data. This suggests that the low-energy and high-energy process spectra strongly overlap as indicated by the dashed line to form the shape of the total spectrum.

The most important process of Fig. 14 for tungsten, copper and aluminum is Auger neutralization (AN). Only in the spectrum of aluminum we find faint features which we attributed to indirect Auger de-excitation (IAD). To demonstrate how the rest of the processes in Fig. 14 may affect the secondary electron emission, we constructed

a hypothetical metal HM which has a smaller than usual work function of $\phi = 3$ eV and $E_\mathrm{F} = 9$ eV. The small work function allows the formation of all excited states and thus opens all channels. Decomposing the spectrum into its originating processes, the low-energy tail of the spectrum is dominated by Auger neutralization, whereas the high-energy tail with its steep cut-off is due to combined Auger de-excitation, with emphasize on direct Auger de-excitation. An additional faint peak is added by autodetachment above the main feature of the spectrum. However, its position is not the expected one [Bor95a; Hem91]. Our analysis showed that the position of the peak is most sensitive to the effective model of the level shifts. Surprisingly, this is not the case with the other Auger processes, but certainly for resonant charge transfer. In our opinion, this should be addressed as one of the first points in an extension of our model.

1.4 Numerical schemes

Two-time Green functions To solve the pseudo-particle Green functions (22)–(24) numerically exact, we adapt the approach of Shao and his colleagues [Sha94a] to the $U \neq 0$ scenario. This adds two more Green functions $D^<(t,t')$ and $D^R(t,t')$ to their discretization strategy. To do this, we summarize their approach in a general way using our placeholder-notation from Eq. (26)–(30). The first step is to discretize the Dyson equations (29) and (30) using the trapezoidal rule to calculate the integral on the right hand side,

$$\int_a^b f(x) \approx \Delta \sum_{k=1}^{N} c_k f(x_k) \tag{54}$$

with $\Delta = (b-a)/N$ and $c_k = 1 - \delta_{1k}/2 - \delta_{Nk}/2$ as well as for solving the differential equation,

$$y_{n+1} = y_n + \frac{\Delta}{2}\big(f(t_{n+1}, y_{n+1}) + f(t_n, y_n)\big)\,. \tag{55}$$

Using the placeholder-notation as in Eq. (26)–(30), we set $H^R(t,t') = -i\Theta(t-t')\,h(t,t')$ and $\Sigma_H^R(t,t') = -i\Theta(t-t')\,\sigma_H(t,t')$. In addition, we factorize the energy $\varepsilon_H(t)$ in Eq. (29) and (30) as outlined in Article II and mark factorized functions with a dash. We find

$$\bar{H}^<_{m+1,n} = \bar{H}^<_{mn} - \frac{\Delta^2}{2}\sum_{i=m}^{m+1}\sum_{j=0}^{i} c_j\,\bar{\sigma}_{H,ij}\,\bar{H}^<_{jn} + \frac{\Delta^2}{2}\sum_{i=m}^{m+1}\sum_{j=0}^{n} c_j\,\Sigma^<_{H,ij}\,h_{jn} \tag{56}$$

for the less-than Dyson equation (29) and

$$\bar{h}_{m+1,n} = \bar{h}_{mn} - \frac{\Delta^2}{2}\sum_{i=m}^{m+1}\sum_{j=n}^{i} c_j\,\bar{\sigma}_{H,ij}\,\bar{h}_{jn} \tag{57}$$

for the retarded Dyson equation (30). The sums of Eq. (56) can be manipulated and rearranged so that each new approximation $\bar{H}^<_{m+1,n}$ and $\bar{\Sigma}^<_{H,m+1,n}$ is on the left side,

$$\Big(1+\frac{\Delta^2}{4}\bar{\sigma}_{H,m+1,m+1}\Big)\bar{H}^<_{m+1,n}-\frac{\Delta^2}{4}\bar{\Sigma}^<_{H,m+1,n}=\Big(1-\frac{\Delta^2}{4}\bar{\sigma}^<_{H,mn}\Big)\bar{H}^<_{m,n}+\frac{\Delta^2}{4}\bar{\Sigma}_{H,mn}$$
$$+\frac{\Delta^2}{2}\sum_{i=m}^{m+1}\sum_{j=0}^{n-1}\Big(1-\frac{\delta_{j0}}{2}\Big)\Big(\bar{\Sigma}^<_{H,ij}\,\bar{h}_{jn}-\bar{\sigma}_{H,ij}\,\big[\bar{H}^<\big]^*_{nj}\Big)-\frac{\Delta^2}{2}\sum_{i=m}^{m+1}\sum_{j=n}^{i-1}\bar{\sigma}_{H,ij}\,\bar{H}^<_{jn} \quad (58)$$

and the same can be done for Eq. (57) with respect to $\bar{h}_{m+1,n}$ and $\bar{\sigma}_{H,m+1,n}$,

$$\Big(1+\frac{\Delta^2}{4}\bar{\sigma}_{m+1,m+1}\Big)\bar{h}_{m+1,n}=\Big(1-\frac{\Delta^2}{4}\bar{\sigma}_{mm}\Big)\bar{h}_{mn}-\frac{\Delta^2}{2}\sum_{i=m}^{m+1}\sum_{j=n}^{i-1}\Big(1-\frac{\delta_{jn}}{2}\Big)\,\bar{\sigma}_{H,ij}\,\bar{h}_{jn}\,. \quad (59)$$

Eq. (59) can be readily solved with $\bar{h}_{mm}=1$ as starting condition. With the known main diagonal h_{mm}, we calculate all the non-diagonal elements in the adjacent diagonal and repeat this with the next adjacent diagonal until all elements of the lower or upper triangular matrix are known. The other half of the matrix is obtained by $h_{mn}=h^*_{nm}$, which follows from $H^R(t,t')=[H^A(t',t)]^*$.

For Eq. (58) this is not so easy, because the left hand side still depends on $\Sigma^<_{H,m+1,n}$ which is proportional to yet another pseudo-particle Green function. We can, however, write down Eq. (58) for every pseudo-particle Green function and arrange them like

$$A_{m+1,n}\cdot\vec{H}^<_{m+1,n}=\vec{C}_{m,n} \quad (60)$$

where $\vec{H}^<_{m+1,n}$ is a vector of all pseudo-particle Green functions, $\vec{C}_{m,n}$ the right hand sides of Eq. (58) and $A_{m+1,n}$ is a 4×4 non-orthogonal matrix. The system of linear equations can be solved algebraically, leading to very long expressions that are best treated with an alert mind. These, however, determine all pseudo-particle Green functions at the current position. Contrary to the retarded case, only the starting conditions $H^<_{00}$ are known a priori. Thus, the calculation scheme differs and we calculate $\bar{H}^<_{mn}$ line by line starting at $(0,0)$ until all elements of the upper or lower triangular matrix are known. This way, we automatically calculate all needed $H^<_{mn}$ for the next line. The other half is then obtained similar to h_{mn} by $H^<_{mn}=[H^<_{nm}]^*$.

We used effective grid-sizes of up to 3000×3000 of which, however, only half of the entries must be allocated and calculated as outlined above. In practice, we found that the values of the end point $H^<_{max,max}$ are surprisingly robust against a reduction of the grid size and converge more rapidly than intermediate grid points which makes a calculation at several different temperatures more feasible as outlined in Article II.

Secondary electron emission In terms of programming, quite different challenges had to be mastered in order to calculate the secondary electron emission. This is, of course, partly due to our modified modeling, which approximates the Dyson equations by rate equations. On the other hand, our model now also contains four new different physical processes, each with its own requirements. For one, the computational effort is thereby completely shifted to the calculation of the rates $\Gamma^{\gtrless}_{\dots}$. The high dimensionality

of up to ten dimensions (Auger neutralization: three times a separate $\vec{k}$-space as well as a time variable) of the Auger matrix elements makes this task a particular difficult one. In the following we give thus some insight into our approach and explain some of our decisions in greater detail than in Article III.

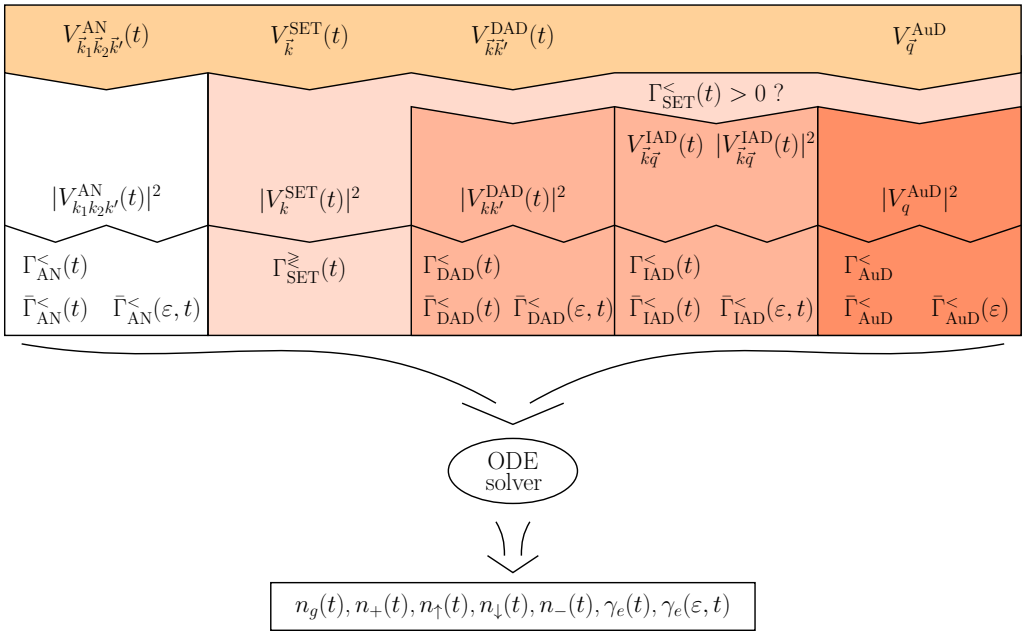

Fig. 17: Representation of the numerical scheme.

Fig. 17 gives an overview of all steps in the calculation. Except for indirect Auger de-excitation, the analytically calculated matrix elements $V^{\mathrm{AN}}_{\vec{k}_1\vec{k}_2\vec{k}'}(t)$, $V^{\mathrm{DAD}}_{\vec{k}\vec{k}'}(t)$, $V^{\mathrm{AuD}}_{\vec{q}}$ and $V^{\mathrm{SET}}_{\vec{k}}(t)$ are the starting points of the numerical calculation, shown on top in Fig. 17. We used the method of lateral Fourier transformation to calculate them in all our articles. A brief description of this otherwise lengthy and tedious calculation can be found in Article II. For DAD, the analytical $V^{\mathrm{DAD}}_{\vec{k}\vec{k}'}(t)$ contains a singularity with which our code had problems. We found that in our integration routine, it is best practice to zero the matrix element within the singularity.

Analytical calculation of the matrix element can not be done with indirect Auger de-excitation due to the special dependencies of the wave functions. Therefore,

$$V^{\mathrm{IAD}}_{\vec{k}\vec{q}\sigma}(t) = \int d^3r \int d^3r'\, \psi^*_{1\downarrow}(\vec{r} - \vec{r}_p(t))\psi^*_{\vec{q}\sigma}(\vec{r}' - \vec{r}_p(t))\frac{e^2}{|\vec{r} - \vec{r}'|}\psi_{2\sigma}(\vec{r}' - \vec{r}_p(t))\psi_{\vec{k}\downarrow}(\vec{r}) \tag{61}$$

has to be calculated numerically. This is accomplished by a MPI (massage passing interface) parallelized Monte Carlo (MC) Vegas [Lep78] routine integrating the six-dimensional vector-space spanned by $\vec{r}$ and $\vec{r}'$ for a small number of discrete different times. The routine makes 10^5 calls to the integrand and up to 10 iterations to achieve convergence. The electronic wavefunctions of the projectile $\psi_{n\sigma}(\vec{r})$, the one of the surface electron $\psi_{\vec{k}\sigma}(\vec{r})$ as well as the one of the free electron $\psi_{\vec{q}\sigma}(\vec{r})$ are supplied in analytical form as outlined in section 1.3 and in Article III. The position vector

$\vec{r}_p(t) = z(t)\,\vec{e}_z$. Assuming we calculate $V^{\mathrm{IAD}}_{\vec{k}\vec{q}\sigma}(t)$ on a discrete $\vec{k}$-$\vec{q}$-t-grid with edge length $n = 10$, then 10^7 grid points have to be calculated. For a single discrete point in time, this calculation takes about 18 hours for 48 cores with a fast HPC (high-performance computing) cluster. However, since the contribution of the indirect Auger excitation to the total number of secondary electrons is very small [Wan01], which we also observe, the time-consuming calculation of this particular matrix element can generally be completely omitted.

Knowing the matrix elements, we integrate over all solid angles of the $\vec{k}$-vectors of the square of their absolute value for any number of different times on the same branch before or after the turning point. As a representative,

$$|V^{\mathrm{AN}}_{k_1 k_2 k'}(t)|^2 = \int d\Omega_1 \int d\Omega_2 \int d\Omega' \, |V^{\mathrm{AN}}_{\vec{k}_1 \vec{k}_2 \vec{k}'}(t)|^2 \,. \tag{62}$$

The reasoning behind this is that Eq. (62) and its analogs is absolute mirror symmetrical in time as long as the trajectory of the projectile $z(t)$ is equally symmetrical. In case of IAD this step is not performed. The integration is again performed by means of a MPI parallelized MC Vegas routine. For AN, the routine does 10^7 calls to the integrand, for DAD $5 \cdot 10^6$ and 10^5 for SET and AuD. Again, the routine does a maximum of 10 iterations to achieve convergence, which is usually achieved much earlier. In terms of numerical quality, these settings have proven to be optimal in operation and testing.

The efficiency is greatly increased by not mapping Eq. (62) and its analogs for the entire residual wavenumber space. Extending the classical k-limits set by the conservation of energy by about 30% to take the quantum character into account suffices. The advantage of not integrating over the entire k-space at once is that we can manipulate Eq. 49 and its analogues to our heart's content and reuse our previously calculated and saved data. The condition is that $V_0 = E_{\mathrm{F}} + \Phi$ and $\varepsilon^{\cdots}_{n\sigma}(t \to -\infty)$ remain constant. In practice, k-grid sizes of up to $10 \times 10 \times 30$ for AN and 20×20 for DAD were used to produce the spectra in Fig. 16. However, reasonable results can already be achieved with fewer points. Decisive for the good quality of the spectra is to choose enough discrete different time points and to position them wisely. For the spectra in Fig. 16, we used 13 exponentially ordered different discrete times on a single branch in such a way that there is a better time resolution near the turning point. Using a HPC cluster with moderate processing power (a fast communication between nodes as well as hyper-threading does actually also play a role), the calculation takes around 68 hours for AN on 96 cores, 40 hours for DAD on 96 cores and less than an hour for SET on 16 cores. However, using a faster cluster that was not available at that time would significantly reduce computation time. As a compromise, relatively good results can also be found with smaller grid sizes, which reduces the calculation time accordingly.

In the next step, we calculate the rates $\Gamma^{\gtrless}_{\cdots}(t)$, modified rates $\bar{\Gamma}^{<}_{\cdots}(t)$ and modified energy-resolved Auger rates $\bar{\Gamma}^{<}_{\cdots}(\varepsilon, t)$ using again a MPI parallelized MC Vegas routine. For this to work in conjunction with the now discrete residual matrix elements Eq. (62) and its analogs, we use multidimensional linear interpolation in the residual k-space. This works amazingly well and the introduced numerical error should be small, since Eq. (62) and its analogs are very smooth. Of course, in the energy-resolved version we do without the integration of the wavenumber of the excited electron and, in addition, apply surface transmission conditions for the excited electron. These are outlined in

detail in Article III. The same surface transmission functions modify $\bar{\Gamma}^{<}_{\cdots}(t)$ as well. In terms of calculation time, this step is usually much faster than the previous one. For AN it is around half an hour, for DAD it is 3 hours and for IAD it takes 15 minutes using the same clusters as before. This does not apply to SET and AuD, since k and q are set to the correct energy by us.

A word of advice: We recommend to check whether metastable helium configurations are actually formed before calculating a DAD, IAD, or AuD rate, since these processes use these configurations as a starting point. This is the case when one of the $\Gamma^{<}_{\mathrm{SET}}(t) > 0$. In addition, the AuD process is independent of the surface material. It therefore makes sense to perform the calculation only once and use its result whenever the situation requires it.

The now calculated rates are then fed to a solver for ordinary differential equations (ODE) which solves Eq. (47) and its analogs as well as Eq. (51). For this, the solver must be able to interpolate between the different discrete times and excitation energies. We tried several techniques like Akima-interpolation [Aki70], splines [Boo78] as well as linear interpolation. In the end it turned out that it is much more important to assume that all Auger rates are exponential in time. This is usually the case in our examined scenarios as we show in Article III. Then, we can easily interpolate the logarithms of the Auger rates linearly and transform the result back without loosing much precision due to using only a select few discrete time points. On the other hand, the interpolation between different discrete excitation energies ε has no such obstacles.

For SET and AuD this is not a problem. The computation is fast enough to easily calculate $\Gamma^{\gtrless}_{\mathrm{SET}}(t)$ at a thousand different discrete times and simply use Akima-interpolation. In addition, it might even be wrong, since the SET rates may not be exponential near the turning point, see Article III. Using our model as it is, the AuD rates are not time-dependent as all dependencies cancel out. Thus, a single calculation suffices. However, corrections resulting from the non-orthogonality of the wavefunctions and an improved description of the level shifts should change this. In this case, a similar approach to SET should be used. Also, the energy dependence of $\Gamma^{<}_{\mathrm{AuD}}(\varepsilon)$ is problematic from a numerical point of view, as it is simply a Dirac delta function peak at a specified energy. To avoid sampling problems, we approximated the delta function by a Lorentz curve,

$$\begin{aligned}\bar{\Gamma}^{<}_{\mathrm{AuD}}(\varepsilon) &= \bar{\Gamma}^{<}_{\mathrm{AuD}}\,\delta(\varepsilon^{*}_{2s\uparrow} - \varepsilon^{0}_{1s\downarrow} + \varepsilon^{-}_{2s\downarrow} - \varepsilon) \\ &\approx \frac{1}{\pi}\frac{(\bar{\Gamma}^{<}_{\mathrm{AuD}})^2}{(\bar{\Gamma}^{<}_{\mathrm{AuD}})^2 + (\varepsilon^{*}_{2s\uparrow} - \varepsilon^{0}_{1s\downarrow} + \varepsilon^{-}_{2s\downarrow} - \varepsilon)^2}\end{aligned} \tag{63}$$

with $\varepsilon^{*}_{2s\uparrow}$, $\varepsilon^{0}_{1s\downarrow}$ and $\varepsilon^{-}_{2s\downarrow}$ being the shifted projectile energy levels for $t \to -\infty$, because the time dependencies cancel each other out.

We employed the explicit embedded Runge-Kutta Cash-Karp routine provided by the GNU scientific library as ODE solver. It does several things. First, it simply solves the rate equation (47) and its analogs of the other helium configurations. At the same time Eq. (51) is solved for a number of interpolated different discrete excitation energies, whereby the spectrum is obtained. Also, Eq. (51) is solved in its energy integrated

form,

$$\frac{d}{dt}\gamma_e(t) = \bar{\Gamma}^{<}_{\mathrm{AN}}(t)\, n_+(t) + \bar{\Gamma}^{<}_{\mathrm{IAD}\uparrow}(t)\, n_\uparrow(t) + \left[\bar{\Gamma}^{<}_{\mathrm{IAD}\downarrow}(t) + \bar{\Gamma}^{<}_{\mathrm{DAD}\downarrow}(t)\right] n_\downarrow(t) + \bar{\Gamma}^{<}_{\mathrm{AuD}}\, n_-(t)\,, \tag{64}$$

providing the γ-coefficient. For safety reasons, we check each time whether the γ-coefficient of Eq. (64) is identical to the coefficient obtained by integrating the calculated spectrum of Eq. (51) with the trapezoidal rule. There are usually only small deviations, which are presumably caused by the interpolation between the different discrete excited energies ε in combination with the ODE solver. Since the corresponding numeric is simpler, Eq. (64) definitely gives the more accurate result for the γ-coefficient. As a correction for the representation of the spectra, the thus-obtained γ-coefficient can be used as a weight. However, this is usually a subtle one.

The completeness Eq. (44) leads to the additional constraint

$$n_+ + n_\downarrow + n_\uparrow + n_- + n_g = 1 \tag{65}$$

which is usually fulfilled automatically. However, propagation of errors might introduce deviations from Eq. (65). These are critical immediately after the turning point and can completely ruin the result. To counteract this we enforce Eq. (65) artificially by re-weighting the sum of occupation probabilities back to unity. In addition, we enforce that the occupation probabilities $n_{\ldots}$ stay physical, thus, assume only values between zero and unity. We pay for this rough intervention with an increased number of time steps of the ODE solver in order to minimize additional errors. Nevertheless, the calculation of the occupation probabilities, the γ-coefficient and the secondary electron emission spectrum is only a matter of minutes on a single core, if the rates $\Gamma^{\gtrless}_{\ldots}(t)$, $\bar{\Gamma}^{\gtrless}_{\ldots}(t)$ and $\bar{\Gamma}^{\gtrless}_{\ldots}(\varepsilon, t)$ are already known.

1.5 Conclusions

In this thesis, we demonstrated the possibilities and capabilities of an effective semiempirical Anderson-Newns model description for charge-transferring atom-surface collisions between several types of projectiles and surfaces and analyzed it within the generic quantum kinetic approach set by Langreth, Nordlander and Shao [Lan91; Sha94a; Sha94b].

The model is very flexible and can be used for any projectile-surface combination. The metal surface is described with a step potential and is determined only with two parameters, the work function and the Fermi energy. By adapting these two parameters, any particular crystallographic orientation of the target can also be taken into account. In particular, the model does not rely on ideal surfaces, which are in no way available for complex experimental situations such as the plasma-wall interface. The projectile on the other hand is described by a time-dependent few-level system and parameterized with ionization energies and electron affinities. The decisive factor is that the physically relevant levels are identified beforehand. With the help of projection operators and auxiliary bosons [Mar12] any number of levels can be modeled in principle.

Accompanying these are supported by several other models, such as for energy shifts and matrix elements, which combined provide a flexible tool for describing charge-transferring atom-surface collisions. This subdivision into several separate submodels

makes it possible, in particular, to describe some aspects in more detail or to adapt to a different physical situation without starting from scratch. For example, for helium ions scattering on metal surfaces, the most time-consuming aspect of the calculation is by far the calculation of the matrix elements. Although Gadzuk's matrix elements [Gad67a; Gad67b] provide an appealing physical description, they do not always match the quality of other, more advanced methods, such as those found in *ab initio* density functional theory. Now, the advantage of our chosen approach is that one can immediately replace them without any disadvantage, assuming one already undertook the task of obtaining alternative ones. This also applies to all other aspects of our description and to new ones as well.

In the first part we used the model to investigate the charge-transferring collisions between magnesium and strontium projectiles and a gold target and subsequently analyzed the experiments of He and Yarmoff [He10; He11] with our newly obtained insight from a many-body theoretical point of view which indicated that they have indeed seen for the first time a mixed-valence resonance affecting the final charge state of the strontium projectile. For this we described both projectiles with a two-level system, used Roothaan-Hartree-Fock wavefunctions for their electronic states and calculated the projectile Green functions on a two-dimensional time grid. Unfortunately, for strontium the model is insufficient to quantitatively simulate the measured neutralization probability, which initially increases and then decreases with temperature. The calculated neutralization probability is, however, of the correct order of magnitude, shows a weak negative temperature dependence and is greatly enhanced compared to the uncorrelated model. Our further analysis of the spectral densities revealed that the strontium gold system is indeed in a mixed-valence situation and that the enhancement is induced by correlations. In addition, we found the mixed-valence resonance to diminish with increasing temperature. Qualitatively, these are all indications that support He and Yarmoff's interpretation of their data in terms of the mixed-valence scenario. Conversely, it can be assumed that these do not occur for magnesium and gold, since a Kondo-type resonance simply can not influence the collision in this case. Therefore, the excellent quantitative agreement in that case can be seen as reference point for the model.

In the second part we employed the model to calculate the probability with which a secondary electron excites due to the neutralization of a positive helium ion on different metal surfaces. We model the helium projectile using a three-level system which takes excited and negative states into account. The wavefunctions of the projectile were approximated by us by employing screened 1s and 2s hydrogen wavefunctions which enable partial analytic calculation for processes associated with excited states. This downgrade from the Roothaan-Hartree-Fock wavefunctions is justified, as in most helium–metal scenarios the dominant rate is the one for Auger neutralization, where deviations between the two variant wavefunctions are negligible. In addition, we included semiclassical WKB corrections in the Auger matrix elements which take the tunneling of the surface electron filling the hole in the 1s shell into account and employed projection operators and auxiliary bosons that are essential for an efficient handling of the few-level system in the first place. In combination, they allow one to take occupation dependent energy levels into account and ensure conservation of energy during configuration switches. In principle, this could allow an unlimited number of processes to act

simultaneously and in an unbiased way.

For helium, correlations do not play a crucial role, as they did before for strontium. We took advantage of this and used a saddle point approximation to derive a set of coupled rate equations for the occurrence probabilities, bypassing thereby the calculation of Green functions on a two-dimensional time grid. We did, however, calculate energy distributed spectra of the secondary electron emission and compared them to measured ones. The high-energy branches of the spectra match very well, the low-energy ones do not, presumably due to unimplemented processes that still need to be identified. Since secondary electron emission coefficients–or short γ-coefficients–are rarely measured, we had only one reference value and found our coefficient a factor of two too small due the unknown and unconsidered process. However, we concluded that the ratio between the emission processes should be nearly constant if the work functions between different surfaces do not differ too much. On this basis, we were able to weight other measured spectra and predict their γ-coefficient, which is otherwise rarely done by experimentalists, as this is a real technological challenge.

The quality of the individual submodels basically determines the overall quality. But depending on the physical scenario, other priorities for improvement must be chosen. For strontium, this should be the one-crossing approximation as it has been already developed for the equilibrium Kondo effect or any other approach that captures the instantaneous energy scales with the required precision. For Helium, on the other hand, first priority should be to work on corrections to the level shifts in order to improve the quality of any processes involving an excited state or to identify and include a model for the unknown low-energy process, depending on whether one is more interested in the high- or low-energy processes. The presented effective and semiempirical model is readily able to accommodate these and any other modification as flexibility was one of our main goals in mind.

2 Thesis Articles

Author Contribution

Article I:
Mixed-valence correlations in charge-transferring atom-surface collisions, M. Pamperin, F. X. Bronold, H. Fehske, *Phys. Scr.* **T165**, 014008 (2015). Copyright (2015) by the Royal Swedish Academy of Sciences.
M. Pamperin, F. X. Bronold, and H. Fehske outlined the scope and strategy of the calculations. The calculations were performed by M. Pamperin. M. Pamperin and F. X. Bronold wrote the manuscript which was edited by all authors.

Article II:
Many-body theory of the neutralization of strontium ions on gold surfaces, M. Pamperin, F. X. Bronold, H. Fehske, *Phys. Rev. B* **91**, 035440 (2015). Copyright (2015) by the American Physical Society.
M. Pamperin, F. X. Bronold, and H. Fehske outlined the scope and strategy of the calculations. The calculations were performed by M. Pamperin. M. Pamperin and F. X. Bronold wrote the manuscript which was edited by all authors.

Article III:
Ion-induced secondary electron emission from metal surfaces, M. Pamperin, F. X. Bronold, H. Fehske, *Plasma Sources Sci. Technol.* **27**, 084003 (2018). Copyright (2018) by IOP Publishing.
M. Pamperin, F. X. Bronold, and H. Fehske outlined the scope and strategy of the calculations. The calculations were performed by M. Pamperin. M. Pamperin and F. X. Bronold wrote the manuscript which was edited by all authors.

Confirmed:

(PD Dr. Franz X. Bronold) Greifswald, March 8, 2019

(Mathias Pamperin) Greifswald, March 8, 2019

IOP Publishing | Royal Swedish Academy of Sciences Physica Scripta

Phys. Scr. **T165** (2015) 014008 (9pp) doi:10.1088/0031-8949/2015/T165/014008

Mixed-valence correlations in charge-transferring atom–surface collisions

M Pamperin, F X Bronold and H Fehske

Institut für Physik, Ernst-Moritz-Arndt-Universität Greifswald, D-17489 Greifswald, Germany

Received 29 March 2014
Accepted for publication 21 November 2014
Published 7 October 2015

Abstract

Motivated by experimental evidence (He and Yarmoff 2010 *Phys. Rev. Lett.* **105** 176806) for a mixed-valence state to occur in the neutralization of strontium ions on gold surfaces we analyze this type of charge-transferring atom–surface collision from a many-body theoretical point of view using quantum-kinetic equations together with a pseudo-particle representation for the electronic configurations of the atomic projectile. Particular attention is paid to the temperature dependence of the neutralization probability which—experimentally—seems to signal mixed-valence-type correlations affecting the charge-transfer between the gold surface and the strontium projectile. We also investigate the neutralization of magnesium ions on a gold surface which shows no evidence for a mixed-valence state. Whereas for magnesium excellent agreement between theory and experiment could be obtained, for strontium we could not reproduce the experimental data. Our results indicate mixed-valence correlations to be in principle present, but for the model mimicking most closely the experimental situation they are not strong enough to affect the neutralization process quantitatively.

Keywords: mixed-valence correlations, charge-transfer, atom–surface collision

(Some figures may appear in colour only in the online journal)

1. Introduction

Charge-exchange between an atomic projectile and a surface plays a central role in surface science [1–6]. Many surface diagnostics, for instance, secondary ion mass spectrometry [7] or meta-stable atom de-excitation spectroscopy [8] utilize surface-based charge-transfer processes. The same holds for plasma science. Surface-based production of negative hydrogen ions, for instance, is currently considered as a pre-stage process in neutral gas heating of fusion plasmas [9]. The operation modii of low-temperature gas discharges [10], which are main work horses in many surface modification and semiconductor industries, depend on secondary electron emission from the plasma walls and thus also on surface-based charge-transfer processes.

Besides their great technological importance, charge-transferring atom–surface collisions are however also of fundamental interest. This type of collision couples a local quantum system with a finite number of discrete states—the projectile—to a large reservoir with a continuum of states—the target. Irrespective of the coupling between the two, either due to tunneling or due to Auger-type Coulomb interaction, charge-transferring atom–surface collisions are thus perfect realizations of time-dependent quantum impurity systems [11, 12]. By a judicious choice of the projectile-target combination as well as the collision parameters Kondo-type features [13] are thus expected as in any other quantum impurity system [14–17].

Indeed a recent experiment by He and Yarmoff [18, 19] provides strong evidence for electron correlations affecting the neutralization of positively charged strontium ions on gold surfaces. The fingerprint of correlations could be the experimentally found negative temperature dependence of the neutralization probability. It may arise [11, 12] from thermally excited conduction band holes occupying the strongly renormalized $5s^1$ configuration of the projectile which effectively stabilizes the impinging ion and reduces thereby the neutralization probability. The purpose of the present work is to analyze the He–Yarmoff experiment [18, 19] from a genuine many-body theoretical point of view, following the seminal work of Nordlander and coworkers [11, 20–23] as well as Merino and Marston [12] and to provide theoretical support for the interpretation of the experiment in terms of a mixed-valence scenario.

We couch—as usual—the theoretical description of the charge-transferring atom–surface collision in a time-dependent Anderson impurity model [3–6, 24–30]. The parameters of the model are critical. To be as realistic as possible without performing an expensive *ab initio* analysis of the ion–surface interaction we employ for the calculation of the model parameters Gadzuk's semi-empirical approach [31, 32] based on image charges and Hartree–Fock wave functions for the projectile states [33]. The time-dependent Anderson model, written in terms of pseudo-operators [34, 35] for the projectile states, is then subjected to a full quantum-kinetic analysis using contour-ordered Green functions [36, 37] and a non-crossing approximation for the hybridization self-energies as originally proposed by Nordlander and coworkers [11, 20–23].

We apply the formalism to analyze, respectively, the neutralization of a strontium and a magnesium ion on a gold surface. For the Mg:Au system, which shows no evidence for mixed-valence correlations affecting the charge-transfer between the surface and the projectile, we find excellent agreement between theory and experiment. For the Sr:Au system, in contrast, we could reproduce only the correct order of magnitude of the neutralization probability. Its temperature dependence could not be reproduced. Our modeling shows however that a mixed-valence scenario could in principle be at work. For the material parameters best suited for the description of the Sr:Au system they are however not strong enough to affect the neutralization probability also quantitatively.

The outline of our presentation is as follows. In the next section we describe the time-dependent Anderson model explaining in particular how we obtained the parameters characterizing it. Section 3 concerns the quantum kinetics and presents the set of coupled two-time integro-differential equations which have to be solved for determining the probabilities with which the various charge states of the projectile occur. They form the basis for the analysis of the temperature dependence of the neutralization probability. Numerical results for a strontium as well as a magnesium ion hitting a gold surface are presented, discussed, and compared to experimental data in section 4. Concluding remarks are given in section 5.

2. Model

When an atomic projectile approaches a surface its energy levels shift and broaden due to direct and exchange Coulomb interactions with the surface. Since the target and the projectile are composite objects the calculation of these shifts and broadenings from first principles is a complicated problem [38]. We follow therefore Gadzuk's semi-empirical approach [31, 32]. From our previous work on secondary electron emission due to de-excitation of meta-stable nitrogen molecules on metal [39] and dielectric [40, 41] surfaces we expect the approach to give reasonable estimates for the level widths as well as the level positions for distances from the surface larger than a few Bohr radii. In addition, the approach has a clear physical picture behind it and is thus intuitively very appealing.

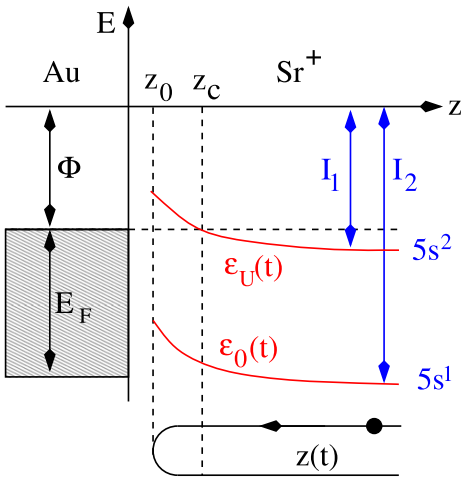

Figure 1. Illustration of the time-dependent quantum impurity model used for the description of the charge-transferring scattering of a Sr^+ ion on a gold surface. The two ionization energies, $\varepsilon_U(t)$ and $\varepsilon_0(t)$, standing for the projectiles' $5s^2$ and $5s^1$ configuration, respectively, shift due to the image interaction with the surface. Far away from the surface the two energies merge, respectively, with the first (I_1) and the second (I_2) ionization energy of a strontium atom. The image interaction also leads to a hybridization of the Sr states with the conduction band states of the surface which is characterized by a step potential at $z = 0$ whose depth is the sum of the work function $\Phi > 0$ and the Fermi energy $E_F > 0$. For simplicity the broadening is not shown. Indicated however is the trajectory $z(t)$ of the ion. Important points along the trajectory are z_0, the turning point, and z_c, the point where the first ionization level crosses the Fermi energy.

The essence of the model is illustrated in figure 1. It shows for the particular case of a strontium ion hitting a gold surface the energy levels of the projectile closest to the Fermi energy of the target. Quite generally, for alkaline-earth (AE) ions the first and the second ionization levels are most important. Identifying the positive ion (AE^+) with a singly occupied impurity and the neutral atom (AE^0) with a doubly occupied impurity, the projectile can be modelled as a non-degenerate, asymmetric Anderson model with on-site energies

$$\varepsilon_U(z) = -I_1 + \frac{e^2}{4|z - z_i|}, \tag{1}$$

$$\varepsilon_0(z) = -I_2 + \frac{3e^2}{4|z - z_i|}, \tag{2}$$

where $I_1 > 0$ and $I_2 > 0$ are, respectively, the first and second ionization energy far away from the surface while z_i is the distance of the metal's image plane from its crystallographic ending at $z = 0$. The on-site Coulomb repulsion $U(z)$ would be the difference of the two energies. Table 1 summarizes the material parameters required for the modeling of the neutralization of strontium and magnesium ions on a gold surface.

Table 1. Material parameters for magnesium, strontium and gold: I_1 and I_2 are the first and the second ionization energy, Z_1 and Z_2 are the effective charges to be used in the calculation of the hybridization matrix element (viz: equation (9)), Φ is the work function, E_F the Fermi energy, z_i the position of the image plane in front of the surface, and m_e^* is the effective mass of an electron.

	I_1(eV)	Z_1	I_2(eV)	Z_2	Φ(eV)	E_F(eV)	z_i(a.u.)	m_e^*/m_e
Sr	5.7	1.65	11.0	2	–	–	–	–
Mg	7.65	1.65	15.04	2	–	–	–	–
Au	–	–	–	–	5.1–5.2	5.53	1.0	1.1

The z-dependent shifts of the ionization levels can be obtained as the energy gain of a virtual process moving the configuration under consideration from the actual position z to $z = \infty$, reducing its electron occupancy by one, and then moving it back to position z, taking into account in both moves—if present—image interactions due to the charge state of the final and initial configurations with the metal [42]. For the upper level, ε_U, that is, the $5s^2$ configuration the cycle is $AE \rightarrow AE^+ + e^- \rightarrow AE^+$, whereas for the lower level, ε_0, that is, the $5s^1$ configuration the cycle is $AE^+ \rightarrow AE^{2+} + e^- \rightarrow AE^{2+}$.

To set up the Hamiltonian we also need the wave functions for the projectile states. For the upper level we use the (ns) Hartree–Fock wave function of an AE atom while for the lower level we use the (ns) Hartree–Fock wave function of an AE^+ ion. According to Clementi and Roetti [33] both can be written in the form

$$\psi_{HF}(\vec{r}\,) = Y_{00}(\theta, \phi) \sum_{j=1}^{N} c_j N_j \, |\vec{r}|^{n_j - 1} e^{-C_j |\vec{r}\,|} \tag{3}$$

with c_j, n_j, C_j, and N_j tabulated parameters and $Y_{00}(\theta, \phi)$ the spherical harmonics with $m = l = 0$.

For simplicity we assume the projectile to approach the surface from $z = \infty$ on a perpendicular trajectory

$$z(t) = z_0 + v|t|, \tag{4}$$

with the turning point z_0 reached at time $t = 0$ and v the velocity of the projectile. The lateral motion of the projectile is thus ignored. To be consistent with this simple trajectory we also neglect the lateral variation of the potential characterizing the metal surface. The electrons of the metal are thus simply described in terms of a potential step at $z = 0$ with depth $-|V_0| = \Phi + E_F$, where $\Phi > 0$ is the work function of the metal and $E_F > 0$ is its Fermi energy measured from the bottom of the conduction band (see table 1), leading to

$$\varepsilon_{\vec{k}} = \frac{\hbar^2}{2m_e^*}\left(k_x^2 + k_y^2 + k_z^2\right) - |V_0|, \tag{5}$$

$$\psi_{\vec{k}}(\vec{r}\,) = \frac{1}{L\sqrt{L}} \, e^{i(k_x x + k_y y)} \Big\{ T_{k_z} e^{-\kappa_{k_z} z} \Theta(z) + \left[e^{ik_z z} + R_{k_z} e^{-ik_z z} \right] \Theta(-z) \Big\}, \tag{6}$$

for the energies and wave functions of the conduction band electrons; L is the spatial width of the step (drops out in the final expressions) and

$$R_{k_z} = \frac{ik_z + \kappa_{k_z}}{ik_z - \kappa_{k_z}}, \tag{7}$$

$$T_{k_z} = \frac{2ik_z}{ik_z - \kappa_{k_z}}, \tag{8}$$

with $\kappa_{k_z} = \sqrt{2m_e^*(|V_0| - k_z^2)/\hbar^2}$ are the reflection and transmission coefficients of the potential step.

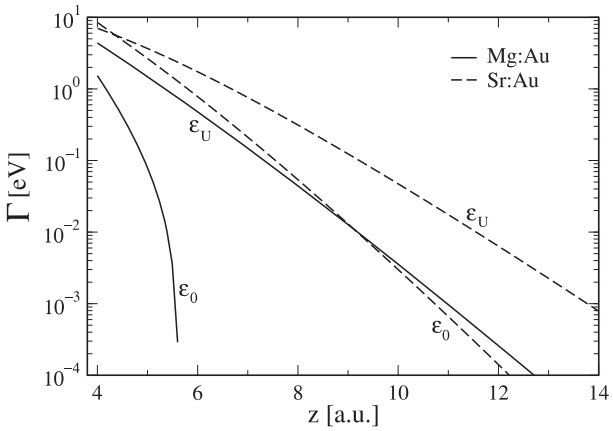

Figure 2. Level widths as obtained from equation (10) for the Mg:Au (solid lines) and the Sr:Au (dashed lines) system.

While the projectile is on its trajectory its ionization levels hybridize with the conduction band. The matrix element for this process is given by [31, 32]

$$V_{\vec{k}}(t) = \int_{z>0} d^3r \, \psi_{\vec{k}}^*(\vec{r}\,) \frac{Ze^2}{|\vec{r} - \vec{r}_p(t)|} \psi_{HF}(\vec{r} - \vec{r}_p(t)), \tag{9}$$

where the potential between the two wave functions is the residual Coulomb interaction of the valence electron with the core of the projectile located at $\vec{r}_p(t) = z(t)\vec{e}_z$. The matrix element can be transformed to a level width

$$\Gamma_{\varepsilon(t)}(t) = 2\pi \sum_{\vec{k}} |V_{\vec{k}}(t)|^2 \, \delta(\varepsilon(t) - \varepsilon_{\vec{k}}) \tag{10}$$

which is an important quantity. The charge Z in equation (9) is the charge of the nucleus screened by all the electrons of the projectile except of the valence electron under consideration. For the hybridization of the lower level, the second ionization level, $Z = 2$ while for the hybridization of the upper level, the first ionization level, $Z = 2 - s$, where $s = 0.35$ is

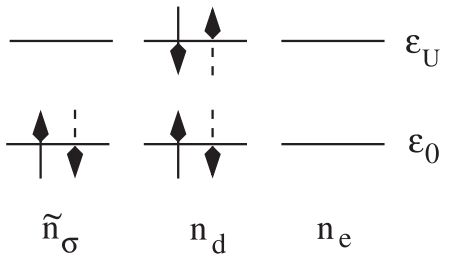

Figure 3. Possible configurations of the AE projectile. Solid and dashed arrows indicate, respectively, spin-reversed states which are energetically degenerate. The quantities $\tilde{n}_\sigma$, n_d, and n_e are, respectively, the (pseudo) probabilities with which the AE^+, the AE^0, and the AE^{2+} configuration occur.

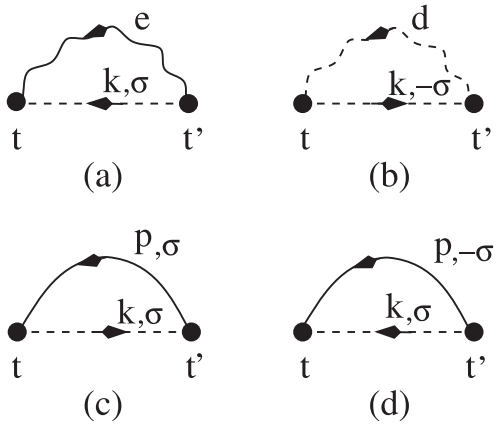

Figure 4. Self-energies in the non-crossing approximation. Straight dashed lines denote bare Green functions for the conduction band electrons. The other lines indicate renormalized Green functions for the singly occupied (p), the empty (e), and the doubly occupied (d) AE projectile. Filled bullets stand for the hybridization matrix element $V_{\vec{k}}(t)$. Diagrams (a) and (b) give, respectively, the self-energies $\Sigma_{0,\sigma}$ and $\Sigma_{U,\sigma}$ for the Green function P_σ. The self-energies Π_e and Π_d for the Green functions E and D, respectively, are shown in (c) and (d).

Slater's shielding constant due to the second electron in the s-valence shell [43].

In figure 2 we show the level widths calculated from equation (10) with $\varepsilon(t)$ set, respectively, to $\varepsilon_U(t)$ and $\varepsilon_0(t)$, for magnesium and strontium using the parameters of table 1. Most probably we overestimate the widths close to the surface. To what extent, however, only precise calculations of the kind performed for alkaline ions by Nordlander and Tully can show [38].

Using Coleman's pseudo-particle representation [34, 35] for the projectile configurations illustrated in figure 3, the Hamiltonian describing the interaction of an AE projectile with a metal surface can be written as [23]

$$\begin{aligned} H(t) = &\sum_\sigma \varepsilon_0(t) p_\sigma^\dagger p_\sigma^\dagger + \left[\varepsilon_0(t) + \varepsilon_U(t)\right] d^\dagger d^\dagger \\ &+ \sum_{\vec{k}\sigma} \varepsilon_{\vec{k}} c_{\vec{k}\sigma}^\dagger c_{\vec{k}\sigma} + \sum_{\vec{k}\sigma}\left[V_{\vec{k}}(t) c_{\vec{k}\sigma}^\dagger e^\dagger p_\sigma^\dagger + \text{h. c.}\right] \\ &+ \sum_{\vec{k}\sigma}\left[V_{\vec{k}}(t) c_{\vec{k}\sigma}^\dagger d^\dagger p_{-\sigma}^\dagger + \text{h. c.}\right] \end{aligned} \tag{11}$$

with $e^\dagger$, $d^\dagger$, and $p_\sigma^\dagger$ denoting, respectively, the creation operators for an empty (AE^{2+}), a doubly occupied (AE^0), and a singly occupied (AE^+) projectile. Since the projectile can be only in either one of these configurations, the Hamiltonian has to be constrained by [34, 35]

$$Q = \sum_\sigma p_\sigma^\dagger p_\sigma^\dagger + d^\dagger d^\dagger + e^\dagger e^\dagger = 1. \tag{12}$$

This completes the description of the model. Combined with measured projectile velocities the model describes the charge-transfer responsible for the neutralization of AE ions on noble metal surfaces.

3. Quantum kinetics

To calculate the neutralization probability for the AE ion hitting the metal surface we follow Nordlander and coworkers [11, 20–23] and set up quantum-kinetic equations for contour-ordered Green functions [36, 37] describing the empty, singly, and doubly occupied projectile. We denote these functions, respectively, by $E(t, t')$, $P_\sigma(t, t')$, and $D(t, t')$ and write their analytic pieces in the form

$$\begin{aligned} H^{\mathrm{R}}(t, t') = &-\mathrm{i}\Theta(t - t') \\ &\times \exp\left[-\mathrm{i}\int_{t'}^{t} \mathrm{d}\bar{t}\,\varepsilon(\bar{t})\right] \bar{H}^{\mathrm{R}}(t, t'), \end{aligned} \tag{13}$$

$$H^{\gtrless}(t, t') = \exp\left[-\mathrm{i}\int_{t'}^{t} \mathrm{d}\bar{t}\,\varepsilon(\bar{t})\right] \bar{H}^{\gtrless}(t, t'), \tag{14}$$

where $H(t, t')$ can be any of the three Green functions and $\varepsilon(t)$ is, depending on the Green function, either identically 0, $\varepsilon_0(t)$, or $\varepsilon_0(t) + \varepsilon_U(t)$.

Using this notation and calculating the self-energies Π_e, $\Sigma_{0,\sigma}$, $\Sigma_{U,\sigma}$, and Π_d in the non-crossing approximation diagrammatically shown in figure 4 leads after application of the Langreth–Wilkins rules [44] and the projection to the $Q = 1$ subspace [16, 20] to [22, 23]

$$\frac{\partial}{\partial t}\bar{E}^{\mathrm{R}}(t, t') = -\sum_\sigma \int_{t'}^{t} \mathrm{d}\bar{t}\,\bar{K}_{\varepsilon_0}^{<}(\bar{t}, t)\bar{P}_\sigma^{\mathrm{R}}(t, \bar{t})\bar{E}^{\mathrm{R}}(\bar{t}, t'), \tag{15}$$

$$\begin{aligned} \frac{\partial}{\partial t}\bar{P}_\sigma^{\mathrm{R}}(t, t') = &-\int_{t'}^{t} \mathrm{d}\bar{t}\,\bar{K}_{\varepsilon_0}^{>}(t, \bar{t})\bar{E}^{\mathrm{R}}(t, \bar{t})\bar{P}_\sigma^{\mathrm{R}}(\bar{t}, t') \\ &- \int_{t'}^{t} \mathrm{d}\bar{t}\,\bar{K}_{\varepsilon_U}^{<}(\bar{t}, t)\bar{D}^{\mathrm{R}}(t, \bar{t})\bar{P}_\sigma^{\mathrm{R}}(\bar{t}, t'), \end{aligned} \tag{16}$$

$$\frac{\partial}{\partial t}\bar{D}^{\mathrm{R}}(t, t') = -\sum_\sigma \int_{t'}^{t} \mathrm{d}\bar{t}\,\bar{K}_{\varepsilon_U}^{>}(t, \bar{t})\bar{P}_{-\sigma}^{\mathrm{R}}(t, \bar{t})\bar{D}^{\mathrm{R}}(\bar{t}, t'), \tag{17}$$

and

$$\frac{\partial}{\partial t}\bar{E}^{<}(t,t') = \sum_{\sigma}\int_{-\infty}^{t'} \mathrm{d}\bar{t}\,\bar{K}^{>}_{\varepsilon_0}(\bar{t},t)\bar{P}^{<}_{\sigma}(t,\bar{t})\left[\bar{E}^{\mathrm{R}}(t',\bar{t})\right]^{*} - \sum_{\sigma}\int_{-\infty}^{t} \mathrm{d}\bar{t}\,\bar{K}^{<}_{\varepsilon_0}(\bar{t},t)\bar{P}^{\mathrm{R}}_{\sigma}(t,\bar{t})\bar{E}^{<}(\bar{t},t'), \tag{18}$$

$$\frac{\partial}{\partial t}\bar{P}^{<}_{\sigma}(t,t') = \int_{-\infty}^{t'} \mathrm{d}\bar{t}\,\bar{K}^{<}_{\varepsilon_0}(t,\bar{t})\bar{E}^{<}(t,\bar{t})\left[\bar{P}^{\mathrm{R}}_{\sigma}(t',\bar{t})\right]^{*} + \int_{-\infty}^{t'} \mathrm{d}\bar{t}\,\bar{K}^{>}_{\varepsilon_U}(\bar{t},t)\bar{D}^{<}(t,\bar{t})\left[\bar{P}^{\mathrm{R}}_{\sigma}(t',\bar{t})\right]^{*} - \int_{-\infty}^{t} \mathrm{d}\bar{t}\,\bar{K}^{>}_{\varepsilon_0}(t,\bar{t})\bar{E}^{\mathrm{R}}(t,\bar{t})\bar{P}^{<}_{\sigma}(\bar{t},t') - \int_{-\infty}^{t} \mathrm{d}\bar{t}\,\bar{K}^{<}_{\varepsilon_U}(\bar{t},t)\bar{D}^{\mathrm{R}}(t,\bar{t})\bar{P}^{<}_{\sigma}(\bar{t},t'), \tag{19}$$

$$\frac{\partial}{\partial t}\bar{D}^{<}(t,t') = \sum_{\sigma}\int_{-\infty}^{t'} \mathrm{d}\bar{t}\,\bar{K}^{<}_{\varepsilon_U}(t,\bar{t})\bar{P}^{<}_{-\sigma}(t,\bar{t})\left[\bar{D}^{\mathrm{R}}(t',\bar{t})\right]^{*} - \sum_{\sigma}\int_{-\infty}^{t} \mathrm{d}\bar{t}\,\bar{K}^{>}_{\varepsilon_U}(t,\bar{t})\bar{P}^{\mathrm{R}}_{-\sigma}(t,\bar{t})\bar{D}^{<}(\bar{t},t') \tag{20}$$

with

$$\bar{K}^{\gtrless}_{\varepsilon}(t,t') = \sqrt{\Gamma_{\varepsilon(t)}(t)\Gamma_{\varepsilon(t')}(t')}\,\bar{f}^{\gtrless}_{\varepsilon}(t,t') \tag{21}$$

and

$$\bar{f}^{\gtrless}_{\varepsilon}(t,t') = \exp\left[+\mathrm{i}\int_{t'}^{t}\mathrm{d}\bar{t}\,\varepsilon(\bar{t})\right] f^{\gtrless}(t-t'), \tag{22}$$

where $f^{<}(t) = 1 - f^{>}(t)$ is the Fourier transform of the Fermi function $f^{<}(\varepsilon)$ defined by

$$f^{<}(t) = \int \frac{\mathrm{d}\varepsilon}{2\pi} f^{<}(\varepsilon)\exp\left[-\mathrm{i}\varepsilon t\right]. \tag{23}$$

The function $\bar{K}^{\gtrless}_{\varepsilon}(t,t')$, which contains the temperature dependence, entails an approximate momentum summation. From the diagrams shown in figure 4 one initially obtains

$$K^{\gtrless}(t,t') = \int \frac{\mathrm{d}\varepsilon}{2\pi}\sqrt{\Gamma_{\varepsilon}(t)\Gamma_{\varepsilon}(t')}f^{\gtrless}(\varepsilon) \times \exp\left[-\mathrm{i}\varepsilon(t-t')\right] \tag{24}$$

with an energy integration extending over the range of the conduction band and $\Gamma_{\varepsilon}(t)$ given by equation (10) with $\varepsilon(t)$ replaced by the integration variable ε. To avoid the numerically costly energy integration Nordlander and co-workers employed two different approximations: in [22] they replaced $\Gamma_{\varepsilon}(t)$ by an average over the energy range of the conduction band while in [23] they replaced it by $\Gamma_{\varepsilon(t)}(t)$ with $\varepsilon(t)$ set to $\varepsilon_0(t)$ or $\varepsilon_U(t)$ depending on which state is considered in the hybridization self-energy. Using the latter leads to

$$K^{\gtrless}_{\varepsilon}(t,t') \simeq \sqrt{\Gamma_{\varepsilon(t)}(t)\Gamma_{\varepsilon(t')}(t')}\,f^{\gtrless}(t-t') \tag{25}$$

and eventually to $\bar{K}^{\gtrless}_{\varepsilon}(t,t')$ as given in equation (21). The subscript ε indicates now not an integration variable but the functional dependence on $\varepsilon(t)$. We employ this form but keep in mind that it is an approximation to the non-crossing self-energies.

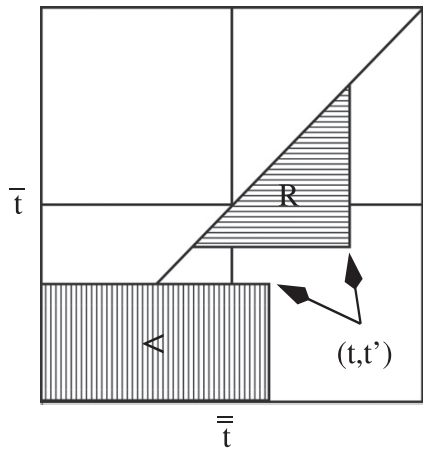

Figure 5. Sketch of the domains in the $(\bar{t},\bar{t})$ plane over which equations (15)–(20) have to be integrated subject to the boundary conditions (30)–(33), respectively, in order to determine the retarded and less-than Green functions at (t,t'). The triangular (rectangular) region denotes the domain required for the calculation of the retarded (less-than) Green functions.

The instantaneous (pseudo) occurrence probabilities for the projectile configurations AE^{2+}, AE^{+}, and AE^{0} are then given by

$$n_e(t) = \bar{E}^{<}(t,t), \tag{26}$$

$$\tilde{n}_{\sigma}(t) = \bar{P}^{<}_{\sigma}(t,t), \tag{27}$$

$$n_d(t) = \bar{D}^{<}(t,t), \tag{28}$$

respectively, where we refer to all of them as (pseudo) occurrence probabilities also strictly speaking n_d and n_e are true ones and only $\tilde{n}_{\sigma}$ is a pseudo occurrence probability in the sense that the true probability with which the AE^{+} configuration occurs is $n_{\sigma} = \tilde{n}_{\sigma} + n_d$ [23]. Sometimes we will also refer to n_e, $\tilde{n}_{\sigma}$, and n_d simply as (pseudo) occupancies. For the AE ion the probability for neutralization at the surface (wall recombination) is the probability for double occupancy after the completion of the trajectory, that is

$$\alpha_w = n_d(\infty), \tag{29}$$

subject to the initial conditions $n_d(-\infty) = n_e(-\infty) = 0$ and $\tilde{n}_{\sigma}(-\infty) = \delta_{\sigma,1/2}$.

We solve the two coupled sets of integro-differential equations (15)–(17) and (18)–(20) on a two-dimensional time grid setting

$$\bar{E}^{\mathrm{R}}(t,t) = \bar{P}^{\mathrm{R}}_{\sigma}(t,t) = \bar{D}^{\mathrm{R}}(t,t) = 1 \tag{30}$$

for the retarded Green functions and

$$E^{<}(-\infty,-\infty) = n_e(-\infty) = 0, \tag{31}$$

$$P^{<}_{\sigma}(-\infty,-\infty) = \tilde{n}_{\sigma}(-\infty) = \delta_{\sigma,1/2}, \tag{32}$$

$$D^{<}(-\infty,-\infty) = n_d(-\infty) = 0 \tag{33}$$

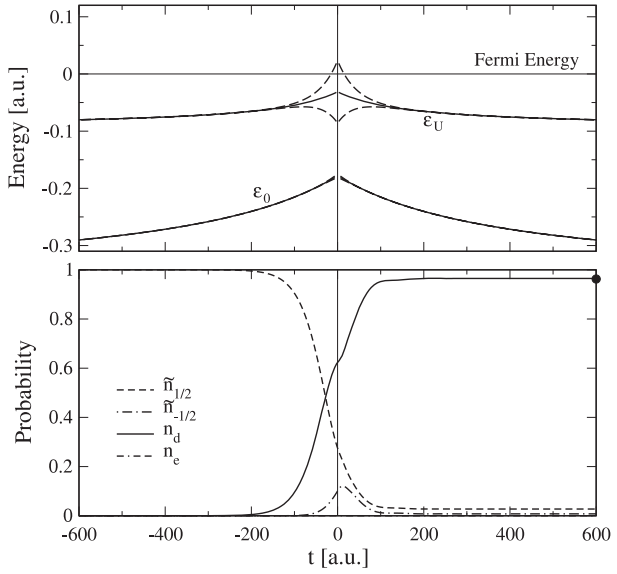

Figure 6. Upper panel: energy level diagram for the Mg:Au system at $T_s = 400$ K as a function of time. The projectile starts at $t = -600$ and $z = z_{\max} = 20$ with velocity $v = 0.024$, reaches at $t = 0$ the turning point $z = z_0 = 5$, and approaches at $t = 600$ again $z_{\max}$. The ionization levels (solid lines) are broadened according to $\epsilon_{0,U} \pm \Gamma_{0,U}$ (dashed lines) with $\Gamma_{0,U}$ as shown in figure 2. Lower panel: instantaneous (pseudo) occurrence probabilities along the trajectory for the Mg^+, the Mg^0, and the Mg^{2+} configurations. Initially, at time $t = -600$, the projectile is in the Mg^+ configuration. The neutralization probability in this particular case is $\alpha_w = n_d(600) = 0.965$ (solid bullet).

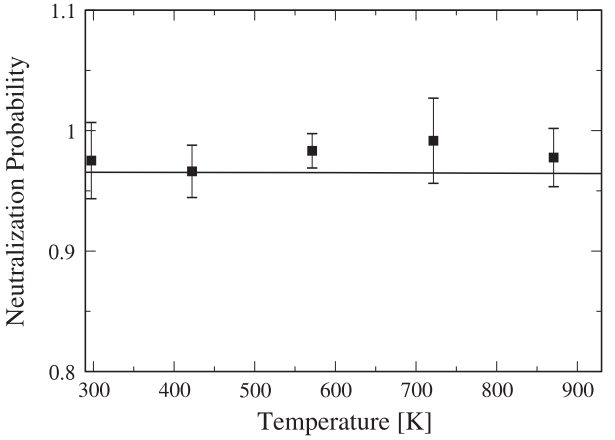

Figure 7. Temperature dependence of the neutralization probability $\alpha_w = n_d(\infty)$ for a Mg^+ ion hitting with $v = 0.024$ a gold surface. The turning point $z_0 = 5$. Also shown are experimental data from [19].

for the less-than Green functions using basically the same numerical strategy as Shao and coworkers [22, 23].

Due to the intertwining of the time integrations the integration domains for the retarded Green functions are triangular whereas for the less-than Green function they are rectangular as shown in figure 5. The size of the time-grid as well as the discretization depend on the velocity of the projectile and the maximum distance it has from the surface. For the He–Yarmoff experiment the velocities are on the order of 0.01 in atomic units. The maximum distance from which the ion starts its journey can be taken to be 20 Bohr radii. At this distance the coupling between the surface and the ion is vanishingly small. We empirically found the algorithm to converge for a $N \times N$ grid with $N = 1000$–3000. Since the Green functions are complex the computations are time and memory consuming.

4. Results

We now analyze the He–Yarmoff experiment [18, 19] quantitatively from a many-body theoretical point of view. For that purpose we combine the model developed in section 2 with the quantum-kinetics described in section 3. Besides the parameters given in table 1 we also need the velocity of the projectile. In general, the velocity will be different on the in- and outgoing branch of the trajectory. The outgoing branch, however, determines the final charge state of the projectile. We take therefore—for both branches—the normal component of the experimentally measured post-collision velocity. If not noted otherwise all quantities are in atomic units, that is, energies are measured in Hartrees and lengths in Bohr radii.

First, we discuss the Mg:Au system. In figure 6 we show the time-dependence of the broadened ionization levels, ε_U and ε_0, together with the instantaneous (pseudo) occurrence probabilities $\tilde{n}_{\pm}1/2$, n_d, and n_e for the Mg^+, the Mg^0, and the Mg^{2+} configuration, respectively. Negative and positive times denote the in- and outcoming branch of the trajectory. The velocity $v = 0.024$ and the surface temperature $T_s = 400$ K. Initially, the projectile is in the Mg^+ configuration, that is, the lower level ε_0, representing single occupancy, is occupied while the upper level ε_U, representing double occupancy, and thus the Mg^0 configuration, is empty. While the projectile is on its way through the trajectory the ionization levels shift and broaden. As a result the occupancies change. The neutralization probability is then the probability for double occupancy at the end of the trajectory.

For the particular case of the Mg:Au system the first ionization level, ε_U, that is, the level which has to accept an electron in order to neutralize the ion, is below the Fermi energy of the metal throughout the whole trajectory. The broadening is also rather weak. It only leaks for a very short time span above the Fermi energy. As a result, the magnesium ion can efficiently soak in a second electron while the electron already present due to the initial condition is basically frozen in the second ionization level. The electron captured from the metal has moreover a strong tendency to stay on the projectile. It only has a chance to leave it in the short time span where the instantaneous broadening $\Gamma_U(t)$ is larger than $|E_F - \varepsilon_U(t)|$. The neutralization probability is thus expected to be close to unity. Indeed, we find for the situation shown in figure 6 $\alpha_w = n_d(\infty) = 0.965$ (solid bullet in figure 6).

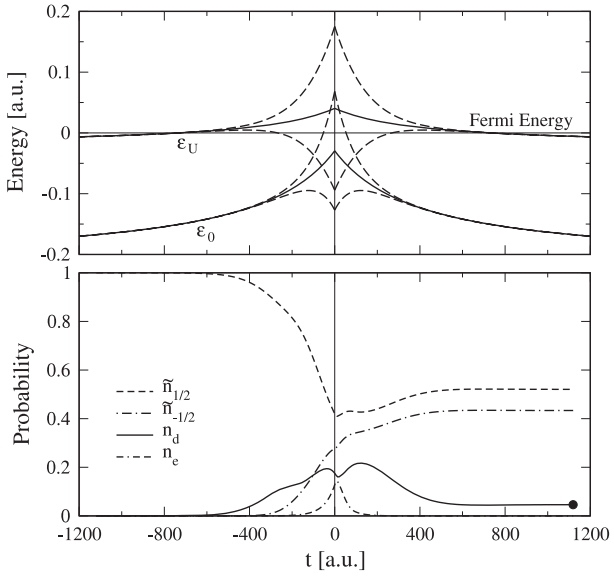

Figure 8. Upper panel: energy level diagram for the Sr:Au system at $T_s = 400$ K as a function of time. The projectile starts at $t = -1120$ and $z = z_{\max} = 20$ with velocity $v = 0.0134$, reaches at $t = 0$ the turning point $z = z_0 = 5$, and approaches at $t = 1120$ again $z = z_{\max}$. The levels (solid lines) are broadened according to $\epsilon_{0,U} \pm \Gamma_{0,U}$ (dashed lines) with $\Gamma_{0,U}$ as shown in figure 2. Lower panel: instantaneous (pseudo) occurrence probabilities along the trajectory for the Sr^+, the Sr^0, and the Sr^{2+} configurations. Initially, at time $t = -1120$, the projectile is in the Sr^+ configuration. The neutralization probability in this particular case is $\alpha_w = n_d(1120) = 0.046$ (solid bullet).

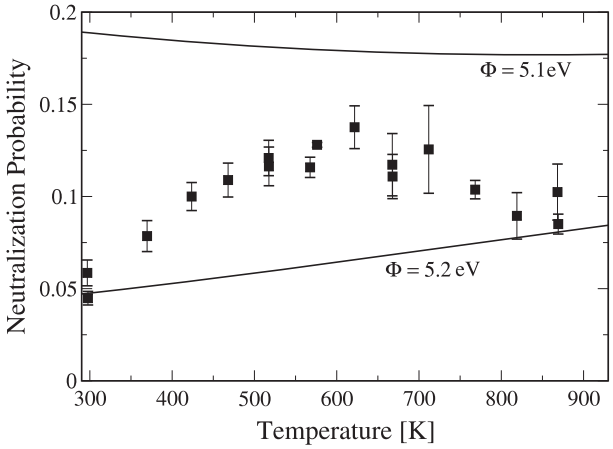

Figure 9. Temperature dependence of the neutralization probability $\alpha_w = n_d(\infty)$ for a Sr^+ ion hitting with $v = 0.0134$ a gold surface. The turning point $z_0 = 5$. Also shown are experimental data from [19].

The temperature dependence of α_w is shown in figure 7. In accordance with experiment we find α_w essentially to be independent of temperature. This is expected because both ionization levels, ε_U and ε_0, are below the Fermi energy and their broadening is too small to allow a charge-transfer from the projectile to empty conduction band states of the surface. Notice, the excellent agreement between theory and experiment indicating that the semi-empirical model we developed in section 2 captures the essential features of the charge-transfer pretty well.

After the successful description of the Mg:Au system let us now turn to the Sr:Au system. In figure 8 we again plot as a function of time the broadened ionization levels and the (pseudo) occurrence probabilities for the three configurations of the projectile. As it was the case for Mg:Au, the configuration of the projectile, which initially was in the configuration representing single occupancy, changes along the trajectory. The changes are however more subtle.

The reason is the level structure. In contrast to the Mg:Au system, the ionization levels are now closer to the Fermi energy of the surface. The first ionization level ε_U even crosses the Fermi energy with far reaching consequences. The part of the trajectory where ε_U is below the Fermi energy, that is, the region where the neutral atom would be energetically favored, the broadening is very small, indicating negligible charge-transfer from the metal to the ion and hence a stabilization of the ion due to lack of coupling. When the broadening and thus the coupling is large ε_U is above the Fermi level. In this part of the trajectory the ion is energetically stabilized. The first ionization level of strontium can capture an electron from the metal only in the time span where $|E_F - \varepsilon_U(t)| < \Gamma_U(t)$. The neutralization probability of a strontium ion should be thus much smaller than the one for a magnesium ion. Indeed we find $\alpha_w = n_d(\infty) = 0.046$ which is much smaller than unity (solid bullet in figure 8).

Due to the shift and broadening of the first ionization level ε_U it is clear that a strontium ion cannot as efficiently neutralize on a gold surface as a magnesium ion. This sets the scale of α_w. In addition, and in great contrast to magnesium, the second ionization level ε_0 is however also close to the Fermi energy. In those parts of the trajectory for which $|E_F - \varepsilon_0(t)| < \Gamma_0(t)$ it can affect the charge-transfer between the metal and the projectile. In fact, taken by itself, it should stabilize the ion and hence decrease the neutralization probability [12]. Qualitatively, this can be understood from a density of states argument. From the upper panel of figure 8 we can infer that the broadened second ionization level is cut by the Fermi energy in the upper half of its local density of states. Hence, close to the surface holes start to occupy the second ionization level at energies where the local density of states is higher than at the energies where electrons are transferred. Increasing temperature enhances thus the tendency of electron loss from the second ionization level. Without interference from the first ionization level the neutralization probability should thus go down with temperature.

That the second ionization level of Sr comes close to the Fermi energy of Au most probably led He and Yarmoff [18, 19] to suggest that the neutralization of strontium ions on gold surfaces is dominated by electron correlations. Indeed the experimentally found negative temperature dependence of α_w above $T_s = 600$ K seems to support their conclusion. However, the temperature dependence of α_w we obtain and

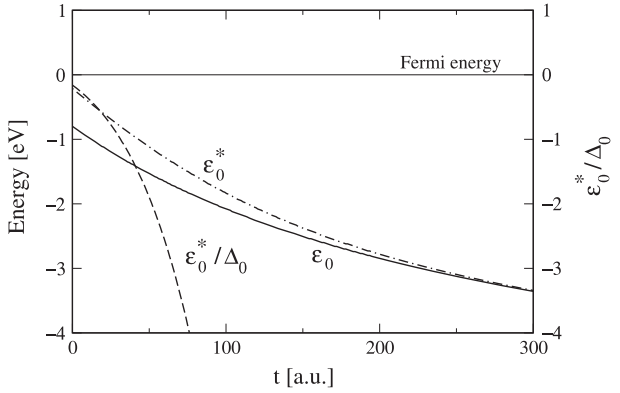

Figure 10. Renormalized (ε_0^*) and bare (ε_0) second ionization level measured from the Fermi energy as a function of time traveled along the outgoing branch of the trajectory for the Sr:Au system with $v = 0.0134$ and $T_s = 400$ K. Also shown as a function of time is the scaling invariant ε_0^*/Δ_0. In the region for which $|\varepsilon_0^*/\Delta_0| < 1$ the system is likely to be in the mixed-valence region. The material parameters are as given in table 1 and $v = 0.0134$.

which we plot in figure 9, does not show this behavior, at least, for the material parameters of table 1 and the experimentally measured post-collision velocity. The reason for the discrepancy between the measured and the calculated data is unclear. The material parameters seem to be reasonable since the theoretical results have the correct order of magnitude. It could be however that the temperature-induced transfer of holes to the second ionization level is overcompensated by the electron-transfer to the first ionization level. In the region where charge-transfer is strongest the two ionization levels overlap. The absence of energy separation together with the conditional temporal weighting due to the dynamics of the collision process makes it very hard to tell *a priori* which process will win and manifest itself in the measured neutralization probability.

So far, the discussion of the data left out the possibility of a correlation-induced sharp resonance in the vicinity of the Fermi energy, that is, the key feature of Kondo-type physics. The numerical results seem to suggest that either there is no resonance or it does not affect the neutralization process. However, from the data itself we cannot determine which one is the case. We can thus not decide whether the Sr:Au system is in a correlated regime or not and hence whether an interpretation of the experimental data in terms of a mixed-valence scenario is in principle plausible or has to be dismissed. A rigorous way to decide this would be to calculate the instantaneous spectral functions for the projectile and to look for sharp resonances in the vicinity of the Fermi energy. This is beyond the scope of the present work.

To get at least a qualitative idea about in what regime the strontium projectile might be along its trajectory we plot in figure 10, following Merino and Marston, [12] Haldane's scaling invariant, [45]

$$\frac{\varepsilon_0^*}{\Delta_0} = \varepsilon_0 + \frac{\Delta_0}{\pi}\log\left(\frac{U}{\Delta_0}\right), \tag{34}$$

as a function of time travelled along the outgoing branch of the trajectory. In the perturbative regime which is strictly applicable only far away from the surface ε_0^* can be interpreted as the renormalized second ionization level and $\Delta_0 = \Gamma_0/2$ [23]. For $|\varepsilon_0^*/\Delta_0| < 1$ the projectile is likely to be in the mixed-valence regime [12]. Since ε_0^* comes very close to the Fermi energy holes are expected to transfer in the mixed-valence regime very efficiently to the projectile. In situations where the projectile stays sufficiently long in the mixed-valence regime before ε_0^* crosses the Fermi energy double occupancy and hence the neutralization probability should be suppressed with increasing temperature.

As can be seen in figure 10 close enough to the surface the strontium projectile is indeed in the mixed-valence regime. For the material parameters given in table 1 and the experimental value for the projectile velocity the time-span however is rather short. Most probably this is the reason why we do not see any reduction of α_w with temperature for the parameters we think to be best suited for the Sr:Au system. Since the experimental data are unambiguous, this indicates perhaps the need for a precise first-principle calculation of the model parameters. Alternative interpretations of the experimental results can however not be ruled out.

5. Conclusions

Motivated by claims that the neutralization of strontium ions on gold surfaces is affected by electron correlations we set up a semi-empirical model for charge-transferring collisions between AE projectiles and noble metal surfaces. The surface is simply modelled by a step potential while the projectile is modelled by its two highest ionization levels which couple to the surface via Gadzuk's image-potential-based projectile-surface interaction. To calculate the neutralization probability we employed a pseudo-particle representation of the projectile's charge states and quantum-kinetic equations for the retarded and less-than Green functions of the projectile as initially suggested by Nordlander, Shao and Langreth. Besides the non-crossing approximation for the self-energies and an approximate momentum summation no further approximations are made. The quantum-kinetic equations are numerically solved on a two-dimensional time-grid using essentially the same strategy as Shao and coworkers.

The absolute values for the neutralization probability we obtain are in good agreement with experimental data, especially for the Mg:Au system, but also for the Sr:Au system, although for the latter we could not reproduce the temperature dependence of the neutralization probability. Our calculations can thus not decide whether the He–Yarmoff experiment can be interpreted in terms of a mixed-valence scenario. From the instantaneous values of Haldane's scaling invariant we see however that the Sr:Au system could be in the mixed-valence regime. The mechanism for a negative temperature dependence, that is, the possibility of efficiently transferring holes to the second ionization level, is thus in principle present. For the material parameters however most appropriate for Sr:Au

the negative temperature dependence arising from this channel seems to be overcompensated by the positive temperature dependence of the electron-transfer to the first ionization level. To prove that He and Yarmoff have indeed seen—for the first time—mixed-valence correlations affecting charge-transfer between an ion and a surface requires therefore further theoretical work.

Acknowledgments

MP was funded by the federal state of Mecklenburg-Western Pomerania through a postgraduate scholarship within the International Helmholtz Graduate School for Plasma Physics. In addition, support from the Deutsche Forschungsgemeinschaft through project B10 of the Transregional Collaborative Research Center SFB/TRR24 is greatly acknowledged.

References

[1] Winter H-P and Burgdörfer J (ed) 2007 *Slow Heavy-Particle Induced Electron Emission From Solid Surface* (Berlin: Springer)
[2] Rabalais J W (ed) 1994 *Low Energy ion–surface Interaction* (New York: Wiley)
[3] Los J and Geerlings J J C 1990 *Phys. Rep.* **190** 133
[4] Brako R and Newns D M 1989 *Rep. Prog. Phys.* **52** 655
[5] Modinos A 1987 *Prog. Surf. Sci.* **26** 19
[6] Yoshimori A and Makoshi K 1986 *Prog. Surf. Sci.* **21** 251
[7] Czanderna A W and Hercules D M 1991 *Ion Spectroscopies for Surface Analysis* (New York: Plenum)
[8] Harada Y, Masuda S and Ozaki H 1997 *Chem. Rev.* **97** 1897
[9] Kraus W, Falter H-D, Fantz U, Franzen P, Heinemann B, McNeely P, Riedl R and Speth E 2008 *Rev. Sci. Instrum.* **79** 02C108
[10] Lieberman M A and Lichtenberg A J 2005 *Principles of Plasma Discharges and Materials Processing* (New York: Wiley)
[11] Shao H, Langreth D C and Nordlander P 1996 *Phys. Rev. Lett.* **77** 948
[12] Merino J and Marston J B 1998 *Phys. Rev.* B **58** 6982
[13] Hewson A C (ed) 1993 *The Kondo Problem to Heavy Fermions* (Cambridge: Cambridge University Press)
[14] Grabert H and Devoret M H (ed) 1992 *Single Charge Tunneling: Coulomb Blockade Phenomena in Nanostructures* (New York: Plenum)
[15] Wingreen N S and Meir Y 1994 *Phys. Rev.* B **49** 11040
[16] Aguado R and Langreth D C 2003 *Phys. Rev.* B **67** 245307
[17] Ternes M, Heinrich A J and Schneider W-D 2009 *J. Phys.: Condens. Matter* **21** 1
[18] He X and Yarmoff J A 2010 *Phys. Rev. Lett.* **105** 176806
[19] He X and Yarmoff J A 2011 *Nucl. Instrum. Meth. Phys. Res.* B **269** 1195
[20] Langreth D C and Nordlander P 1991 *Phys. Rev.* B **43** 2541
[21] Nordlander P, Shao H and Langreth D C 1993 *Nucl. Instrum. Meth. Phys. Res.* B **78** 11
[22] Shao H, Langreth D C and Nordlander P 1994 *Phys. Rev.* B **49** 13929
[23] Shao H, Langreth D C and Nordlander P 1994 *Low Energy Ion–surface Interaction* ed J W Rabalais (New York: Wiley) p 117
[24] Kasai H and Okiji A 1987 *Surf. Sci.* **183** 147
[25] Nakanishi H, Kasai H and Okiji A 1988 *Surf. Sci.* **197** 515
[26] Romero M A, Flores F and Goldberg E C 2009 *Phys. Rev.* B **80** 235427
[27] Bajales N, Ferrón J and Goldberg E C 2007 *Phys. Rev.* B **76** 245431
[28] Goldberg E C, Flores F and Monreal R C 2005 *Phys. Rev.* B **71** 035112
[29] Onufriev A V and Marston J B 1996 *Phys. Rev.* B **53** 13340
[30] Marston J B, Andersson D R, Behringer E R, Cooper B H, DiRubio C A, Kimmel G A and Richardson C 1993 *Phys. Rev.* B **48** 7809
[31] Gadzuk J W 1967a *Surf. Sci.* **6** 133
[32] Gadzuk J W 1967b *Surf. Sci.* **6** 159
[33] Clementi E and Roetti C 1974 *At. Data Nucl. Data Tables* **14** 177
[34] Coleman P 1984 *Phys. Rev.* B **29** 3035
[35] Kotliar G and Ruckenstein A E 1986 *Phys. Rev. Lett.* **57** 1362
[36] Kadanoff L P and Baym G 1962 *Quantum Statistical Mechanics* (New York: Benjamin)
[37] Keldysh L V 1965 *Sov. Phys.—JETP* **20** 1018
Keldysh L V 1964 *J. Exp. Theor. Phys. (USSR)* **47** 1515 (in Russian)
[38] Nordlander P and Tully J C 1990 *Phys. Rev.* B **42** 5564
[39] Marbach J, Bronold F X and Fehske H 2011 *Phys. Rev.* B **84** 085443
[40] Marbach J, Bronold F X and Fehske H 2012 *Eur. Phys. J.* D **66** 106
[41] Marbach J, Bronold F X and Fehske H 2012 *Phys. Rev.* B **86** 115417
[42] Newns D M, Makoshi K, Brako R and van Wunnik J N M 1983 *Phys. Scr.* **T6** 5
[43] Slater J C 1930 *Phys. Rev.* **36** 57
[44] Langreth D C and Wilkins J W 1972 *Phys. Rev.* B **6** 3189
[45] Haldane F D M 1978 *Phys. Rev. Lett.* **40** 416

PHYSICAL REVIEW B **91**, 035440 (2015)

Many-body theory of the neutralization of strontium ions on gold surfaces

M. Pamperin, F. X. Bronold, and H. Fehske
Institut für Physik, Ernst-Moritz-Arndt-Universität Greifswald, 17489 Greifswald, Germany
(Received 1 October 2014; revised manuscript received 13 January 2015; published 29 January 2015)

Motivated by experimental evidence for mixed-valence correlations affecting the neutralization of strontium ions on gold surfaces, we set up an Anderson-Newns model for the Sr:Au system and calculate the neutralization probability α as a function of temperature. We employ quantum-kinetic equations for the projectile Green functions in the finite-U noncrossing approximation. Our results for α agree reasonably well with the experimental data as far as the overall order of magnitude is concerned, showing in particular the correlation-induced enhancement of α. The experimentally found nonmonotonous temperature dependence, however, could not be reproduced. Instead of an initially increasing and then decreasing α, we find over the whole temperature range only a weak negative temperature dependence. It arises, however, clearly from a mixed-valence resonance in the projectile's spectral density and thus supports qualitatively the interpretation of the experimental data in terms of a mixed-valence scenario.

DOI: 10.1103/PhysRevB.91.035440 PACS number(s): 34.35.+a, 79.20.Rf, 72.10.Fk

I. INTRODUCTION

Charge-transferring atom-surface collisions [1–9] are of great technological interest in surface science. The complex process of neutral gas heating in fusion plasmas [10], for instance, starts with the surface-based conversion of neutral hydrogen atoms to negatively charged ions. The operation modii of low-temperature plasmas used, for instance, in flat panel displays or in surface modification devices depend strongly on secondary electrons originating from the substrate due to impact of ions and radicals and thus also on surface-based charge-transfer processes [11]. Many surface diagnostics, finally, for instance, ion neutralization spectroscopy [12] and metastable atom deexcitation spectroscopy [13] utilize charge-transfer processes to gain information about the constituents of the surface. At the same time, however, charge-transferring atom-surface collisions are of fundamental interest as well because they are particular realizations of a quantum-impurity system out of equilibrium.

The archetypical quantum impurity is a local spin (more generally, a local moment) in a metal coupled to the itinerant electrons of the conduction band. Its well-documented properties [14,15], arising from an emerging resonance at the Fermi energy of the metal, are however also present in other quantum systems with a finite number of correlated internal states interacting via tunneling with a reservoir of external states. In particular, semiconductor quantum dots coupled to metallic leads are ideal platforms for studying local-moment physics in a well-controlled setting [16–23]. By a suitable time-dependent gating the dot can be driven out of equilibrium. Of particular recent theoretical interest are the temporal buildup and/or decay of local-moment-type correlations and how they affect the electron transport through these devices [24–27]. As pointed out a long time ago by Shao and co-workers [28] as well as Merino and Marston [29], similar transient correlations should also occur in charge-transferring atom-surface collisions where the projectile with its finite number of electron states mimics the quantum dot while the target with its continuum of states replaces the lead.

A recent experiment by He and Yarmoff indeed provided strong evidence for local-moment-type correlations to affect the neutralization probability of strontium ions on gold surfaces [30,31]. They found a nonmonotonous temperature dependence of the neutralization probability which first increases and then decreases with temperature. The initial increase with temperature is most probably a thermal single-particle effect, but the latter could be the long-sought fingerprint for a transient mixed-valence resonance formed during an electron transfer from a surface to an atomic projectile [28,29].

In this work, following the lead of Nordlander and co-workers [28,32–34] as well as Merino and Marston [29], we analyze He and Yarmoff's experiment [30,31] from a many-body theoretical point of view. In particular, we test the claim that the negative temperature dependence at high temperatures arises from the local moment of the unpaired electron in the 5*s* shell of the approaching ion. For that purpose we first set up, as usual for the description of charge-transferring atom-surface collisions, an Anderson-Newns Hamiltonian [5–9,35–41]. To obtain its single-particle matrix elements, we employ Hartree-Fock wave functions for the strontium projectile [42], a step-potential description for the gold target, and Gadzuk's semiempirical construction [43–45] for the projectile-target interaction. The model rewritten in terms of Coleman's pseudoparticle operators [46,47] is then analyzed within the finite-U noncrossing approximation employing contour-ordered Green functions [48,49] as originally suggested by Nordlander and co-workers [28,32–34]. Aside from the instantaneous occupancies and the neutralization probability we also calculate the instantaneous spectral densities. The latter are of particular interest because if the interpretation of the experimental findings in terms of a mixed-valence scenario is correct, the projectile's spectral density should feature a transient resonance at the target's Fermi energy.

For the material parameters best suited for the Sr:Au system, we find neutralization probabilities slightly above the experimental data but still of the correct order of magnitude indicating that the single-particle matrix elements of the Anderson-Newns model are sufficiently close to reality. Moreover, for the model without correlations the neutralization probabilities turn out to be too small, showing that agreement with experiment can be only achieved due to the correlation-

induced enhancement of the neutralization probability. We also find a transient resonance in the instantaneous spectral densities hinting mixed-valence correlations to be present in certain parts of the collision trajectory. The nonmonotonous temperature dependence of the neutralization probability, however, could not be reproduced. Instead, we find the resonance to lead only to a weak negative temperature dependence over the whole temperature range.

Due to lack of data for comparison, we cannot judge the validity of the single-particle parametrization we developed for the Sr:Au system. At the moment, it is the most realistic one. We attribute therefore the failure of the present calculation to reproduce the temperature anomaly of the neutralization probability while having at the same time mixed-valence features in the instantaneous spectral densities primarily to the finite-U noncrossing approximation which seems to be unable to capture the instantaneous energy scales with the required precision. A quantitative description of the experiment has thus to be based either on the dynamical $1/N$ expansion initially used by Merino and Marston [29], equation of motions for the correlation functions of the physical degrees of freedom instead of the pseudoparticles [39], or on the one-crossing approximation as it has been developed for the equilibrium Kondo effect [50–54]. Numerically, this will be rather demanding. But demonstrating that He and Yarmoff have indeed seen local-moment physics in a charge-transferring atom-surface collision may well be worth the effort.

The paper is organized as follows. In the next section, we introduce the Anderson-Newns model, its parametrization for the Sr:Au system, and its representation in terms of pseudoparticle operators. In Sec. III, we recapitulate briefly the quantum kinetics of the Anderson-Newns model as pioneered by Nordlander and co-workers. Basic definitions and the main steps of the derivation of the set of Dyson equations for the analytic pieces of the projectile Green functions within the finite-U noncrossing approximation, which is the set of equations to be numerically solved, can be found in an appendix to make the paper self-contained. Numerical results are presented, discussed, and compared to the experimental data in Sec. IV and concluding remarks with an outlook are given in Sec. V.

II. MODEL

The interaction of an atomic projectile with a surface is a complicated many-body process. Within the adiabatic approximation, which treats the center-of-mass motion of the projectile along the collision trajectory classically [8], it leads to a position- and hence time-dependent broadening and shifting of the projectile's energy levels. The adiabatic modification of the atomic energy levels as a function of distance can be calculated from first principles [55–59]. As in our previous work on secondary electron emission from metallic [60] and dielectric [61,62] surfaces, we employ, however, Gadzuk's semiempirical approach [43,44], based on classical image shifts and a golden rule calculation of the level widths, which not only provides a very appealing physical picture of the interaction process [45], but produces for distances larger than a few Bohr radii also reasonable level widths and shifts [57–59].

Indeed, first-principles investigations of Auger neutralization of helium ions on aluminum surfaces by Monreal and co-workers [58,59] showed that for distances larger than five Bohr radii the level shift follows the classical image shift. Only for shorter distances chemical interactions lead to a substantial deviation between the two. Borisov and Wille [57], on the other hand, found the level width of hydrogen ions approaching an aluminum surface to be for distances larger than five Bohr radii also not too far off the widths obtained from Gadzuk's golden rule calculation, that is, the widths are perhaps off by a factor 2. The reason most probably is Gadzuk's ingenious choice of the tunneling matrix element (see below) which takes care of the nonorthogonality of the projectile and target states [44]. Since the turning point of the strontium ion is sufficiently far away from the first atomic layer, we estimate it to be around five Bohr radii, we expect Gadzuk's semiempirical approach to also provide a reasonable parametrization of the Sr:Au system investigated by He and Yarmoff [30,31]. The corrections due to chemical interactions between the strontium projectile and the gold surface, occurring at shorter distances and included in first-principles approaches [55–59], should not yet play a role.

We now set up Gadzuk's approach step by step [43,44]. For the charge-transfer process we are interested in, the first two ionization levels of the strontium projectile are most important. They are closest to the Fermi energy of the gold target and may hence accept or donate an electron. In terms of the Anderson-Newns model, the two levels constitute, respectively, the upper and lower charge-transfer level. The difference of the two can thus be identified with the time-dependent onsite Coulomb repulsion. Figure 1 schematically shows the essence of the Anderson-Newns model for the Sr:Au system. The energy

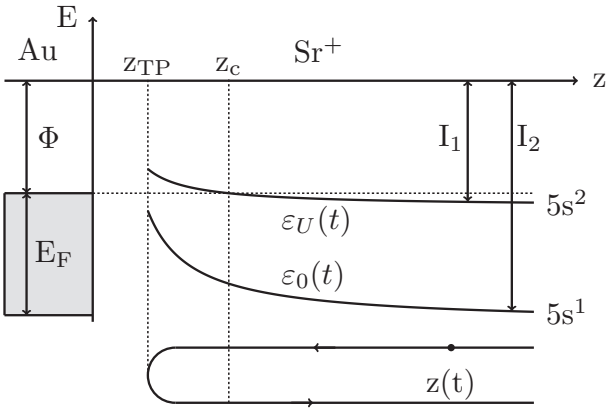

FIG. 1. Illustration of the time-dependent charge-transferring scattering of a Sr^+ ion on a gold surface. Far from the surface, the two ionization energies $\varepsilon_0(t)$ and $\varepsilon_U(t)$ are equal to the first two ionization energies of a strontium atom and represent the projectile's $5s^1$ and $5s^2$ configurations. They shift upward due to the image interaction of the projectile with the surface. For simplicity, not shown is the hybridization between the projectile and surface states as the projectile closes its distance to the surface which is idealized by a step potential whose depth is the sum of the work function $\Phi > 0$ and the Fermi energy $E_F > 0$. The energies are on scale and the points indicated along the trajectory $z(t)$ are z_{TP}, the turning point, and z_c, the point where the first ionization level crosses the Fermi energy.

levels are on scale. Mathematically, the onsite energies are given by

$$\varepsilon_U(t) = -I_1 + \frac{e^2}{4|z(t) - z_i|}, \tag{1}$$

$$\varepsilon_0(t) = -I_2 + \frac{3e^2}{4|z(t) - z_i|}, \tag{2}$$

where $I_1 > 0$ and $I_2 > 0$ are the first and second ionization energies far from the surface and z_i is the distance of the metal's image plane from its crystallographic ending at $z = 0$. For simplicity, the projectile is assumed to approach the surface perpendicularly along the trajectory

$$z(t) = z_{\mathrm{TP}} + v\,|t|\,, \tag{3}$$

where z_{TP} is the turning point and v is the velocity.

The shift of the onsite energies with time can be interpreted as the negative of the energy gain of a virtual process which moves the configuration under consideration from the actual position z to $z = \infty$, reduces its electron occupancy by one, and then moves it back to its former position z, taking into account in both moves possible image interactions due to the initial and final charge states of the projectile with the metal [9].

For the upper level $\varepsilon_U(z)$, corresponding to the first ionization level, this means shifting the charge-neutral $5s^2$ configuration from z to $z = \infty$, turning it into a single-charged $5s^1$ configuration, which is then moved back to z. In the first leg, no image shift occurs while in the second one the image shift is $-e^2/4|z - z_i|$. The net energy gain of the whole process is therefore $-e^2/4|z - z_i|$ leading to a shift of the upper onsite level of $+e^2/4|z - z_i|$. Similarly, for the lower level $\varepsilon_0(z)$, which is the second ionization level, one imagines moving a $5s^1$ configuration from z to $z = \infty$ and then a $5s^0$ configuration from $z = \infty$ back to z. In both moves, image shifts occur adding up to $-3e^2/4|z - z_i|$ because the energy pay in the first half of the trip is due to a single-charged projectile, while the energy gain on the return trip arises from a double-charged one. The shift of the lower onsite level is thus $+3e^2/4|z - z_i|$.

Aside from the onsite energies we also need the hybridization matrix elements which depend on projectile and metal wave functions. Ignoring the lateral variation of the surface potential, we take for the latter simply the wave functions of a step potential with depth $V_0 = -\Phi - E_F$ where $\Phi > 0$ and $E_F > 0$ are the work function and the Fermi energy of the surface, respectively, measured as illustrated in Fig. 1. Hence, the energies and wave functions for the conduction band electrons are

$$\varepsilon_{\vec{k}} = \frac{\hbar^2}{2m_e^*}\left(k_x^2 + k_y^2 + k_z^2\right) - |V_0|\,, \tag{4}$$

$$\psi_{\vec{k}}(\vec{r}) = \frac{1}{L^{3/2}} e^{i(k_x x + k_y y)}\left\{\Theta(z) T_{k_z} e^{-\kappa_z z} + \Theta(-z)\left[e^{ik_z z} + R_{k_z} e^{-ik_z z}\right]\right\}, \tag{5}$$

where L is the spatial width of the step, which drops out in the final expressions, and

$$T_{k_z} = \frac{2ik_z}{ik_z - \kappa_z}, \quad R_{k_z} = \frac{ik_z + \kappa_z}{ik_z - \kappa_z}, \tag{6}$$

with $\kappa_z = \sqrt{2m_e(|V_0| - k_z^2)/\hbar^2}$ are, respectively, the transmission and reflection coefficients of the step potential. More sophisticated surface potentials are conceivable, but from the work of Kürpick and Thumm [63] we expect the final result for the neutralization probability to depend not too strongly on the choice of the surface potential.

For the calculation of the hybridization matrix element, we also need $5s$ wave functions for the neutral and single-charged projectile. Both are radially symmetric and in the Hartree-Fock approximation can be written in the general form

$$\psi_{\mathrm{HF}}(\vec{r}) = \sum_{j=1}^{N} \frac{c_j N_j}{\sqrt{4\pi}} |\vec{r}\,|^{n_j - 1}\, e^{-C_j|\vec{r}\,|} \tag{7}$$

with N, c_j, N_j, n_j, and C_j tabulated parameters [42].

The transfer of an electron between the target and the projectile is a rearrangement collision. According to Gadzuk [43,44], the matrix element for this process which is also the hybridization matrix element of the Anderson-Newns model is given by

$$V_{\vec{k}}(t) = \int_{z>0} d^3r\, \psi_{\vec{k}}^*(\vec{r}) \frac{Ze^2}{|\vec{r} - \vec{r}_p(t)|} \psi_{\mathrm{HF}}(\vec{r} - \vec{r}_p(t)), \tag{8}$$

where the potential between the two wave functions is the Coulomb interaction of the transferring electron with the core of the projectile located at $\vec{r}_p(t) = z(t)\vec{e}_z$. This choice of the matrix element takes into account the nonorthogonality of the projectile and target states [44]. The charge of the core Ze is screened by the residual valence electrons of the projectile, that is, for the lower level $Z = Z_2 = 2$ while for the upper level $Z = Z_1 = 2 - s$ with $s = 0.35$ the Slater shielding constant for a $5s$ electron [64]. Material parameters required for the modeling of the Sr:Au system are listed in Table I.

The multidimensional integral (8) can be analytically reduced to a one-dimensional integral by a lateral Fourier transformation of the product of the residual Coulomb interaction with the Hartree-Fock projectile wave function. The resulting sum contains modified Bessel functions of the second kind K_α [65]. Transforming formally back and reversing the order of integration yields after successively integrating first along the

TABLE I. Material parameters for strontium and gold: I_1 and I_2 are the first and the second ionization energies, Z_1 and Z_2 are the effective charges to be used in the calculation of the hybridization matrix element [viz., Eq. (8)], Φ is the work function, E_F the Fermi energy, z_i the position of the image plane in front of the surface for which we take a typical value, and m_e^* is the effective mass of an electron in the conduction band of gold.

	I_1 (eV)	Z_1	I_2 (eV)	Z_2	Φ (eV)	E_F (eV)	z_i (a.u.)	m_e^*/m_e
Sr	5.7	1.65	11.0	2				
Au					5.1	5.53	1.0	1.1

x, y and then along the p_x, p_y directions

$$V_{\vec{k}}(t) = \sqrt{2}\frac{Ze^2}{L^{3/2}} T^*_{k_z}(\theta,\phi) \sum_{j=1}^{N} \sum_{n=0}^{(n_j-1)/2} (-1)^n c_j N_j C_j^{n_j-1-2n} \times \left(C_j^2 + k_x^2 + k_y^2\right)^{-(n_j-1/2-n)/2} A_{n_j n} \times \int_0^\infty dz\, e^{-\kappa_z z}\, |z - z_p(t)|^{n_j-1/2-n} \times K_{n_j-1/2-n}\left(|z - z_p(t)|\sqrt{C_j^2 + k_x^2 + k_y^2}\right), \quad (9)$$

where

$$A_{n_j n} = \begin{pmatrix} 1 & 0 & 0 \\ 1 & 0 & 0 \\ 1 & 1 & 0 \\ 1 & 3 & 0 \\ 1 & 6 & 3 \end{pmatrix} \quad (10)$$

are numerical coefficients ($n_j \in \{1,\ldots,5\}$ and $n = 0,1,2$ for $5s$ functions [42]) and $T^*_{k_z}$ is the complex conjugate of T_{k_z}.

Inserting the matrix element (9) into the golden rule expression for the transition rate gives the level width

$$\Gamma_{\varepsilon(t)}(t) = \frac{2\pi}{\hbar} \sum_{\vec{k}} |V_{\vec{k}}(t)|^2 \delta(\varepsilon(t) - \varepsilon_{\vec{k}}). \quad (11)$$

It is an important quantity characterizing the strength of the charge transfer. Turning the momentum summation into an integral eliminates the width L of the step potential. The integrals have to be done numerically and lead due primarily to the modified Bessel functions to level widths exponentially decreasing with distance as it is generally expected.

In Fig. 2, we show the widths of the first two ionization levels of the strontium projectile hitting a gold surface as obtained from Eq. (11) by setting $\varepsilon(t)$ to $\varepsilon_U(t)$ and $\varepsilon_0(t)$, respectively, and using the material parameters given in Table I. To demonstrate that the widths we get are of the correct order of magnitude, we also plot the width of a rubidium $5s$ level in front of an aluminum surface and compare it with the width obtained by Nordlander and Tully using a complex scaling technique [56]. In qualitative agreement with Borisov and Wille's investigation [57] of Gadzuk's approach, our rubidium width is a factor 2–3 too small for $z > 7a_B$ and a factor 2 too large for $z = 5a_B$. Between $7a_B$ and $9a_B$, however, the widths fortuitously agree with each other. The same trend we found for the other alkaline-metal combinations investigated by Nordlander and Tully [56]. From this comparison we expect the widths of the strontium levels to be of the correct order of magnitude for intermediate distances between $5a_B$ and $12a_B$. This is the range required for the description of the collision process we are interested in. For smaller and larger distances, the semiempirical approach breaks down and should be replaced by quantum-chemical methods [55–59].

With the single-particle matrix elements at hand, the Anderson-Newns Hamiltonian [5–8,35–41] describing the charge transfer between the strontium ion and the gold surface

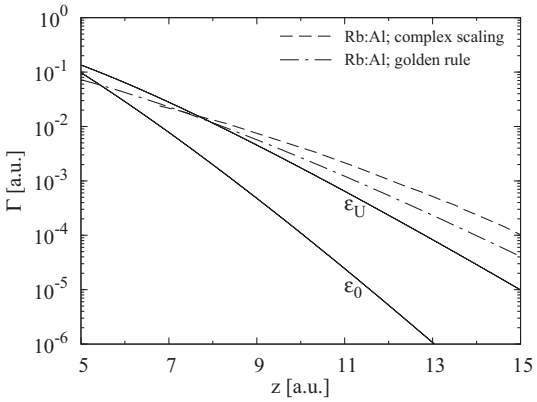

FIG. 2. Widths of the first (ε_U) and second (ε_0) ionization levels of a strontium projectile approaching a gold surface as computed from Eq. (11) on the basis of Hartree-Fock wave functions for the projectile and simple step-potential wave functions for the target. Atomic units are used, that is, energy is measured in hartrees and length in Bohr radii. Data are shown only for distances larger than 5 Bohr radii, which is the turning point of the collision trajectory. The width of a rubidium $5s$ level is also shown and contrasted with the width obtained for that level by Nordlander and Tully using the complex-scaling approach [56]. Notice, in contrast to Nordlander and Tully's Eq. (4.1) [56], our widths (11) contain a factor 2π and not a factor π. For the comparison, we corrected for this difference.

is given by

$$H(t) = \sum_\sigma \varepsilon_0(t) c_\sigma^\dagger c_\sigma + \sum_{\vec{k}\sigma} \varepsilon_{\vec{k}} c_{\vec{k}\sigma}^\dagger c_{\vec{k}\sigma} + \frac{1}{2}[\varepsilon_U(t) - \varepsilon_0(t)] \sum_\sigma c_\sigma^\dagger c_\sigma c_{-\sigma}^\dagger c_{-\sigma} + \sum_{\vec{k}\sigma} [V_{\vec{k}}(t) c_{\vec{k}\sigma}^\dagger c_\sigma + \text{H.c}]. \quad (12)$$

with $c_\sigma^\dagger$ creating an electron with spin polarization σ in the $5s$ shell of strontium and $c_{\vec{k}\sigma}^\dagger$ creating an electron with spin polarization σ and momentum $\vec{k}$ in the conduction band of the gold surface. Using Coleman's pseudoparticle representation [46,47]

$$c_\sigma = e^\dagger p_\sigma + p_{-\sigma}^\dagger d\ , \quad (13)$$

$$c_\sigma^\dagger = e\ p_\sigma^\dagger + p_{-\sigma} d^\dagger \quad (14)$$

with $e^\dagger$, $p_\sigma^\dagger$, and $d^\dagger$ creating, respectively, an empty (Sr^{2+}), a single-occupied (Sr^+) and a double-occupied (Sr^0) strontium projectile (see Fig. 3), the Hamiltonian becomes [33]

$$H(t) = \sum_\sigma \varepsilon_0(t) p_\sigma^\dagger p_\sigma + [\varepsilon_0(t) + \varepsilon_U(t)] d^\dagger d + \sum_{\vec{k}\sigma} \varepsilon_{\vec{k}} c_{\vec{k}\sigma}^\dagger c_{\vec{k}\sigma} + \sum_{\vec{k}\sigma} [V_{\vec{k}}(t) c_{\vec{k}\sigma}^\dagger e^\dagger p_\sigma + \text{H.c.}] + \sum_{\vec{k}\sigma} [V_{\vec{k}}(t) c_{\vec{k}\sigma}^\dagger d\ p_{-\sigma}^\dagger + \text{H.c.}], \quad (15)$$

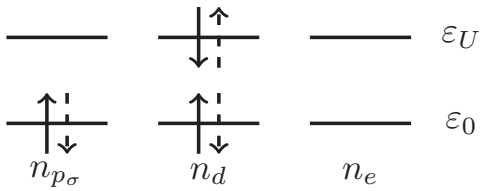

FIG. 3. Coleman's pseudoparticle representation for the strontium projectile. Shown are the occupancies of the two ionization levels ε_0 and ε_U. The two single-occupied configurations n_{p_σ} contain an electron only in the second ionization level. In the double-occupied state n_d both ionization levels are occupied by electrons with opposite spin, whereas in the empty configuration none of the ionization levels are occupied.

where the pseudoparticle operators obey the constraint

$$Q = \sum_\sigma p_\sigma^\dagger p_\sigma + d^\dagger d \ + e^\dagger e \ = 1 \tag{16}$$

since only one of the four possible projectile configurations can be ever realized.

III. QUANTUM KINETICS

To calculate the probability for the neutralization of a strontium ion on a gold surface, we employ the formalism developed by Nordlander and co-workers. The formalism, based on contour-ordered Green functions [48,49], has been developed in a series of papers [28,32–34]. However, the finite-U equations, which we have to adopt and solve for the Sr:Au system, can be found only in the book edited by Rabalais [33], which may no longer by easily accessible. It is thus helpful to briefly summarize the finite-U quantum kinetics as it is applied to the problem at hand. Basic definitions and the main steps of the derivation of the most relevant equations can be found in the Appendix.

The central objects of the formalism are the contour-ordered Green functions for the empty, single-, and double-occupied projectiles. They are denoted, respectively, by $E(t,t')$, $P_\sigma(t,t')$, and $D(t,t')$. The analytic pieces of these functions can be factorized ($\hbar = 1$)

$$H^{\rm R}(t,t') = -i\Theta(t-t')\exp\left(-i\int_{t'}^{t} d\bar{t}\,\varepsilon(\bar{t})\right)\bar{H}^{\rm R}(t,t'), \tag{17}$$

$$H^{\gtrless}(t,t') = \exp\left(-i\int_{t'}^{t} d\bar{t}\,\varepsilon(\bar{t})\right)\bar{H}^{\gtrless}(t,t'), \tag{18}$$

where $H(t,t')$ can be any of the three Green functions and $\varepsilon(t)$ is either identical to zero, $\varepsilon_0(t)$, or $\varepsilon_0(t)+\varepsilon_U(t)$, depending on the function. The superscripts R, $<$, and $>$ stand for, respectively, retarded, less-than, and greater-than Green functions.

Using this notation and the noncrossing self-energies diagrammatically shown in Fig. 4 gives after a projection to the $Q = 1$ subspace [18,22,34] and an application of the Langreth-Wilkins rules [66] the equations of motion for the

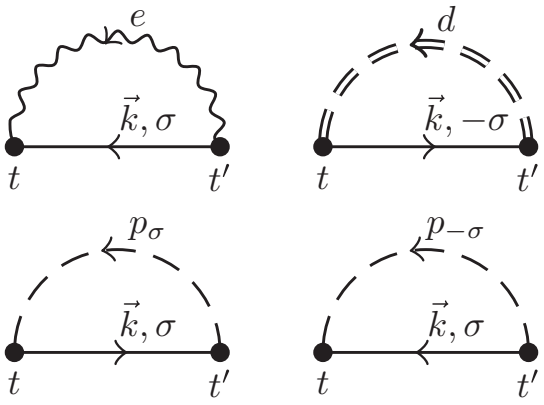

FIG. 4. Self-energies in the noncrossing approximation. Wavy, dashed, and double-dashed lines denote, respectively, fully dressed propagators for the empty (e), the single-occupied (p), and the double-occupied (d) configurations. The solid line is the bare Green function for the electrons of the surface. Starting at the left upper corner and proceeding clockwise, the diagrams denote, respectively, the self-energies $\Sigma_{0,\sigma}$ $\Sigma_{U,\sigma}$, Π_d, and Π_e for the Green functions P_σ, D, and E.

analytic pieces of the Green functions:

$$\frac{\partial}{\partial t}\bar{E}^{\rm R}(t,t') = -\sum_\sigma \int_{t'}^{t} d\bar{t}\,\bar{K}^{<}_{\varepsilon_0}(\bar{t},t)\bar{P}^{\rm R}_\sigma(t,\bar{t})\bar{E}^{\rm R}(\bar{t},t'), \tag{19}$$

$$\frac{\partial}{\partial t}\bar{P}^{\rm R}_\sigma(t,t') = -\int_{t'}^{t} d\bar{t}\,\bar{K}^{>}_{\varepsilon_0}(t,\bar{t})\bar{E}^{\rm R}(t,\bar{t})\bar{P}^{\rm R}_\sigma(\bar{t},t') - \int_{t'}^{t} d\bar{t}\,\bar{K}^{<}_{\varepsilon_U}(\bar{t},t)\bar{D}^{\rm R}(t,\bar{t})\bar{P}^{\rm R}_\sigma(\bar{t},t'), \tag{20}$$

$$\frac{\partial}{\partial t}\bar{D}^{\rm R}(t,t') = -\sum_\sigma \int_{t'}^{t} d\bar{t}\,\bar{K}^{>}_{\varepsilon_U}(t,\bar{t})\bar{P}^{\rm R}_{-\sigma}(t,\bar{t})\bar{D}^{\rm R}(\bar{t},t'), \tag{21}$$

and

$$\frac{\partial}{\partial t}\bar{E}^{<}(t,t') = \sum_\sigma \int_{-\infty}^{t'} d\bar{t}\,\bar{K}^{>}_{\varepsilon_0}(\bar{t},t)\bar{P}^{<}_\sigma(t,\bar{t})[\bar{E}^{\rm R}(t',\bar{t})]^* - \sum_\sigma \int_{-\infty}^{t} d\bar{t}\bar{K}^{<}_{\varepsilon_0}(\bar{t},t)\bar{P}^{\rm R}_\sigma(t,\bar{t})\bar{E}^{<}(\bar{t},t'), \tag{22}$$

$$\begin{aligned}\frac{\partial}{\partial t}\bar{P}^{<}_\sigma(t,t') = &\int_{-\infty}^{t'} d\bar{t}\,\bar{K}^{<}_{\varepsilon_0}(t,\bar{t})\bar{E}^{<}(t,\bar{t})\left[\bar{P}^{\rm R}_\sigma(t',\bar{t})\right]^* \\ &+\int_{-\infty}^{t'} d\bar{t}\,\bar{K}^{>}_{\varepsilon_U}(\bar{t},t)\bar{D}^{<}(t,\bar{t})\left[\bar{P}^{\rm R}_\sigma(t',\bar{t})\right]^* \\ &-\int_{-\infty}^{t} d\bar{t}\,\bar{K}^{>}_{\varepsilon_0}(t,\bar{t})\bar{E}^{\rm R}(t,\bar{t})\bar{P}^{<}_\sigma(\bar{t},t') \\ &-\int_{-\infty}^{t} d\bar{t}\,\bar{K}^{<}_{\varepsilon_U}(\bar{t},t)\bar{D}^{\rm R}(t,\bar{t})\bar{P}^{<}_\sigma(\bar{t},t'),\end{aligned} \tag{23}$$

$$\frac{\partial}{\partial t}\bar{D}^{<}(t,t') = \sum_\sigma \int_{-\infty}^{t'} d\bar{t}\,\bar{K}^{<}_{\varepsilon_U}(t,\bar{t})\bar{P}^{<}_{-\sigma}(t,\bar{t})[\bar{D}^{\rm R}(t',\bar{t})]^* - \sum_\sigma \int_{-\infty}^{t} d\bar{t}\,\bar{K}^{>}_{\varepsilon_U}(t,\bar{t})\bar{P}^{\rm R}_{-\sigma}(t,\bar{t})\bar{D}^{<}(\bar{t},t') \tag{24}$$

with

$$\bar{K}_{\varepsilon}^{\gtrless}(t,t') = \sqrt{\Gamma_{\varepsilon(t)}(t)\Gamma_{\varepsilon(t')}(t')}\,\bar{f}_{\varepsilon}^{\gtrless}(t,t') \tag{25}$$

and

$$\bar{f}_{\varepsilon}^{\gtrless}(t,t') = \exp\left[i\int_{t'}^{t} d\bar{t}\,\varepsilon(\bar{t})\right] f^{\gtrless}(t-t'), \tag{26}$$

where $\varepsilon(t)$ is either $\varepsilon_0(t)$ or $\varepsilon_U(t)$ and $f^{<}(t) = 1 - f^{>}(t)$ is the Fourier transform of the Fermi function $f^{<}(\varepsilon)$ defined by

$$f^{<}(t) = \int \frac{d\varepsilon}{2\pi} f^{<}(\varepsilon)\exp\left[-i\varepsilon t\right] \tag{27}$$

with the energy integration taken over the conduction band. The temperature dependence, which is of main interest, is contained in the integral kernels $\bar{K}_{\varepsilon}^{\gtrless}(t,t')$ defined by Eq. (25). In the Appendix, where the details of the derivation of Eqs. (19)–(24) can be found, we explain how these functions enter the formalism.

The initial conditions for Eqs. (19)–(24) depend on the particular scattering process and how it is modeled. In our case, the initial conditions are

$$\bar{E}^{\mathrm{R}}(t,t) = \bar{P}_{\sigma}^{\mathrm{R}}(t,t) = \bar{D}^{\mathrm{R}}(t,t) = 1, \tag{28}$$

and

$$E^{<}(-\infty,-\infty) = n_e(-\infty) = 0, \tag{29}$$

$$P_{\sigma}^{<}(-\infty,-\infty) = n_{p_\sigma}(-\infty) = \delta_{\sigma,1/2}, \tag{30}$$

$$D^{<}(-\infty,-\infty) = n_d(-\infty) = 0. \tag{31}$$

Once the equations of motions are solved on a two-dimensional time grid, the instantaneous (pseudo)occurrence probabilities for the Sr^{2+}, Sr^{+}, and Sr^{0} configurations are simply given by the equal-time Green functions

$$n_e(t) = \bar{E}^{<}(t,t), \tag{32}$$

$$n_{p_\sigma}(t) = \bar{P}_{\sigma}^{<}(t,t), \tag{33}$$

$$n_d(t) = \bar{D}^{<}(t,t). \tag{34}$$

Hence, in the notation of pseudoparticles, the neutralization probability

$$\alpha = n_d(\infty), \tag{35}$$

that is, it is the probability of double occupancy after completion of the trajectory.

Nordlander and co-workers [28,32–34] also derived master equations for the occurrence probabilities by approximating the time integrals in the Dyson equations for the Green functions. Depending on the level of sophistication they obtained what they called simple master equations and generalized master equations. In the Appendix we state the two sets of master equations arising from Eqs. (19)–(24) by adapting this strategy. The reduction of the set of Dyson equations to a set of master equations utilizes the fact that the functions $\bar{f}_{\varepsilon}^{\gtrless}(t,\bar{t})$ localize the self-energies around the time diagonal. Thus, provided the Green functions vary not too strongly, they can be put in front of the time integrals. Mathematically, this leads to the constraint [34]

$$R_{0,U}(z) = \left|\frac{v\alpha_{0,U}(z) - 2\Gamma_{\varepsilon_{0,\varepsilon_U}(z)}}{\varepsilon_{0,U}(z) - \varepsilon_F}\right| \ll 1, \tag{36}$$

where v is the projectile velocity. The functions $\alpha_{0,U}(z)$ are defined by requiring $\Gamma_{0,U}(z) = \Delta_{0,U}\exp[-\alpha_{0,U}(z)z]$ which leads to nearly constant values for $\alpha_{0,U}$ verifying thereby the exponential dependence of our level widths. For the upper level, the inequality obviously breaks down at the $z = z_c$ where it crosses the Fermi energy. As shown by Langreth and Nordlander [34], the master equations can still be used at this point if essentially no charge is transferred during the time span the level crosses the Fermi energy. This leads to an additional criterion at $z = z_c$. In the next section, we will see, however, that for the upper level of the Sr:Au system investigated by He and Yarmoff [30,31], the constraint (36) is violated not only at $z = z_c$ but for almost the whole trajectory. Hence, in order to analyze the correlation-driven local-moment physics possibly at work in this experiment, the solutions of the full quantum-kinetic equations are needed.

The physical Green functions $G_{\sigma}^{\lessgtr}$ needed for the calculation of the instantaneous spectral densities can be constructed from the standard definition of the less-than and greater-than Green functions [48] by replacing the original electron operators c_σ and $c_\sigma^{\dagger}$ by pseudoparticle operators according to Eqs. (13) and (14), neglecting vertex corrections, and projecting onto the physical subspace $Q = 1$. Thus, $G_{\sigma}^{<}(t,t') = \langle c_\sigma^{\dagger}(t')c_\sigma(t)\rangle$, for instance, becomes

$$G_{\sigma}^{<}(t,t') = \langle p_\sigma^{\dagger}(t')e(t')e^{\dagger}(t)p_\sigma(t)\rangle + \langle d^{\dagger}(t')p_{-\sigma}(t')p_{-\sigma}^{\dagger}(t)d(t)\rangle, \tag{37}$$

which upon employing $E^{\mathrm{R}}(t,t') = -i\theta(t-t')e^{\mathrm{R}}(t,t')$ and $P_{\sigma}^{\mathrm{R}}(t,t') = -i\theta(t-t')p_{\sigma}^{\mathrm{R}}(t,t')$ reduces to

$$G_{\sigma}^{<}(t,t') = P_{\sigma}^{<}(t,t')\left[e^{\mathrm{R}}(t',t) + E^{<}(t',t)\right] + D^{<}(t,t')\left[p_{-\sigma}^{\mathrm{R}}(t',t) - P_{-\sigma}^{<}(t,t)\right], \tag{38}$$

where the products $P_{\sigma}^{<}(t,t')E^{<}(t',t)$ and $D^{<}(t,t')P_{-\sigma}^{<}(t',t)$ are of order Q^2 and must thus be projected out to yield

$$G_{\sigma}^{<}(t,t') = P_{\sigma}^{<}(t,t')e^{\mathrm{R}}(t',t) + D^{<}(t,t')p_{-\sigma}^{\mathrm{R}}(t',t). \tag{39}$$

A similar calculation leads to

$$G_{\sigma}^{>}(t,t') = p_{\sigma}^{\mathrm{R}}(t,t')E^{<}(t',t) + d^{\mathrm{R}}(t,t')P_{-\sigma}^{<}(t',t), \tag{40}$$

where $D^{\mathrm{R}}(t,t') = -i\theta(t-t')d^{\mathrm{R}}(t,t')$ has been used. Note, in the derivation of the formulas for the physical Green functions we introduced Green functions e^{R}, p_{σ}^{R}, and d^{R}, which, in contrast to the Green functions defined in Eq. (17) are retarded Green functions with only the Heaviside function split off but the phase factor arising from the onsite energies still included.

The spectral densities for removing or adding at time T a physical electron with energy ω can be obtained from Eqs. (39) and (40) by using difference variables $T = (t+t')/2$ and $\tau = t - t'$. A Fourier transformation with respect to $\tau = t - t'$ yields

$$\rho_{\sigma}^{\lessgtr}(\omega,T) = \frac{1}{2\pi}\int_{-\infty}^{\infty} d\tau\, G_{\sigma}^{\lessgtr}(T+\tau/2, T-\tau/2)\,e^{i\omega\tau}. \tag{41}$$

The normalization of the spectral densities

$$\int_{-\infty}^{\infty} d\omega\,\rho_{\sigma}^{<}(\omega,T) = n_{p_\sigma}(T) + n_d(T), \tag{42}$$

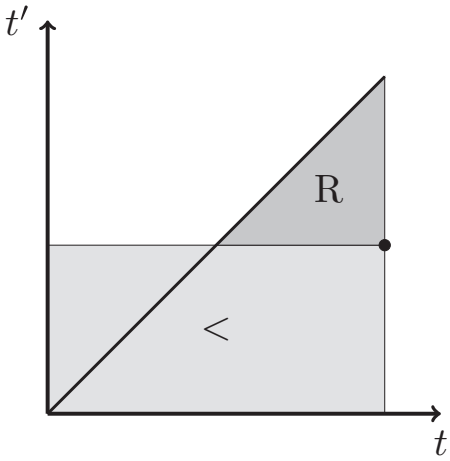

FIG. 5. Sketch of the numerical scheme used to solve the double-time equations of motion (19)–(24). The triangle marks the region in the two-dimensional time grid in which the entries of retarded Green functions have to be known in order to calculate retarded Green functions at the point indicated by the bullet. Likewise, the rectangle marks the region in which the entries of (retarded and less-than) Green functions are required in order to compute less-than Green functions at the point indicated by the bullet.

$$\int_{-\infty}^{\infty} d\omega\, \rho_\sigma^{>}(\omega,T) = n_{p_{-\sigma}}(T) + n_e(T) \tag{43}$$

is given by the instantaneous occupation of the projectile with a physical electron or a physical hole, respectively, written in terms of the occurrence probabilities introduced above. This follows directly from the equal-time limit of Eqs. (39) and (40) by using $e^{\mathrm{R}}(t,t) = d^{\mathrm{R}}(t,t) = p_\sigma^{\mathrm{R}}(t,t) = 1$.

At the end of this section, let us say a few words about the numerics required to solve the two-dimensional integro-differential equations (19)–(24). The discretization strategy proposed by Shao and co-workers [32] for $U = \infty$ can be also employed for finite U. The main difference is that two more Green functions have to be calculated on the time grid: $\bar{D}^{\mathrm{R}}$ and $\bar{D}^{<}$. The particular structure of the time integrals leads to the numerical strategy shown in Fig. 5. First, the retarded Green functions are calculated, starting from the time diagonal where their values are simply set to unity because of the initial condition and then working through the grid points which are on lines parallel to the time diagonal. To compute retarded Green functions at (t,t'), only the points in the dark triangle depicted in Fig. 5 have to be sampled. The calculation of the less-than Green functions requires a slightly different scheme. Here, the computation first proceeds in the t and then in the t' direction, starting from $(-t_{\max},-t_{\max})$ where the initial condition can be employed and redoing this until one arrives at the desired grid point. Only grid points in the bright rectangular region of Fig. 5 contribute then to the calculation of less-than functions at the point (t,t').

The computations are time and memory consuming. We employ grid sizes of up to 3000×3000. Taking advantage of the symmetry of the Green functions, the Green functions in the upper half of the grid can be obtained from the Green functions of the lower half by complex conjugation which reduces memory space and number of calculations by one-half. Even then, however, the calculation of one trajectory requires on a 2000×2000 time grid including the computation of the level widths eight hours of processing time and 400 Mb memory on a single core. To obtain the temperature dependence of the neutralization probability, we let the projectile run through the trajectory for 50 different temperatures. Fortunately, the final charge state is surprisingly robust against a reduction of the size of the time grid. Empirically, we found the neutralization probability (but not necessarily the occurrence probabilities at intermediate times) to be converged already for a 1000×1000 time grid. A run for a single temperature requires then only half an hour, making an investigation of the temperature dependence of the neutralization process feasible.

IV. RESULTS

We now present numerical results. Aside from the material parameters listed in Table I which should be quite realistic for the Sr:Au system investigated by He and Yarmoff, we need the turning point z_{TP} and the velocity v of the strontium projectile. The radius of a strontium atom is around 2.2 Å. It is thus very unlikely for the strontium projectile to come closer to the surface than 4–5 Bohr radii. In atomic units, measuring length in Bohr radii and energy in hartrees, which we use below if not indicated otherwise, we set therefore $z_{\mathrm{TP}} = 5$. For the velocity, we take the experimentally determined post-collision velocity for the whole trajectory since it is known that due to loss of memory [40] the outgoing branch determines the final charge state of the projectile. In atomic units, $v = 0.134$ [31].

First, we investigate if the He-Yarmoff experiment [30,31] can be described by the numerically less demanding master equations (either the simple or the generalized set, see Appendix). As pointed out in the previous section, the master equations should provide a reasonable description of the charge transfer if $R_{0,U}(z) \ll 1$. In Fig. 6, we plot $R_{0,U}(z)$ for $v = 0.0134$ and the level widths and energies obtained in Sec. II. For the second ionization level ε_0 master equations could be in fact used all the way down to $z \approx 6$. For the first ionization level ε_U master equations break down not only at the point where the level crosses the Fermi energy, but also close to the turning point, where the level width turns out to be too large, and far away from the surface, where the projectile velocity is too high for the master equations to be applicable. Only in a narrow interval around $z \approx 9$, where the high velocity is compensated by the level broadening leading to a small numerator in Eq. (36), R_U is small enough to justify master equations also for ε_U. Since the two ionization levels are coupled and the charge transfer occurs not only in the narrow range where master equations are applicable to both levels this implies that neither the simple nor the generalized master equations can be used to analyze the Sr:Au system investigated by He and Yarmoff. Instead, the full double-time quantum kinetics has to be implemented.

Let us now trace, based on the numerical solution of the double-time Dyson equations, for a fixed surface temperature $T_s = 400$ K important physical quantities while the projectile is on its way through the trajectory. Figure 7 shows in

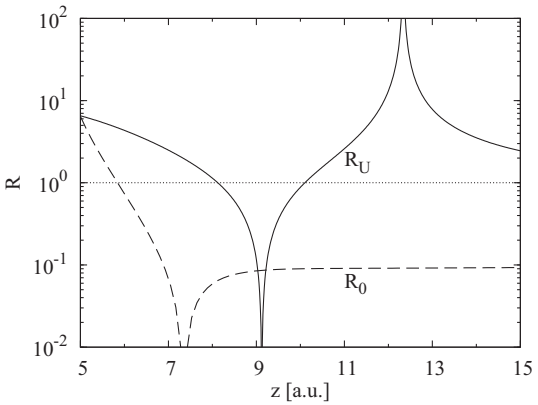

FIG. 6. The constraints R_0 and R_U as a function of z for the Sr:Au system investigated by He and Yarmoff [30,31]. The approximations reducing the double-time quantum kinetics of the Dyson equations to either a set of simple or generalized master equations (see Appendix) are valid only for $R_{0,U} \ll 1$. Hence, for ε_0 master equations could be used for $z > 6$. But, for ε_U master equations break down for almost the whole trajectory except for the narrow interval around $z \approx 9$ where the vanishing of the numerator in Eq. (36) leads to small values for R_U. The peak in R_U around $z \approx 12$ signals the point where ε_U crosses the Fermi energy.

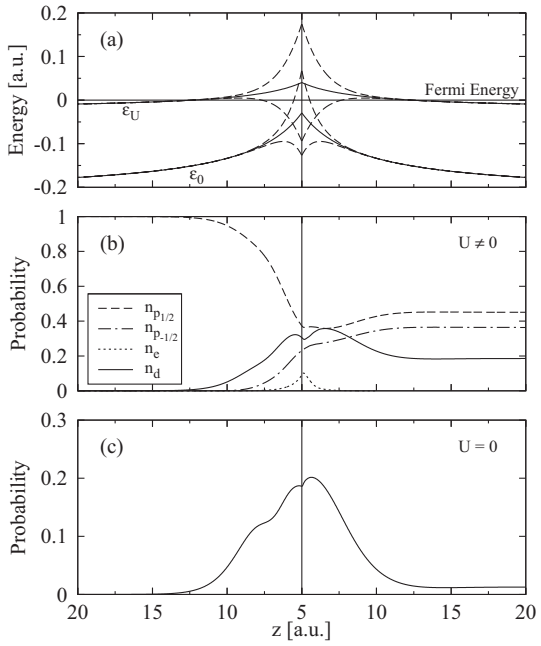

FIG. 7. Instantaneous physical quantities along the trajectory. The strontium projectile starts on the left as an ion at a distance $z = 20$ with a velocity $v = 0.0134$, reaches the turning point at $z_{TP} = 5$, and approaches $z = 20$ again thereafter on the right. (a) Energy-level diagram. Both levels (solid lines) are broadened according to $\varepsilon \pm \Gamma$ (dashed lines) with the instantaneous Γ shown in Fig. 2. (b) Occurrence probabilities at $T_s = 400$ K for Sr^+ (dashed and dashed-dotted lines), Sr^0 (solid line), and Sr^{2+} (dotted line) as obtained from the finite-U model. The neutralization probability in this case is $\alpha = n_d(20) = 0.185$. (c) Occurrence probability of Sr^0 as obtained from the uncorrelated $U = 0$ model which keeps only the first ionization level, that is, the upper onsite energy ε_U. In this case the $\alpha = 0.01$. For other surface temperatures T_s the results look similar.

the upper panel the shift and broadening of the ionization levels ε_U and ε_0 while the middle panel depicts the instantaneous occurrence probabilities n_e, $n_{p_{\pm 1/2}}$, and n_d for the Sr^{2+}, Sr^+, and Sr^0 configurations, respectively. The projectile starts at $z = 20$ on the left, moves along the incoming branch towards the turning point $z = 5$ from which it returns on the outgoing branch again to the distance $z = 20$. The strontium projectile starts in the Sr^+ configuration. Thus, only the ε_0 level is occupied while the ε_U level is empty. During the collision, both levels shift upward and broaden. The upper level crosses the Fermi energy at $z = z_c \approx 12$. In the course of the collision, the occupation probabilities change and the projectile has a certain chance to be at the end in a different charge state than initially. For the run plotted in Fig. 7 the probability for double occupancy at the end, that is, the probability for neutralization is $\alpha = n_d(20) = 0.185$. For comparison, we show in the lower panel the instantaneous occupation of ε_U as it is obtained when only this level is kept in the modeling, that is, for a single-level, uncorrelated $U = 0$ model. In this case, the neutralization probability $\alpha = 0.01$, that is, one order of magnitude smaller.

The physics behind the results shown in Fig. 7 is as follows. Let us first focus on the first ionization level. Initially, ε_U is below the Fermi energy. Hence, energetically, not the ionic Sr^+ but the neutral Sr^0 configuration is actually favored. However, as can be seen from the vanishing broadening of the level, far away from the surface charge transfer is negligible. The approaching ion is thus initially stabilized due to lack of coupling. When the coupling becomes stronger for smaller distances ε_U crosses, however, the Fermi energy. The ion is then energetically stabilized. Roughly speaking, the first ionization level has a chance to capture an electron from the metal only when $|E_F - \varepsilon_U(t)| < \Gamma_U(t)$; in the notation of Sosolik and co-workers, the Sr:Au system is in the coupling-dominated regime [67]. From the upper panel in Fig. 7, we see that this is the case only for a very small portion of the trajectory, close to the turning point. As a result, the neutralization probability α should be in any case much smaller than unity as indeed it is. Due to the thermal broadening of the target's Fermi edge, the efficiency of electron capture into the first ionization level increases with temperature. Thus, if this was the only process involved in the charge transfer, the neutralization probability should monotonously increase with temperature, contrary to the experimental data which initially increase and then decrease (see below). The charge transfer must be thus more involved. Indeed, as can be seen in the upper panel in Fig. 7, the second ionization level ε_0 comes also close to the Fermi energy. In those parts of the trajectory where $|E_F - \varepsilon_0(t)| < \Gamma_0(t)$, it is thus conceivable that the electron initially occupying ε_0 may leave the projectile. That is, holes may transfer from the surface to the second ionization level thereby compensating the electron transfer into the first. The hole transfer, absent in the uncorrelated $U = 0$ model, tendentiously favors the ion with increasing temperature and

should by itself lead to a neutralization probability decreasing with temperature.

That during the collision the ionization levels of strontium come so close to the Fermi energy of the gold target, with the first one crossing it and the second one coming so close to it to enable hole transfer, led He and Yarmoff to suggest that the neutralization process is driven by electron correlations. The experimentally found negative temperature dependence of α above $T_s = 600$ K strengthened their conclusion. It agrees qualitatively with what Merino and Marston predicted theoretically on the basis of a correlated-electron model for the neutralization of calcium ions on copper surfaces [29]. The work of Shao and co-workers [28] suggested moreover that the negative temperature dependence of α is caused by a mixed-valence resonance transiently formed in the course of the collision.

After these qualitative remarks, we now discuss the temperature dependence of the neutralization probability quantitatively. In Fig. 8, we show the experimental data of He and Yarmoff [31] and compare it with our theoretical results. For the parameters of Table I, the theoretical neutralization probability (solid line) turns out a bit too large but it is still of the correct order of magnitude indicating that the material parameters as well as the procedures for calculating the level widths are reasonable. In contrast to the experimental data we find, however, over the whole temperature range only a weak negative temperature dependence. Also plotted in Fig. 8 is the temperature dependence of the neutralization probability

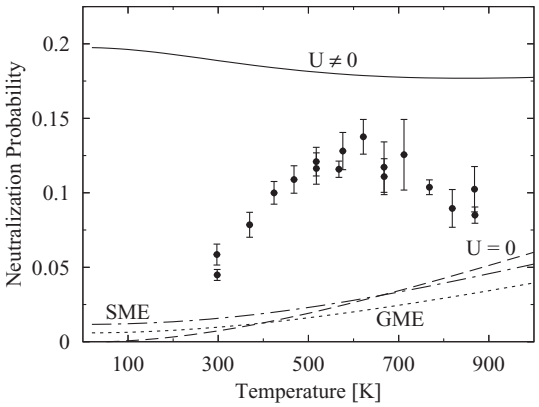

FIG. 8. Temperature dependence of the neutralization probability $\alpha = n_d(20)$ for a Sr^+ ion hitting with $v = 0.0134$ a gold surface. The turning point $z_{TP} = 5$. Also shown are the data of He and Yarmoff [31]. The solid and long-dashed lines are for the finite-U and the uncorrelated $U = 0$ model, respectively, showing that correlations enhance the neutralization probability to the experimental order of magnitude. By moving the turning point farther away from the surface, we could make the results for $U \neq 0$ to overlap with the experimental data. However, we do not use z_{TP} as a fit parameter for reasons explained in the main text. The nonmonotonous temperature dependence of the experimental data cannot be reproduced regardless of the value of the turning point. The dashed-dotted and the dotted lines are the neutralization probabilities arising, respectively, from the numerical solution of the set of simple or the set of generalized master equations given in the Appendix.

arising from the uncorrelated $U = 0$ model (long-dashed line) and, for completeness, the one obtained from the numerical solution of either the set of simple (dashed-dotted line) or the set of generalized master equations (dotted lines) listed at the end of the Appendix.

Clearly, without correlations the neutralization probability is too small indicating that correlations play an important role in the charge transfer from the gold target to the strontium projectile. The chosen turning point $z_{TP} = 5$ is in fact most favorable for the uncorrelated model. In reality, the turning point may be farther away from the surface. A larger value of z_{TP} leads, however, to smaller neutralization probabilities. Hence, the results for the uncorrelated model would be pushed farther away from the experimental data, while the results for the correlated model would come closer to it. We hesitate, however, to use z_{TP} as a fit parameter because of the shortcomings of the finite-U noncrossing approximation discussed in the next section.

The neutralization probabilities arising from the master equations are also much smaller than those obtained from the full quantum kinetics. Decreasing the turning point would push them of course closer to the experimental data (without reproducing the nonmonotonous temperature dependence). However, the numerical values for $R_{0,U}(z)$ shown in Fig. 6 indicate that the approximations leading to the master equations cannot be justified. Hence, the results for α obtained from the master equations should not be artificially pushed towards experimental data by manipulating the turning point. Instead, one should, if at all, try to push the correlated $U \neq 0$ data closer to the experimental data by changing the parameters of the Sr:Au system within physically sensible bounds.

Any attempt, however, to improve the theoretical data by changing the material parameters and hence the single-particle matrix elements of the Anderson-Newns Hamiltonian was unsuccessful. A slight increase of the metal's work function from $\phi = 5.1$ to 5.15 eV, for instance, decreased the neutralization rate but eliminated at the same time the weak negative temperature dependence. Decreasing the work function from $\phi = 5.1$ to 5.05 eV, on the other hand, increased the theoretical neutralization rate but did also not lead to a stronger negative temperature dependence let alone to a nonmonotonous one. Changing the turning point z_{TP} affects the neutralization probability as indicated in the previous paragraph but again wipes out the weak negative temperature dependence. The effect of the Doppler broadening [3,67,68] we did not investigate. We take all this as an indication that the correlation effects encoded in the finite-U noncrossing approximation are too fragile. Going beyond this approximation is thus unavoidable.

Another observation should be mentioned. The starting point $z = 20$ can be relatively freely chosen. If it is closer to the surface, the slopes of the instantaneous occurrence probabilities in Fig. 7 are steeper so that there is hardly any difference in the probabilities at the turning point and no difference at the end of the trajectory. As a result, the final neutralization probability is independent of the precise starting conditions. The loss of memory in charge-transferring atom-surface collisions has been also found by Onufriev and Marston [40]. It justifies using the precollision velocity for the whole trajectory.

In the region where charge transfer is strongest, the two ionization levels overlap. The absence of energy separation together with the conditional temporal weighting due to the dynamics of the collision process makes it very hard to tell *a priori* whether electron or hole transfer dominates the outcome of the collision. Simply changing the matrix elements of the Anderson-Newns model in the hope to reproduce the experimentally found temperature anomaly is pointless as we have indeed seen. Even more so, since the hypothesized electron correlations of the local-moment type strongly distort the projectile's density of states in the vicinity of the target's Fermi energy. Any attempt to guess the projectile's final charge state on the basis of the single-particle quantities shown in the upper panel of Fig. 7 has thus to fail. In order to see whether the weak negative temperature dependence of α is already a qualitative hint for a mixed-valence scenario to be at work in the neutralization of strontium ions on gold surfaces, we calculated therefore the instantaneous spectral densities for the projectile. If local-moment physics is present, these functions should feature transient resonances at the target's Fermi energy.

In Fig. 9, we present for a selected set of distances along the outgoing branch of the trajectory and for $T_s = 400$ K the instantaneous spectral densities summed over the two spin orientations. The occupied part of the spectral densities (solid black lines), that is, the spectrally resolved probability for removing a physical electron, as well as the total spectral densities (dashed black lines), which, in addition, contain also the spectrally resolved probability for adding an electron, are shown. For orientation we also plot the equilibrated spectral densities (solid and dashed orange lines) which we obtained by fixing the widths and energetic positions of the levels to the values at that particular distance and then letting the system evolve in time up to the point where it reaches a quasistationary state. The negative values of the instantaneous spectral densities close to and at the turning point should not be interpreted too literally. First, we cannot rule out that in the numerical Fourier transformation the Gibbs phenomenon occurs although the results for the equilibrated spectral densities speak against it. Second, and most importantly, the instantaneous spectral densities $\rho_\sigma^{\lessgtr}(\omega,T)$ are Wigner distributions in energy ω and time T. These two quantities, however, cannot be measured simultaneously. Usually, Wigner distributions deal with quantum-mechanical uncertainties by becoming negative in some regions of the space in which they are defined [69]. Integrated over energy, that is, the zeroth-order moments of the Wigner distributions $\rho_\sigma^{\lessgtr}(\omega,T)$ give, however, always the correct occupancies at the particular time as can be easily checked by a comparison with the data obtained from the integration of the equations of motion.

Let us start with Fig. 9(a) which shows the spectral densities at the closest encounter. The overlapping ionization levels are

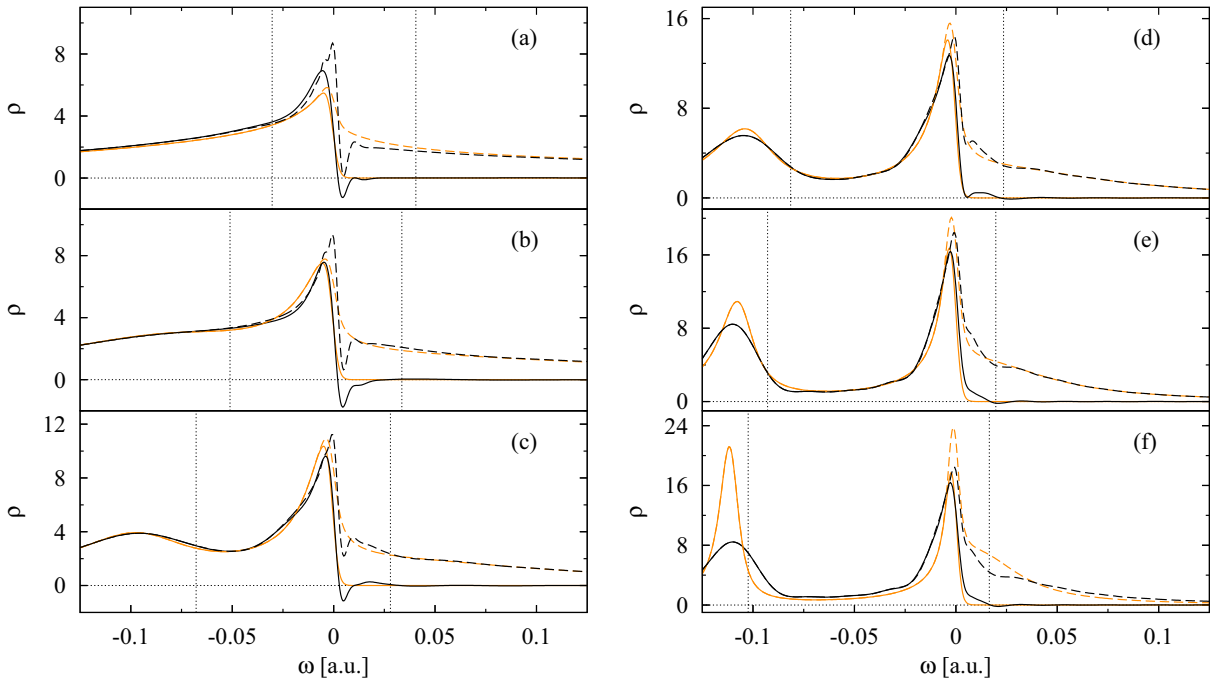

FIG. 9. (Color online) Projectile spectral densities summed over the two spin orientations, respectively, at $z = 5.0$, 5.5, 6.0, 6.5, 7.0, and 7.5 on the outgoing branch of the trajectory [panels (a) to (f)] for a Sr^+ ion hitting with $v = 0.0134$ a gold surface at temperature $T_s = 400$ K. For other surface temperatures in the range relevant for the experiment, the spectral functions look qualitatively similar. The black lines correspond to the instantaneous spectral densities at the given positions with the solid lines denoting the occupied and the dashed lines the total spectral densities. The vertical dotted lines indicate the instantaneous positions of the onsite energies ε_0 and ε_U while the orange lines give the equilibrated occupied (solid lines) and total (dashed lines) spectral densities at the corresponding positions. The target's Fermi energy is located at $\omega = 0$.

very broad at this point leading, however, to a spectral density which due to electronic correlations is enhanced at the Fermi energy $\omega = 0$. The uncorrelated model would not give this enhancement. Moving outwards [Figs. 9(b)–9(f)], the spectral densities change, because of the decreasing widths and the shifting of the ionization levels, developing in addition to the resonance at $\omega = 0$ features in the vicinity of the two instantaneous ionization levels which are indicated by the two vertical dotted lines. Although the additional structure due to the upper ionization level is only a high-energy shoulder to the peak at $\omega = 0$, the spectral densities develop the shape expected from a quantum impurity: two charge-transfer peaks and a resonance at the Fermi energy. This can be most clearly seen in Fig. 9(f). Since close to the surface the upper charge-transfer peak merges more or less with the peak at the Fermi energy to form a mixed-valence resonance, the Sr:Au system is in the mixed-valence regime.

The dominating spectral feature at all the distances shown in Fig. 9 is the enhancement at the target's Fermi energy. Despite the quantitative discrepancies between the measured and the computed neutralization probabilities, our theoretical results for the spectral densities suggest, for realistic single-particle parameters and without any fit parameter, that local-moment physics is present in the Sr:Au system and may thus control the neutralization of Sr^+ on Au surfaces as anticipated by He and Yarmoff [31]. More specifically, from Fig. 7 we read off that most of the charge transfer occurs between the turning point $z_{TP} = 5$ and the crossing point $z_c \approx 12$, whereas from Fig. 9 we see that for these distances the Sr:Au system develops at the Fermi energy of the Au target a mixed-valence resonance with a high-energy tail varying on the scale of the thermal energy. The weak negative temperature dependence we obtain for α is thus due to the mixed-valence resonance in the projectile's spectral density in accordance with what Merino and Marston predicted for the correlated Ca:Cu system [29]. The comparison in Fig. 8 with the results obtained from the uncorrelated $U = 0$ model suggests moreover that it is also the mixed-valence resonance which enhances the neutralization probabilities to the experimentally found order of magnitude.

Obviously, our results support He and Yarmoff's mixed-valence scenario [30,31] only qualitatively but not quantitatively. Either the transient local-moment correlations are too weak, occur at the wrong distance, or are simply too short lived. It requires further theoretical work to tell which one of these possibilities applies.

V. CONCLUSIONS

We presented a realistically parametrized Anderson-Newns model for charge-transferring collisions between a strontium projectile and a gold target and used the model to analyze from a many-body theoretical point of view the experiment of He and Yarmoff [30,31] which indicated that in this type of surface collision, a mixed-valence resonance affects the final charge state of the projectile.

In contrast to the measured neutralization probability which initially increases and then decreases with temperature, the computed data show only the correlation-induced enhancement, making the calculated neutralization probability of the correct order of magnitude, and a weak negative temperature dependence. The analysis of the projectile's instantaneous spectral densities revealed, however, that both the enhancement and the negative temperature dependence arise from a mixed-valence resonance at the target's Fermi energy in qualitative agreement with what Merino and Marston found for the Ca:Cu system [29], which is another projectile-target combination which could display local-moment physics. Thus, qualitatively, our results support He and Yarmoff's interpretation of their data in terms of a mixed-valence resonance.

We followed the theoretical approach of Nordlander and co-workers [28,32–34]. It is based on the noncrossing approximation for Anderson-impurity–type models and contour-ordered Green functions. That we do not find the anomalous temperature dependence of the neutralization probability while having a transient mixed-valence resonance in the instantaneous spectral densities could have two reasons. First, the accuracy of the semiempirical estimates we developed for the single-particle matrix elements of the Anderson-Newns Hamiltonian may be not enough. The shift of the two ionization levels was obtained from classical considerations based on image charges while the width of the levels was computed from Hartree-Fock and step-potential wave functions. *Ab initio* calculations or measurements of these two quantities would be very helpful, in particular, for distances close to the turning point. Second, the finite-U noncrossing approximation most probably does not yield the correct energy scale of the resonance transiently formed at the Fermi energy of the target. Indeed, for finite U the noncrossing approximation does not self-consistently sum up all leading terms in $1/N$ where $N = 2$ is the degeneracy of the $5s$ level. In equilibrium, it is known that the noncrossing approximation underestimates due to this inconsistency the width of the Kondo resonance considerable [54]. Systematically summing up all diagrams to leading order by the one-crossing approximation [50–54] remedies this shortcoming as does the dynamical $1/N$ approximation used by Merino and Marston [29] and equation-of-motion approaches working directly with the physical Green functions defining the spectral densities [39]. It should be also noted that the temperature anomaly occurs over an interval of only 600 K corresponding to an energy interval $\Delta E \approx 0.002$ in atomic units. The spectral features in the vicinity of the Fermi energy which drive the anomaly have thus to be known with an energy resolution better than 10^{-3}.

Specifically, our results for the spectral densities make us adhere to the mixed-valence scenario. Aside from the above-mentioned improvements on the theoretical side, further experimental analysis would be, however, also required to clarify the issue. The velocity dependence of the effect, for instance, would be of great interest because it is the projectile velocity which determines whether the instantaneous correlations get frozen in and manifest themselves in the final charge state of the projectile. We would thus expect the experimentally observed temperature anomaly to depend strongly on the projectile's velocity. Changing the work function and the collision geometry would be also of interest. The former manipulates the point where the upper ionization level crosses the target's Fermi energy, whereas the latter changes the effective temperature via Doppler broadening. The temperature anomaly of the neutralization probability should

hence also depend on the work function of the surface and the angle of incident.

It may be easier to realize local-moment physics in electrically biased semiconductor nanostructures but demonstrating it to be also present in charge-transferring atom-surface collisions may open up avenues for further research which are not yet anticipated. The Sr:Au system investigated by He and Yarmoff may well be a very promising candidate.

ACKNOWLEDGMENTS

M.P. was funded by the federal state of Mecklenburg-Western Pomerania through a postgraduate scholarship within the International Helmholtz Graduate School for Plasma Physics. In addition, support from the Deutsche Forschungsgemeinschaft through Project No. B10 of the Transregional Collaborative Research Center SFB/TRR24 is greatly acknowledged.

APPENDIX

In this Appendix, we lay out the basic definitions and notations we used in setting up the quantum kinetic equations (19)–(24) of Sec. III. The equations have been originally derived by Shao and co-workers [33]. As in our previous work on the deexcitation of metastable molecules at surfaces [61], we stay as closely as possible to the notation of Nordlander and co-workers [32–34] and deviate from it only when it improves the readability of the equations.

Contour-ordered Green functions [48,49] describing the empty, the single-occupied, and the double-occupied projectiles

$$i\,E(t,t') = \langle T_{\mathcal{C}}\, e(t)\, e^{\dagger}(t')\rangle, \tag{A1}$$

$$i\,P_{\sigma}(t,t') = \langle T_{\mathcal{C}}\, p_{\sigma}(t)\, p_{\sigma}^{\dagger}(t')\rangle, \tag{A2}$$

$$i\,D(t,t') = \langle T_{\mathcal{C}}\, d(t)\, d^{\dagger}(t')\rangle, \tag{A3}$$

as well as metal electrons

$$i\,G_{\vec{k},\sigma}(t,t') = \langle T_{\mathcal{C}}\, c_{\vec{k},\sigma}(t)\, c_{\vec{k},\sigma}^{\dagger}(t')\rangle, \tag{A4}$$

where the brackets denote the statistical average with respect to the initial density matrix, constitute the basis of the formalism. The functions D and E are bosonic propagators while P_{σ} and $G_{\vec{k},\sigma}$ are fermionic. For any of the four Green functions listed above, the analytic pieces, that is, the less-than and the greater-than functions, are given by

$$i\,H(t,t') = \Theta_{\mathcal{C}}(t-t')\,H^{>}(t,t') \mp \Theta_{\mathcal{C}}(t'-t)\,H^{<}(t,t'), \tag{A5}$$

where H stands for E, P_{σ}, D, or $G_{\vec{k},\sigma}$ and $\Theta_{\mathcal{C}}$ is the Heaviside function defined on the complex time contour. The upper sign holds for fermionic and the lower sign for bosonic Green functions. As usual, the corresponding retarded functions read as

$$i\,H^{R}(t,t') = \theta(t-t')[H^{>}(t,t') \pm H^{<}(t,t')], \tag{A6}$$

where again the upper (lower) sign holds for fermionic (bosonic) functions and θ is now the Heaviside function on the real-time axis.

Similarly, the self-energies Σ_{σ}, Π_{e}, and Π_{d} for the single-occupied, the empty, and the double-occupied projectiles can be split into analytic pieces which in turn give rise to retarded self-energies

$$i\,\Sigma_{\sigma}^{\mathrm{R}}(t,t') = \theta(t-t')[\Sigma_{\sigma}^{>}(t,t') + \Sigma_{\sigma}^{<}(t,t')], \tag{A7}$$

$$i\,\Pi_{\mathrm{e,d}}^{\mathrm{R}}(t,t') = \theta(t-t')[\Pi_{\mathrm{e,d}}^{>}(t,t') - \Pi_{\mathrm{e,d}}^{<}(t,t')]. \tag{A8}$$

Within the noncrossing approximation, the metal electrons are undressed. Hence, below $G_{\vec{k},\sigma}$ is always the bare propagator and no self-energy has to be specified for the metal electrons [28,32–34].

On the real-time axis the analytic pieces of the Green function obey the set of Dyson equations ($\hbar = 1$):

$$i\frac{\partial}{\partial t}E^{\mathrm{R}}(t,t') = \delta(t-t') + \int_{-\infty}^{\infty} d\bar{t}\;\Pi_{\mathrm{e}}^{\mathrm{R}}(t,\bar{t})E^{\mathrm{R}}(\bar{t},t'), \tag{A9}$$

$$\left[i\frac{\partial}{\partial t} - \varepsilon_0(t)\right]P_{\sigma}^{\mathrm{R}}(t,t') = \delta(t-t') + \int_{-\infty}^{\infty} d\bar{t}\;\Sigma_{\sigma}^{\mathrm{R}}(t,\bar{t})P_{\sigma}^{\mathrm{R}}(\bar{t},t'), \tag{A10}$$

$$\left[i\frac{\partial}{\partial t} - \varepsilon_0(t) - \varepsilon_U(t)\right]D^{\mathrm{R}}(t,t') = \delta(t-t') + \int_{-\infty}^{\infty} d\bar{t}\;\Pi_{\mathrm{d}}^{\mathrm{R}}(\bar{t},t)D^{\mathrm{R}}(\bar{t},t'), \tag{A11}$$

$$i\frac{\partial}{\partial t}E^{<}(t,t') = \int_{-\infty}^{\infty} d\bar{t}\;\Pi_{\mathrm{e}}^{\mathrm{R}}(t,\bar{t})E^{<}(\bar{t},t') + \int_{-\infty}^{\infty} d\bar{t}\;\Pi_{\mathrm{e}}^{<}(t,\bar{t})E^{\mathrm{A}}(\bar{t},t'), \tag{A12}$$

$$\left[i\frac{\partial}{\partial t} - \varepsilon_0(t)\right]P_{\sigma}^{<}(t,t') = \int_{-\infty}^{\infty} d\bar{t}\;\Sigma_{\sigma}^{\mathrm{R}}(t,\bar{t})P_{\sigma}^{<}(\bar{t},t') + \int_{-\infty}^{\infty} d\bar{t}\;\Sigma_{\sigma}^{<}(t,\bar{t})P_{\sigma}^{\mathrm{A}}(\bar{t},t'), \tag{A13}$$

$$\left[i\frac{\partial}{\partial t} - \varepsilon_0(t) - \varepsilon_U(t)\right]D^{<}(t,t') = \int_{-\infty}^{\infty} d\bar{t}\;\Pi_{\mathrm{d}}^{\mathrm{R}}(t,\bar{t})D^{<}(\bar{t},t') + \int_{-\infty}^{\infty} d\bar{t}\;\Pi_{\mathrm{d}}^{<}(t,\bar{t})D^{\mathrm{A}}(\bar{t},t'). \tag{A14}$$

The self-energies in the noncrossing approximation are shown in Fig. 4, where the self-energy Σ_{σ} for the single-occupied projectile is split into two pieces $\Sigma_{\sigma,0}$ and $\Sigma_{\sigma,U}$, depending on whether the empty or the double-occupied state appears as a virtual state. Applying standard diagrammatic rules [70] together with the Langreth-Wilkins rules [66] given in our notation in Ref. [61] yields after projection to the $Q = 1$ subspace [18,22,34] the following mathematical expressions for the analytic pieces of the self-energies:

$$\Pi_{\mathrm{d}}^{\gtrless}(t,t') = \sum_{\sigma}\int\frac{d\varepsilon}{2\pi}K_{\varepsilon}^{\gtrless}(t,t')P_{-\sigma}^{\gtrless}(t,t'), \tag{A15}$$

$$\Pi_{\mathrm{d}}^{\mathrm{R}}(t,t') = \sum_{\sigma}\int\frac{d\varepsilon}{2\pi}K_{\varepsilon}^{>}(t,t')P_{-\sigma}^{\mathrm{R}}(t,t'), \tag{A16}$$

$$\Pi_e^{\gtrless}(t,t') = \sum_\sigma \int \frac{d\varepsilon}{2\pi} K_\varepsilon^{\lessgtr}(t',t) P_\sigma^{\gtrless}(t,t'), \tag{A17}$$

$$\Pi_e^{\mathrm{R}}(t,t') = \sum_\sigma \int \frac{d\varepsilon}{2\pi} K_\varepsilon^{<}(t',t) P_\sigma^{\mathrm{R}}(t,t'), \tag{A18}$$

$$\Sigma_{\sigma,0}^{\gtrless}(t,t') = \int \frac{d\varepsilon}{2\pi} K_\varepsilon^{\gtrless}(t,t') E^{\gtrless}(t,t'), \tag{A19}$$

$$\Sigma_{\sigma,0}^{\mathrm{R}}(t,t') = \int \frac{d\varepsilon}{2\pi} K_\varepsilon^{>}(t,t') E^{\mathrm{R}}(t,t'), \tag{A20}$$

$$\Sigma_{\sigma,U}^{\gtrless}(t,t') = \int \frac{d\varepsilon}{2\pi} K_\varepsilon^{\lessgtr}(t',t) D^{\gtrless}(t,t'), \tag{A21}$$

$$\Sigma_{\sigma,U}^{\mathrm{R}}(t,t') = \int \frac{d\varepsilon}{2\pi} K_\varepsilon^{<}(t',t) D^{\mathrm{R}}(t,t') \tag{A22}$$

with

$$K_\varepsilon^{\gtrless}(t,t') = \sqrt{\Gamma_\varepsilon(t)\Gamma_\varepsilon(t')} f^{\gtrless}(\varepsilon) e^{-i\varepsilon(t-t')}, \tag{A23}$$

where ε is an energy variable to be integrated over.

In obtaining the self-energies we took advantage of the fact that the propagator of the metal electrons is undressed and spin independent. As a result, $\Sigma_{\sigma,0}$ and $\Sigma_{\sigma,U}$ (and thus Σ_σ) are independent of the electron spin. Furthermore, we assumed the tunneling matrix element $V_{\vec{k}}(t)$ to factorize in the variables t and $\vec{k}$. In our case, this is approximately true since the strongest time dependence in Eq. (9) comes from the modified Bessel function K_α giving rise to a nearly exponential time dependence of $V_{\vec{k}}(t)$. The function

$$\Gamma_\varepsilon(t,t') = 2\pi \sum_{\vec{k}} V_{\vec{k}}(t) V_{\vec{k}}^*(t') \delta(\varepsilon - \varepsilon_{\vec{k}}) \tag{A24}$$

initially appearing in the self-energies can thus be approximately rewritten as [32,34]

$$\Gamma_\varepsilon(t,t') \simeq \sqrt{\Gamma_\varepsilon(t)\Gamma_\varepsilon(t')} \tag{A25}$$

with $\Gamma_\varepsilon(t)$ defined by Eq. (11) leading eventually to the expressions for the self-energies given above.

Inserting the self-energies (A15)–(A22) into the Dyson equations (A9)–(A14) and rewriting the equations in terms of the reduced Green functions defined by Eqs. (17) and (18) yields after an approximate ε integration Eqs. (19)–(24) of Sec. III.

Due to the approximate ε integration, the functions $\bar{K}_\varepsilon^{\gtrless}(t,t')$ enter the formalism. In the definition (25) of these functions the subscript ε denotes not an energy variable, but the functional dependence on $\varepsilon(t)$. To see this, consider the Dyson equation (A9). In terms of reduced Green functions it reads as

$$\begin{aligned}\partial_t \bar{E}^{\mathrm{R}}(t,t') &= -\sum_\sigma \int_{t'}^t d\bar{t} \int \frac{d\varepsilon}{2\pi} \sqrt{\Gamma_\varepsilon(t)\Gamma_\varepsilon(\bar{t})} f^<(\varepsilon) \\ &\quad \times \exp\left[-i\int_{\bar{t}}^t d\tau\, (\varepsilon_0(\tau) - \varepsilon)\right] \bar{P}_\sigma^{\mathrm{R}}(t,\bar{t}) \bar{E}^{\mathrm{R}}(\bar{t},t') \qquad \text{(A26)} \\ &\simeq -\sum_\sigma \int_{t'}^t d\bar{t} \sqrt{\Gamma_{\varepsilon_0(t)}(t)\Gamma_{\varepsilon_0(\bar{t})}(\bar{t})} f^<(\bar{t}-t) \\ &\quad \times \exp\left[-i\int_{\bar{t}}^t d\tau\, \varepsilon_0(\tau)\right] \bar{P}_\sigma^{\mathrm{R}}(t,\bar{t}) \bar{E}^{\mathrm{R}}(\bar{t},t') \qquad \text{(A27)} \\ &= -\sum_\sigma \int_{t'}^t d\bar{t} \sqrt{\Gamma_{\varepsilon_0(t)}(t)\Gamma_{\varepsilon_0(\bar{t})}(\bar{t})} \bar{f}_{\varepsilon_0}^<(\bar{t},t) \\ &\quad \times \bar{P}_\sigma^{\mathrm{R}}(t,\bar{t}) \bar{E}^{\mathrm{R}}(\bar{t},t') \qquad \text{(A28)} \\ &= -\sum_\sigma \int_{t'}^t d\bar{t}\, \bar{K}_{\varepsilon_0}^<(\bar{t},t) \bar{P}_\sigma^{\mathrm{R}}(t,\bar{t}) \bar{E}^{\mathrm{R}}(\bar{t},t') \qquad \text{(A29)}\end{aligned}$$

with $\bar{K}_{\varepsilon_0}^<(\bar{t},t)$ as defined in Eq. (25). The step from the first to the second line involves the approximate ε integration resulting in the Fourier transformation of the Fermi function and in fixing the energy variables of the level widths as indicated. We did not attempt to derive it mathematically by an asymptotic stationary-phase analysis [71]. Instead, we followed Shao and co-workers [33] and adopted a qualitative, physics-based reasoning. It yields the very intuitive equation (A27) and reduces moreover the numerical effort considerably because it is no longer necessary to perform at each time-grid point (t,t') an ε integration. Alternatively, $\Gamma_\varepsilon(t)$ could be replaced in (A26) by an average over the energy range of the conduction band and then put in front of the ε integral [32]. But, this seems to be even more *ad hoc*.

Similar manipulations can be performed for the other Dyson equations. At the end, one obtains Eqs. (19)–(24) of Sec. III. The equations are identical to the ones given by Shao and co-workers in the book edited by Rabalais [33] if, as we did, the pseudoparticle operator p_σ is taken to be fermionic.

The kinetic equations (19)–(24) are a complicated set of two-dimensional integrodifferential equations. Nordlander and co-workers [32–34] showed, however, that in situations where the functions $\bar{f}_\varepsilon^{\gtrless}(t,\bar{t})$ and hence the self-energies are sufficiently peaked at $t = \bar{t}$ the Dyson equations for the less-than Green functions can be reduced to master equations for the occurrence probabilities which are numerically less expensive. Depending on whether retarded Green functions are taken at equal times and hence pushed in front of the time integrals or not, two sets of master equations can be derived: the simple and the generalized master equations [32–34]. Applying this reasoning to Eqs. (19)–(24) yields at the level where retarded Green functions are taken at equal times a set of simple master equations

$$\begin{aligned}\frac{d}{dt} n_e(t) &= -2\Gamma_0(t) f^<(\varepsilon_0(t)) n_e(t) + \Gamma_0(t) \\ &\quad \times f^>(\varepsilon_0(t)) \big(n_{p_{1/2}}(t) + n_{p_{-1/2}}(t)\big), \qquad \text{(A30)} \\ \frac{d}{dt} n_{p_\sigma}(t) &= -\big(\Gamma_0(t) f^>(\varepsilon_0(t)) + \Gamma_U(t) f^<(\varepsilon_U(t))\big) n_{p_\sigma}(t) \\ &\quad + \Gamma_0(t) f^<(\varepsilon_0(t)) n_e(t) + \Gamma_U(t) f^>(\varepsilon_U(t)) n_d(t), \qquad \text{(A31)} \\ \frac{d}{dt} n_d(t) &= -2\Gamma_U(t) f^>(\varepsilon_U(t)) n_d(t) \\ &\quad + \Gamma_U(t) f^<(\varepsilon_U(t)) \big(n_{p_{1/2}}(t) + n_{p_{-1/2}}(t)\big), \qquad \text{(A32)}\end{aligned}$$

and at the advanced level, where retarded Green functions are kept nondiagonal in time, a set of generalized master equations

$$\frac{d}{dt}n_e(t) = -2n_e(t)\sum_\sigma \int_{-\infty}^{t} d\bar{t}\ \mathrm{Im}\left(\bar{K}^{<}_{\varepsilon_0}(\bar{t},t)\bar{P}^{\mathrm{R}}_\sigma(t,\bar{t})\right) + 2\sum_\sigma n_{p_\sigma}(t)\int_{-\infty}^{t} d\bar{t}\ \mathrm{Im}\left(\bar{K}^{>}_{\varepsilon_0}(\bar{t},t)[\bar{E}^{\mathrm{R}}(t,\bar{t})]^*\right), \tag{A33}$$

$$\frac{d}{dt}n_{p_\sigma}(t) = -2n_{p_\sigma}(t)\int_{-\infty}^{t} d\bar{t}\ \mathrm{Im}\left(\bar{K}^{>}_{\varepsilon_0}(t,\bar{t})\bar{E}^{\mathrm{R}}(t,\bar{t}) + \bar{K}^{<}_{\varepsilon_U}(\bar{t},t)\bar{D}^{\mathrm{R}}(t,\bar{t})\right)$$
$$+2n_e(t)\int_{-\infty}^{t} d\bar{t}\ \mathrm{Im}\left(\bar{K}^{<}_{\varepsilon_0}(t,\bar{t})\left[\bar{P}^{\mathrm{R}}_\sigma(t,\bar{t})\right]^*\right) + 2n_d(t)\int_{-\infty}^{t} d\bar{t}\ \mathrm{Im}\left(\bar{K}^{>}_{\varepsilon_U}(\bar{t},t)\left[\bar{P}^{\mathrm{R}}_\sigma(t,\bar{t})\right]^*\right), \tag{A34}$$

$$\frac{d}{dt}n_d(t) = -2n_d(t)\sum_\sigma \int_{-\infty}^{t} d\bar{t}\ \mathrm{Im}\left(\bar{K}^{>}_{\varepsilon_U}(t,\bar{t})\bar{P}^{\mathrm{R}}_\sigma(t,\bar{t})\right) + 2\sum_\sigma n_{p_\sigma}(t)\int_{-\infty}^{t} d\bar{t}\ \mathrm{Im}\left(\bar{K}^{<}_{\varepsilon_U}(t,\bar{t})[\bar{D}^{\mathrm{R}}(t,\bar{t})]^*\right) \tag{A35}$$

with occurrence probabilities $n_e(t)$, $n_{p_\sigma}(t)$, and $n_d(t)$ as defined in Eqs. (32)–(34). The retarded Green functions required in the generalized master equations can be obtained by utilizing the localization of $\bar{f}^{\gtrless}_\varepsilon(t,\bar{t})$ around the time diagonal also in the Dyson equations for the retarded Green functions. As a result, one obtains

$$\bar{E}^{\mathrm{R}}(t,t') = \exp\left[-\sum_\sigma \int_{t'}^{t} d\tau \int_{t'}^{\tau} d\bar{t}\ \bar{K}^{<}_{\varepsilon_0}(\bar{t},\tau)\bar{P}^{\mathrm{R}}_\sigma(\tau,\bar{t})\right], \tag{A36}$$

$$\bar{P}^{\mathrm{R}}_\sigma(t,t') = \exp\left[-\int_{t'}^{t} d\tau \int_{t'}^{\tau} d\bar{t}\left(\bar{K}^{>}_{\varepsilon_0}(\tau,\bar{t})\bar{E}^{\mathrm{R}}(\tau,\bar{t}) + \bar{K}^{<}_{\varepsilon_U}(\bar{t},\tau)\bar{D}^{\mathrm{R}}(\tau,\bar{t})\right)\right], \tag{A37}$$

$$\bar{D}^{\mathrm{R}}(t,t') = \exp\left[-\sum_\sigma \int_{t'}^{t} d\tau \int_{t'}^{\tau} d\bar{t}\ \bar{K}^{>}_{\varepsilon_U}(\tau,\bar{t})\bar{P}^{\mathrm{R}}_{-\sigma}(\tau,\bar{t})\right]. \tag{A38}$$

A rigorous determination of the range of validity of these equations by asymptotic techniques [71] is complicated because the functions $\bar{f}^{\gtrless}_\varepsilon(t,\bar{t})$ are not only localized around the time diagonal, but also strongly oscillating. Simple saddle-point arguments are thus not sufficient but have to be augmented by a stationary-phase analysis. Analyzing moreover the whole set of Dyson equations by these techniques seems to be impractical. Langreth and Nordlander [34] investigated therefore the validity of the approximations empirically and developed qualitative criteria which have to be satisfied for master equations to provide a reasonable description of the charge transfer between the projectile and the target surface. As shown in Sec. IV, the basic constraint (36) they developed is not satisfied for the Sr:Au system investigated by He and Yarmoff [30,31]. The full double-time quantum-kinetic equations have thus to be solved to analyze this experiment.

[1] R. C. Monreal, Prog. Surf. Sci. **89**, 80 (2014).
[2] *Slow Heavy-Particle Induced Electron Emission from Solid Surface*, edited by H.-P. Winter and J. Burgdörfer (Springer, Berlin, 2007).
[3] H. Winter, Phys. Rep. **367**, 387 (2002).
[4] *Low Energy Ion-Surface Interaction*, edited by J. W. Rabalais (Wiley, New York, 1994).
[5] J. Los and J. J. C. Geerlings, Phys. Rep. **190**, 133 (1990).
[6] R. Brako and D. M. Newns, Rep. Prog. Phys. **52**, 655 (1989).
[7] A. Modinos, Prog. Surf. Sci. **26**, 19 (1987).
[8] A. Yoshimori and K. Makoshi, Prog. Surf. Sci. **21**, 251 (1986).
[9] D. M. Newns, K. Makoshi, R. Brako, and J. N. M. van Wunnik, Phys. Scr. **T6**, 5 (1983).
[10] W. Kraus, H.-D. Falter, U. Fantz, P. Franzen, B. Heinemann, P. McNeely, R. Riedl, and E. Speth, Rev. Sci. Instrum. **79**, 02C108 (2008).
[11] M. A. Lieberman and A. J. Lichtenberg, *Principles of Plasma Discharges and Materials Processing* (Wiley, New York, 2005).
[12] J. W. Rabalais, *Principles and Applications of Ion Scattering Spectrometry: Surface Chemical and Structural Analysis* (Wiley, New York, 2003).
[13] Y. Harada, S. Masuda, and H. Ozaki, Chem. Rev. **97**, 1897 (1997).
[14] A. C. Hewson, *The Kondo Problem to Heavy Fermions* (Cambridge University Press, Cambridge, 1993).
[15] P. Fulde, *Electron Correlations in Molecules and Solids* (Springer, Berlin, 1995).
[16] A. M. Chang and J. C. Chen, Rep. Prog. Phys. **72**, 096501 (2009).
[17] M. Pustilnik and L. Glazman, J. Phys.: Condens. Matter **16**, R513 (2004).
[18] R. Aguado and D. C. Langreth, Phys. Rev. B **67**, 245307 (2003).
[19] D. Goldhaber-Gordon, H. Shtrikman, D. Mahalu, D. Abusch-Magder, U. Meirav, and M. A. Kastner, Nature (London) **391**, 156 (1998).
[20] S. M. Cronenwett, T. H. Oosterkamp, and L. P. Kouwenhoven, Science **281**, 540 (1998).
[21] D. Goldhaber-Gordon, J. Gores, M. A. Kastner, H. Shtrikman, D. Mahalu, and U. Meirav, Phys. Rev. Lett. **81**, 5225 (1998).

[22] N. S. Wingreen and Y. Meir, Phys. Rev. B **49**, 11040 (1994).
[23] *Single Charge Tunneling: Coulomb Blockade Phenomena in Nanostructures*, edited by H. Grabert and M. H. Devoret (Plenum, New York, 1992).
[24] H. T. M. Nghiem and T. A. Costi, Phys. Rev. B **90**, 035129 (2014).
[25] B. Lechtenberg and F. B. Anders, Phys. Rev. B **90**, 045117 (2014).
[26] L. Mühlbacher, D. F. Urban, and A. Komnik, Phys. Rev. B **83**, 075107 (2011).
[27] G. Cohen and E. Rabani, Phys. Rev. B **84**, 075150 (2011).
[28] H. Shao, P. Nordlander, and D. C. Langreth, Phys. Rev. Lett. **77**, 948 (1996).
[29] J. Merino and J. B. Marston, Phys. Rev. B **58**, 6982 (1998).
[30] X. He and J. A. Yarmoff, Nucl. Instrum. Meth. Phys. Res., Sect. B **269**, 1195 (2011).
[31] X. He and J. A. Yarmoff, Phys. Rev. Lett. **105**, 176806 (2010).
[32] H. Shao, D. C. Langreth, and P. Nordlander, Phys. Rev. B **49**, 13929 (1994).
[33] H. Shao, D. C. Langreth, and P. Nordlander, in *Low Energy Ion-Surface Interaction*, edited by J. W. Rabalais (Wiley, New York, 1994), p. 117.
[34] D. C. Langreth and P. Nordlander, Phys. Rev. B **43**, 2541 (1991).
[35] H. Kasai and A. Okiji, Surf. Sci. **183**, 147 (1987).
[36] H. Nakanishi, H. Kasai, and A. Okiji, Surf. Sci. **197**, 515 (1988).
[37] M. A. Romero, F. Flores, and E. C. Goldberg, Phys. Rev. B **80**, 235427 (2009).
[38] N. Bajales, J. Ferrón, and E. C. Goldberg, Phys. Rev. B **76**, 245431 (2007).
[39] E. C. Goldberg, F. Flores, and R. C. Monreal, Phys. Rev. B **71**, 035112 (2005).
[40] A. V. Onufriev and J. B. Marston, Phys. Rev. B **53**, 13340 (1996).
[41] J. B. Marston, D. R. Andersson, E. R. Behringer, B. H. Cooper, C. A. DiRubio, G. A. Kimmel, and C. Richardson, Phys. Rev. B **48**, 7809 (1993).
[42] E. Clementi and C. Roetti, At. Data Nucl. Data Tables **14**, 177 (1974).
[43] J. W. Gadzuk, Surf. Sci. **6**, 133 (1967).
[44] J. W. Gadzuk, Surf. Sci. **6**, 159 (1967).
[45] J. W. Gadzuk, Phys. Rev. B **79**, 073411 (2009).
[46] P. Coleman, Phys. Rev. B **29**, 3035 (1984).
[47] G. Kotliar and A. E. Ruckenstein, Phys. Rev. Lett. **57**, 1362 (1986).
[48] L. P. Kadanoff and G. Baym, *Quantum Statistical Mechanics* (Benjamin, New York, 1962).
[49] L. V. Keldysh, J. Exptl. Theoret. Phys. (U.S.S.R.) **47**, 1515 (1964) [Sov. Phys. JETP **20**, 1018 (1965)].
[50] J. Otsuki and Y. Kuramoto, J. Phys. Soc. Jpn. **75**, 064707 (2006).
[51] J. Kroha and P. Wölfle, J. Phys. Soc. Jpn. **74**, 16 (2005).
[52] T. Pruschke and N. Grewe, Z. Phys. B: Condens. Matter **74**, 439 (1989).
[53] J. Holm and K. Schönhammer, Solid State Commun. **69**, 969 (1989).
[54] O. Sakai, M. Motizuki, and T. Kasuya, in *Core Level Spectroscopy in Condensed Systems*, edited by J. Kanamori and A. Kotani (Springer, Berlin, 1988), p. 45.
[55] P. Nordlander and J. C. Tully, Phys. Rev. Lett. **61**, 990 (1988).
[56] P. Nordlander and J. C. Tully, Phys. Rev. B **42**, 5564 (1990).
[57] A. G. Borisov and U. Wille, Surf. Sci. **338**, L875 (1995).
[58] W. More, J. Merino, R. Monreal, P. Pou, and F. Flores, Phys. Rev. B **58**, 7385 (1998).
[59] D. Valdés, E. C. Goldberg, J. M. Blanco, and R. C. Monreal, Phys. Rev. B **71**, 245417 (2005).
[60] J. Marbach, F. X. Bronold, and H. Fehske, Eur. Phys. J. D **66**, 106 (2012).
[61] J. Marbach, F. X. Bronold, and H. Fehske, Phys. Rev. B **86**, 115417 (2012).
[62] J. Marbach, F. X. Bronold, and H. Fehske, Phys. Rev. B **84**, 085443 (2011).
[63] P. Kürpick and U. Thumm, Phys. Rev. A **54**, 1487 (1996).
[64] J. C. Slater, Phys. Rev. **36**, 57 (1930).
[65] *Handbook of Mathematical Functions*, edited by M. Abramowitz and I. A. Stegun (Dover, New York, 1973).
[66] D. C. Langreth and J. W. Wilkins, Phys. Rev. B **6**, 3189 (1972).
[67] C. E. Sosolik, J. R. Hampton, A. C. Lavery, B. H. Cooper, and J. B. Marston, Phys. Rev. Lett. **90**, 013201 (2003).
[68] M. Plihal, D. C. Langreth, and P. Nordlander, Phys. Rev. B **59**, 13322 (1999).
[69] G. A. Baker, Jr., Phys. Rev. **109**, 2198 (1958).
[70] E. M. Lifshitz and L. P. Pitaevskii, *Physical Kinetics* (Pergamon, New York, 1981).
[71] N. Bleistein and R. A. Handelsman, *Asymptotic Expansion of Integrals* (Dover, New York, 1986).

IOP Publishing Plasma Sources Science and Technology

Plasma Sources Sci. Technol. **27** (2018) 084003 (22pp) https://doi.org/10.1088/1361-6595/aad4db

Ion-induced secondary electron emission from metal surfaces

M Pamperin, F X Bronold and H Fehske

Institut für Physik, Ernst-Moritz-Arndt-Universität Greifswald, D-17489 Greifswald, Germany

E-mail: bronold@physik.uni-greifswald.de

Received 28 March 2018, revised 6 July 2018
Accepted for publication 20 July 2018
Published 13 August 2018

Abstract

Using a helium ion hitting various metal surfaces as a model system, we describe a general quantum-kinetic approach for calculating ion-induced secondary electron emission spectra at impact energies where the emission is driven by the internal potential energy of the ion. It is based on an effective model of the Anderson−Newns-type for the subset of electronic states of the ion−surface system most strongly affected by the collision. Central to our approach is a pseudo-particle representation for the electronic configurations of the projectile which enables us, by combining it with two additional auxiliary bosons, to describe in a single Hamiltonian emission channels involving electronic configurations with different internal potential energies. It is thus possible to treat Auger neutralization of the ion on an equal footing with Auger de-excitation of temporarily formed radicals and/or negative ions. From the Dyson equations for the projectile propagators and an approximate evaluation of the self-energies, rate equations are obtained for the probabilities with which the projectile configurations occur and an electron is emitted in the course of the collision. Encouraging numerical results, especially for the helium −tungsten system, indicate the potential of our approach.

Keywords: secondary electron emission, ion scattering from surfaces, charge-transferring atom-surface collisions

1. Introduction

In low-temperature gas discharges, secondary electron emission from the walls confining the plasma is an important surface collision process caused by atomic constituents of the plasma hitting the wall [1]. Known since the early days of gaseous electronics [2], it has moved into the focus of interest again quite recently. For instance, it has been shown that the ionization dynamics [3, 4], the electron power absorption [5], and a number of other quantities and processes [6] in capacitively coupled discharges depend significantly on the secondary electron emission coefficient—that is, the probability with which an electron is released in the course of an atom −surface collision. It has also been demonstrated that the structure of the plasma sheath is strongly affected by secondary electron emission [7–10]. The impact energies are typically in the range where electron emission is driven by the internal potential energy stored in the electronic configuration of the projectile. Auger neutralization of ions and/or Auger de-excitation of metastable species are thus the main channels of secondary electron emission [11]. Ion- and radical-induced secondary electron emission can thus be distinguished, depending on the initial state of the projectile. Since the processes are also of interest for themselves as well as of importance for various kinds of surface diagnostics—for instance, secondary ion mass spectroscopy [12] or metastable atom de-excitation spectroscopy [13]—Auger and related charge-transfer processes have been reviewed several times [14–22] since the early studies [23–28] dating back to the very beginning of modern condensed matter physics. There can thus be no doubt that the basic mechanisms of secondary electron emission from surfaces have by now been identified.

Although the principles of secondary electron emission are known, it is still a great challenge to measure or to calculate secondary electron emission spectra, even for free-standing surfaces not in contact with a plasma. Experimentally, it requires sophisticated instrumentation [16, 29–38], whereas theoretically, the challenge is to find an efficient way to deal with a many-body scattering problem giving rise to a great variety of collision pathways [39–54]. It is thus not surprising that the data base for secondary electron emission is rather sparse, especially for materials used as walls in

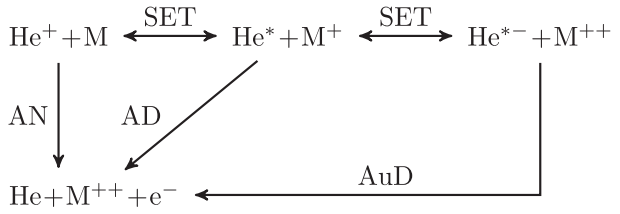

Figure 1. Schematic representation of possible charge transfer processes which may take place during a collision of a He^+ ion with a metal surface, depending on the occupancies of the electronic states, their coupling, and the collision dynamics. The ion may capture electrons from the metal M by single-electron transfer (SET), changing its configuration from He^+ (1s) to He*(1s2s) or even to $He^{*-}(1s2s^2)$, if two sequential SET processes occur. SET processes may, however, also work in the other direction—that is, the projectile may also lose electrons. Autodetachment (AuD) may lead to an electron loss and a reconfiguration of $He^{*-}(1s2s^2)$ to $He(1s^2)$. In addition, Auger neutralization (AN) and Auger de-excitation (AD) due to the Coulomb interaction between two electrons may take place, pushing the projectile to its ground-state configuration $He(1s^2)$ and thereby also releasing an electron. The charge state of the metal M is indicated to emphasize the charge-transfer taking place due to the various processes.

laboratory gas discharges. There have been only a few experimental efforts devoted to measuring secondary electron emission coefficients specifically for such materials [55, 56].

To illustrate the complexity of the physics involved, we show in figure 1 the collision channels which may be open when a positive helium ion hits a metal surface and releases an electron. Besides Auger neutralization of the positive ion itself, there is a sequence of single-electron transfers possible, leading to neutral and negatively charged metastable states which may Auger de-excite or autodetach to the helium ground state, thereby also releasing an electron. Which one of the three channels dominates depends on the collision parameters and the metal. An unbiased description of the collision thus requires a theoretical model capable of treating all channels having a chance to be involved in the electron emission simultaneously. To present such a theory is the purpose of this work.

We do not attempt a description from first principles [40–42, 44, 45, 48]. Instead, we use an Anderson−Newns−Hamiltonian for the subset of electronic degrees of freedom which are dominantly involved in the collision process. Combined with Gadzuk's semiempirical approach [57, 58] of determining the matrix elements of this Hamiltonian from classical image shifts, it yields a rather flexible basis for the modeling of a great variety of projectile−target combinations. We consider this type of effective modeling—ultimately requiring only a few parameters with a clear physical interpretation—particularly appropriate for describing secondary electron emission from plasma walls, which are often not well characterized microscopically and thus not amenable to more sophisticated modeling. Local correlations on the projectile can be taken into account by a projection operator and pseudo-particle technique pioneered by Langreth *et al* [59–61]. Combining this with additional auxiliary bosons to accommodate the energy defects between different electronic configurations of the projectile leads to a Hamiltonian containing as many projectile configurations as one wishes to include and at the same time is amenable to a quantum-kinetic analysis [59–61]. Ultimately, it leads to rate equations for the probabilities with which the electronic configurations of the projectile occur and an electron is emitted in the course of the collision. We employed this approach previously to describe electron emission from metal and dielectric surfaces due to the de-excitation of metastable nitrogen molecules [62–64] and to the neutralization of positive strontium and magnesium ions at gold surfaces [65, 66]. In this work, we apply it to a positive helium ion hitting various metal surfaces. Confronted with experimental data [30, 35], the approach turns out to yield secondary electron emission coefficients of the correct order of magnitude, and might even be able to produce the correct shape of the emission spectrum if it were augmented by scattering processes [29, 36, 38]—which we so far, however, have not included in the model.

The outline of the remainder of the paper is as follows. In the next section, we set up the Anderson−Newns model for the emission channels shown in figure 1. Besides explaining how the matrix elements of the Hamiltonian are obtained from Gadzuk's reasonings, we also give the details of the projection operator and pseudo-particle technique which enables us to encode into a single Hamiltonian electronic configurations with different internal potential energies. Section 3 together with an appendix describes the quantum-kinetic derivation of the rate equations for the probabilities with which the various electronic configurations of the projectile are realized in the collision and an electron is emitted. Numerical results are presented in section 4, and concluding remarks summarize and assess our approach in section 5.

2. Model

When an atomic projectile approaches a surface, direct and exchange Coulomb interactions take place between their individual constituents leading to a modification of the projectile's and target's electronic structure. In some cases, this may cause a redistribution of electrons between them, accompanied perhaps by the emission of an electron. Since the projectile and the target are composite systems, to analyze these processes theoretically is a complicated many-body problem. It can be approached either with first-principles methods [40–42, 44, 45, 48], ideally containing the full electronic structure of the target and the projectile, or with model Hamiltonians focusing only on the subset of electronic states which are actively involved in the collision—as pioneered by Gadzuk [57, 58]. The former is computationally very expensive. In addition, it requires a rather complete characterization of the structure and chemical composition of the surface. Working atom-by-atom, *ab initio* methods have to know precisely which atom is sitting where. For plasma-exposed surfaces, this information is not available in most cases. It is thus better not to rely on it at all and—following the second approach—to construct instead an effective Hamiltonian for that part of the electronic structure which is

expected to be foremostly involved in the collision process. Physical considerations may then be invoked to parameterize the model by a few quantities which are easily available and at the same time have a clear physical meaning.

The particular approach we employ is based on an Anderson−Newns-type effective Hamiltonian. Following Gadzuk [57, 58] it uses classical image charges to mimic the long-range exchange interactions (polarization interactions) and a multi-channel scattering theory to account in the matrix elements for single-electron transfer for the non-orthogonality of the target and projectile wavefunctions. The non-orthogonality of the wavefunctions is also an issue in the Auger channels [44]. Taking it into account, however, makes the calculation of the Auger matrix elements even more complicated than it already is. In the model presented below, we therefore ignore the non-orthogonality of the wavefunctions in the Auger matrix elements, assuming implicitly that it is less important than the tunneling of the metal wavefunction through the potential barrier, arising from the overlap of the ion and surface potentials, which we take into account. The good agreement of the rate we get for Auger neutralization with the rate given by Wang *et al* [46], as well as with the rate obtained by an approach based in part on first principles [44], supports this assumption. What speaks against it is the too large ion survival probability we obtain for large angles of incidence. However, the reason for this is most probably the neglect of single-electron transfer from deeper lying levels of the surface (core levels) to the 1s shell. It is beyond the scope of the present work to include this process as well.

To furnish the formalism with wavefunctions, simple models are used for the surface potential and the electronic structure of the projectile—parameterized, however, such that it reproduces measured ionization energies and electron affinities. From our previous work on the de-excitation of metastable nitrogen molecules on surfaces [62–64] and the neutralization of alkaline-earth ions on gold surfaces [65, 66], we expect this type of modeling also to provide reasonable matrix elements for the Anderson−Newns Hamiltonian describing ion-induced electron ejection from metal surfaces.

2.1. Electronic configurations and energy levels

To analyze the chain of processes outlined in figure 1, we consider the following electronic configurations for the He projectile: $He^{+}(1s)$, $He^{0}(1s^{2})$, $He^{*}(1s2s)$, and $He^{*-}(1s2s^{2})$. Without loss of generality, we assume the electron of the $He^{+}(1s)$ ion to have spin up. This leaves us with two non-degenerate metastable levels $He^{*}(1s2s)$, a triplet $2^{3}S_{1}$ and a singlet $2^{1}S_{0}$ with, respectively, a spin-up and spin-down electron in the 2*s* shell. The term symbols for the positive ion and the ground-state atom are $1^{2}S_{1/2}$ and $1^{1}S_{0}$. We also consider the negative ion $He^{*-}(1s2s^{2})$ arising from either one of the metastable states. In both cases, the term symbol is $2^{2}S_{1/2}$ because the two electrons in the 2s shell have anti-parallel spin. This is the lowest lying negatively charged state, and known to act as an intermediary in surface-induced spin-flip collisions [67, 68]. It may thus also play a role in secondary electron emission. In principle, there are of course additional configurations possible. For instance, the metastable state He*(1s2p) could also be involved. We expect it, however, to be less important for the collision we consider because p orbitals lead to smaller matrix elements and thus to smaller transition rates.

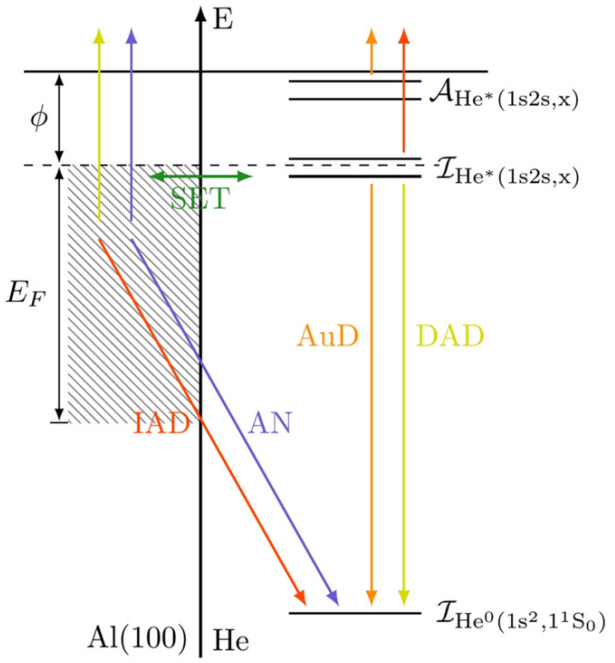

Figure 2. On scale representation of the electronic states involved in the neutralization of a $He^{+}(1s)$ ion on an Al(100) surface due to the processes introduced and discussed in figure 1. The situation shown corresponds to the case where projectile and target are infinitely far apart. Polarization-induced shifts of the ionization energies, $\mathcal{I}_{He^0(1s^2,1^1S_0)}$, $\mathcal{I}_{He^*(1s2s,2^1S_0)}$, and $\mathcal{I}_{He^*(1s2s,2^3S_1)}$ and the electron affinities $\mathcal{A}_{He^*(1s2s,2^1S_0)}$ and $\mathcal{A}_{He^*(1s2s,2^3S_1)}$ encoded in equations (1)–(5) are not shown. The shaded region on the left indicates the occupied states of the conduction band of the Al(100) surface, the label 'x' in the ionization and affinity levels of the metastable configuration stands for either the triplet or the singlet term symbol, and the color-coded arrows give the transitions involved in secondary electron emission due to Auger neutralization (AN, blue), direct and indirect Auger de-excitation (DAD, yellow; IAD, red), and autodetachment (AuD, orange), where the latter two take place only after single-electron transfers (SET, green) have occurred.

Far away from the surface, the projectile configurations are characterized by a discrete set of energies representing the ionization energies or electron affinities depending on whether the configurations are electrically neutral, positive, or negative. For the reaction scheme shown in figure 1 we need the single-electron ionization energies $\mathcal{I}_{He^0(1s^2,1^1S_0)}$, $\mathcal{I}_{He^*(1s2s,2^1S_0)}$, and $\mathcal{I}_{He^*(1s2s,2^3S_1)}$, that is, the thresholds of the first ionization continua of the helium configurations given in the subscripts, as well as the single-electron affinities $\mathcal{A}_{He^*(1s2s,2^1S_0)}$ and $\mathcal{A}_{He^*(1s2s,2^3S_1)}$, where the subscripts indicate again the configurations the energies belong to. How these (positive) energies relate to the vacuum level is shown in figure 2, together with the processes they are involved in. While the projectile approaches the surface, the energy levels shift. Assuming a polarization-induced image charge

interaction to be responsible for the shifts, the ionization levels move upward in energy whereas affinity levels move downwards [22]. Close to the surface, short-range interactions may modify the shifts [48]. The processes we are interested in occur, however, sufficiently far away from the surface that short-range interactions are not yet important. To take all this into account, we define five time-dependent single-electron energy levels,

$$\varepsilon^{0}_{1s\downarrow}(t) = -\mathcal{I}_{\mathrm{He}^0(1s^2,{}^1S_0)} + \frac{e^2}{4(z(t)-z_i)}, \tag{1}$$

$$\varepsilon^{*}_{2s\downarrow}(t) = -\mathcal{I}_{\mathrm{He}^*(1s2s,{}^1S_0)} + \frac{e^2}{4(z(t)-z_i)}, \tag{2}$$

$$\varepsilon^{*}_{2s\uparrow}(t) = -\mathcal{I}_{\mathrm{He}^*(1s2s,{}^3S_1)} + \frac{e^2}{4(z(t)-z_i)}, \tag{3}$$

$$\varepsilon^{-}_{2s\downarrow}(t) = -\mathcal{A}_{\mathrm{He}^*(1s2s,{}^1S_0)} - \frac{e^2}{4(z(t)-z_i)}, \tag{4}$$

$$\varepsilon^{-}_{2s\uparrow}(t) = -\mathcal{A}_{\mathrm{He}^*(1s2s,{}^3S_1)} - \frac{e^2}{4(z(t)-z_i)}, \tag{5}$$

with the subscript indicating the shell and the spin of the electron and the time-dependence arising from the collision trajectory,

$$z(t) = z_{\mathrm{TP}} + v_\perp |t|, \tag{6}$$

where $v_\perp$ is the projectile's velocity component perpendicular to the surface and z_{TP} is the turning point of the trajectory. The energy levels (1)–(5) are thus time-dependent ionization energies and electron affinities. Note that $z(t)$ describes the classical center-of-mass motion of the projectile resulting from the trajectory approximation [20], which is justified because of the large mass of the projectile. The turning point z_{TP} is usually a few Bohr radii before the crystallographic ending of the surface. It arises from short-range repulsive forces. Our choice for z_{TP}, which in general depends on the projectile and the target, is guided by the calculations of Lancaster *et al* [30] showing that the neutralization of He^+ ions at impact energies $E_{\mathrm{kin}\perp} < 60\,\mathrm{eV}$, which is also the upper limit in the gracing incident experiments with which we compare our results, takes typically place 2–5 a_B in front of the surface, where a_B denotes the Bohr radius. We can thus chose $z_{\mathrm{TP}} = 2.27\,\mathrm{a_B}$, as suggested by Modinos and Easa [54], without affecting the charge-transfer too much. Indeed our final results are rather robust against changes in z_{TP} up to $\pm \mathrm{a_B}/2$. The position of the image plane z_i, appearing in (1)–(5), is used as a fitting parameter but it should be around $1 - 2\mathrm{a_B}$ [69].

In addition to the energy levels of the projectile, we also need the energy $\varepsilon_{\vec{k}\sigma}$ of an electron in the conduction band of the metal and the energy $\varepsilon_{\vec{q}\sigma}(t)$ of an unbound electron at position $z(t)$ in front of the surface. Modeling the metal, as in our previous work [62–66], by a three-dimensional step potential,

$$V_\mathrm{S}(z) = -V_0\theta(-z) \tag{7}$$

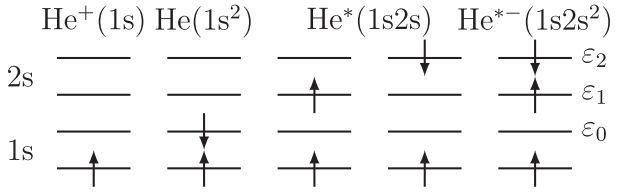

Figure 3. Electronic configurations of the He projectile included into our modeling. As indicated on the left, the lowest two levels stand for the 1s shell and the upper two for the 2s shell. Since the 1s shell is by assumption always occupied by a spin-up electron, only the energy levels ε_0, ε_1, and ε_2 are of interest. The ground state arises if ε_0 is occupied by a spin-down electron, the metastable triplet (singlet) state if ε_1 (ε_2) is occupied by a spin-up (spin-down) electron, and the negative ion state if ε_1 and ε_2 are occupied, respectively, by a spin-up and a spin-down electron. Depending on the occupancy and the way it is realized, the energy levels ε_1 and ε_2 take on different numerical values. This can be organized with projection operators. Two auxiliary bosons finally allow switching as required between the configurations.

with depth $V_0 = E_\mathrm{F} + \phi$, where $E_\mathrm{F} > 0$ is the Fermi energy of the metal and $\phi > 0$ the work function,

$$\varepsilon_{\vec{k}\sigma} = \frac{\hbar^2\vec{k}^2}{2m^*_\mathrm{e}} - V_0 \tag{8}$$

with m^*_e the effective mass of an electron in the conduction band of the metal. Assuming moreover a plane wave for the wavefunction of an unbound electron in front of the surface, its energy is given by

$$\varepsilon_{\vec{q}\sigma}(t) = \frac{\hbar^2\vec{q}^{\,2}}{2m_\mathrm{e}} - \frac{e^2}{4(z(t)-z_i)}, \tag{9}$$

where the second term takes the interaction of the electron with its image into account.

Since by assumption the 1s shell is always occupied by a spin-up electron, we in effect model the projectile by a three-level system with energies ε_0, ε_1, and ε_2 as illustrated in figure 3. An important feature of the model is that the energies depend on the occupancy of the levels and—in the case of the negative ion configurations—on the way the occupancy was built up. To take this into account, we employ operators

$$P_{n_0n_1n_2} = |n_0n_1n_2\rangle\langle n_0n_1n_2| \tag{10}$$

projecting onto states $|n_0n_1n_2\rangle$ of the three-level system containing $n_i = 0, 1$ electrons in the energy levels ε_i. Defining

$$P_{100}\varepsilon_0(t) = \varepsilon^{0}_{1s\downarrow}(t), \tag{11}$$

$$P_{010}\varepsilon_1(t) = \varepsilon^{*}_{2s\uparrow}(t), \tag{12}$$

$$P_{001}\varepsilon_2(t) = \varepsilon^{*}_{2s\downarrow}(t), \tag{13}$$

$$P_{011}\varepsilon_1(t) = \varepsilon^{-}_{2s\uparrow}(t), \tag{14}$$

$$P_{011}\varepsilon_2(t) = \varepsilon^{-}_{2s\downarrow}(t) \tag{15}$$

with projections to the remaining states required for completeness

$$Q = \sum_{n_0}\sum_{n_1}\sum_{n_2}|n_0n_1n_2\rangle\langle n_0n_1n_2| = 1 \tag{16}$$

to be zero, it is possible to adjust ε_0, ε_1, and ε_2 to the internal energetics of the projectile configurations involved in the atom−surface collision we want to model. The operator Q defined in (16) will also be required in the quantum-kinetic approach described in the section 3.

2.2. Wavefunctions and matrix elements

To set up the Anderson−Newns Hamiltonian for the charge-transferring atom−surface collision processes we are interested in, we require a series of matrix elements. Their calculation is based on a particular choice of wavefunctions, which we now describe.

As in our previous work [65], the electronic states of the metal are the wavefunctions $\psi_{\vec{k}\sigma}(\vec{r})$ of the step potential (7). For $k_z < \sqrt{2m_e^* V_0/\hbar^2}$, they describe bound electrons whereas for $k_z > \sqrt{2m_e^* V_0/\hbar^2}$, they contain a transmitted and a reflected wave. From the work of Kürpick and Thumm [70], we would expect little change had we used other wavefunctions for the surface—based, for instance, on the Jennings−Jones−Weinert potential [71] instead of the potential step. For the states of the projectile's 1s and 2s shell, we take hydrogen wavefunctions $\psi_{1\sigma}(\vec{r})$ and $\psi_{2\sigma}(\vec{r}\,)$ with effective charges $Z_{\rm eff}$ adjusted to reproduce the ionization energies and electron affinities, $\mathcal{I}_{\mathrm{He}^0(1s^2,{}^1S_0)}$, $\mathcal{I}_{\mathrm{He}^*(1s2s,2^1S_0)}$, $\mathcal{I}_{\mathrm{He}^*(1s2s,2^3S_1)}$, $\mathcal{A}_{\mathrm{He}^*(1s2s,2^1S_0)}$, and $\mathcal{A}_{\mathrm{He}^*(1s2s,2^3S_1)}$. For the 1s shell, the modified hydrogen wavefunction is in excellent agreement with the Roothaan−Hartree–Fock 1s wavefunction for the helium ground state given by Clementi and Roetti [72]. To estimate the quality of the wavefunction for the 2s shell we compared it—due to lack of Roothaan−Hartree–Fock calculations for excited helium states—with the Roothaan−Hartree–Fock 2*s* wavefunction of the lithium ground state [72]. As expected, the agreement is not as good as for the 1s shell. Since, however, we found charge-transfer for the metals we investigated to be dominated by Auger neutralization, which involves only the 1s shell, we did not attempt to improve the wavefunction for the 2s shell. The projectile's continuum states are—as mentioned above—approximated by plane waves $\psi_{\vec{q}\sigma}(\vec{r})$. Thereby, we ignore distortions of the wavefunctions due to the core potential of the projectile, turning plane waves into Coulomb waves. It is only an issue for Auger de-excitation and autodetachment—which we found, however, not to be the dominant scattering channels. We did not, therefore, include this complication.

Having wavefunctions, we can construct matrix elements for the processes shown in figure 2. Denoting the position of the projectile by $\vec{r}_p(t) = z(t)\vec{e}_z$ with $z(t)$ defined in (6) and following Gadzuk [57, 58] as well as our earlier work [63, 65, 66], we obtain

$$V_{\vec{k}\sigma}(t) = \int \mathrm{d}^3 r\ \psi^*_{\vec{k}}(\vec{r}) \frac{e^2}{|\vec{r} - \vec{r}_p(t)|} \psi_{2\sigma}(\vec{r} - \vec{r}_p(t)) \tag{17}$$

for the matrix element controlling single-electron transfer between the conduction band of the surface and the ionization/affinity levels of the projectile originating from its 2s shell,

$$V_{\vec{k}_1\vec{k}_2\vec{k}'\sigma}(t) = \int \mathrm{d}^3 r \int \mathrm{d}^3 r' \psi^*_{1\downarrow}(\vec{r} - \vec{r}_p(t)) \psi^*_{\vec{k}'\sigma}(\vec{r}') \times \frac{e^2}{|\vec{r} - \vec{r}'|} \psi_{\vec{k}_1\downarrow}(\vec{r}) \psi_{\vec{k}_2\sigma}(\vec{r}') \tag{18}$$

for the matrix element driving Auger neutralization into the ground state, that is, the 1s shell of the projectile, and

$$V_{\vec{k}\vec{k}'\sigma}(t) = \int \mathrm{d}^3 r \int \mathrm{d}^3 r' \psi^*_{1\downarrow}(\vec{r} - \vec{r}_p(t)) \psi^*_{\vec{k}'\sigma}(\vec{r}') \times \frac{e^2}{|\vec{r} - \vec{r}'|} \psi_{2\downarrow}(\vec{r} - \vec{r}_p(t)) \psi_{\vec{k}\sigma}(\vec{r}'), \tag{19}$$

$$V_{\vec{k}\vec{q}\sigma}(t) = \int \mathrm{d}^3 r \int \mathrm{d}^3 r' \psi^*_{1\downarrow}(\vec{r} - \vec{r}_p(t)) \psi^*_{\vec{q}\sigma}(\vec{r}' - \vec{r}_p(t)) \times \frac{e^2}{|\vec{r} - \vec{r}'|} \psi_{2\sigma}(\vec{r}' - \vec{r}_p(t)) \psi_{\vec{k}\downarrow}(\vec{r}) \tag{20}$$

for the direct and indirect Auger de-excitation, respectively, involving the projectile's 1s and 2s shells. Finally, the matrix element for autodetachment reads

$$V_{\vec{q}} = \int \mathrm{d}^3 r \int \mathrm{d}^3 r'\ \psi^*_{1\downarrow}(\vec{r}) \psi^*_{\vec{q}\uparrow}(\vec{r}') \times \frac{e^2}{|\vec{r} - \vec{r}'|} \psi_{2\downarrow}(\vec{r}) \psi_{2\uparrow}(\vec{r}'). \tag{21}$$

In contrast to the other matrix elements, it is—within our model—independent of time (that is, independent of the distance $z(t)$) since it describes a local interaction acting at the instantaneous position of the projectile.

Although the assumptions about the wavefunctions used in (17)–(21) are strong, we stick to it because they allow us to pursue the calculation of the matrix elements to a large extent analytically by means of lateral Fourier transformation, which in turn substantially reduces the numerical effort (which is still large) when it comes to the solution of the kinetic equations. To estimate the validity of our approach, we compare our results with experimental data. As we will see, the agreement is sufficiently good to suggest that the approximate matrix elements we use are not too far away from the exact matrix elements (which we do not, however, know). Our matrix elements contain a number of parameters, which we list in table 1. As indicated in the caption of the table we use parameters from different sources. If the parameters were given directly for the experiments we compare our data with, we took these values. This was the case for the work functions of copper and aluminum and for the affinity levels. The rest of the parameters we collected from data tables. The effective charge $Z_{\rm eff}$ and the position of the image plane z_i were determined as stated above.

An important additional aspect affecting Auger neutralization and indirect Auger de-excitation into the projectile ground state is the enhancement of the wavefunction of the surface electron which fills the hole in the 1s shell of the projectile. It arises from the modification of the step potential mimicking the surface by the Coulomb potentials of the He^+ ion and its image and the image potential of the electron. In

Table 1. Material parameters used in our calculations. The energies $\mathcal{I}$ and $\mathcal{A}$ denote ionization and affinity levels of the indicated helium configurations [68, 73], $Z_{\rm eff}$ is the effective charge used in the hydrogen-like wavefunctions $\psi_{1\downarrow}(\vec{r})$ and $\psi_{2\sigma}(\vec{r})$ (required for the calculation of the matrix elements) to reproduce these energies, $z_{\rm i}$ is the position of the image plane, and ϕ, $E_{\rm F}$, and $m_{\rm e}^*$ are the work function, the Fermi energy, and the effective mass of an electron in the conduction band of the metal surface [28, 30, 65, 74, 75].

	$\mathcal{I}$[eV]	$\mathcal{A}$[eV]	$Z_{\rm eff}$	z_i[a_B]	ϕ[eV]	$E_{\rm F}$[eV]	$m_{\rm e}^*/m_{\rm e}$
He(1^1S_0)	24.587 5	—	1.68	—	—	—	—
He*(2^3S_1)	4.767 8	—	1.18	—	—	—	—
He*(2^1S_0)	3.971 6	—	1.08	—	—	—	—
He*(2^3S_1)	—	1.25	0.61	—	—	—	—
He*(2^1S_0)	—	0.45	0.36	—	—	—	—
W(110)	—	—	—	1.3	5.22	6.4	1.1
Cu(100)	—	—	—	1.3	5.1	7	1.1
Al(100)	—	—	—	1.5	4.25	11.7	1.1
HM	—	—	—	1.3	3	9	1.1

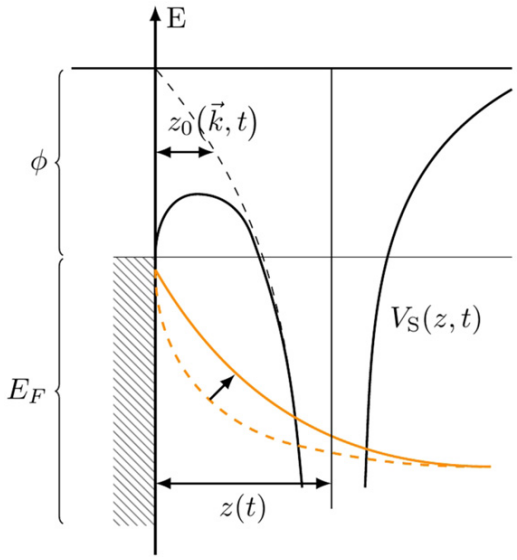

Figure 4. Illustration of the ion-induced modification of the step potential used for the surface. The ion, at position $z = z(t)$, creates a potential barrier $V_s(z, z(t))$ through which an electron from the conduction band can tunnel. The under-the-barrier motion occurs between the turning points $z = 0$ and $z = z_0(\vec{k}, t)$. Approximating the latter by the black dashed line simplifies the numerical treatment without losing accuracy below the Fermi energy $E_{\rm F}$ which is the energy range of interest. The enhancement of the wavefunction for the metal electron filling in an Auger process the projectile's 1s shell at the position of the ion is qualitatively indicated by the solid and dashed orange lines.

effect, the step potential (7) becomes a potential barrier,

$$V_{\rm S}(z) = V_{\rm S}(z, z(t))\theta(-z) \tag{22}$$

with

$$V_{\rm S}(z, z(t)) = -\frac{e^2}{|z(t) - z|} + \frac{e^2}{|z(t) + z|} - \frac{e^2}{4(z - z_{\rm i})}, \tag{23}$$

as shown in figure 4, through which the surface electron can tunnel. Following Propst [38] and Penn and Apell [76], we take this into account by a semiclassical correction to the electron's wavefunction using the WKB approximation. The z-dependence of the wavefunction of a metal electron with $k_z < \sqrt{2m_{\rm e}^*V_0/\hbar^2}$ is given by

$$\psi_{\vec{k}\sigma}(z(t)) \propto \exp(\Delta(\varepsilon_{\vec{k}\sigma}, z(t))). \tag{24}$$

For the step potential,

$$\Delta_{\rm step}(\varepsilon_{\vec{k}\sigma}, z(t)) = \kappa_z z(t) \tag{25}$$

with $\kappa_z = {\rm i}\sqrt{k_z^2 - 2m_{\rm e}^*V_0/\hbar^2}$. Using the WKB method to account for the tunneling of the electron through the barrier (see figure 4),

$$\Delta_{\rm WKB}(\varepsilon_{\vec{k}\sigma}, z(t)) = \int_0^{z_0(\varepsilon_{\vec{k}\sigma}, z(t))} K(\varepsilon_{\vec{k}\sigma}, z(t); z){\rm d}z \tag{26}$$

with $K(\varepsilon_{\vec{k}\sigma}, z(t); z) = {\rm i}\sqrt{k_z^2 - 2m_{\rm e}^*V_{\rm S}(z, z(t))/\hbar^2}$ and $z = 0$ and $z = z_0(\varepsilon_{\vec{k}\sigma}, z(t))$ the turning points of the under-the-barrier motion of the electron. Neglecting in (23) the image potential of the metal electron—that is, the third term —$z_0(\varepsilon_{\vec{k}\sigma}, z(t))$ can be determined analytically, leading to the dashed black line in figure 4. By numerical integration, we then find the adjustment ratio,

$$\Delta_{\rm adjust}(\varepsilon_{\vec{k}\sigma}, z(t)) = \frac{\Delta_{\rm WKB}(\varepsilon_{\vec{k}\sigma}, z(t))}{\Delta_{\rm step}(\varepsilon_{\vec{k}\sigma}, z(t))} \approx 0.15\sqrt{z(t)}, \tag{27}$$

which depends only weakly on $\vec{k}$. Hence, by replacing κ_z in equation (25) by

$$\kappa_z(t) = \Delta_{\rm adjust}(t)\kappa_z, \tag{28}$$

we approximately take into account the tunneling-induced enhancement of the metal electron wavefunction at the projectile position $z(t)$, as illustrated in figure 4. The assumptions made in the calculation of (27) hold as long as $\varepsilon_{\vec{k}\sigma}$ is below the Fermi energy $E_{\rm F}$. This is, however, the case—since the electron filling the 1s shell in an Auger process originates from an occupied state of the conduction band of the surface. In section 4, we will see that the WKB correction brings the transition rate for Auger neutralization we obtain in very good agreement with the rate given by Wang *et al* [46]. It is based on the work of Lorente and Monreal [51], and has been also used by others [30, 48]. It is, moreover, in reasonable agreement with calculations based in part on first principles for the distances we are interested in [44].

2.3. Hamiltonian

We now have everything needed to begin the construction of the Hamiltonian for the processes outlined in figure 1. With the energy shifts and matrix elements given above it reads

$$\begin{aligned}
H(t) = & \sum_{n_0 n_1 n_2} P_{n_0 n_1 n_2}(\varepsilon_0(t) c_0^\dagger c_0 + \varepsilon_1(t) c_1^\dagger c_1 + \varepsilon_2(t) c_2^\dagger c_2) \\
& + \sum_\sigma \omega_\sigma(t) b_\sigma^\dagger b_\sigma + \sum_{\vec{k}\sigma} \varepsilon_{\vec{k}\sigma} c_{\vec{k}\sigma}^\dagger c_{\vec{k}\sigma} \\
& + \sum_{\vec{q}\sigma} \varepsilon_{\vec{q}\sigma}(t) c_{\vec{q}\sigma}^\dagger c_{\vec{q}\sigma} \\
& + \sum_{\vec{k}} [(P_{000} + P_{010}) V_{\vec{k}\uparrow}(t) c_{\vec{k}\uparrow}^\dagger c_1 + \text{H.c.}] \\
& + \sum_{\vec{k}} [(P_{000} + P_{001}) V_{\vec{k}\downarrow}(t) c_{\vec{k}\downarrow}^\dagger c_2 + \text{H.c.}] \\
& + \sum_{\vec{k}} [(P_{001} + P_{011}) V_{\vec{k}\uparrow}(t) c_{\vec{k}\uparrow}^\dagger b_\uparrow^\dagger c_1 + \text{H.c.}] \\
& + \sum_{\vec{k}} [(P_{010} + P_{011}) V_{\vec{k}\downarrow}(t) c_{\vec{k}\downarrow}^\dagger b_\downarrow^\dagger c_2 + \text{H.c.}] \\
& + \sum_{\vec{k}_1 \vec{k}_2 \vec{k}'\sigma} [(P_{000} + P_{100}) V_{\vec{k}_1 \vec{k}_2 \vec{k}'\sigma} \\
& \times (t) c_{\vec{k}'\sigma}^\dagger c_0^\dagger c_{\vec{k}_1\downarrow} c_{\vec{k}_2\sigma} + \text{H.c.}] \\
& + \sum_{\vec{k}\vec{k}'\sigma} [(P_{100} + P_{001}) V_{\vec{k}\vec{k}'\sigma}(t) c_{\vec{k}'\sigma}^\dagger c_0^\dagger c_{\vec{k}\sigma} c_2 + \text{H.c.}] \\
& + \sum_{\vec{k}\vec{q}} [(P_{100} + P_{010}) V_{\vec{k}\vec{q}\uparrow}(t) c_{\vec{q}\uparrow}^\dagger c_0^\dagger c_{\vec{k}\downarrow} c_1 + \text{H.c.}] \\
& + \sum_{\vec{k}\vec{q}} [(P_{100} + P_{001}) V_{\vec{k}\vec{q}\downarrow}(t) c_{\vec{q}\downarrow}^\dagger c_0^\dagger c_{\vec{k}\downarrow} c_2 + \text{H.c.}] \\
& + \sum_{\vec{q}} [(P_{100} + P_{011}) V_{\vec{q}} c_{\vec{q}\uparrow}^\dagger c_0^\dagger c_1 c_2 + \text{H.c.}],
\end{aligned} \tag{29}$$

where the fermionic operators $c_i^{(\dagger)}$ annihilate (create) an electron in the level ε_i with the spin as indicated in figure 3. Likewise the fermionic operators $c_{\vec{k}\sigma}^{(\dagger)}$ and $c_{\vec{q}\sigma}^{(\dagger)}$ annihilate (create), respectively, an electron with spin σ in the conduction band of the target surface or the continuum of the projectile. The projection operators as defined in (10) guarantee that each individual term is projected onto that subspace of the three-level system representing its physical domain of applicability. For instance, the term describing Auger neutralization (fifth last term) must contain a factor $P_{000} + P_{100}$ because it involves only the positive ion and the ground state —that is, in the notation of the three-level system, the states $|000\rangle$ and $|100\rangle$.

An essential aspect of our approach is that it allows one to treat electronic configurations of the projectile with defects in their internal energies. More specifically, the numerical value of the energy level ε_2 depends on the occupancy of the three-level system. In case ε_1 and ε_2 are occupied, ε_2 denotes an affinity level of either He*(1s2s, 2^1S_0) or He*(1s2s, 2^3S_1) whereas in the case ε_1 is empty, ε_2 stands for the ionization level of either He*(1s2s, 2^1S_0) or He*(1s2s, 2^3S_1). To switch between ionization and affinity levels, we introduce two auxiliary bosons $b_\uparrow^{(\dagger)}$ and $b_\downarrow^{(\dagger)}$ with energy

$$\omega_\sigma(t) = \varepsilon_{2s-\sigma}^-(t) - \varepsilon_{2s-\sigma}^*(t), \tag{30}$$

where $\sigma = \uparrow, \downarrow$ labels the complementary spin orientation of the electron in the 2s shell of the two configurations between which the boson is expected to switch. With this trick [64], all processes encoded in the Hamiltonian conserve energy irrespective of whether a negative ion or a metastable configuration is involved.

The Hamiltonian (29) is rather involved, but the physical meaning of the various terms is almost self-explanatory. For instance, the first term describes the ionization and affinity levels of the projectile, while the next three denote the auxiliary bosons, the continuum of surface states, and the continuum of the projectile. The following four terms are the single-electron transfers into and out of the metastable ionization and affinity levels. Auger neutralization of the positive ion, direct Auger de-excitation of the metastable singlet configuration, indirect Auger de-excitation of the metastable triplet and singlet configurations, and the autodetachment of the negative ion are given by the last five terms. Note that due to the Pauli principle, direct Auger de-excitation is only possible for the singlet metastable state (see figures 3 and 2). Hence, it affects only the levels ε_2 and ε_0. Indirect Auger de-excitation, in contrast, is not restricted in such a way.

Working directly with the Hamiltonian (29) is cumbersome, because it is not suited for a diagrammatic analysis—which on the other hand is a powerful tool to derive kinetic equations as shown by Langreth *et al* [59–61]. We therefore rewrite the states making up the projection operators in terms of pseudo-particle operators $e^\dagger$, $d^\dagger$ and $s_{n\sigma}^\dagger$ defined by

$$\begin{aligned}
&|000\rangle = e^\dagger|\text{vac}\rangle,\ |011\rangle = d^\dagger|\text{vac}\rangle,\ |100\rangle = s_{1\downarrow}^\dagger|\text{vac}\rangle, \\
&|010\rangle = s_{2\uparrow}^\dagger|\text{vac}\rangle,\ |001\rangle = s_{2\downarrow}^\dagger|\text{vac}\rangle.
\end{aligned} \tag{31}$$

Hence, $e^\dagger$, $d^\dagger$, $s_{1\downarrow}^\dagger$, $s_{2\uparrow}^\dagger$, and $s_{2\downarrow}^\dagger$ create, respectively, the positive ion, the negative ion, the ground state, the triplet metastable state, and the singlet metastable state. The statistics of the operators is fixed by the Fermi statistics of the operators $c_i^{(\dagger)}$ and physical considerations [64]. Since the positive and negative ion represented, respectively, by $|000\rangle$ and $|011\rangle$ contain an odd number of electrons, because of the spin-up electron always present in the 1s shell, but not explicitly included in the three-level system (see figure 3), the operators $e^{(\dagger)}$ and $d^{(\dagger)}$ should be endorsed with Fermi statistics. The ground state and the metastable configurations, $|100\rangle$, $|010\rangle$, and $|001\rangle$, on the other hand, carry an even number of electrons. Hence, it is natural to endorse the operators $s_{1\downarrow}^{(\dagger)}$, $s_{2\uparrow}^{(\dagger)}$, and $s_{2\downarrow}^{(\dagger)}$ with Bose statistics.

The relation between the operators c_0, c_1, and c_2, which are single-electron operators, and the pseudo-particle operators defined in (31), which create many-electron states—that is, whole electronic configurations—is found by letting the former act on the completeness relation (16). The result is

$$\begin{aligned}
c_0 = c_0 * 1 = & |000\rangle\langle 100| - |010\rangle\langle 110| \\
& - |001\rangle\langle 101| + |011\rangle\langle 111|,
\end{aligned} \tag{32}$$

$$\begin{aligned}
c_0^\dagger = c_0^\dagger * 1 = & |100\rangle\langle 000| - |110\rangle\langle 010| \\
& - |101\rangle\langle 001| + |111\rangle\langle 011|,
\end{aligned} \tag{33}$$

$$c_1 = c_1 \ * \ 1 = |000\rangle\langle 010| + |100\rangle\langle 110| - |001\rangle\langle 011| - |101\rangle\langle 111|, \quad (34)$$

$$c_1^\dagger = c_1^\dagger \ * \ 1 = |010\rangle\langle 000| + |110\rangle\langle 100| - |011\rangle\langle 001| - |111\rangle\langle 101|, \quad (35)$$

$$c_2 = c_2 \ * \ 1 = |000\rangle\langle 001| + |100\rangle\langle 101| + |010\rangle\langle 011| + |110\rangle\langle 111|, \quad (36)$$

$$c_2^\dagger = c_2^\dagger \ * \ 1 = |001\rangle\langle 000| + |101\rangle\langle 100| + |011\rangle\langle 010| + |111\rangle\langle 110|, \quad (37)$$

where the minus signs guarantee the fulfilment of the anti-commutation relations. Inserting (32)–(37) into (29), carrying out all projections, and lastly making replacements of the sort $|000\rangle\langle 100| \to e^\dagger s_{1\downarrow}$, we finally obtain the Anderson—Newns Hamiltonian in pseudo-particle representation:

$$\begin{aligned} H(t) = {} & \varepsilon^0_{1s\downarrow}(t) s^\dagger_{1\downarrow} s_{1\downarrow} + \sum_\sigma \varepsilon^*_{2s\sigma}(t) s^\dagger_{2\sigma} s_{2\sigma} \\ & + [\bar{\varepsilon}^-_{2s\uparrow}(t) + \bar{\varepsilon}^-_{2s\downarrow}(t)] d^\dagger d \ + \sum_\sigma \omega_\sigma(t) b^\dagger_\sigma b_\sigma \\ & + \sum_{\vec{k}\sigma} \varepsilon_{\vec{k}\sigma} c^\dagger_{\vec{k}\sigma} c_{\vec{k}\sigma} + \sum_{\vec{q}\sigma} \varepsilon_{\vec{q}\sigma}(t) c^\dagger_{\vec{q}\sigma} c_{\vec{q}\sigma} \\ & + \sum_{\vec{k}\sigma} [V_{\vec{k}\sigma}(t) c^\dagger_{\vec{k}\sigma} e^\dagger s_{2\sigma} + \text{H.c.}] \\ & - \sum_{\vec{k}\sigma} [\text{sgn}(\sigma) V_{\vec{k}\sigma}(t) c^\dagger_{\vec{k}\sigma} b^\dagger_\sigma s^\dagger_{2-\sigma} d \ + \text{H.c.}] \\ & + \sum_{\vec{k}_1\vec{k}_2\vec{k}'\sigma} [V_{\vec{k}_1\vec{k}_2\vec{k}'\sigma}(t) c^\dagger_{\vec{k}'\sigma} s^\dagger_{1\downarrow} e \ c_{\vec{k}_1\downarrow} c_{\vec{k}_2\sigma} + \text{H.c.}] \\ & + \sum_{\vec{k}\vec{k}'\sigma} [V_{\vec{k}\vec{k}'\sigma}(t) c^\dagger_{\vec{k}'\sigma} s^\dagger_{1\downarrow} c_{\vec{k}\sigma} s_{2\downarrow} + \text{H.c.}] \\ & + \sum_{\vec{k}\vec{q}\sigma} [V_{\vec{k}\vec{q}\sigma}(t) c^\dagger_{\vec{q}\sigma} s^\dagger_{1\downarrow} c_{\vec{k}\downarrow} s_{2\sigma} + \text{H.c.}] \\ & + \sum_{\vec{q}} [V_{\vec{q}} \ c^\dagger_{\vec{q}\uparrow} s^\dagger_{1\downarrow} d \ + \text{H.c.}]. \end{aligned} \quad (38)$$

The physical meaning of the various terms of the Hamiltonian is now particularly transparent. Consider, for instance, the fourth last term. It describes Auger neutralization (and its reverse, which has to be included to make the Hamiltonian Hermitian) and hence the creation/annihilation of the projectile ground state and a secondary electron by simultaneously annihilating/creating a positive ion and two metal electrons. Likewise the last term describes autodetachment (and its reverse)—that is, the creation/annihilation of the ground state by annihilation/creation of the negative ion due to creating/annihilating an electron in the continuum of the projectile. In the next section, we will use this Hamiltonian to determine the probabilities with which the various projectile configurations appear and an electron is emitted in the course of the atom−surface collision.

3. Quantum kinetics

With the electronic configurations of the He projectile encoded in an effective three-level system holding either no, one, or two electrons with the spin polarizations given in figure 3, we can now calculate the probability with which an electron is emitted via Auger neutralization or the sequence of single-electron transfers leading to Auger de-excitation or autodetachment as shown in figure 1. For that purpose we use the quantum-kinetic method which rests in our case on the contour-ordered Green functions [77, 78],

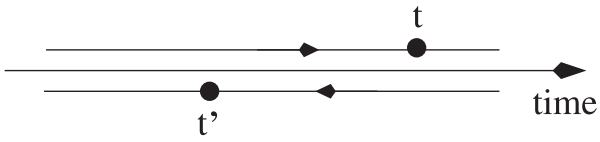

Figure 5. Keldysh contour in the complex time domain running infinitesimally above and below the real-time axis from $t = -\infty$ to $t = +\infty$ and back. The time variables t and t' of the contour-ordered Green functions (39)–(45) and the self-energies associated with them vary along this contour. To obtain the analytic pieces of these functions—denoted by less-than, greater-than, and retarded—an analytic continuation to the real-time axis is performed after the time-ordering along the contour has been taken into account. This is equivalent to Keldysh's matrix notation for the Green functions [77].

$$\mathrm{i}E(t, t') = \langle T_\mathcal{C}\, e(t)\, e^\dagger(t')\rangle, \quad (39)$$

$$\mathrm{i}S_{1\downarrow}(t, t') = \langle T_\mathcal{C}\, s_{1\downarrow}(t)\, s^\dagger_{1\downarrow}(t')\rangle, \quad (40)$$

$$\mathrm{i}S_{2\sigma}(t, t') = \langle T_\mathcal{C}\, s_{2\sigma}(t)\, s^\dagger_{2\sigma}(t')\rangle, \quad (41)$$

$$\mathrm{i}D(t, t') = \langle T_\mathcal{C}\, d(t)\, d^\dagger(t')\rangle, \quad (42)$$

$$\mathrm{i}G_{\vec{q}\sigma}(t, t') = \langle T_\mathcal{C}\, c_{\vec{q}\sigma}(t)\, c^\dagger_{\vec{q}\sigma}(t')\rangle, \quad (43)$$

$$\mathrm{i}G_{\vec{k}\sigma}(t, t') = \langle T_\mathcal{C}\, c_{\vec{k}\sigma}(t)\, c^\dagger_{\vec{k}\sigma}(t')\rangle, \quad (44)$$

$$\mathrm{i}B_\sigma(t, t') = \langle T_\mathcal{C}\, b_\sigma(t)\, b^\dagger_\sigma(t')\rangle, \quad (45)$$

where the time variables run over the Keldysh contour shown in figure 5. The first four functions describe the positive ion, the ground state, the two metastable states, and the negative ion, while the last three apply, respectively, to an unbound electron in the projectile's continuum, the electrons in the conduction band of the target surface, and the auxiliary bosons. The operators making up the Green functions evolve in time with the full Hamiltonian (38) and the brackets denote the statistical average with respect to the initial density matrix describing one-auxiliary-boson states, surface electrons in thermal equilibrium, and an empty projectile—that is, a positive ion.

Following the work of Langreth *et al* [59–61] we use Dyson equations for these functions to derive a set of equations for the occurrence probabilities/occupancies of the bound projectile states—that is, the affinity and ionization levels. Introducing the self-energies $\Pi_e(t, t')$, $\Sigma_{1\downarrow}(t, t')$, $\Sigma_{2\sigma}(t, t')$, and $\Pi_d(t, t')$ for the Green functions $\mathrm{i}E(t, t')$, $\mathrm{i}S_{1\downarrow}(t, t')$, $\mathrm{i}S_{2\sigma}(t, t')$, and $\mathrm{i}D(t, t')$, we obtain ($\hbar = 1$ in this section and the two appendices)

$$\frac{\mathrm{d}}{\mathrm{d}t} n_+(t) = 2\,\mathrm{Im} \int_{-\infty}^{\infty} \mathrm{d}\bar{t} E^<(\bar{t}, t) \Pi^R_\mathrm{e}(t, \bar{t}) - 2\,\mathrm{Im} \int_{-\infty}^{\infty} \mathrm{d}\bar{t} E^R(t, \bar{t}) \Pi^<_\mathrm{e}(\bar{t}, t), \quad (46)$$

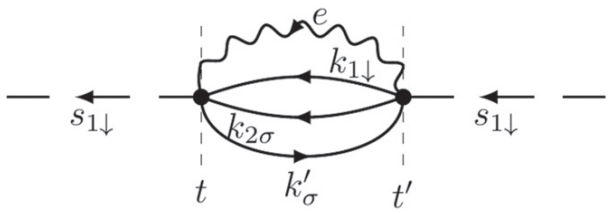

Figure 6. Diagrammatic representation of the self-energy due to Auger neutralization, $\Sigma^{\mathrm{AN}}_{1s\downarrow}(t, t')$, entering the Dyson equation for the ground-state propagator $\mathrm{i}S_{1\downarrow}(t, t')$ in the non-crossing approximation. The dashed and wavy lines are the dressed propagators of the ground state and positive ion, whereas the solid lines mark the undressed propagators for surface electrons. Standard diagrammatic rules [79] can be applied to diagrams of this type if one keeps in mind that time integrations/variables run over the Keldysh contour [77, 78]. Details can be found in our previous work [62–65].

$$\frac{\mathrm{d}}{\mathrm{d}t}n_g(t) = 2\,\mathrm{Im}\int_{-\infty}^{\infty}\mathrm{d}\bar{t}S^{<}_{1\downarrow}(\bar{t}, t)\Sigma^{R}_{1\downarrow}(t, \bar{t}) - 2\,\mathrm{Im}\int_{-\infty}^{\infty}\mathrm{d}\bar{t}S^{R}_{1\downarrow}(t, \bar{t})\Sigma^{<}_{1\downarrow}(\bar{t}, t), \tag{47}$$

$$\frac{\mathrm{d}}{\mathrm{d}t}n_\sigma(t) = 2\,\mathrm{Im}\int_{-\infty}^{\infty}\mathrm{d}\bar{t}S^{<}_{2\sigma}(\bar{t}, t)\Sigma^{R}_{2\sigma}(t, \bar{t}) - 2\,\mathrm{Im}\int_{-\infty}^{\infty}\mathrm{d}\bar{t}S^{R}_{2\sigma}(t, \bar{t})\Sigma^{<}_{2\sigma}(\bar{t}, t), \tag{48}$$

$$\frac{\mathrm{d}}{\mathrm{d}t}n_-(t) = 2\,\mathrm{Im}\int_{-\infty}^{\infty}\mathrm{d}\bar{t}D^{<}(\bar{t}, t)\Pi^{R}_{\mathrm{d}}(t, \bar{t}) - 2\,\mathrm{Im}\int_{-\infty}^{\infty}\mathrm{d}\bar{t}D^{R}(t, \bar{t})\Pi^{<}_{\mathrm{d}}(\bar{t}, t), \tag{49}$$

for the time evolution of the probabilities $n_e(t)$, $n_g(t)$, $n_\sigma(t)$, and $n_-(t)$ with which, respectively, the positive ion, the ground state, the two metastable states ($\sigma = \uparrow$ denoting the triplet and $\sigma = \downarrow$ the singlet), and the negative ion occur.

Equations (46)–(49) are exact but of course not closed in terms of the occurrence probabilities. To proceed, we set up the self-energies in the non-crossing approximation, use the fact that the matrix elements (17)–(21) factorize approximately in functions of t and the set of $\vec{k}$ vectors, and finally apply the semiclassical approximation to (46)–(49) developed by Langreth *et al* [59–61] which in essence is a saddle-point integration in time.

In order to get an impression about how the self-energies look, we show in figure 6 the contribution to the self-energy $\Sigma_{1s\downarrow}(t, t')$, entering the Dyson equation of the ground-state propagator $\mathrm{i}S_{1\downarrow}(t, t')$, which arises from the Auger neutralization. There are also contributions to $\Sigma_{1s\downarrow}(t, t')$ due to direct and indirect Auger de-excitation as well as autodetachment. They are given in appendix A together with the other self-energies entering equations (46)–(49) and some details concerning their calculation. Using standard diagrammatic rules [79] the diagram shown in figure 6 translates to

$$-\mathrm{i}\Sigma^{\mathrm{AN}}_{1s\downarrow}(t, t') = -(\mathrm{i})^2\sum_{\vec{k}_1\vec{k}_2\vec{k}'\sigma}V_{\vec{k}_1\vec{k}_2\vec{k}'\sigma}(t)V^{*}_{\vec{k}_1\vec{k}_2\vec{k}'\sigma}(t') \times \mathrm{i}E(t, t')\mathrm{i}G_{\vec{k}_1\downarrow}(t, t')\mathrm{i}G_{\vec{k}_2\sigma}(t, t')\mathrm{i}G_{\vec{k}'\sigma}(t', t). \tag{50}$$

The time variables run over the (Keldysh) contour, that is, from $t = -\infty$ to $t = +\infty$ and back as shown in figure 5. Application of the Langreth–Wilkins rules [80] with a subsequent projection to the subspace encoded in the completeness relation (16) yields the analytic pieces of the self-energies, where the time variables are now taken from the real-time axis,

$$\Sigma^{\mathrm{AN},\gtrless}_{1\downarrow}(t, t') = \sum_{\vec{k}_1\vec{k}_2\vec{k}'\sigma}V_{\vec{k}_1\vec{k}_2\vec{k}'\sigma}(t)V^{*}_{\vec{k}_1\vec{k}_2\vec{k}'\sigma}(t') \times E^{\gtrless}(t, t')G^{\gtrless}_{\vec{k}_1\downarrow}(t, t')G^{\gtrless}_{\vec{k}_2\sigma}(t, t')G^{\lessgtr}_{\vec{k}'\sigma}(t', t), \tag{51}$$

$$\Sigma^{\mathrm{AN},R}_{1\downarrow}(t, t') = \sum_{\vec{k}_1\vec{k}_2\vec{k}'\sigma}V_{\vec{k}_1\vec{k}_2\vec{k}'\sigma}(t)V^{*}_{\vec{k}_1\vec{k}_2\vec{k}'\sigma}(t') \times E^{R}(t, t')G^{>}_{\vec{k}_1\downarrow}(t, t')G^{>}_{\vec{k}_2\sigma}(t, t')G^{<}_{\vec{k}'\sigma}(t', t), \tag{52}$$

with the superscripts $>$, $<$, and R indicating the less-than, greater-than, and retarded pieces of the self-energy (50). In accordance with the non-crossing approximation the surface electrons are propagated by the undressed Green function,

$$G^{\gtrless}_{\vec{k}\sigma}(t, t') = f^{\gtrless}(\varepsilon_{\vec{k}\sigma})\mathrm{e}^{-\mathrm{i}\varepsilon_{\vec{k}\sigma}(t-t')}. \tag{53}$$

Only the propagators applying to the ionization and affinity levels of the projectile, $\mathrm{i}E(t, t')$, $\mathrm{i}S_{1\downarrow}(t, t')$, $\mathrm{i}S_{2\sigma}(t, t')$, and $\mathrm{i}D(t, t')$ are modified by self-energies.

Due to the approximate factorization of the time and momentum dependencies of the matrix elements, it is possible to express the self-energies by functions arising from the application of the golden rule to the respective interaction terms in the Hamiltonian. The physical meaning of the functions is that of a (partial) level width. Since they eventually determine the rates entering the rate equations for the occurrence probabilities given below, we list the functions—however, without derivation (which is quite lengthy). An exemplary calculation is presented in appendix B.

Single-electron processes are characterized by

$$\Gamma_{\varepsilon^{*}_{2s\sigma}}(t) = 2\pi\sum_{\vec{k}}|V_{\vec{k}\sigma}(t)|^2\delta(\varepsilon^{*}_{2s\sigma}(t) - \varepsilon_{\vec{k}\sigma}), \tag{54}$$

$$\Gamma_{\varepsilon^{-}_{2s\sigma}}(t) = 2\pi\sum_{\vec{k}}|V_{\vec{k}\sigma}(t)|^2\delta(\varepsilon^{-}_{2s\sigma}(t) - \varepsilon_{\vec{k}\sigma}), \tag{55}$$

while Auger processes are encoded in

$$\Gamma_{\mathrm{AN}}(t) = 2\pi\sum_{\vec{k}_1\vec{k}_2\vec{k}'\sigma}|V_{\vec{k}_1\vec{k}_2\vec{k}'\sigma}(t)|^2\,\rho_{\vec{k}_1\vec{k}_2\vec{k}'\sigma}(t), \tag{56}$$

$$\Gamma_{\mathrm{DAD}\downarrow}(t) = 2\pi\sum_{\vec{k}\vec{k}'\sigma}|V_{\vec{k}\vec{k}'\sigma}(t)|^2\,\rho_{\vec{k}\vec{k}'\sigma}(t), \tag{57}$$

$$\Gamma_{\mathrm{IAD}\sigma}(t) = 2\pi\sum_{\vec{k}\vec{q}}|V_{\vec{k}\vec{q}\sigma}(t)|^2\,\rho_{\vec{k}\vec{q}\sigma}(t), \tag{58}$$

$$\Gamma_{\mathrm{AuD}} = 2\pi\sum_{\vec{q}}|V_{\vec{q}}|^2\,\rho_{\vec{q}}, \tag{59}$$

with

$$\rho_{\vec{k}_1\vec{k}_2\vec{k}'\sigma}(t) = f^{<}(\varepsilon_{\vec{k}_1\downarrow})f^{<}(\varepsilon_{\vec{k}_2\sigma})f^{>}(\varepsilon_{\vec{k}'\sigma}) \times \delta(\varepsilon^{0}_{1s\downarrow}(t) - \varepsilon_{\vec{k}_1\downarrow} - \varepsilon_{\vec{k}_2\sigma} + \varepsilon_{\vec{k}'\sigma}), \tag{60}$$

$$\rho_{\vec{k}\vec{k}'\sigma}(t) = f^{<}(\varepsilon_{\vec{k}\sigma}) f^{>}(\varepsilon_{\vec{k}'\sigma}) \times \delta(\varepsilon^{0}_{1s\downarrow}(t) - \varepsilon^{*}_{2s\downarrow}(t) - \varepsilon_{\vec{k}\sigma} + \varepsilon_{\vec{k}'\sigma}), \quad (61)$$

$$\rho_{\vec{k}\vec{q}\sigma}(t) = f^{<}(\varepsilon_{\vec{k}\downarrow}) f^{>}(\varepsilon_{\vec{q}\sigma}(t)) \times \delta(\varepsilon^{0}_{1s\downarrow}(t) - \varepsilon^{*}_{2s\sigma}(t) - \varepsilon_{\vec{k}\downarrow} + \varepsilon_{\vec{q}\sigma}(t)), \quad (62)$$

$$\rho_{\vec{q}} = g^{>}(\varepsilon_{\vec{q}\uparrow})\, \delta(\varepsilon^{0}_{1s\downarrow}(t) - \varepsilon^{-}_{2s-\sigma}(t) - \varepsilon^{*}_{2s\sigma}(t) + \varepsilon_{\vec{q}\uparrow}(t)), \quad (63)$$

where on the rhs of the last equation $\sigma = \downarrow$ or $\uparrow$ depending on whether the negative ion is formed out of He*(1s2s, 2^1S_0) or He*(1s2s, 2^3S_1). Note that, in contrast to the other level width functions, Γ_{AuD} does not depend on time, since the matrix element $V_{\vec{q}}$ is independent of time and the time dependencies of the energies in the delta function contained in $\rho_{\vec{q}}$ cancel.

To get these expressions, we used the arguments Langreth and Nordlander [59] developed for simplifying self-energies due to single-electron transfer with the exception that in the level widths arising from Auger and autodetachment processes the distribution functions for the surface and continuum electrons, $f^{\gtrless}(\varepsilon_{\vec{k}\sigma})$ and $g^{>}(\varepsilon_{\vec{q}\uparrow})$, are not separated out from the summations in momentum space. The functions $f^{<}(\varepsilon)$ and $f^{>}(\varepsilon) = 1 - f^{<}(\varepsilon)$ encode, respectively, initially occupied and empty states of the conduction band of the metal. Hence, $f^{<}(\varepsilon)$ is the Fermi–Dirac distribution function at temperature T_s of the surface. The distribution function for an electron in the continuum of the projectile $g^{>}(\varepsilon_{\vec{q}\uparrow}) = 1$ for $\varepsilon_{\vec{q}\uparrow} > 0$ and equal to zero otherwise.

The saddle-point integration in time uses the fact that the Green functions lead to self-energies which are strongly peaked at equal times. In effect, the time variables of the projectile Green functions (including the ones entering the self-energies) on the rhs of equations (46)–(49) are set to equal times once the time integrations are carried out. Identifying less-than functions at equal times with occurrence probabilities/occupancies and realizing that retarded functions at equal times are simply equal to unity in the time intervals where they do not vanish, we obtain the rate equations

$$\frac{\mathrm{d}}{\mathrm{d}t}\begin{pmatrix} n_+ \\ n_\uparrow \\ n_\downarrow \\ n_- \\ n_g \end{pmatrix} = \begin{pmatrix} -[\Gamma^{<}_{\uparrow}+\Gamma^{<}_{\downarrow}+\Gamma^{<}_{\mathrm{AN}}] & \Gamma^{>}_{\uparrow} & \Gamma^{>}_{\downarrow} & 0 & 0 \\ \Gamma^{<}_{\uparrow} & -[\Gamma^{>}_{\uparrow}+\Gamma^{<}_{-,\downarrow}+\Gamma^{<}_{\mathrm{IAD}\uparrow}] & 0 & \Gamma^{>}_{-,\downarrow} & 0 \\ \Gamma^{<}_{\downarrow} & 0 & -[\Gamma^{>}_{\downarrow}+\Gamma^{<}_{-,\uparrow}+\Gamma^{<}_{\mathrm{IAD}\downarrow}+\Gamma^{<}_{\mathrm{DAD}\downarrow}] & \Gamma^{>}_{-,\uparrow} & 0 \\ 0 & \Gamma^{<}_{-,\downarrow} & \Gamma^{<}_{-,\uparrow} & -[\Gamma^{>}_{-,\uparrow}+\Gamma^{>}_{-,\downarrow}+\Gamma^{<}_{\mathrm{AuD}}] & 0 \\ \Gamma^{<}_{\mathrm{AN}} & \Gamma^{<}_{\mathrm{IAD}\uparrow} & \Gamma^{<}_{\mathrm{IAD}\downarrow}+\Gamma^{<}_{\mathrm{DAD}\downarrow} & \Gamma^{<}_{\mathrm{AuD}} & 0 \end{pmatrix} \cdot \begin{pmatrix} n_+ \\ n_\uparrow \\ n_\downarrow \\ n_- \\ n_g \end{pmatrix} \quad (64)$$

which are, due to the completeness (16), subject to the constraint

$$n_+ + n_\uparrow + n_\downarrow + n_- + n_g = 1. \quad (65)$$

The compliance of (65) can be easily verified by noting

$$\frac{\mathrm{d}}{\mathrm{d}t}(n_+ + n_\uparrow + n_\downarrow + n_- + n_g) = 0, \quad (66)$$

and summing each column of (64), which results in the nullifying of the rates. Thus, constraint (65) is fulfilled. Also note, with respect to the diagonal of the coefficient matrix in (64), the entries in the lower triangle comprise only less-than rates $\Gamma^{<}_{\cdots}$ whereas in the upper triangle only greater-than rates $\Gamma^{>}_{\cdots}$ appear. Besides having no entries of greater Auger rates $\Gamma^{>}_{\mathrm{AN}}$, $\Gamma^{>}_{\mathrm{DAD}\downarrow}$, $\Gamma^{>}_{\mathrm{IAD}\downarrow}$, $\Gamma^{>}_{\mathrm{IAD}\uparrow}$, and $\Gamma^{>}_{\mathrm{AuD}}$ the matrix is symmetric.

For the interpretation and numerical solution of (64) we apply to the rates the adiabatic approximation. The rates in (64) can then be expressed by the level width functions. For the single-electron transfers the adiabatic approximation yields [59]

$$\Gamma^{\gtrless}_{\sigma}(t) = \Gamma_{\varepsilon^{*}_{2s\sigma}}(t) f^{\gtrless}(\varepsilon^{*}_{2s\sigma}(t)), \quad (67)$$

$$\Gamma^{\gtrless}_{-,\sigma}(t) = \Gamma_{\varepsilon^{-}_{2s\sigma}}(t) f^{\gtrless}(\varepsilon^{-}_{2s\sigma}(t)) \quad (68)$$

with $\Gamma_{\varepsilon^{*}_{2s\sigma}}(t)$ and $\Gamma_{\varepsilon^{-}_{2s\sigma}}(t)$ as defined in (54) and (55) respectively. The Auger and autodetachment transition rates reduce in the adiabatic approximation simply to the level width functions given in equations (56)–(59). Hence,

$$\Gamma^{<}_{\mathrm{AN}}(t) = \Gamma_{\mathrm{AN}}(t), \quad (69)$$

$$\Gamma^{<}_{\mathrm{DAD}\downarrow}(t) = \Gamma_{\mathrm{DAD}\downarrow}(t), \quad (70)$$

$$\Gamma^{<}_{\mathrm{IAD}\sigma}(t) = \Gamma_{\mathrm{IAD}\sigma}(t), \quad (71)$$

$$\Gamma^{<}_{\mathrm{AuD}} = \Gamma_{\mathrm{AuD}}. \quad (72)$$

At this point, one clearly sees that in the derivation of the level widths due to Auger and autodetachment processes, we did not factorize out the distribution functions as was the case in the derivation of the level widths due to single-electron transfers. As a result, the distribution functions for the metal electron appear in front of the width functions in (67) and (68) but not in (69)–(72), where they are contained in the width functions themselves.

A particular characteristic of the adiabatic rates, in contrast to the quantum-kinetic rates coming out directly from the saddle-point approximation to (46)–(49) as discussed in appendix A, is that they are positive semidefinite. With the adiabatic rates, equation (64) can thus be interpreted straightforwardly: the lower triangle describes the gain of the projectile configurations by the processes entering this part of the matrix. In terms of figure 1, the lower triangle encodes the transitions from left to right and from top to bottom, starting with the positive ion which is the initial configuration. The diagonal of the matrix gives the losses of the configurations. In contrast to the lower triangle, the upper triangle describes indirect gains for the configurations. It encodes the transitions in figure 1 from right to left. Moving from bottom to top is not

allowed energetically. Should it have been, the last column of the matrix would be filled with greater-than Auger rates.

With the rate equation (64) it is now particularly easy to write down a differential equation for the probability of emitting a secondary electron. Every process outlined in figure 1 that leads to the occurrence of the ground state $He^0(1s^2,\ ^1S_0)$ generates an excited electron (see figure 2). Thus, the rate equation for the probability to emit a secondary electron at time t with energy ε is

$$\begin{aligned}\frac{\mathrm{d}}{\mathrm{d}t}\gamma_e(\varepsilon, t) = {} & n_+(t)\bar{\Gamma}^<_{\mathrm{AN}}(\varepsilon, t) + n_\uparrow(t)\bar{\Gamma}^<_{\mathrm{IAD}\uparrow}(\varepsilon, t) \\ & + n_\downarrow(t)[\bar{\Gamma}^<_{\mathrm{IAD}\downarrow}(\varepsilon, t) + \bar{\Gamma}^<_{\mathrm{DAD}\downarrow}(\varepsilon, t)] \\ & + n_-(t)\bar{\Gamma}^<_{\mathrm{AuD}}(\varepsilon, t). \end{aligned} \tag{73}$$

It has the same structure as the rate equation for the ground state. The spectrally resolved rates $\bar{\Gamma}^<_{\ldots}(\varepsilon, t)$ entering this equation are essentially the ones given in (69)–(72) except that the integration over the magnitude of the wave vector $\vec{k}$ of the excited electron is not carried out and that the conditions for escaping from the surface have to be taken into account [17]. The reason is the following: an excited electron becomes a secondary electron only if it is also able to escape from the location where it is generated. If it is created on-site due to autodetachment or indirect Auger de-excitation, the electron has to overcome its image potential $V_i(z(t)) = e^2/4(z(t) - z_i)$ requiring, in the spirit of the escape cone model [81], $q_z > 0$ and

$$\theta < \theta^{\max}(\varepsilon) = \arccos\sqrt{V_i(z(t))/\varepsilon}\,, \tag{74}$$

where θ is the angle between $\vec{q}$ and the outward surface normal. The $\vec{q}$-integration in $\Gamma^<_{\mathrm{AuD,\ IAD}}(\varepsilon, t)$ is thus cropped leading to modified rates which we denote in (73) by $\bar{\Gamma}^<_{\mathrm{AuD,\ IAD}}(\varepsilon, t)$. In case the electron is generated inside the solid surface, that is, by Auger neutralization or direct Auger de-excitation, the escape of the electron is also affected by scattering processes. Assuming elastic scattering to be most important, the electron arrives isotropically at the interface leading to the rates $\bar{\Gamma}^<_{\mathrm{AN,\ DAD}}(\varepsilon, t) = \mathcal{T}(\varepsilon)\Gamma^<_{\mathrm{AN,\ DAD}}(\varepsilon, t)$ with

$$\mathcal{T}(\varepsilon) = \frac{1}{2}\left(1 - \sqrt{\frac{V_0}{\varepsilon + V_0}}\right), \tag{75}$$

the surface transmission function [17].

Solving (73), the energy spectrum of the emitted secondary electron is obtained from

$$\gamma_e(\varepsilon) = \gamma_e(\varepsilon, t\to\infty), \tag{76}$$

and the probability that an electron gets emitted at all—that is, the secondary electron emission coefficient (γ–coefficient)—follows by integration over all energies:

$$\gamma_e = \int \mathrm{d}\varepsilon\ \gamma_e(\varepsilon, t\to\infty). \tag{77}$$

In order to compare our results with experiments, we apply one more modification. Surface scattering experiments typically occur under conditions of grazing incidence [16, 35]. The lateral velocity $v_\parallel$ of the projectile is thus very large. To account in our calculations for the smearing of the metal electron's Fermi–Dirac distribution induced by the lateral motion of the projectile, in addition to the thermal smearing of the distribution function due to the surface temperature T_s, we replaced, for the numerical calculations, the function $f^<(\varepsilon)$ in the formulas given above by an angle-averaged velocity-shifted distribution [31],

$$f^<(\varepsilon, v_\parallel) = \frac{\ln(1 + \mathrm{e}^{-\beta(\varepsilon+\phi-\delta)}) - \ln(1 + \mathrm{e}^{-\beta(\varepsilon+\phi+\delta)})}{2\beta\delta} \tag{78}$$

with ϕ the work function of the surface, $\beta = 1/k_B T_s$, and $\delta = k_F v_\parallel$, where k_F is the surface's Fermi wave number. From the projectile's perspective the velocity smearing populates surface states above the Fermi energy thereby potentially strengthening charge-transfer processes from the metal to the He metastable states, which, due to image shifting, turn out to be well above the Fermi energy.

Let us finally say a few words about the numerics we have applied. The calculation of the level widths (54)–(59) requires at least a two-dimensional integration over the solid angle of $\vec{k}$ or $\vec{q}$ and at worst, in the case of Auger neutralization, an integration in nine dimensions. In the case of indirect Auger de-excitation, an additional six-dimensional numerical integration must be performed over $\vec{r}$ and $\vec{r}\,'$, since the method of lateral Fourier transformation, unlike for the other channels, does not lead to an analytic result. The integrations are done by a MPI parallelized Monte Carlo Vegas code [82] for a discrete number of different times. To obtain the matrix elements at times in between, we used multi-dimensional-linear interpolation. The same strategy was used for the additional integrals of the indirect Auger de-excitation. Because of the multidimensionality, using more advanced interpolation methods, e.g. splines, would be a difficult undertaking, not necessarily leading to better results. In addition, an interpolation of the time-arguments of the rates (67)–(71) is necessary to solve the rate equation (64). Here, when interpolating, we take advantage of the fact that the rates are almost exponential, which greatly improves the results. To solve the rate equation (64), finally, we employed the explicit embedded Runge−Kutta Cash−Karp method also provided by the GNU scientific library. We have put importance on a reasonable error propagation resulting in a relative numerical error of the calculated occurrence/occupation probabilities of less than 10^{-4}.

4. Results

In this section we present numerical results calculated for the material parameters listed in table 1. We use atomic units measuring length in Bohr radii and energy in Hartrees. The

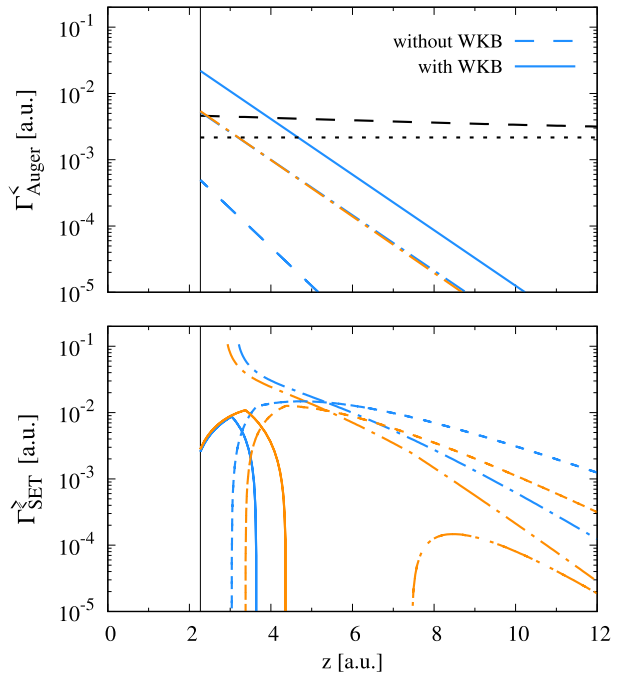

Figure 7. Transition rates (67)–(71) entering (64) for a $He^+(1s,\ ^2S_{1/2})$ ion hitting an aluminum surface with $E_{\mathrm{kin}} = 60$ eV and angle of incidence $\alpha = 15°$. The turning point $z_{\mathrm{TP}} = 2.27$ is indicated by the thin vertical lines. The upper panel shows the rates for autodetachment Γ_{AuD} (dotted black) and the Auger processes, $\Gamma^{<}_{\mathrm{DAD}\downarrow}$ (dashed black), $\Gamma^{<}_{\mathrm{IAD}\uparrow}$ (dash-dotted orange), and $\Gamma^{<}_{\mathrm{IAD}\downarrow}$ (dash-dotted blue). The latter two turn out to be almost identical, but this must not always be the case. In addition, $\Gamma^{<}_{\mathrm{AN}}$ is shown with (solid blue) and without (dashed blue) WKB correction. Including it increases $\Gamma^{<}_{\mathrm{AN}}$ by two orders of magnitude, causing it to coincide in the intervals most relevant for the charge transfer we discuss with the rates obtained by other means (see figure 8 and discussion in main text). The lower panel presents the rates due to single-electron transfer: $\Gamma^{<}_{\uparrow}$ (dotted orange), $\Gamma^{>}_{\uparrow}$ (dash-dotted orange), $\Gamma^{>}_{\downarrow}$ (dashed-dotted blue), $\Gamma^{<}_{-,\uparrow}$ (solid orange), $\Gamma^{<}_{-,\downarrow}$ (solid blue), $\Gamma^{>}_{-,\uparrow}$ (dashed orange), and $\Gamma^{>}_{-,\downarrow}$ (dashed blue). The rate $\Gamma^{<}_{\downarrow}$ is not shown. It is less than 10^{-10} and thus negligible.

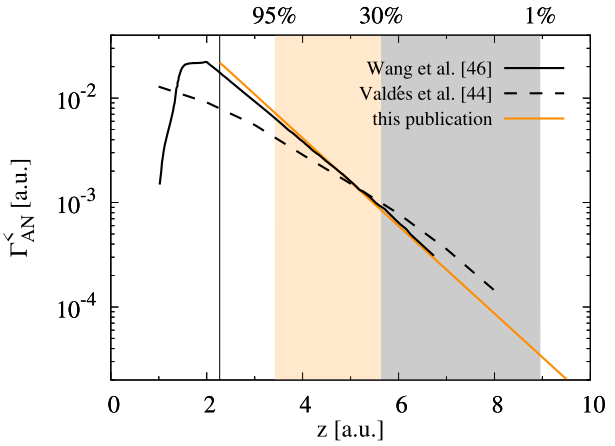

Figure 8. Comparison of the WKB-correct Auger neutralization rate with the rates obtained by Wang *et al* [46] and Valdés *et al* [44]. The collision parameters are the same as in figure 7, the surface is Al(100), and the turning point $z_{\mathrm{TP}} = 2.27$ is indicated by the vertical line. For distances $z \gtrsim 3.5$, where we shall find 95% of the reaction to take place for an angle of incidence of 15°, the agreement is rather good although the rates have been obtained by different methods using different approximations. Close to the turning point our rate (and that of Wang *et al*) is about a factor of two too large compared to the rate of Valdés *et al*, which is based in part on first principles. As far as our rate is concerned, we take this as an indication that non-orthogonality corrections (which we neglect) are already sizeable at $z \lesssim 3.5$. The percentiles of the reaction change with angle of incidence. For perpendicular incidence, the 95% line is closer to the turning point. The neglect of the corrections thus becomes more important in this case.

surface is assumed to be at room temperature, leading to a thermal broadening of the Fermi–Dirac distribution which is much less than the velocity-induced smearing. In the calculations, we therefore used (78) in the limit $T_s \to 0$.

We start the discussion with figure 7, where we plot the transition rates entering the rate equation (64) for a $He^+(1s,\ ^2S_{1/2})$ ion hitting an aluminum surface with $E_{\mathrm{kin}} = 60$ eV and angle of incidence $\alpha = 15°$. The upper panel shows the Auger rates whereas the rates due to single-electron transfer are shown in the lower panel. To demonstrate the importance of the WKB correction to the Auger rates, we plot in the upper panel $\Gamma^{<}_{\mathrm{AN}}(t)$ calculated with and without it. Clearly, the WKB correction to the metal wavefunction has a dramatic effect. It increases $\Gamma^{<}_{\mathrm{AN}}(t)$ by two orders of magnitude. A comparison with the results from other groups, discussed in the next paragraph, indicates that the WKB correction is essential for producing the correct order of magnitude. The WKB correction is also important for indirect Auger de-excitation. Due to lack of data, however, we cannot compare it with other results. Before discussing the reliability of the rates, a few general remarks are in order. The rates for indirect Auger de-excitation and Auger neutralization decrease with distance whereas the rate for direct Auger de-excitation remains almost constant. This is simply because it is a transition between two ionization levels which shift more or less identically. In this respect, it resembles the rate for autodetachment Γ_{AuD}, which is exactly a constant within our model and moreover independent of the target surface. Comparing the Auger rates with the rates for single-electron transfer (plotted in the lower panel) shows that Auger rates are in general smaller, implying that the latter dominate the former in situations where both are possible. The spin-dependence of the rates arises primarily from the energy difference of the singlet and triplet ionization/affinity levels. The closer the levels to the vacuum level, the more extended is the wavefunction of the surface electron taking part in the process leading to a larger matrix element and hence transition rate. For the same reason, $\Gamma^{\gtrless}_{-,\sigma}$ decreases near the turning point.

To estimate the quality of our WKB-modified rate for Auger neutralization we compare it in figure 8 with the rate given by Wang *et al* [46]. It is essentially an extension of the Auger neutralization rate worked out by Lorente and Monreal [51] to distances $z < 2a_B$ and well established [30, 48]. The agreement for $z > z_{\mathrm{TP}} = 2.27a_B$ is almost perfect, although the two rates are obtained by different methods. Additional

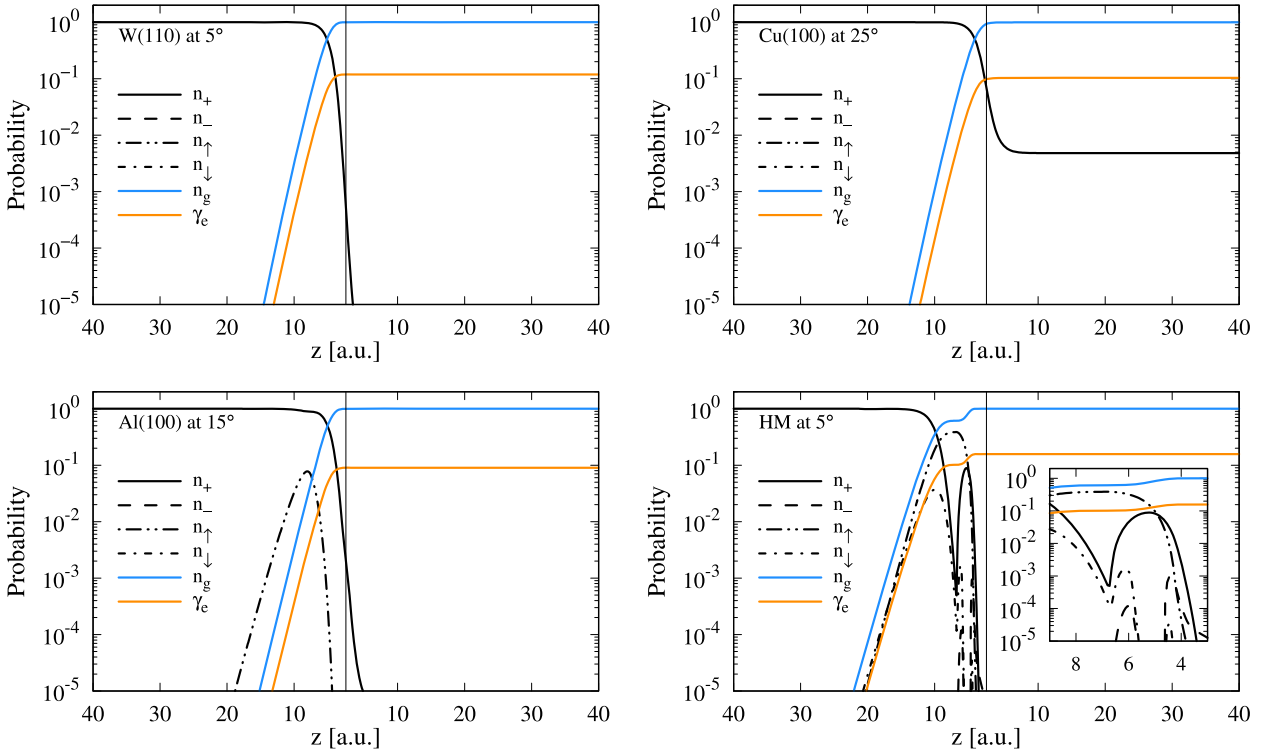

Figure 9. Instantaneous probabilities for electron emission and the occurrence of the various electronic configurations of the He projectile, which was initially in the $He^+(1s,\ ^2S_{1/2})$ configuration, obtained from (64) using the transition rates defined in equations (67)–(68). The species for which no data are shown do not affect the charge transfer. Their occurrence probabilities are less than 10^{-5} and thus negligible. The kinetic energy of the initial He^+ ion scattering off the different surfaces is $E_{kin} = 50$ eV [W(110)], $E_{kin} = 25$ eV [Cu(100)], $E_{kin} = 60$ eV [Al(100)], and $E_{kin} = 50$ eV [HM]. The turning point $z_{TP} = 2.27$ is indicated by the thin vertical line in the middle of the plots, and the inset in the lower right panel provides an enlarged look on the incoming branch in front of the turning point.

support for our rate (and hence also for that of Wang *et al*) stems from the comparison with the rate obtained by Valdés *et al* [44] using an approach based in part on first principles. At distances at which Auger neutralization is expected to take place, there is an astonishingly good agreement between the three rates, indicating that the three approaches contain the essential physics operating at these distance. Hence, they differ only in aspects becoming important at high impact energies, when the projectile gets closer to the target or may even penetrate it, as can be seen by the deviations at short distances. Since the model assumptions are the same for the other rates we calculate, we expect them also to be of the correct order of magnitude for $z \gtrsim 2a_B$—that is, at distances for which charge-transfer takes place at moderate impact energies.

Having calculated the transition rates, we can solve the rate equation for the instantaneous occurrence probabilities $n_+(t)$, $n_\uparrow(t)$, $n_\downarrow(t)$, $n_-(t)$, and $n_g(t)$, applying respectively to the positive ion, the triplet and singlet metastable state, the negative ion, and the ground state. Figure 9 shows results for these quantities for a $He^+(1s,\ ^2S_{1/2})$ ion hitting different surfaces at different angles of incident and different kinetic energies. The abscissas show the separation of the projectile from the surface. Starting on the left at a distance $z = 40$, it moves along the incoming branch of the trajectory towards the turning point $z_{TP} = 2.27$, indicated by the thin vertical line, where it is specularly reflected to move back to the distance $z = 40$ along the outgoing branch of the trajectory shown on the right. The kinetic energy of the projectile was set to $E_{kin} = 50$ eV [W(110)], $E_{kin} = 25$ eV [Cu(100)], and $E_{kin} = 60$ eV [Al(100)], which are the kinetic energies at which the electron emission spectra have been determined experimentally for these metals [30, 35]. Below, we will compare the calculated spectra with the experimentally measured ones. We also studied a hypothetical metal, termed 'HM', with $E_F = 9$ eV and $\phi = 3$ eV to make all processes outlined in figure 1 work in concert for an ion with $E_{kin} = 50$ eV and $\alpha = 5°$. In case of tungsten and copper, the work functions, $\phi = 5.22$ eV (tungsten) and $\phi = 5.1$ eV (copper), are too large to enable resonant single-electron transfer into the metastable states $He^*(1s2s,\ ^2S_0)$ and $He^*(1s2s,\ ^2S_1)$. Hence, ultimately, only the ground state $He^0(1s^2,\ ^1S_0)$ becomes occupied via Auger neutralization, with probability unity for tungsten and near unity for copper. The ion is thus very efficiently neutralized at both surfaces. For copper, however, the positive ion has a slim chance to survive. Its occurrence probability at the end of the collision $n_+(t\to\infty) \approx 0.004$. The secondary electron emission probability, the γ-coefficient, is for both cases around 0.1. Analyzing the two cases a bit deeper one realizes that the larger angle of incidence makes the projectile hit the copper

surface with a much larger perpendicular kinetic energy. Since the major part of the reaction still takes place for distances $z < 10$, the interaction time for copper is much shorter than for tungsten. This may be the reason for the ion to survive the collision, albeit only with a very small probability.

For an aluminum surface, the work function is low enough also to allow the formation of the $He^*(1s2s, 2^3S_1)$ configuration on the incoming branch of the trajectory. Its occurrence probability $n_\uparrow(t)$ rises to sizeable values around $z = 10$ (double-dot-dashed line in the lower left panel of figure 9). Secondary electron emission due to the indirect Auger de-excitation it enables is, however, very weak. We find only one percent of the total emission probability to be due to this process, consistent with the statement of Wang *et al* [46] that it is negligible. As can be seen in the lower left panel of figure 9, secondary electron emission due to indirect Auger de-excitation becomes small compared to emission due to Auger neutralization because its starting point, the metastable states, are most of the time much less probable than the positive ion, the starting point for Auger neutralization. Hence, although the rates for indirect Auger de-excitation and Auger neutralization are of the same order of magnitude, differing only by a factor two (see figure 7), the efficiency of the two processes is very different due to the collision dynamics. Iglesias-García and coworkers [40], in contrast, report on the importance of single-electron transfer, and hence the formation of metastable states, for the neutralization of a helium ion at an aluminum surface. The noticeable temporary occurrence probability we find for $He^*(1s2s, 2^3S_1)$ seems to support their view. However, its role for the outcome of the collision process is very sensitive to the position of the Fermi energy and the shift of the ionization level $\mathcal{I}_{He^*(1s2s,2^3S_1)}$ encoded in equation (5). In our case, we find that, in the end, $He^*(1s2s, 2^3S_1)$ plays a subdominant role. Further investigations are required to clarify the issue, taking improved models for the electronic structure of the surface and the polarization-induced level shifts into account.

The situation we termed 'HM' was constructed to demonstrate the interplay of all channels outlined in figure 1. For this case, the instantaneous occupancies shown in the lower right panel of figure 9 and its inset are more involved. During the approach of the projectile to the surface, both metastable states—$He^*(1s2s, 2^1S_0)$ and $He^*(1s2s, 2^3S_1)$—become occupied, enabling thereby direct (from the singlet configuration) and indirect (from the singlet and triplet configurations) Auger de-excitation, in addition to Auger neutralization. The occurrence probability of the positive ion drops accordingly. At $z \approx 4$ before the turning point $n_+(t)$ reaches a local minimum but starts to rise again for a brief amount of time before it drops to very small values. At the same time, the probability for $He^*(1s2s, 2^1S_0)$ decreases after reaching its maximum. Having only an ionization energy of around $\mathcal{I}_{He^*(1s2s,2^1S_0)} \approx 3.9$ eV, the drop is due to the image-shift encoded in (2), which pushes the ionization level above the Fermi energy, thereby turning the weak gain due to single-electron transfer off and the strong electron loss due to the process on. In addition, there is a strong loss due to direct Auger de-excitation. The triplet configuration $He^*(1s2s, 2^3S_1)$ is affected similarly, albeit at a later time due to the greater ionization energy and the lack of strong direct Auger de-excitation (which is absent because of the Pauli principle). When the electron transfers from the metastable states back to the surface via single-electron transfer, the positive ion is restored. Hence, the occurrence probability for the positive ion rises again near the surface, allowing for a revival of the Auger neutralization. As a result, the occurrence probability $n_g(t)$ jumps close to the surface to near unity. The affinity levels, of course, shift along with the ionization levels. If they approach the Fermi energy from above, a negative ion becomes possible. Hence, for a very short time interval, when the occurrence probabilities for the two metastable configurations are already decreasing, a negative ion is formed. It decays nearly instantly, however, because of single-electron transfer and autodetachment.

In all four cases depicted in figure 9, the outgoing branch lacks complex behavior. For the chosen angles of incidence and kinetic energies, the ground state is always formed very efficiently along the incoming branch. Since the ground state is not subject to a loss channel, it cannot be destroyed. The constraint (65), which has to be satisfied at any instant of time, ensures then that the other configurations vanish as soon as the ground state appears with probability near unity. At the end of the collision, the ground state configuration dominates. Only for copper do we find a noticeable probability of also detecting a positive ion in the end. Although the other configurations ultimately have vanishingly small probabilities, they may nevertheless affect the outcome of the collision by their presence at intermediate times.

Only those probabilities at the end of the collision are experimentally accessible. Let us thus investigate their dependence on impact energy and angle of incidence. Figure 10 shows, for the same impact energies as in figure 9, the angle dependence of the probabilities for detecting the configurations included into our model at the end of the collision, as well as for emitting an electron. The results for tungsten and copper are again very similar. At small angles, essentially only the ground state is formed, because Auger neutralization is the dominant process. As the angle increases, the kinetic energy perpendicular to the surface also increases, lowering thereby the interaction time for all channels. This leads to a steady increase of the occurrence probability for the positive ion, although it remains much smaller for all angles than the probability for the ground state. The ion survival probability is largest for perpendicular incidence, which is also most relevant for plasma applications. For tungsten, we obtain around 0.3, which is two orders of magnitude too large compared to the experimental data Hagstrum [83] found long ago. But survival probabilities on the order of 10^{-3} are typical (see for, instance, figure 26 in [14]). Moving the turning point closer to the surface reduces the survival probability, but not by two orders of magnitude. It is not possible to push this number to the correct order of magnitude by simply adjusting model parameters. We expect the neglect of single-electron transfer to the 1s shell to be responsible for the too large survival probability at perpendicular incidence. The impact energy of the $He^+(1s, 1^2S_{1/2})$ projectile is highest in this case,

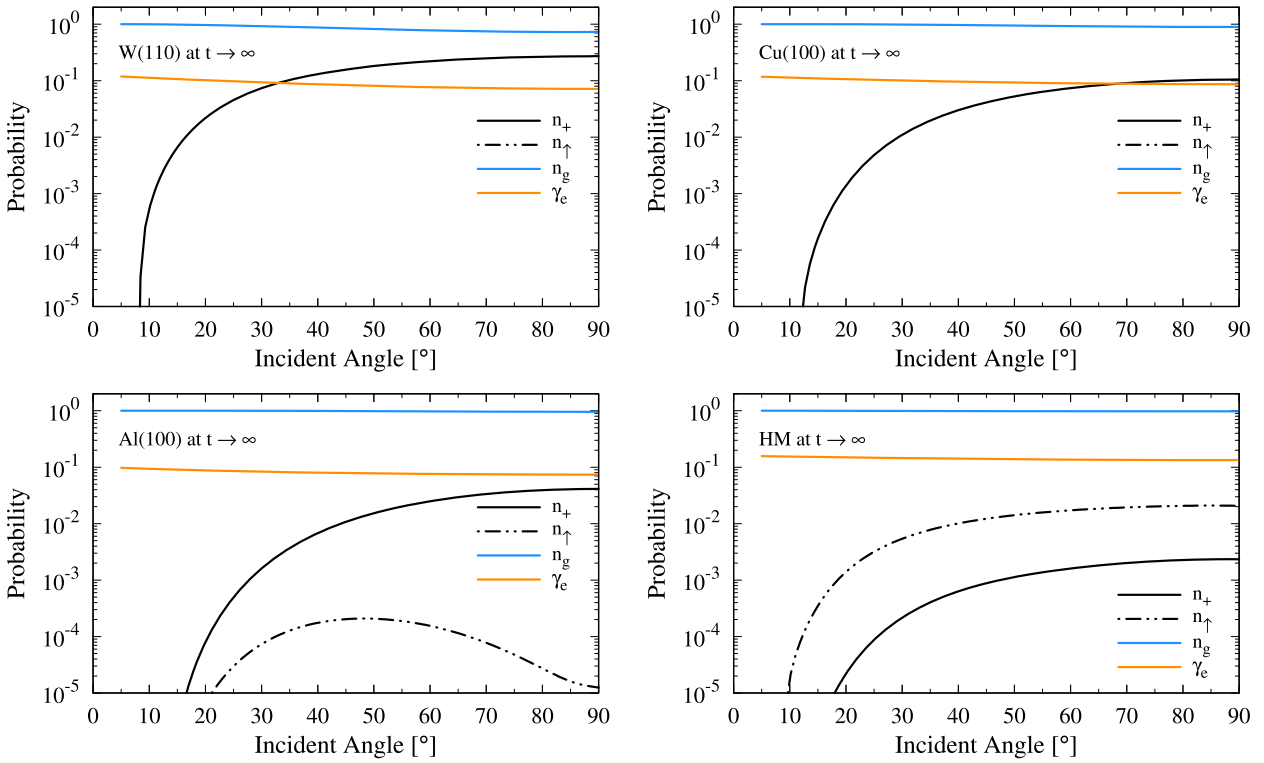

Figure 10. Final probabilities γ_e, n_+, n_g, and $n_\uparrow$ for electron emission and the occurrence of the $He^+(1s,\ 1^2S_{1/2})$, $He^0(1s^2,\ 1^1S_0)$, and $He^*(1s2s,\ 2^3S_1)$ configurations as a function of the angle of incidence. The kinetic energy of the helium projectile is $E_{kin} = 50$ eV [W(110)], $E_{kin} = 25$ eV [Cu(100)], $E_{kin} = 60$ eV [Al(100)], and $E_{kin} = 50$ eV [HM]. Only the positive ion, the ground state, and the triplet metastable state occur at the end of the collision with a noticeable probability. Negative ion and singlet metastable state are only temporarily formed. At the end of the collision, their occurrence probabilities are vanishingly small.

leading to the closest encounter with the surface, where single-electron transfer from core levels may already become important. To include it is, however, beyond the scope of the present work. In addition, non-orthogonality corrections to the Auger rates may also become an issue for perpendicular incidence.

The final probabilities for aluminum and the hypothetical metal, shown in the lower two panels, also behave similarly. The main difference from tungsten and copper is the formation of the metastable triplet state $He^*(1s2s,\ 2^3S_1)$. This forms on the incoming branch of the trajectory because the lowering of the work function enables single-electron transfer into the metastable state and the shortening of the interaction time reduces the electron transfer back to the metal which, in effect, leads to a freezing-in of the metastable state. For the hypothetical case, the occurrence probability for the metastable triplet state is even larger than that for the positive ion, indicating that at intermediate times the singlet metastable state as well as the negative ion state may also have played an active role in the collision.

We now turn to the energy spectrum of the emitted electron. In figure 11, we present results based on equations (73) and (76) together with experimental data for tungsten from Müller *et al* [35] and copper and aluminum from Lancaster *et al* [30]. Only the former group gives also an estimate for the total emission probability—that is, the γ-coefficient. As far as the data for tungsten are concerned, we can thus compare absolute numbers. For copper and aluminum, this is not possible since no value for the γ-coefficient was given by the experimentalists. In addition, the area embraced by the measured emission spectra, which would give the emission coefficient according to (77), cannot be used either, because the experimental data are presented in arbitrary units.

Müller *et al* estimate $\gamma_e^{exp} = 0.22$ for a $He^+(1s,\ 1^2S_{1/2})$ ion hitting a tungsten surface with $E_{kin} = 50$ eV and $\alpha = 5°$. We weighted their emission spectrum according to (77) to match this number. A comparison of the weighted experimental spectrum with our data is shown in figure 11. The agreement is quite satisfying, particularly as far as the high-energy side of the spectrum is concerned. The high-energy cut-off and the maximum of the emission spectrum match quite well, indicating that our approach may be able to estimate at least the order of magnitude of secondary electron emission in cases where no experimental data are available. At low energies, experimental and theoretical data deviate. The theoretical secondary electron emission coefficient $\gamma_e^{theo} = 0.12$ is thus roughly only one-half of the experimental estimate. The reason is the following: we did not include processes relaxing the energy of the excited electron. Scattering cascades [29, 38] and higher-order Auger processes [36] involving more than two electrons are often

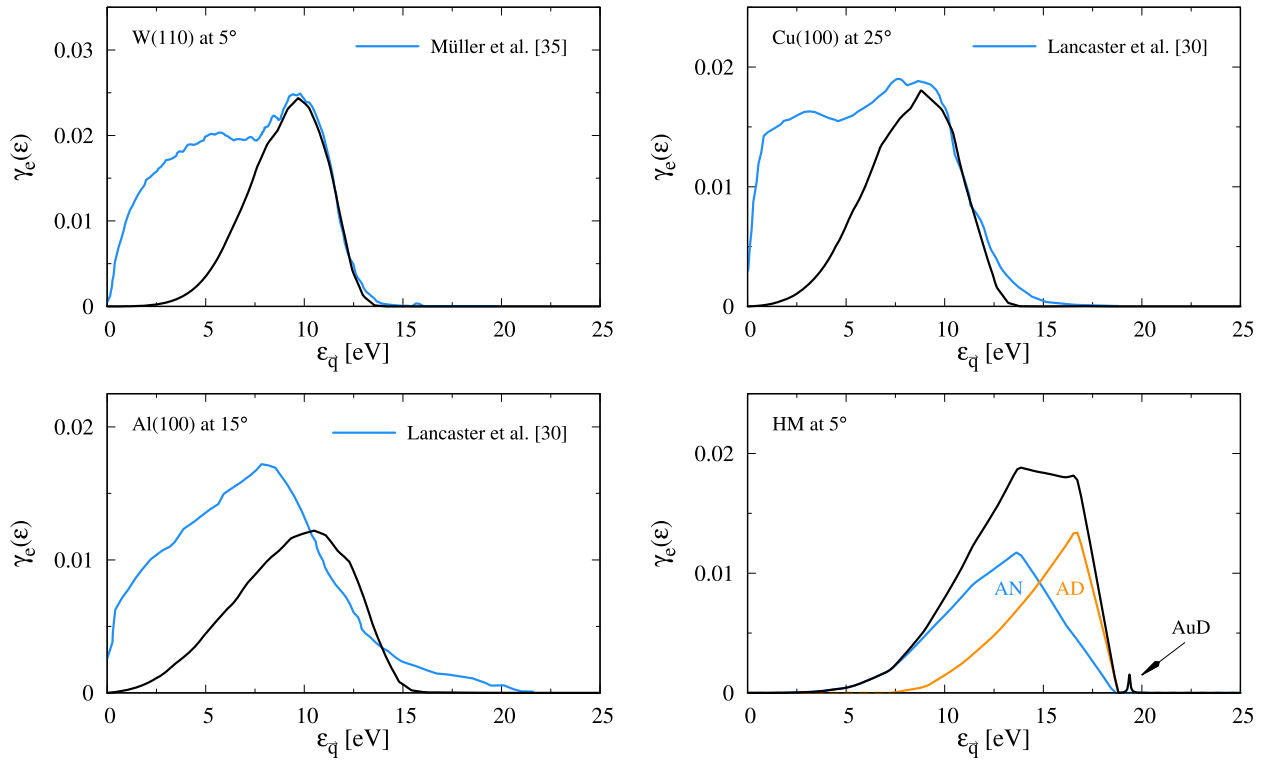

Figure 11. Energy spectrum of the emitted electron once the collision is completed. The kinetic energy of the initial He^+ ion is $E_{kin} = 50$ eV [W(110)], $E_{kin} = 25$ eV [Cu(100)], $E_{kin} = 60$ eV [Al(100)], and $E_{kin} = 50$ eV [HM]. The experimental data for tungsten [35] are weighted to the electron emission coefficient $\gamma_e^{exp} = 0.22$ found experimentally. For the aluminum and copper data [30] this was not possible because no estimates are given for the γ-coefficients. The weighting of the experimental data for copper and aluminum was thus performed using the tungsten data, as described in the main text. We then obtain $\gamma_e^{exp} \approx 0.19$ and $\gamma_e^{exp} \approx 0.18$ for copper and aluminum respectively.

attributed for this. Since the physical origin is not yet quite clear, we did not consider it for the purpose of this work. Our energy spectrum for the secondary electron leaving the tungsten surface is entirely due to Auger neutralization; the other channels of figure 1 are energetically closed. Without scattering cascades and higher-order Auger processes included, it applies only to the high-energy side of the spectrum. There, however, the agreement is rather good.

The good match of the theoretical and experimental emission spectra for tungsten at high energies suggests a way to scale the data of Lancaster *et al* such that they can be compared to the calculated spectra. An important consequence of the scaling is that we can then also estimate the γ-coefficients for copper and aluminum. The ratio $r = \gamma_e^{theo}/\gamma_e^{exp}$ of the theoretical and experimental secondary electron emission coefficients for tungsten is roughly one-half because of the neglect of scattering cascades and higher-order Auger processes. Assuming that both types of process are essentially the same for the metals under discussion, we also scale the emission spectra of Lancaster *et al* in this manner. Hence, we set $\int dE\gamma_e(E, t\to\infty)/\int dE\gamma_e^{exp}(E) = r$, where r is the ratio obtained from the tungsten data. The scaling provides an absolute scale to the experimental data and hence also the γ-coefficients.

As can be seen from figure 11, applying the scaling to the data for copper leads at high energies to a good agreement again between the experimental and theoretical emission spectra. As for tungsten, the high-energy side of the spectrum is determined largely by Auger neutralization. From the calculation, we obtain for copper $\gamma_e^{theo} = 0.1$, producing $\gamma_e^{exp} \approx 0.19$. For aluminum, the matching of the high-energy tails is not as good. The small work function and the large Fermi energy lead in this case to a broad spectrum for the electron emitted by Auger neutralization. In addition, the low work function enables indirect Auger de-excitation, although it provides only a small number of secondary electrons between 15 and 20 eV. For aluminum, our approach yields $\gamma_e^{theo} = 0.09$, a bit lower than for tungsten and copper. The estimate for the experimental value is thus $\gamma_e^{exp} \approx 0.18$. For aluminum, the theoretically obtained emission spectrum does not even match the measured data at high energies. In the case of tungsten and copper, the processes leading to electron emission at lower energies are well separated from electron emission due to Auger neutralization. The latter leads to a maximum at the high-energy side, while the former produces a flat low-energy shoulder. The experimental data for aluminum feature, in contrast, a single asymmetric emission peak, suggesting that Auger neutralization and the low-energy processes strongly overlap. It is thus clear that the scaling deduced from the tungsten data necessarily produces a maximum in the experimental data for aluminum which is above the maximum of the calculated spectrum. In order to achieve

better agreement between theory and experiment, the modeling has thus also to include the processes leading to electron emission at low energies. This is, however, beyond the scope of the present work.

The analysis of the experimental emission spectra indicates that Auger neutralization is by far the most important process listed in figure 1. In the spectra, we find no features which could be attributed to Auger de-excitation or autodetachment. To demonstrate how these processes may in principle affect secondary electron emission, we therefore constructed the hypothetical metal termed 'HM'. Its secondary electron emission spectrum is shown in the lower right panel of figure 11. With the processes of figure 1 simultaneously active, the emission spectrum becomes asymmetric. Decomposing the spectrum into the contributions originating from Auger neutralization, direct and indirect Auger de-excitation, and autodetachment shows that Auger de-excitation is responsible for the steep high-energy cut-off whereas Auger neutralization gives rise to the low-energy tail of the emission spectrum. Autodetachment adds only a faint peak above the main feature. Our model is, however, not able to get the autodetachment peak at the energy expected from other studies [67, 68]. This is most probably due to the incompleteness of the level shifts. In addition to the shifts induced by the image interaction, there are contributions arising from the non-orthogonality of the surface and projectile states. To include them was, however, also beyond the scope of the present work.

5. Conclusions

In this work, we have presented a generic quantum-kinetic approach for calculating the probability with which a secondary electron arises due to the neutralization of a positive ion on a surface, as well as the energy with which it emerges. Focusing on impact energies where the internal potential energy of the projectile drives the emission, and taking a $He^+(1s,\ 1^2S_{1/2})$ ion hitting a metal surface as an example, we showed that the approach is able to treat the three main emission channels which may be open in this energy range on an equal footing: Auger neutralization to the projectile's ground state, single-electron transfers to excited (metastable) states followed either by indirect/direct Auger de-excitation, in case the states are neutral, or autodetachment in case the states are negatively charged.

The approach is based on a semiempirical Anderson −Newns model. It describes the projectile with a time-dependent few-level system and the target surface with a step potential. Parameterizing the few-level system and the step potential by experimental values for the energy levels involved (work function, Fermi energy, electron affinities, and ionization energies), and employing models for energy shifts and approximate wavefunctions of the correct symmetry for the calculation of matrix elements, it provides a flexible tool for describing charge-transferring atom−surface collisions. It can be applied to any projectile−target combination. In particular, it is not restricted to ideal surfaces or to a particular crystallographic orientation of the surface. Both can be taken into account by a suitable choice of the work function and the Fermi energy. To implement an Anderson −Newns model for a charge-transferring atom−surface collision it is thus necessary (i) to identify the ionization and affinity levels which may become active in the charge transfer, (ii) to parameterize and furnish the model as described above, and (iii) to calculate the matrix elements. After the model is constructed, the analysis of the charge−transfer proceeds in a canonical manner using the quantum-kinetic framework of contour-ordered Green functions. An advantage of the approach is thus that it separates the quantum kinetics of charge-transfer from the many-body theoretical description of the non-interacting projectile and target. The latter is simply encoded in the matrix elements of the model Hamiltonian serving as the starting point to the former. Had the matrix elements been obtained by a different method—for instance, by an *ab initio* density functional approach—the quantum kinetics would be the same.

To model the helium projectile, we constructed an effective three-level system. It represents the ground state $He^0(1s^2,\ 1^1S_0)$, the singlet and triplet metastable states, $He^*(1s2s,\ 2^1S_0)$ and $He^*(1s2s,\ 2^3S_1)$, and the negative ion $He^{*-}(1s2s^2,\ 2^2S_{1/2})$. The ionization and affinity levels associated with these states shift while the projectile approaches and retreats from the surface. The energies of the three levels are thus time-dependent. We mimic these dependencies by polarization-induced image shifts. At short distances, corrections to the shifts occur due to the non-orthogonality of the surface and target wavefunctions. Since, in the situations we have studied, the charge transfer occurs preferentially at relatively large distances from the surface, we did not include the corrections in the present work. Discrepancies we found between calculated and measured data indicate, however, that they have to be included in the future. The matrix elements coupling the projectile and the target also depend on time. To obtain numerical values for these, we approximated the electron wavefunctions of the surface by the wavefunctions of the step potential and the electron wavefunctions of the helium projectile by screened 1s and 2s hydrogen wavefunctions. A comparison with helium and lithium Roothaan −Hartree–Fock wavefunctions indicated that this approximation, which enables at least in part an analytical treatment of the matrix elements, is justified. In fact, it turns out that the rate for Auger neutralization we obtain from the hydrogen-like wavefunction for the projectile's 1s shell and the wavefunctions of the step potential is in good agreement with the rate obtained by an investigation based at least in part on *ab initio* methods, if the tunneling of the surface electron filling the hole in the 1s shell is taken into account semiclassically with a WKB correction. We included the corrections in the other Auger matrix elements, where tunneling through the barrier takes place, as well. We thus expect them also to be of the correct order of magnitude.

Essential for an efficient handling of the few-level system is the use of projection operators and auxiliary boson(s). The projection operators allow one to account, within the same few-level system, for projectile states with different internal

energies–assigning different energies to the levels depending on the occupancy and hence the configuration represented–while the auxiliary boson(s) allow switching between the configurations as required by the interactions included in the Hamiltonian without violating energy conservation. For the helium projectile, two auxiliary bosons are needed. Other projectiles may require more than two. Applying the technique to the helium projectile enabled us to treat Auger neutralization, Auger de-excitation, and autodetachment on an equal footing. For the quantum-kinetic analysis of the collision dynamics, the projection operators are rewritten in terms of pseudo-particle operators. It is then straightforward —using standard techniques of many-body theory—to set up the quantum-kinetic approach from which the rate equation is obtained for the probabilities with which the projectile configurations occur and an electron is emitted in the course of the collision.

The rate equation follows from a saddle-point approximation to the equations of motion for the occurrence probabilities in the non-crossing approximation, which is sufficient because we do not expect Kondo-type correlations to occur on the projectile under typical plasma conditions. In addition to these approximations, we postulated an approximate factorization of the t and $\vec{k}$-dependence of the matrix elements to stabilize and speed-up the numerics. At the moment, due to the absence of exact expressions for the transition rates, its validity cannot be verified. However, the final results for the occurrence probabilities and the secondary electron emission coefficient compare favorably with measured data, with differences attributable to physical processes not included in the modeling, suggesting that the factorization is not too critical.

The numerical solution of the rate equations showed that the occurrence probabilities for the projectile configurations are determined along the incoming branch of the collision trajectory. On the outgoing branch, they essentially do not change anymore. This is the case because there is no channel leading from the ground state $He^0(1s^2,\ ^1S_0)$ back to any of the other configurations considered in the model. The angle dependencies of the final occurrence and electron emission probabilities show that for perpendicular incidence—the case most relevant for plasma walls—the projectile has a small chance of returning as a positive ion after having induced a secondary electron. However, due to the neglect of single-electron transfer from deeper lying levels of the surface to the 1s shell, we found the ion survival probability two orders of magnitude too large compared to experimental values. The γ-coefficient we obtained is much better. It is only a factor two too small compared to experimental data (where available). The discrepancy arises from the neglect of higher-order Auger processes and/or scattering cascades. That these processes are important, we deduced from an analysis of the emission spectra. At high energies, the spectra we obtained compare favorably with experimental data from different groups, especially for tungsten. The mismatch is at low energies where one expects higher-order Auger processes and/or inelastic scattering cascades to affect the emission spectra. Using the ratio of the calculated and measured secondary electron emission coefficients for tungsten, we tried to quantify the contribution of the neglected processes to the secondary electron emission coefficient. We found that they roughly lead to its doubling. We also used the ratio to scale the measured emission spectra for copper and aluminum, which were given in arbitrary units. As a result, we could also estimate the secondary electron emission coefficient for these two metals. The results obtained are quite reasonable, indicating that our approach may have the potential not only for qualitative studies of ion-induced secondary electron emission, but also for producing quantitative data, giving at least estimates of the correct order of magnitude. Although we included all three possible emission channels, for the metals investigated, Auger neutralization turned out to be always the dominant one for electron emission—the work functions being simply too large for an efficient direct/indirect Auger de-excitation to take place.

For plasma applications, a compact formula for the secondary electron emission coefficient would be very useful. It is, however, unlikely to exist due to the complexity of charge-transferring atom−surface collisions and their non-universality. What could be hoped for instead is a semiempirical description of the charge-transfer processes, adjustable to various situations of interest. Based on the results presented in this work, we identify four main issues which have to be tackled in order to achieve such a description, as follows. (i) Non-orthogonality corrections to the level shifts and Auger rates at short projectile-target separations should be included. This is particularly important for processes involving metastable configurations of the projectile. (ii) Single-electron transfer from deeper lying states of the surface to the projectile's ground state should be taken into account. This is important for obtaining realistic values for the ion survival probability. (iii) Energy loss of the escaping electron due to scattering cascades and higher-order Auger processes should be considered in order to obtain the energy spectrum of the emitted electron also correct at low energies. (iv) Accurate, numerically efficient approximation schemes should be developed for the high-dimensional integrals defining the transition rates in terms of the matrix elements.

Additional issues—which we consider, however, less critical because they can be overcome at the expense of additional numerical burden, without changing the organization of the calculation—are the use of (effective) hydrogen wavefunctions for the projectile and the potential step for the surface potential. The former can be replaced by other wavefunctions of quantum-chemistry; if not available for the considered projectile they have to be worked out—while the latter can be replaced by another potential (which most probably implies, however, a numerical construction of the surface wavefunctions). Our results suggest, however, that the gain due to these modifications is most probably small. One has to address the three main issues to make a significant step forward.

Not all materials presently used as plasma walls require the simultaneous inclusion of Auger neutralization, Auger de-excitation, and autodetachment. But having a formalism

capable of doing this will enable exploration of the possibility of engineering the spectrum of the emitted electron by judiciously modifying the surface, opening-up or closing-down thereby one or the other channel. With this goal in mind, we have developed the multi-channel approach for calculating secondary electron emission coefficients and spectra described in this work.

Acknowledgments

MP was funded by the federal state of Mecklenburg-Western Pomerania through a postgraduate scholarship within the International Helmholtz Graduate School for Plasma Physics. In addition, support from the Deutsche Forschungsgemeinschaft through project B10 of the Transregional Collaborative Research Center SFB/TRR24 is greatly acknowledged.

Appendix A. Self-energies

In this appendix, the self-energies from which we calculate the rates (67)–(72) are listed. The self-energies, implicitly defined in (46)–(49), are all constructed in the non-crossing approximation as suggested by Langreth *et al* [59–61]. It contains the leading contributions of the second-order (in the interaction matrix elements) self-energies renormalizing the Green functions of the projectile. First order corrections are absent. Vertex renormalizations (diagrams with crossed lines) are ignored, but they are relevant only in situations where Kondo-type correlations [84] occur. For surfaces in contact with a plasma, we do not expect this.

The fermionic self-energies $\Pi_{\mathrm{e,d}}(t, t')$, belonging to the fermionic propagators $E(t, t')$ and $D(t, t')$, respectively apply to the empty and doubly filled configurations, that is, the positive and negative ion. Likewise the bosonic self-energies $\Sigma_{n\sigma}(t, t')$, belonging to the bosonic propagators $S_{n\sigma}(t, t')$, apply to the configurations with a single electron—that is, the ground state and the metastable states. In the expressions to follow, the sums in the various terms indicate their physical origin: Sums over $\vec{k}$ are contributions due to single-electron transfer; sums over $\vec{k}\vec{k}'$ due to direct Auger de-excitation; sums over $\vec{k}\vec{q}$ due to indirect Auger de-excitation; sums over $\vec{q}$ due to autodetachment; and sums over $\vec{k}_1\vec{k}_2\vec{k}'$ due to Auger neutralization. Using Langreth−Wilkins rules [80], the greater-than and less-than self-energies obtained from diagrams of the type shown in figure 6 are

$$\begin{aligned}\Pi_{\mathrm{e}}^{\gtrless}(t, t') = &\sum_{\vec{k}_1\vec{k}_2\vec{k}'\sigma} V^{*}_{\vec{k}_1\vec{k}_2\vec{k}'\sigma}(t) V_{\vec{k}_1\vec{k}_2\vec{k}'\sigma}(t') S_{1\downarrow}^{\gtrless}(t, t') G_{\vec{k}_1\downarrow}^{\lessgtr}(t', t)\\ &\times G_{\vec{k}_2\sigma}^{\lessgtr}(t', t) G_{\vec{k}'\sigma}^{\gtrless}(t, t') + \sum_{\vec{k}\sigma} V_{\vec{k}\sigma}(t) V^{*}_{\vec{k}\sigma}(t') S_{2\sigma}^{\gtrless}(t, t')\\ &\times G_{\vec{k}\sigma}^{\lessgtr}(t', t),\end{aligned} \tag{A1}$$

$$\begin{aligned}\Pi_{\mathrm{d}}^{\gtrless}(t, t') = &\sum_{\vec{k}\sigma} V^{*}_{\vec{k}\sigma}(t) V_{\vec{k}\sigma}(t') S_{2-\sigma}^{\gtrless}(t, t') B_{\sigma}^{\gtrless}(t, t') G_{\vec{k}\sigma}^{\gtrless}(t, t')\\ &+ \sum_{\vec{q}} V^{*}_{\vec{q}} V_{\vec{q}}\, S_{1\downarrow}^{\gtrless}(t, t') G_{\vec{q}\uparrow}^{\gtrless}(t, t'),\end{aligned} \tag{A2}$$

$$\begin{aligned}\Sigma_{1\downarrow}^{\gtrless}(t, t') = &\sum_{\vec{k}_1\vec{k}_2\vec{k}'\sigma} V_{\vec{k}_1\vec{k}_2\vec{k}'\sigma}(t) V^{*}_{\vec{k}_1\vec{k}_2\vec{k}'\sigma}(t') E^{\gtrless}(t, t') G_{\vec{k}_1\downarrow}^{\gtrless}(t, t')\\ &G_{\vec{k}_2\sigma}^{\gtrless}(t, t') G_{\vec{k}'\sigma}^{\lessgtr}(t', t) + \sum_{\vec{q}} V_{\vec{q}} V^{*}_{\vec{q}}\, D^{\gtrless}(t, t') G_{\vec{q}\uparrow}^{\lessgtr}(t', t)\\ &+ \sum_{\vec{k}\vec{k}'\sigma} V_{\vec{k}\vec{k}'\sigma}(t) V^{*}_{\vec{k}\vec{k}'\sigma}(t') S_{2\downarrow}^{\gtrless}(t, t') G_{\vec{k}\sigma}^{\gtrless}(t, t') G_{\vec{k}'\sigma}^{\lessgtr}(t', t)\\ &+ \sum_{\vec{k}\vec{q}\sigma} V_{\vec{k}\vec{q}\sigma}(t) V^{*}_{\vec{k}\vec{q}\sigma}(t') S_{2\sigma}^{\gtrless}(t, t') G_{\vec{k}\downarrow}^{\gtrless}(t, t') G_{\vec{q}\sigma}^{\lessgtr}(t', t),\end{aligned} \tag{A3}$$

$$\begin{aligned}\Sigma_{2\sigma}^{\gtrless}(t, t') = &\sum_{\vec{k}} V^{*}_{\vec{k}\sigma}(t) V_{\vec{k}\sigma}(t') E^{\gtrless}(t, t') G_{\vec{k}\sigma}^{\gtrless}(t, t')\\ &+ \sum_{\vec{k}} V_{\vec{k}-\sigma}(t) V^{*}_{\vec{k}-\sigma}(t') D^{\gtrless}(t, t') B_{-\sigma}^{\lessgtr}(t', t)\\ &\times G_{\vec{k}-\sigma}^{\lessgtr}(t', t) + \delta_{\downarrow\sigma} \sum_{\vec{k}\vec{k}'\sigma'} V^{*}_{\vec{k}\vec{k}'\sigma'}(t) V_{\vec{k}\vec{k}'\sigma'}(t') S_{1\downarrow}^{\gtrless}(t, t')\\ &\times G_{\vec{k}\sigma'}^{\lessgtr}(t', t) G_{\vec{k}'\sigma'}^{\gtrless}(t, t') + \sum_{\vec{k}\vec{q}} V^{*}_{\vec{k}\vec{q}\sigma}(t) V_{\vec{k}\vec{q}\sigma}(t') S_{1\downarrow}^{\gtrless}(t, t')\\ &\times G_{\vec{k}\downarrow}^{\lessgtr}(t', t) G_{\vec{q}\sigma}^{\gtrless}(t, t').\end{aligned} \tag{A4}$$

The retarded self-energies, which we also need, can be obtained from these expressions using the identity

$$iH^{R}(t, t') = \theta(t - t')[H^{>}(t, t') \pm H^{<}(t, t')], \tag{A5}$$

where the minus sign applies to bosons. As explained by Langreth *et al* [59–61] by applying (A5) to the self-energies listed above it has to be kept in mind that retarded Green functions are of order Q^0, while less-than and greater-than Green functions are of order Q^1, where Q defined in (16) is the projector accounting for the completeness of the projectile states. Hence, by constructing the retarded self-energies via (A5) only terms which ultimately lead to contributions $\propto Q^0$ should be kept. The result is

$$\begin{aligned}\Pi_{\mathrm{e}}^{R}(t, t') = &\sum_{\vec{k}_1\vec{k}_2\vec{k}'\sigma} V^{*}_{\vec{k}_1\vec{k}_2\vec{k}'\sigma}(t) V_{\vec{k}_1\vec{k}_2\vec{k}'\sigma}(t') S_{1\downarrow}^{R}(t, t') G_{\vec{k}_1\downarrow}^{<}(t', t)\\ &\times G_{\vec{k}_2\sigma}^{<}(t', t) G_{\vec{k}'\sigma}^{>}(t, t') + \sum_{\vec{k}\sigma} V_{\vec{k}\sigma}(t) V^{*}_{\vec{k}\sigma}(t') S_{2\sigma}^{R}(t, t')\\ &\times G_{\vec{k}\sigma}^{<}(t', t),\end{aligned} \tag{A6}$$

$$\begin{aligned}\Pi_{\mathrm{d}}^{R}(t, t') = &\sum_{\vec{k}\sigma} V^{*}_{\vec{k}\sigma}(t) V_{\vec{k}\sigma}(t') S_{2-\sigma}^{R}(t, t') B_{\sigma}^{>}(t, t') G_{\vec{k}\sigma}^{>}(t, t')\\ &+ \sum_{\vec{q}} V^{*}_{\vec{q}} V_{\vec{q}}\, S_{1\downarrow}^{R}(t, t') G_{\vec{q}\uparrow}^{>}(t, t'),\end{aligned} \tag{A7}$$

$$\Sigma^R_{1\downarrow}(t,t') = \sum_{\vec{k}_1\vec{k}_2\vec{k}'\sigma} V_{\vec{k}_1\vec{k}_2\vec{k}'\sigma}(t) V^*_{\vec{k}_1\vec{k}_2\vec{k}'\sigma}(t') E^R(t,t') \times G^>_{\vec{k}_1\downarrow}(t,t') G^>_{\vec{k}_2\sigma}(t,t') G^<_{\vec{k}'\sigma}(t',t) + \sum_{\vec{q}} V_{\vec{q}} V^*_{\vec{q}}\, D^R(t,t') \times G^<_{\vec{q}\uparrow}(t',t) + \sum_{\vec{k}\vec{k}'\sigma} V_{\vec{k}\vec{k}'\sigma}(t) V^*_{\vec{k}\vec{k}'\sigma}(t') S^R_{2\downarrow}(t,t') G^>_{\vec{k}\sigma}(t,t') \times G^<_{\vec{k}'\sigma}(t',t) + \sum_{\vec{k}\vec{q}\sigma} V_{\vec{k}\vec{q}\sigma}(t) V^*_{\vec{k}\vec{q}\sigma}(t') S^R_{2\sigma}(t,t') G^>_{\vec{k}\downarrow}(t,t') \times G^<_{\vec{q}\sigma}(t',t), \tag{A8}$$

$$\Sigma^R_{2\sigma}(t,t') = \sum_{\vec{k}} V^*_{\vec{k}\sigma}(t) V_{\vec{k}\sigma}(t') E^R(t,t') G^>_{\vec{k}\sigma}(t,t') + \sum_{\vec{k}} V_{\vec{k}-\sigma}(t) V^*_{\vec{k}-\sigma}(t') D^R(t,t') B^<_{-\sigma}(t',t) \times G^<_{\vec{k}-\sigma}(t',t) + \delta_{\downarrow\sigma} \sum_{\vec{k}\vec{k}'\sigma'} V^*_{\vec{k}\vec{k}'\sigma'}(t) V_{\vec{k}\vec{k}'\sigma'}(t') S^R_{1\downarrow}(t,t') G^<_{\vec{k}\sigma'}(t',t) \times G^>_{\vec{k}'\sigma'}(t,t') + \sum_{\vec{k}\vec{q}} V^*_{\vec{k}\vec{q}\sigma}(t) V_{\vec{k}\vec{q}\sigma}(t') S^R_{1\downarrow}(t,t') G^<_{\vec{k}\downarrow}(t',t) \times G^>_{\vec{q}\sigma}(t,t'), \tag{A9}$$

where the physical origin of the various terms can again be identified by the type of the sum.

Appendix B. Auger level widths

In this appendix, we indicate the main steps leading to the rate $\Gamma^<_{\mathrm{AN}}(t)$ in equation (64). The other rates in this equation can be obtained similarly.

As pointed out by Langreth *et al* [59–61] the essential step for obtaining (64) is to note that the self-energies are peaked around the time-diagonal. Hence, the time integrals in (46)–(49) effectively set the time variables in the Green functions $E(t,t')$, $D(t,t')$, and $S_{n\sigma}(t,t')$—applying to the affinity and ionization levels of the projectile—to equal times (semiclassical approximation). Under the time integral of (46), for instance, the function $iE^<(t,\bar{t})$ can be replaced by $n_+(t)$, while the function $iE^R(t,\bar{t})$ reduces to unity for $t > \bar{t}$ and vanishes otherwise. As a result of the semiclassical approximation, the quantum-kinetic equations (46)–(49) reduce to (64)—with rates, however, not yet in a form numerically tractable.

For a numerical treatment of (64), the rates have to be simplified. Taking Auger neutralization as an example, we now explain the main steps of the simplification. The Auger rate initially appearing in (64) follows from the self-energy (51). It reads

$$\Gamma^<_{\mathrm{AN}}(t) = 2\,\mathrm{Re}\int_{-\infty}^{t} \mathrm{d}\bar{t} \sum_{\vec{k}_1\vec{k}_2\vec{k}'\sigma} V^*_{\vec{k}_1\vec{k}_2\vec{k}'\sigma}(t) V_{\vec{k}_1\vec{k}_2\vec{k}'\sigma}(\bar{t}) \times f^<(\varepsilon_{\vec{k}_1\downarrow}) f^<(\varepsilon_{\vec{k}_2\sigma}) f^>(\varepsilon_{\vec{k}'\sigma}) \times \exp\left(i\int_{\bar{t}}^{t} \mathrm{d}\tau(\varepsilon_{\vec{k}_1\downarrow} + \varepsilon_{\vec{k}_2\sigma} - \varepsilon_{\vec{k}'\sigma} - \varepsilon^0_{1s\downarrow}(\tau))\right). \tag{B1}$$

Adding an integration over ε by inserting the delta function $\delta(\varepsilon_{\vec{k}_1\downarrow} + \varepsilon_{\vec{k}_2\sigma} - \varepsilon_{\vec{k}'\sigma} - \varepsilon)$, we rewrite this expression as

$$\Gamma^<_{\mathrm{AN}}(t) = 2\,\mathrm{Re}\int_{-\infty}^{t} \mathrm{d}\bar{t} \int \frac{\mathrm{d}\varepsilon}{2\pi}\, \Gamma^{\mathrm{AN}}_{\varepsilon}(t,t') \times \exp\left(i\int_{\bar{t}}^{t} \mathrm{d}\tau(\varepsilon - \varepsilon^0_{1s\downarrow}(\tau))\right) \tag{B2}$$

with

$$\Gamma^{\mathrm{AN}}_{\varepsilon}(t,t') = 2\pi \sum_{\vec{k}_1\vec{k}_2\vec{k}'\sigma} V^*_{\vec{k}_1\vec{k}_2\vec{k}'\sigma}(t) V_{\vec{k}_1\vec{k}_2\vec{k}'\sigma}(\bar{t}) \times \delta(\varepsilon_{\vec{k}_1\downarrow} + \varepsilon_{\vec{k}_2\sigma} - \varepsilon_{\vec{k}'\sigma} - \varepsilon) \times f^<(\varepsilon_{\vec{k}_1\downarrow}) f^<(\varepsilon_{\vec{k}_2\sigma}) f^>(\varepsilon_{\vec{k}'\sigma}), \tag{B3}$$

a function which can be simplified on noting that the time and momentum dependencies of the Auger matrix elements $V_{\vec{k}_1\vec{k}_2\vec{k}'\sigma}(t)$ and $V_{\vec{k}_1\vec{k}_2\vec{k}'\sigma}(\bar{t})$ approximately factorize. As for single-electron transfer processes [59–61], we can thus approximately write

$$\Gamma^{\mathrm{AN}}_{\varepsilon}(t,t') \approx \sqrt{\Gamma^{\mathrm{AN}}_{\varepsilon}(t)\Gamma^{\mathrm{AN}}_{\varepsilon}(t')}, \tag{B4}$$

where

$$\Gamma^{\mathrm{AN}}_{\varepsilon}(t) = 2\pi \sum_{\vec{k}_1\vec{k}_2\vec{k}'\sigma} |V_{\vec{k}_1\vec{k}_2\vec{k}'\sigma}(t)|^2 \times \delta(\varepsilon_{\vec{k}_1\downarrow} + \varepsilon_{\vec{k}_2\sigma} - \varepsilon_{\vec{k}'\sigma} - \varepsilon) \times f^<(\varepsilon_{\vec{k}_1\downarrow}) f^<(\varepsilon_{\vec{k}_2\sigma}) f^>(\varepsilon_{\vec{k}'\sigma}) \tag{B5}$$

is essentially the level width introduced in (56) except that the energy ε is not yet pinned to $\varepsilon^0_{1s\downarrow}$. This is accomplished by the time integration. Indeed, inserting (B4) into (B2) and applying again a saddle-point approximation, we obtain

$$\begin{aligned}\Gamma^<_{\mathrm{AN}}(t) &= 2\,\mathrm{Re}\int_{-\infty}^{t} \mathrm{d}\bar{t} \int \frac{\mathrm{d}\varepsilon}{2\pi} \sqrt{\Gamma^{\mathrm{AN}}_{\varepsilon}(t)\Gamma^{\mathrm{AN}}_{\varepsilon}(\bar{t})} \times \exp\left(\mathrm{i}\int_{\bar{t}}^{t} \mathrm{d}\tau(\varepsilon - \varepsilon^0_{1s\downarrow}(\tau))\right) \\ &\simeq 2\,\mathrm{Re}\int_{-\infty}^{t} \mathrm{d}\bar{t}\, \sqrt{\Gamma^{\mathrm{AN}}_{\varepsilon^0_{1s\downarrow}(t)}(t)\Gamma^{\mathrm{AN}}_{\varepsilon^0_{1s\downarrow}(\bar{t})}(\bar{t})} \times \int \frac{\mathrm{d}\varepsilon}{2\pi} \exp\left(\mathrm{i}\int_{\bar{t}}^{t} \mathrm{d}\tau(\varepsilon - \varepsilon^0_{1s\downarrow}(\tau))\right) \\ &= 2\,\mathrm{Re}\int_{-\infty}^{t} \mathrm{d}\bar{t}\, \sqrt{\Gamma^{\mathrm{AN}}_{\varepsilon^0_{1s\downarrow}(t)}(t)\Gamma^{\mathrm{AN}}_{\varepsilon^0_{1s\downarrow}(\bar{t})}(\bar{t})}\, \delta(t-\bar{t}),\end{aligned} \tag{B6}$$

where the last line, when the time integration is carried out, yields $\Gamma^<_{\mathrm{AN}}(t) = \Gamma_{\mathrm{AN}}(t)$. The main gain numerically is that for $\Gamma_{\mathrm{AN}}(t)$ given by (69) it is only necessary to calculate the squared modulus of the Auger matrix element at the time also appearing in the rate equation (64) whereas in (B1) the matrix element has also to be determined for all times past the actual time.

For single-electron transfer processes, Langreth *et al* [59–61] investigated the range of validity of the simplified rates in great detail. It depends on a number of conditions which are almost never rigorously satisfied. The original rates dropping out from equations (46)–(49) are, however,

numerically too expensive to handle. From a practical point of view, the simplification described in this appendix seems to be unavoidable in producing numerical data. It has to be applied to all the rates of equation (64).

ORCID iDs

F X Bronold https://orcid.org/0000-0001-7802-1387

References

[1] Lieberman M A and Lichtenberg A J 2005 *Principles of Plasma Discharges and Materials Processing* (New York: Wiley-Interscience)
[2] Langmuir I and Mott-Smith H 1924 *Gen. Electr. Rev.* **27** 449
[3] Schulze J, Donkó Z, Schlüngel E and Czarnetzki U 2011 *Plasma Sources Sci. Technol.* **20** 045007
[4] Greb A, Niemi K, O'Connell D and Gans T 2013 *Appl. Phys. Lett.* **103** 244101
[5] Daksha M, Derzsi A, Wilczek S, Trieschmann J, Mussenbrock T, Awakowicz P, Donkó Z and Schulze J 2017 *Plasma Sources Sci. Technol.* **26** 085006
[6] Hannesdottir H and Gudmundsson J T 2016 *Plasma Sources Sci. Technol.* **25** 055002
[7] Campanell M D and Umansky M V 2016 *Phys. Rev. Lett.* **116** 085003
[8] Langendorf S and Walker M 2015 *Phys. Plasma* **22** 033515
[9] Sydorenko D, Kaganovich I D, Raitses Y and Smolyakov A 2009 *Phys. Rev. Lett.* **103** 145004
[10] Taccogna F, Longo S and Capitelli M 2004 *Phys. Plasma* **11** 1220
[11] Phelps A V and Petrović Z L 1999 *Plasma Sources Sci. Technol.* **8** R21
[12] Czanderna A W and Hercules D M 1991 *Ion Spectroscopies for Surface Analysis* (New York: Plenum Press)
[13] Harada Y, Masuda S and Ozaki H 1997 *Chem. Rev.* **97** 1897
[14] Monreal R C 2014 *Progr. Surf. Sci.* **89** 80
[15] Winter H P and Burgdörfer J (ed) 2007 *Slow Heavy-Particle Induced Electron Emission from Solid Surface* (Berlin: Springer)
[16] Winter H 2002 *Phys. Rep.* **367** 387
[17] Baragiola R A 1994 *Low Energy Ion-Surface Interaction* ed J W Rabalais (New York: Wiley and Sons) p 187
[18] Los J and Geerlings J J C 1990 *Phys. Rep.* **190** 133
[19] Brako R and Newns D M 1989 *Rep. Prog. Phys.* **52** 655
[20] Modinos A 1987 *Progr. Surf. Sci.* **26** 19
[21] Yoshimori A and Makoshi K 1986 *Prog. Surf. Sci.* **21** 251
[22] Newns D M, Makoshi K, Brako R and van Wunnik J N M 1983 *Phys. Scr.* T **6** 5
[23] Oliphant M L E and Moon P B 1930 *Proc. Roy. Soc. (London)* A **127** 388
[24] Massey H S W 1930 *Proc. Cambridge Phil. Soc.* **26** 386
[25] Shekhter S S 1937 *J. Exp. Theoret. Phys. (USSR)* **7** 750
[26] Cobas A and Lamb W E 1944 *Phys. Rev.* **65** 327
[27] Hagstrum H D 1953 *Phys. Rev.* **91** 543
[28] Hagstrum H D 1954 *Phys. Rev.* **96** 325
[29] Lancaster J, Kontur F, Walters G and Dunning F 2007 *Nucl. Instr. Meth. Phys. Res.* B **256** 37
[30] Lancaster J C, Kontur F J, Walters G K and Dunning F B 2003 *Phys. Rev.* B **67** 115413
[31] Sosolik C E, Hampton J R, Lavery A C, Cooper B H and Marston J B 2003 *Phys. Rev. Lett.* **90** 013201
[32] Hecht T, Winter H and Borisov A G 1998 *Surf. Sci.* **406** L607
[33] Winter H 1993 *J. Phys. C: Condens. Matter* **5** A295
[34] Kimmel G A and Cooper B H 1993 *Phys. Rev.* B **48** 12164
[35] Müller H, Hausmann R, Brenten H, Niehaus A and Kempter V 1993 *Z. Phys.* D **28** 109
[36] Brenten H, Müller H, Niehaus A and Kempter V 1992 *Surf. Sci.* **278** 183
[37] Sesselmann W, Woratschek B, Küppers J, Ertl G and Haberland H 1987 *Phys. Rev.* B **35** 1547
[38] Propst F M 1963 *Phys. Rev.* **129** 7
[39] Bonetto F, Gonzalez C and Goldberg E C 2016 *PRB* **93** 195439
[40] Iglesias-García A, García E A and Goldberg E C 2014 *Phys. Rev.* B **90** 195416
[41] Iglesias-García A, García E A and Goldberg E C 2013 *Phys. Rev.* B **87** 075434
[42] Monreal R C, Goebl D, Primetzhofer D and Bauer P 2013 *Nucl. Instrum. Meth. Phys. Res.* B **315** 206
[43] Masuda S, Sasaki K, Sogo M, Aoki M and Morikawa Y 2009 *Phys. Rev.* A **80** 040901(R)
[44] Valdés D, Goldberg E C, Blanco J M and Monreal R C 2005 *Phys. Rev.* B **71** 245417
[45] García E A, Wang N P, Monreal R C and Goldberg E C 2003 *Phys. Rev.* B **67** 205426
[46] Wang N P, García E A, Monreal R, Flores F, Goldberg E C, Brongersma H H and Bauer P 2001 *Phys. Rev.* A **64** 012901
[47] van Someren B, van Emmichoven P A Z and Niehaus A 2000 *Phys. Rev.* A **61** 022902
[48] More W, Merino J, Monreal R, Pou P and Flores F 1998 *Phys. Rev.* B **58** 7385
[49] Lorente N, Cazalilla M A, Gauyacq J P, Teillet-Billy D and Echenique P M 1998 *Surf. Sci.* **411** L888
[50] Cazalilla M A, Lorente N, Muino R D, Gauyacq J P, Teillet-Billy D and Echenique P M 1998 *Phys. Rev.* B **58** 13991
[51] Lorente N and Monreal R 1996 *Phys. Rev.* B **53** 9622
[52] Lorente N, Monreal R and Alducin M 1994 *Phys. Rev.* A **49** 4716
[53] Marston J B, Andersson D R, Behringer E R, Cooper B H, DiRubio C A, Kimmel G A and Richardson C 1993 *Phys. Rev.* B **48** 7809
[54] Modinos A and Easa S I 1987 *Surf. Sci.* **185** 569
[55] Daksha M, Berger B, Schuengel E, Korolov I, Derzsi A, Koepke M, Donko Z and Schulze J 2016 *J. Phys. D: Appl. Phys.* **49** 234001
[56] Marcak A, Corbella C, de los Arcos T and von Keudell A 2015 *Rev. Sci. Instrum.* **86** 106102
[57] Gadzuk J W 1967 *Surf. Sci.* **6** 133
[58] Gadzuk J W 1967 *Surf. Sci.* **6** 159
[59] Langreth D C and Nordlander P 1991 *Phys. Rev.* B **43** 2541
[60] Shao H, Langreth D C and Nordlander P 1994 *Phys. Rev.* B **49** 13929
[61] Shao H, Langreth D C and Nordlander P 1994 *Low Energy Ion-Surface Interaction* ed J W Rabalais (New York: Wiley and Sons) p 117
[62] Marbach J, Bronold F X and Fehske H 2011 *Phys. Rev.* B **84** 085443
[63] Marbach J, Bronold F X and Fehske H 2012 *Eur. Phys. J.* D **66** 106
[64] Marbach J, Bronold F X and Fehske H 2012 *Phys. Rev.* B **86** 115417
[65] Pamperin M, Bronold F X and Fehske H 2015 *Phys. Rev.* B **91** 035440
[66] Pamperin M, Bronold F X and Fehske H 2015 *Phys. Scr.* T **165** 014008
[67] Hemmen R and Conrad H 1991 *Phys. Rev. Lett.* **67** 1314
[68] Borisov A, Teillet-Billy D and Gauyacq J 1995 *Surf. Sci.* **325** 323
[69] Lang N D and Kohn W 1970 *Phys. Rev.* B **1** 4555
[70] Kürpick P and Thumm U 1996 *Phys. Rev.* A **54** 1487

[71] Jennings P J, Jones R O and Weinert M 1988 *Phys. Rev.* B **37** 6113
[72] Clementi E and Roetti C 1974 *At. Data Nucl. Data tables* **14** 177
[73] Sansonetti J E and Martin W C 2005 *J. Phys. Chem. Ref. Data* **34** 1559
[74] Hölzl J and Schulte F K 1979 *Solid Surface Physics* ed G Höhler (Berlin: Springer) p 1
[75] Ashcroft N W and Mermin N D 1976 *Solid State Physics* (Philadelphia: Saunders College Publishing)
[76] Penn D R and Apell P 1990 *Phys. Rev.* B **41** 3303
[77] Keldysh L V 1965 *Sov. Phys. JETP* **20** 1018
[78] Kadanoff L P and Baym G 1962 *Quantum Statistical Mechanics* (New York: Benjamin)
[79] Lifshitz E M and Pitaevskii L P 1981 *Physical Kinetics* (New York: Pergamon)
[80] Langreth D C and Wilkins J W 1972 *Phys. Rev.* B **6** 3189
[81] Feuerbacher B and Wallis R F 1976 *J. Phys. C: Solid State Phys.* **9** 169
[82] Lepage G P 1978 *J. Comput. Phys.* **27** 192
[83] Hagstrum H D 1961 *Phys. Rev.* **123** 758
[84] Hewson A C 1993 *The Kondo Problem to Heavy Fermions* (Cambridge: Cambridge University Press)

Bibliography

[Agu03] R. Aguado and D. C. Langreth, "Kondo effect in coupled quantum dots: A nonsing approximation study", Phys. Rev. B **67**, 245307 (2003).

[Aki70] H. Akima, "A New Method of Interpolation and Smooth Curve Fitting Based on Local Procedures", J. ACM **17**, 589 (1970).

[And80] N. Andrei, "Diagonalization of the Kondo Hamiltonian", Phys. Rev. Lett. **45**, 379 (1980).

[Ash76] N. W. Ashcroft and N. D. Mermin, *Solid State Physics* (Saunders College Publishing, Philadelphia, 1976).

[Aum07] F. Aumayr and HP. Winter, "Potential Electron Emission from Metal and Insulator Surfaces", in *Slow Heavy-Particle Induced Electron Emission from Solid Surfaces*, ed. by HP. Winter and J. Burgdörfer (Springer-Verlag, Berlin, 2007), p. 78.

[Baj07] N. Bajales, J. Ferrón, and E. C. Goldberg, "Coulomb blockade in ion-induced electron emission and neutralization mechanisms", Phys. Rev. B **76**, 245431 (2007).

[Bar94] R. A. Baragiola, "Electron Emission from Slow Ion-Solid Interactions", in *Low Energy Ion-Surface Interaction*, ed. by J. W. Rabalais (Wiley, New York, 1994), p. 187.

[Ble86] N. Bleistein and R. A. Handelsman, *Asymptotic Expansion of Integrals* (Dover Publications, New York, 1986).

[Bon16] F. Bonetto, C. Gonzalez, and E. C. Goldberg, "Signals of strong electronic correlation in ion scattering processes", Phys. Rev. B **93**, 195439 (2016).

[Boo78] C. de Boor, *A Practical Guide to Splines* (Springer-Verlag, New York, 1978).

[Bor95a] A. Borisov, D. Teillet-Billy, and J. Gauyacq, "Singlet to triplet conversion in low energy metastable helium-metal surface collisions: Auger deexcitation process", Surf. Sci. **325**, 323 (1995).

[Bor95b] A. Borisov and U. Wille, "Broadening of atomic levels near metal surfaces: first-order model versus coupled-angular-mode method", Surf. Sci. **338**, L875 (1995).

[Bra89] R. Brako and D. M. Newns, "Theory of electronic processes in atom scattering from surfaces", Rep. Prog. Phys. **52**, 655 (1989).

[Bre92a] H. Brenten, H. Müller, and V. Kempter, "Intra- and inter-atomic Auger processes in collisions of low energy He^{++}, He^{+}, $He^{*}(2^3S, 2^1S)$ and Li^{+} with Li covered W(110) surfaces", Z. Phys. D **22**, 563 (1992).

[Bre92b] H. Brenten, H. Müller, A. Niehaus, and V. Kempter, "Autoionization and autodetachment in collisions of slow inert gas ions with partially K covered W(110) surfaces", Surf. Sci. **278**.1, 183 (1992).

[Cam16] M. D. Campanell and M. V. Umansky, "Strongly Emitting Surfaces Unable to Float below Plasma Potential", Phys. Rev. Lett. **116**, 085003 (2016).

[Caz98] M. A. Cazalilla, N. Lorente, R. D. Muino, J. P. Gauyacq, D. Teillet-Billy, and P. M. Echenique, "Theory of Auger neutralization and deexcitation of slow ions at metal surfaces", Phys. Rev. B **58**, 13991 (1998).

[Cha09] A. M. Chang and J. C. Chen, "The Kondo effect in coupled-quantum dots", Rep. Prog. Phys. **72**, 096501 (2009).

[Cle63] E. Clementi and D. L. Raimondi, "Atomic Screening Constants from SCF Functions", J. Chem. Phys. **38**, 2686 (1963).

[Cle67] E. Clementi, D. L. Raimondi, and W. P. Reinhardt, "Atomic Screening Constants from SCF Functions. II. Atoms with 37 to 86 Electrons", J. Chem. Phys. **47**, 1300 (1967).

[Cle74] E. Clementi and C. Roetti, "Roothaan-Hartree-Fock atomic wavefunctions: Basis functions and their coefficients for ground and certain excited states of neutral and ionized atoms, $Z \leq 54$", At. Data Nucl. Data Tables **14**, 177 (1974).

[Cob44] A. Cobas and W. E. Lamb, "On the Extraction of Electrons from a Metal Surface by Ions and Metastable Atoms", Phys. Rev. **65**, 327 (1944).

[Coh11] G. Cohen and E. Rabani, "Memory effects in nonequilibrium quantum impurity models", Phys. Rev. B **84**, 075150 (2011).

[Col84] P. Coleman, "New approach to the mixed-valence problem", Phys. Rev. B **29**, 3035 (1984).

[Cro98] S. M. Cronenwett, T. H. Oosterkamp, and L. P. Kouwenhoven, "A Tunable Kondo Effect in Quantum Dots", Science **281**, 540 (1998).

[Cza91] A. W. Czanderna and D. M. Hercules, eds., *Ion Spectroscopies for Surface Analysis* (Plenum Press, New York, 1991).

[Dak16] M. Daksha, B. Berger, E. Schuengel, I. Korolov, A. Derzsi, M. Koepke, Z. Donkó, and J. Schulze, "A computationally assisted spectroscopic technique to measure secondary electron emission coefficients in radio frequency plasmas", J. Phys. D: Appl. Phys. **49**, 234001 (2016).

[Des80] J.-L. Desplat and C. Papageorgopoulos, "Interaction of cesium and oxygen on W(110): I. Cesium adsorption on oxygenated and oxidized W(110)", Surf. Sci. **92**, 97 (1980).

[Dir27] P. A. M. Dirac, "The quantum theory of the emission and absorption of radiation", Proc. R. Soc. Lond. A **114**, 243 (1927).

[Fer50] E. Fermi, *Nuclear Physics* (University of Chicago Press, Chicago, 1950).

[Feu76] B. Feuerbacher and R. F. Willis, "Photoemission and electron states at clean surfaces", J. Phys. C: Solid State Phys. **9**, 169 (1976).

[Ful91] P. Fulde, ed., *Electron Correlations in Molecules and Solids* (Springer-Verlag, Berlin, 1991).

[Gad09] J. W. Gadzuk, "Simple connections in alkali adsorption", Phys. Rev. B **79**, 073411 (2009).

[Gad67a] J. W. Gadzuk, "Theory of atom-metal interactions I. Alkali atom adsorption", Surf. Sci. **6**, 133 (1967).

[Gad67b] J. W. Gadzuk, "Theory of atom-metal interactions II. One-electron transition matrix elements", Surf. Sci. **6**, 159 (1967).

[Gar03] E. A. García, N. P. Wang, R. C. Monreal, and E. C. Goldberg, "Interference between resonant and Auger mechanisms for charge-exchange processes near surfaces", Phys. Rev. B **67**, 205426 (2003).

[Gib98] J. W. Gibbs, "Fourier's Series", Nature **59**, 200 (1898).

[Gib99] J. W. Gibbs, "Fourier's Series", Nature **59**, 606 (1899).

[Gna99] H. Gnaser, *Low-Energy Ion Irradiation of Solid Surfaces* (Springer-Verlag, Berlin, 1999).

[Gol05] E. C. Goldberg, F. Flores, and R. C. Monreal, "Stationary and dynamical descriptions of strong correlated systems", Phys. Rev. B **71**, 035112 (2005).

[Gol98a] D. Goldhaber-Gordon, J. Göres, M. A. Kastner, H. Shtrikman, D. Mahalu, and U. Meirav, "From the Kondo Regime to the Mixed-Valence Regime in a Single-Electron Transistor", Phys. Rev. Lett. **81**, 5225 (1998).

[Gol98b] D. Goldhaber-Gordon, H. Shtrikman, D. Mahalu, D. Abusch-Magder, U. Meirav, and M. A. Kastner, "Kondo effect in a single-electron transistor", Nature **391**, 156 (1998).

[Gra92] H. Grabert and M. H. Devoret, eds., *Single Charge Tunneling: Coulomb Blockade Phenomena in Nanostructures* (Plenum Press, New York, 1992).

[Haa34] W. J. de Haas, J. de Boer, and G. J. van den Berg, "The electrical resistance of gold, copper and lead at low temperatures", Physica **1**, 1115 (1934).

[Hag53] H. D. Hagstrum, "Electron Ejection from Ta by He^+, He^{++}, and He_2^+", Phys. Rev. **91**, 543 (1953).

[Hag54] H. D. Hagstrum, "Auger Ejection of Electrons from Tungsten by Noble Gas Ions", Phys. Rev. **96**, 325 (1954).

[Har97] Y. Harada, S. Masuda, and H. Ozaki, "Electron Spectroscopy Using Metastable Atoms as Probes for Solid Surfaces", Chem. Rev. **97**, 1897 (1997).

[He10] X. He and J. A. Yarmoff, "Correlated electron effects in low energy Sr^+ ion scattering", Phys. Rev. Lett. **105**, 176806 (2010).

[He11] X. He and J. A. Yarmoff, "Measuring correlated-electron effects with low energy alkaline earth ion scattering", Nucl. Instr. Meth. Phys. Res. B **269**, 1195 (2011).

[Hec98] T. Hecht, H. Winter, and A. G. Borisov, "Auger transition rates for the neutralization of He^+ ions in front of an aluminum surface", Surf. Sci. **406**, L607 (1998).

[Hem91] R. Hemmen and H. Conrad, "New interpretation of Penning spectra from alkali-metal atoms chemisorbed on metal surfaces", Phys. Rev. Lett. **67**, 1314 (1991).

[Hew93] A. C. Hewson, *The Kondo Problem to Heavy Fermions* (Cambridge University Press, Cambridge, 1993).

[Höl79] J. Hölzl and F. K. Schulte, "Work Functions of Metals", in *Solid Surface Physics*, ed. by G. Höhler (Springer-Verlag, Berlin, 1979), p. 1.

[Igl13] A. Iglesias-García, E. A. García, and E. C. Goldberg, "Role of He excited configurations in the neutralization of He^+ ions colliding with a HOPG surface", Phys. Rev. B **87**, 075434 (2013).

[Igl14] A. Iglesias-García, E. A. García, and E. C. Goldberg, "Importance of considering helium excited states in He^+ scattering by aluminum surfaces", Phys. Rev. B **90**, 195416 (2014).

[Jon84] R. O. Jones, P. J. Jennings, and O. Jepsen, "Surface barrier in metals: A new model with application to W(001)", Phys. Rev. B **29**, 6474 (1984).

[Kad62] L. P. Kadanoff and G. Baym, *Quantum Statistical Mechanics* (Benjamin, New York, 1962).

[Kas87] H. Kasai and A. Okiji, "Equation of motion method for the time-dependent Newns-Anderson model", Surf. Sci. **183**, 147 (1987).

[Kel64] L. V. Keldysh, "Diagram technique for non-equilibrium processes", J. Exptl. Theoret. Phys. (U.S.S.R.) **47**, 1515 (1964). [J. Exptl. Theoret. Phys. **20**, 1018 (1965)].

[Kim93] G. A. Kimmel and B. H. Cooper, "Dynamics of resonant charge transfer in low-energy alkali-metal-ion scattering", Phys. Rev. B **48**, 12164 (1993).

[Kon64] J. Kondo, "Resistance Minimum in Dilute Magnetic Alloys", Progr. Theor. Phys. **32**, 37 (1964).

[Kot86] G. Kotliar and A. E. Ruckenstein, "New functional integral approach to strongly correlated Fermi systems: The Gutzwiller approximation as a saddle point", Phys. Rev. Lett. **57**, 1362 (1986).

[Kra08] W. Kraus, H.-D. Falter, U. Fantz, P. Franzen, B. Heinemann, P. McNeely, R. Riedl, and E. Speth, "Long pulse large area beam extraction with a rf driven H^-/D^- source", Rev. Sci. Instrum. **79**, 02C108 (2008).

[Kür96] P. Kürpick and U. Thumm, "Basic matrix elements for level shifts and widths of hydrogenic levels in ion-surface interactions", Phys. Rev. A **54**, 1487 (1996).

[Lai18] H.-H. Lai, S. E. Grefe, S. Paschen, and Q. Si, "Weyl–Kondo semimetal in heavy-fermion systems", Proc. Natl. Acad. Sci. **115**, 93 (2018).

[Lan03] J. C. Lancaster, F. J. Kontur, G. K. Walters, and F. B. Dunning, "Dynamics of He^+ ion neutralization at clean metal surfaces: Energy- and spin-resolved studies", Phys. Rev. B **67**, 115413 (2003).

[Lan07] J. Lancaster, F. Kontur, G. Walters, and F. Dunning, "Neutralization of low-energy He^+ ions at a magnesium surface", Nucl. Instr. Meth. Phys. Res. B **256**, 37 (2007).

[Lan15] S. Langendorf and M. Walker, "Effect of secondary electron emission on the plasma sheath", Phys. Plasmas **22**, 033515 (2015).

[Lan91] D. C. Langreth and P. Nordlander, "Derivation of a master equation for charge-transfer processes in atom-surface collisions", Phys. Rev. B **43**, 2541 (1991).

[Lec14] B. Lechtenberg and F. B. Anders, "Spatial and temporal propagation of Kondo correlations", Phys. Rev. B **90**, 045117 (2014).

[Lep78] G. P. Lepage, "A new algorithm for adaptive multidimensional integration", Journal of Computational Physics **27**.2, 192 (1978). ISSN: 0021-9991.

[Lie05] M. A. Lieberman and A. J. Lichtenberg, *Principles of Plasma Discharges and Materials Processing* (Wiley, New York, 2005).

[Lif81] E. M. Lifshitz and L. P. Pitaevskii, *Physical Kinetics* (Pergamon Press, New York, 1981).

[Lor94] N. Lorente, R. Monreal, and M. Alducin, "Local theory of Auger neutralization for slow and compact ions interacting with metal surfaces", Phys. Rev. A **49**, 4716 (1994).

[Lor96] N. Lorente and R. Monreal, "Multielectron neutralization channels in ion-surface scattering", Phys. Rev. B **53**, 9622 (1996).

[Lor98] N. Lorente, M. A. Cazalilla, J. P. Gauyacq, D. Teillet-Billy, and P. M. Echenique, "Auger neutralization and de-excitation of helium at an aluminum surface: a unified treatment", Surf. Sci. **411**, L888 (1998).

[Los90] J. Los and J. Geerlings, "Charge exchange in atom-surface collisions", Phys. Rep. **190**, 133 (1990).

[Mar12] J. Marbach, F. X. Bronold, and H. Fehske, "Pseudoparticle approach for charge-transferring molecule-surface collisions", Phys. Rev. B **86**, 115417 (2012).

[Mar15] A. Marcak, C. Corbella, T. de los Arcos, and A. von Keudell, "Note: Ion-induced secondary electron emission from oxidized metal surfaces measured in a particle beam reactor", Rev. Sci. Instrum. **86**, 106102 (2015).

[Mar93] J. B. Marston, D. R. Andersson, E. R. Behringer, B. H. Cooper, C. A. DiRubio, G. A. Kimmel, and C. Richardson, "Many-body theory of charge transfer in hyperthermal atomic scattering", Phys. Rev. B **48**, 7809 (1993).

[Mas09] S. Masuda, K. Sasaki, M. Sogo, M. Aoki, and Y. Morikawa, "Electron emission spectra of thermal collisions of He metastable atoms with Au(111) and Pt(111) surfaces: Evidence for Penning ionization", Phys. Rev. A **80**, 040901(R) (2009).

[Mas30] H. S. W. Massey, "The theory of the extraction of electrons from metals by positive ions and metastable atoms", Math. Proc. Camb. Philos. Soc. **26**, 386 (1930).

[Mer98] J. Merino and J. B. Marston, "Room-temperature Kondo effect in atom-surface scattering: Dynamical $1/N$ approach", Phys. Rev. B **58**, 6982 (1998).

[Mod87a] A. Modinos, "Resonance charge transfer in atom-surface scattering", Prog. Surf. Sci. **26**, 19 (1987).

[Mod87b] A. Modinos and S. I. Easa, "On the interpretation of ion neutralization spectra at metal surfaces", Surf. Sci. **185**, 569 (1987).

[Mon13] R. C. Monreal, D. Goebl, D. Primetzhofer, and P. Bauer, "Effects of the atomic level shift in the Auger neutralization rates of noble metal surfaces", Nucl. Instr. Meth. Phys. Res. B **315**, 206 (2013).

[Mon14] R. C. Monreal, "Auger neutralization and ionization processes for charge exchange between slow noble gas atoms and solid surfaces", Progress in Surface Science **89**, 80 (2014).

[Mor98] W. More, J. Merino, R. Monreal, P. Pou, and F. Flores, "Role of energy-level shifts on Auger neutralization processes: A calculation beyond the image potential", Phys. Rev. B **58**, 7385 (1998).

[Müh11] L. Mühlbacher, D. F. Urban, and A. Komnik, "Anderson impurity model in nonequilibrium: Analytical results versus quantum Monte Carlo data", Phys. Rev. B **83**, 075107 (2011).

[Mül93] H. Müller, R. Hausmann, H. Brenten, A. Niehaus, and V. Kempter, "Electron emission in collisions of slow rare gas ions with partially cesiated W(110)", Z. Phys. D **28**, 109 (1993).

[Nak88] H. Nakanishi, H. Kasai, and A. Okiji, "Charge exchange scattering of particles from metal surfaces", Surf. Sci. **197**, 515 (1988).

[New83] D. M. Newns, K. Makoshi, R. Brako, and J. N. M. van Wunnik, "Charge Transfer in Inelastic Ion and Atom-Surface Collisions", Phys. Scr. **T6**, 5 (1983).

[Ngh14] H. T. M. Nghiem and T. A. Costi, "Time-dependent numerical renormalization group method for multiple quenches: Application to general pulses and periodic driving", Phys. Rev. B **90**, 035129 (2014).

[Nor93] P. Nordlander, H. Shao, and D. C. Langreth, "Intra-atomic correlation effects in charge transfer", Nucl. Instr. Meth. Phys. Res. B **78**, 11 (1993).

[Oli30] M. L. E. Oliphant and P. B. Moon, "The liberation of electrons from metal surfaces by positive ions. Part II.-Theoretical", Proc. R. Soc. Lond. A **127**, 388 (1930).

[Onu96] A. V. Onufriev and J. B. Marston, "Memory loss and Auger processes in a many-body theory of charge transfer", Phys. Rev. B **53**, 13340 (1996).

[Pap80] C. Papageorgopoulos and J.-L. Desplat, "Interaction of cesium and oxygen on W(110): II. Codeposition: cesium oxide formation", Surf. Sci. **92**, 119 (1980).

[Pen90] D. R. Penn and P. Apell, "Theory of spin-polarized metastable-atom-deexcitation spectroscopy: Ni-He", Phys. Rev. B **41**, 3303 (1990).

[Phe99] A. V. Phelps and Z. L. Petrovic, "Cold-cathode discharges and breakdown in argon: surface and gas phase production of secondary electrons", Plasma Sources Sci. Technol. **8**, R21 (1999).

[Pie10] A. Piel, ed., *Plasma Physics. An Introduction to Laboratory, Space, and Fusion Plasmas* (Springer-Verlag, Berlin, 2010).

[Pro63] F. M. Propst, "Energy Distribution of Electrons Ejected from Tungsten by He^+", Phys. Rev. **129**, 7 (1963).

[Pus04] M. Pustilnik and L. Glazman, "Kondo effect in quantum dots", J. Phys.: Condens. Matter **16**, R513 (2004).

[Rab03] J. W. Rabalais, *Principles and Applications of Ion Scattering Spectrometry: Surface Chemical and Structural Analysis* (Wiley, New York, 2003).

[Rab94] J. W. Rabalais, ed., *Low Energy Ion-Surface Interaction* (Wiley, New York, 1994).

[Rom09] M. A. Romero, F. Flores, and E. C. Goldberg, "Effective treatment of charge and spin fluctuations in dynamical and static atom-surface interactions", Phys. Rev. B **80**, 235427 (2009).

[Sch66] J. R. Schrieffer and P. A. Wolff, "Relation between the Anderson and Kondo Hamiltonians", Phys. Rev. **149**, 491 (1966).

[Ses87] W. Sesselmann, B. Woratschek, J. Küppers, G. Ertl, and H. Haberland, "Interaction of metastable noble-gas atoms with transition-metal surfaces: Resonant ionization and Auger neutralization", Phys. Rev. B **35**, 1547 (1987).

[Sha94a] H. Shao, D. C. Langreth, and P. Nordlander, "Many-body theory for charge transfer in atom-surface collisions", Phys. Rev. B **49**, 13929 (1994).

[Sha94b] H. Shao, D. C. Langreth, and P. Nordlander, "Theoretical description of charge transfer in atom-surface collisions", in *Low Energy Ion-Surface Interaction*, ed. by J. W. Rabalais (Wiley and Sons, New York, 1994), p. 117.

[Sha96] H. Shao, P. Nordlander, and D. C. Langreth, "Probing the Highly Correlated Mixed-Valent State via Charge Transfer with Atoms Moving Out from a Surface", Phys. Rev. Lett. **77**, 948 (1996).

[She37] S. S. Shekther, "Neutralization of positive ions and the emission of secondary electrons", J. Exp. Theor. Phys. (U.S.S.R.) **7**, 750 (1937).

[Shi18] J. Shim, H.-S. Sim, and S.-S. B. Lee, "Numerical renormalization group method for entanglement negativity at finite temperature", Phys. Rev. B **97**, 155123 (2018).

[Sig92] P. Sigmund, ed., *Fundamental Processes in Sputtering of Atoms and Molecules (SPUT92)* (Matematisk-fysiske Meddelelser, Copenhagen, 1992).

[Sla30] J. C. Slater, "Atomic Shielding Constants", Phys. Rev. **36**, 57 (1930).

[Sla64] J. C. Slater, "Atomic Radii in Crystals", J. Chem. Phys. **41**, 3199 (1964).

[Som00] B. van Someren, P. A. Z. van Emmichoven, and A. Niehaus, "Neutralization of He^+ ions in front of an aluminum surface", Phys. Rev. A **61**, 022902 (2000).

[Sos03] C. E. Sosolik, J. R. Hampton, A. C. Lavery, B. H. Cooper, and J. B. Marston, "Thermally enhanced neutralization in hyperthermal energy ion scattering", Phys. Rev. Lett. **90**, 013201 (2003).

[Syd09] D. Sydorenko, I. Kaganovich, Y. Raitses, and A. Smolyakov, "Breakdown of a Space Charge Limited Regime of a Sheath in a Weakly Collisional Plasma Bounded by Walls with Secondary Electron Emission", Phys. Rev. Lett. **103**, 145004 (2009).

[Tac04] F. Taccogna, S. Longo, and M. Capitelli, "Plasma-surface interaction model with secondary electron emission effects", Phys. Plasmas **11**, 1220 (2004).

[Ter09] M. Ternes, A. J. Heinrich, and W.-D. Schneider, "Spectroscopic manifestations of the Kondo effect on single adatoms", J. Phys.: Condens. Matter **21**, 053001 (2009).

[Tos10] L. Tosi, P. R. Bas, A. M. Llois, and L. O. Manuel, "Effects of vertex corrections on diagrammatic approximations applied to the study of transport through a quantum dot", Phys. Rev. B **83**, 073301 (2010).

[Val05] D. Valdés, E. C. Goldberg, J. M. Blanco, and R. C. Monreal, "Linear combination of atomic orbitals calculation of the Auger neutralization rate of He^+ on Al(111), (100), and (110) surfaces", Phys. Rev. B **71**, 245417 (2005).

[Vig80] P. B. Vigman, "Exact solution of $s-d$ exchange model at $T = 0$", J. Exptl. Theoret. Phys. Lett. (USSR) **31**, 392 (1980). [P. B. Wiegmann, J. Exptl. Theoret. Phys. Lett. **31**, 364 (1980)].

[Wan01] N. P. Wang, E. A. García, R. Monreal, F. Flores, E. C. Goldberg, H. H. Brongersma, and P. Bauer, "Low-energy ion neutralization at surfaces: Resonant and Auger processes", Phys. Rev. A **64**, 012901 (2001).

[Wic50] G. C. Wick, "The Evaluation of the Collision Matrix", Phys. Rev. **80**, 268 (1950).

[Wil48] H. Wilbraham, "On a certain periodic function", The Cambridge and Dublin mathematical journal **3**, 198 (1848).

[Win02] H. Winter, "Collisions of atoms and ions with surfaces under grazing incidence", Phys. Rep. **367**, 387 (2002).

[Win07] HP. Winter and J. Burgdörfer, *Slow Heavy-Particle Induced Electron Emission from Solid Surfaces* (Springer-Verlag, Berlin, 2007).

[Win93] H. Winter, "A study of the neutralization of He^+ ions in grazing collisions with an Al(111) surface", J. Phys.: Condens. Matter **5**, A295 (1993).

[Win94] N. S. Wingreen and Y. Meir, "Anderson model out of equilibrium: Noncrossing-approximation approach to transport through a quantum dot", Phys. Rev. B **49**, 11040 (1994).

[Yos86] A. Yoshimori and K. Makoshi, "Time-dependent Newns-Anderson model", Prog. Surf. Sci. **21**, 251 (1986).

Scientific Contributions

Publications

(a) M. Pamperin, F. X. Bronold and H. Fehske, *Mixed-valence correlations in charge-transferring atom-surface collisions*, *Phys. Scr.* **T165**, 014008 (2015). Copyright (2015) by the Royal Swedish Academy of Sciences.

(b) M. Pamperin, F. X. Bronold and H. Fehske, *Many-body theory of the neutralization of strontium ions on gold surfaces*, *Phys. Rev. B* **91**, 035440 (2015). Copyright (2015) by the American Physical Society.

(c) F. X. Bronold, H. Fehske, M. Pamperin and E. Thiessen, *Electron kinetics at the plasma interface*, *Eur. Phys. J. D* **72**, 88 (2018). Copyright (2018) by EDP Sciences, Società Italiana di Fisica, Springer-Verlag 2018.

(d) M. Pamperin, F. X. Bronold and H. Fehske, *Ion-induced secondary electron emission from metal surfaces*, *Plasma Sources Sci. Technol.* **27**, 084003 (2018). Copyright (2018) by IOP Publishing.

(e) M. Bonitz, A. Filinov, J.-W. Abraham, K. Balzer, H. Kählert, E. Pehlke, F. X. Bronold, M. Pamperin, M. Becker, D. Loffhagen and H. Fehske, *Towards an integrated modeling of the plasma-solid interface*, accepted for publication in *Frontiers of Chemical Sciences and Engineering*. arXiv:1809.02473.

Conferences and Workshops

(a) M. Pamperin, F. X. Bronold, and H. Fehske, *Possibility of a Kondo resonance at the wall recombination of positive ions*, poster at the DPG Spring Meeting, Berlin, 2014

(b) M. Pamperin, F. X. Bronold, and H. Fehske, *Electronic correlations during the neutralization of strontium ions on gold surfaces*, talk at the DPG Spring Meeting, Bochum, 2015

(c) M. Pamperin, F. X. Bronold, and H. Fehske, *Neutralization of positive ions at metallic and dielectric plasma walls*, poster at the DPG Spring Meeting, Hannover, 2016

(d) M. Pamperin, F. X. Bronold, and H. Fehske, *Quantum kinetics of the neutralization of positive ions at plasma walls*, poster at the Conference Quo vadis – Complex plasmas, Hamburg, 2016

(e) M. Pamperin, F. X. Bronold, and H. Fehske, *Quantum kinetic theory of ion-induced secondary electron emission from surfaces*, poster at the DPG Spring Meeting, Erlangen, 2018

Erklärung

Hiermit erkläre ich, dass diese Arbeit bisher von mir weder an der Mathematisch-Naturwissenschaftlichen Fakultät der Universität Greifswald noch einer anderen wissenschaftlichen Einrichtung zum Zwecke der Promotion eingereicht wurde. Ferner erkläre ich, dass ich diese Arbeit selbständig verfasst und keine anderen als die darin angegebenen Hilfsmittel und Hilfen benutzt und keine Textabschnitte eines Dritten ohne Kennzeichnung übernommen habe.

(Mathias Pamperin) Greifswald, 8. März 2019

Acknowledgement

Diese Arbeit wäre ohne die fortlaufende Unterstützung einer Vielzahl an Personen vermutlich in dieser Form nie zustande gekommen. Mein tiefster Dank gilt PD Dr. Franz X. Bronold, der mich als Mentor, Vorbild und Ratgeber maßgeblich durch so manche Irrungen und Wirrungen geleitet hat. Weiteren Dank schulde ich Prof. Dr. Holger Fehske, der als Kopf der Arbeitsgruppe die Infrastruktur beigesteuert hat, um diese Arbeit zu fertigen. Außerdem möchte ich Dr. Thomas Meyer und Jens Schleede nicht unerwähnt lassen, die sich stets engagiert und vorbildlich um jedes meiner technischen Probleme gekümmert haben. Ich möchte mich auch noch bei allen Kollegen des Büros B203, insbesondere bei Elena Thiessen, Christian Wurl und Dr. Bernd Zenker, bedanken für die vielen Hinweise, Anregungen und Diskussionen. Ein Mensch ist letztlich immer die Summe seiner Erfahrung. Daher muss ich auch meinen Großeltern danken, dass sie mich von Kindheit an stets gefördert haben und meinen Weg so geduldig und liebevoll begleitet haben. Abschließend möchte ich noch meinen Freunden und meiner großen Liebe Susanne für die stetige Kraft und Motivation in schweren Zeiten danken, die diese mir immer wieder haben zuteil kommen lassen. Vielen Dank!